Autonomous quantum error correction with superconducting qubits

Joachim Cohen

To cite this version:

Joachim Cohen. Autonomous quantum error correction with superconducting qubits. Physics [physics]. Université Paris sciences et lettres, 2017. English. NNT : 2017PSLEE008 . tel-01545186

HAL Id: tel-01545186
https://theses.hal.science/tel-01545186v1
Submitted on 22 Jun 2017

THÈSE DE DOCTORAT

de l'Université de recherche Paris Sciences et Lettres
PSL Research University

Préparée à Ecole Normale Supérieure

Autonomous quantum error correction with superconducting qubits

Vers le calcul quantique tolérant à l'erreur adapté aux expériences en circuit QED

Ecole doctorale n°564

Ecole Doctorale de Physique d'Ile de France

Spécialité PHYSIQUE QUANTIQUE

COMPOSITION DU JURY :

M. ESTEVE Daniel
CEA Saclay, Président du jury

M. BLAIS Alexandre
Université de Sherbrooke

M. JOHANSSON Göran
Chalmers University of Technology

M. CIUTI Cristiano
LMPQ à Paris Diderot

Mme. COTTET Audrey
Laboratoire Pierre Aigrain à l'ENS Paris

M. HOFHEINZ Max
CEA Grenoble

M. MIRRAHIMI Mazyar
INRIA Paris

Soutenue par **Joachim COHEN**
le 3 février 2017

Dirigée par **Mazyar MIRRAHIMI**

ENS
ÉCOLE NORMALE SUPÉRIEURE

PSL
RESEARCH UNIVERSITY PARIS

Acknowledgements

Tout d'abord, j'aimerais chaudement remercier Mazyar Mirrahimi, pour avoir été un directeur de thèse remarquable. Sans une supervision scientifique de cette qualité, ce travail n'aurait jamais vu le jour. En particulier, je lui suis reconnaissant d'avoir été très présent tout au long de ces trois années.

A second set of thanks goes to my direct collaborators, Clarke Smith and Michel Devoret. In particular, I would like to express my gratitude to Michel for welcoming me several times in his lab at Yale. It was a great opportunity to work in such a stimulating environment. I am also grateful to my friends and colleagues Ananda Roy and Zlatko Minev, who have made my stays in New Haven all the more enjoyable.

Ensuite, j'aimerais remercier tous les membres de l'équipe Quantic à Paris : les théoriciens de l'INRIA et du CAS aux Mines, ainsi que les expérimentateurs du LPA à l'ENS. Ce travail a grandement bénéficié de cet environnement scientifique de qualité. Tout particulièrement, je remercie Pierre Rouchon and Rémi Azouit pour les discussions très utiles à ce travail, et Lucas Verney pour ses commentaires sur ce manuscrit. De plus, j'aimerais remercier également tous les membres du CAS y compris ceux qui ne font pas partie de l'équipe Quantic, pour leur accueil chaleureux durant les deux premières années de thèse.

I would like to thank Alexandre Blais and Göran Johansson for accepting to be my referees, and Daniel Esteve, Audrey Cottet, Max Hofheinz and Cristiano Ciuti for accepting to be members of the jury. Their thorough comments led to significant improvements of this manuscript. In particular, it was an honor to count Daniel Esteve among the members of the jury, who introduced me to the field of cQED through a fascinating course during my Master studies, and who got me in touch with Mazyar Mirrahimi.

Enfin, j'aimerais exprimer ma reconnaissance à mes parents pour leur soutien continu dans mes études, et en particulier à mon père, qui m'a sans doute communiqué ce goût de la physique et des sciences.

Abstract

Quantum systems can be used as a resourceful support for information processing. However, because of their interaction with a noisy environment, the coherence times of these systems remain relatively short, leading to a major obstacle in the development of quantum information processing. Quantum Error Correction (QEC) has emerged as an inevitable and viable tool to overcome these limitations. By redundantly encoding the information in a subtle manner, the damage to the system is identified by probing some observables, and the logical information can be recovered. The common approach consists in measuring these observables in a quantum non-demolition manner and next performing an error correction, through an appropriate real-time feedback strategy. Autonomous QEC proposes to circumvent the need for fast real-time analysis of these error syndrome measurements and the associated feedback control, by directly building the feedback loop into the system. Such autonomous schemes usually lead to major experimental simplifications as they are more robust against the variations of the system's parameters and do not require extensive experimental calibrations.

In this thesis, we develop several tools in the direction of autonomous QEC with superconducting qubits. The lifetime improvement of superconducting qubits over the past twenty years, as well as their high degree of controllability, has made them well-suited entities for quantum information processing. Building on this progress, here we design an autonomous QEC scheme based on quantum reservoir engineering, in which transmon qubits are coupled to lossy modes. Through an engineered interaction between these systems, the entropy created by eventual errors is evacuated via the dissipative modes.

The second part of this work focus on the recently developed cat codes, through which the logical information is encoded in the large Hilbert space of a harmonic oscillator. We propose a scheme to perform continuous and quantum non-demolition measurements of photon-number parity in a microwave cavity, which corresponds to the error syndrome in the cat code. In our design, we exploit the strongly nonlinear Hamiltonian of a high-impedance Josephson circuit, coupling a high-Q storage cavity mode to a low-Q readout one. Last, as a follow up of the above results, we present several continuous and/or autonomous QEC schemes using the cat code. These schemes provide a robust protection against dominant error channels in the presence of multi-photon driven dissipation.

Résumé

Les systèmes quantiques constituent des supports potentiels riches en application pour le traitement de l'information. Cependant, les interactions non contrôlées de ces systèmes avec leur environnement limitent leurs temps de cohérence et constituent un obstacle majeur pour le développement du traitement de l'information quantique. La Correction d'Erreur Quantique (CEQ) s'est imposée comme un outil incontournable et viable afin de combattre ces limitations. A travers un encodage redondant et subtil de l'information, les dégâts causés sur le système sont identifiés par la mesure d'observables physiques, permettant ainsi de récupérer l'information logique. L'approche usuelle consiste à réaliser une mesure de ces observables sans perturber l'état du système, mesure dite non-destructrice, suivie par la correction d'éventuelles erreurs dans le cadre d'une stratégie de rétroaction en temps réel. La CEQ autonome propose de s'affranchir de l'analyse rapide en temps réel des mesures de syndromes d'erreurs ainsi que de la rétroaction associée, en implémentant la boucle de rétroaction directement dans le système. Ces protocoles autonomes mènent bien souvent à de grandes simplifications expérimentales, car ils s'avèrent robustes aux variations des paramètres du système, et ne nécessitent pas de calibrations expérimentales poussées.

Dans cette thèse, nous développons plusieurs outils pour la CEQ autonome avec les qubits supraconducteurs. L'amélioration du temps de vie des qubits supraconducteurs au cours des vingt dernières années, ainsi que leur haut niveau de contrôlabilité, en font des candidats potentiels pour le traitement de l'information quantique. Ici, nous proposons un schéma de CEQ autonome qui repose sur la technique du « reservoir engineering », dans lequel trois qubits de type transmon sont couplés à un ou plusieurs modes dissipatifs. Grâce à la mise au point d'une interaction effective entre les systèmes, l'entropie créée par les éventuelles erreurs est évacuée à travers les modes dissipatifs.

La deuxième partie de ce travail porte sur un type de code récemment développé, le code des chats, à travers lequel l'information logique est encodée dans le vaste espace de Hilbert d'un oscillateur harmonique. Nous proposons un protocole pour réaliser des mesures continues et non-perturbatrices de la parité du nombre de photons dans une cavité micro-onde, ce qui correspond au syndrome d'erreur pour le code des chats. Notre schéma exploite le Hamiltonien fortement non-linéaire d'un circuit Josephson de haute impédance qui couple un mode de cavité de stockage haut-Q avec un mode de lecture bas-Q. Enfin, en utilisant les résultats précédents, nous présentons plusieurs protocoles de CEQ continus et/ou autonomes basés sur le code des chats. Ces protocoles offrent une protection robuste contre les canaux d'erreur dominants en présence de dissipation stimulée à plusieurs photons.

Table of contents

Chapter 1

Introduction

Table of contents

1.1 Quantum Error Correction

1.1.1 Overview

Decoherence is regarded as the major obstacle towards scalable and robust processing of quantum information. It is caused by the interaction of a quantum system with its noisy environment, through which the system gets entangled with an infinite number of degrees of freedom. Despite one's effort to isolate the quantum system of interest, some amount of undesired interaction persists limiting the lifetime of the information. In the case of superconducting qubits, this effort over the past two decades has led to an increase of the lifetime from a few nano-seconds [56] to 100 μs in best cases [61, 72]. Quantum Error Correction (QEC) has emerged as an inevitable tool to go beyond this limitation and significantly enhance the lifetime of quantum information [57, 18]. By designing an encoded logical qubit, possibly using many physical qubits, one protects the quantum information against major decoherence channels and hence ensures a longer coherence time than a physical qubit [80, 81].

The contents of this section are strongly inspired by [57] and [66], and set a general framework for QEC. In Subsection 1.1.2, we briefly introduce the formalism of open quantum systems. More precisely, we give a general description of quantum operations acting on a system and in particular modeling the occurring errors. Such a quantum error channel is described in Subsection 1.1.3 through the analysis of a quantum code, the three-qubit bit-flip code. Next, the Subsection 1.1.4 recalls some general results on QEC. In particular, given a quantum code, it provides a necessary and sufficient condition for a set of errors to be correctable. Finally, in Subsection 1.1.5, we present the concepts of continuous QEC and quantum reservoir engineering. We illustrate how one can combine these methodologies to achieve autonomous quantum error correction schemes, leading to hardware shortcuts for experimental developments.

1.1.2 Quantum maps and decoherence

The state of an open quantum system S is described by a density matrix $\boldsymbol{\rho}_S$, a semi-definite positive hermitian operator of unit trace, defined on the Hilbert space $\mathscr{H}_S$ of the system. Its dynamics over a time interval τ, is given by a trace-preserving *quantum operation*

$$\forall \boldsymbol{\rho}_S,\ \mathbb{E}(\boldsymbol{\rho}_S) = \sum_{\mu} \mathbf{M}_\mu \boldsymbol{\rho}_S \mathbf{M}_\mu^\dagger. \tag{1.1}$$

Here, the trace-preserving property of the above operation is ensured via the relation $\sum_\mu \mathbf{M}_\mu^\dagger \mathbf{M}_\mu = \mathbf{I}_S$. The *superoperator* $\mathbb{E}$ is also called a quantum map or a Kraus map, and $\{\mathbf{M}_\mu\}$ is a set of associated Kraus operators. This choice of Kraus operators is not unique as the operators $\tilde{\mathbf{M}}_\mu = \sum_\nu r_{\mu,\nu}\mathbf{M}_\nu$, with $(r_{\mu,\nu})$ an arbitrary unitary matrix, satisfy $\sum_\mu \tilde{\mathbf{M}}_\mu \boldsymbol{\rho}_S \tilde{\mathbf{M}}_\mu^\dagger = \sum_\mu \mathbf{M}_\mu \boldsymbol{\rho}_S \mathbf{M}_\mu^\dagger$ for all $\boldsymbol{\rho}_S$. Note that, a pure state of the quantum system S, corresponding to a density matrix of the form $\boldsymbol{\rho}_S = |\psi\rangle\langle\psi|$, is generally mapped to a mixed state, therefore leading to its decoherence.

So far, we have modeled the harmful decoherence phenomena as a quantum operation. We will see throughout this thesis, that it is also possible to engineer a particular quantum operation that rather purifies a state by evacuating the entropy of the quantum system. More precisely, such a quantum operation $\mathbb{R}$ can correct the decoherence (given by $\mathbb{E}$) acting on a manifold $\mathscr{C} \subset \mathscr{H}_S$, where the information is encoded:

$$(\mathbb{R} \circ \mathbb{E})(\boldsymbol{\rho}) = \boldsymbol{\rho} \qquad \forall \boldsymbol{\rho} \in \mathscr{C}.$$

1.1.3 An example: three-qubit bit-flip code

In classical information theory, one can protect a logical bit of information against bit-flip errors, by encoding it, redundantly, in three bits: $0 \rightarrow 0_L = 000$ and $1 \rightarrow 111$. Provided that the probability p for an error to occur on a bit is small, this code prevents these errors from damaging the information. Indeed, through a majority voting, the erroneous state 100, is associated to 000. This reduces the error probability from p to $3p^2$ (case where two bits have flipped).

There exists a direct quantum analog, called the three-qubit bit-flip code, which protects the information against single bit-flip errors mapping an arbitrary superposition state $c_0|0\rangle + c_1|1\rangle$ of a qubit to $c_0|1\rangle + c_1|0\rangle$. Three qubits are used to encode a single logical qubit with $|0_L\rangle = |000\rangle$ and $|1_L\rangle = |111\rangle$. Starting from a superposition in the *code space* $\mathscr{E}_0 = \text{span}\{|000\rangle, |111\rangle\}$, a single bit-flip error maps the states to one of the *error subspaces* $\mathscr{E}_1 = \text{span}\{|100\rangle, |011\rangle\}$, $\mathscr{E}_2 = \text{span}\{|010\rangle, |101\rangle\}$ or $\mathscr{E}_3 = \text{span}\{|001\rangle, |110\rangle\}$. We can associate to these error processes, the Kraus operators $\mathscr{M}_0 = \sqrt{1-3p}\mathbf{I}$, $\mathscr{M}_1 = \sqrt{p}\boldsymbol{\sigma}_x^1$, $\mathscr{M}_2 = \sqrt{p}\boldsymbol{\sigma}_x^2$ and $\mathscr{M}_3 = \sqrt{p}\boldsymbol{\sigma}_x^3$, where $p \ll 1$ is the probability of a single bit-flip, $\mathbf{I}$ is the identity on the qubits Hilbert space, and $\boldsymbol{\sigma}_x^k$ is the Pauli matrix along the X axis of the k'th qubit. The associated quantum operation $\mathbb{E}$ reads

$$\forall \boldsymbol{\rho},\ \mathbb{E}(\boldsymbol{\rho}) = (1-3p)\boldsymbol{\rho} + p\boldsymbol{\sigma}_x^1\boldsymbol{\rho}\boldsymbol{\sigma}_x^1 + p\boldsymbol{\sigma}_x^2\boldsymbol{\rho}\boldsymbol{\sigma}_x^2 + p\boldsymbol{\sigma}_x^3\boldsymbol{\rho}\boldsymbol{\sigma}_x^3.$$

The measurement of the two-qubit parities $\boldsymbol{\sigma}_z^1\boldsymbol{\sigma}_z^2$ and $\boldsymbol{\sigma}_z^2\boldsymbol{\sigma}_z^3$ reveals the subspace on which the three-qubit system lies, without leaking information about the quantum superposition. The subspace $\mathscr{E}_0$ corresponds the error syndrome $\{\boldsymbol{\sigma}_z^1\boldsymbol{\sigma}_z^2, \boldsymbol{\sigma}_z^2\boldsymbol{\sigma}_z^3\} = \{1,1\}$, $\mathscr{E}_1$ to $\{-1,1\}$, $\mathscr{E}_2$ to $\{-1,-1\}$, and $\mathscr{E}_3$ to $\{1,-1\}$. One can recover the initial state by applying the inverse operation. Here, it corresponds to flipping back the qubit on which the error occurred. This recovery operation $\mathbb{R}$ is defined by

$$\forall \boldsymbol{\rho},\ \mathbb{R}(\boldsymbol{\rho}) = \boldsymbol{\Pi}_{\mathscr{E}_0}\boldsymbol{\rho}\boldsymbol{\Pi}_{\mathscr{E}_0} + \boldsymbol{\sigma}_x^1\boldsymbol{\Pi}_{\mathscr{E}_1}\boldsymbol{\rho}\boldsymbol{\Pi}_{\mathscr{E}_1}\boldsymbol{\sigma}_x^1 + \boldsymbol{\sigma}_x^2\boldsymbol{\Pi}_{\mathscr{E}_2}\boldsymbol{\rho}\boldsymbol{\Pi}_{\mathscr{E}_2}\boldsymbol{\sigma}_x^2 + \boldsymbol{\sigma}_x^3\boldsymbol{\Pi}_{\mathscr{E}_3}\boldsymbol{\rho}\boldsymbol{\Pi}_{\mathscr{E}_3}\boldsymbol{\sigma}_x^3,$$

where $\boldsymbol{\Pi}_{\mathscr{E}_i}$ is the projector on the subspace $\mathscr{E}_i$. One can easily check that $\mathbb{R}$ is a recovery operation for the error map $\mathbb{E}$, with

$$\forall \boldsymbol{\rho} \in \mathscr{E}_0,\ (\mathbb{R} \circ \mathbb{E})(\boldsymbol{\rho}) = \boldsymbol{\rho}.$$

Similarly, the three-qubit phase-flip code protects a logical qubit against single phase flips, mapping $c_0|0\rangle + c_1|1\rangle$ to $c_0|0\rangle - c_1|1\rangle$. Encoding the information in the basis $|0_L\rangle = |+++\rangle$

and $|1_L\rangle = |---\rangle$ with $|\pm\rangle = (|0\rangle \pm |1\rangle)/\sqrt{2}$, the error syndromes are provided by the measurement of the two-qubit operators $\boldsymbol{\sigma}_x^1\boldsymbol{\sigma}_x^2$ and $\boldsymbol{\sigma}_x^2\boldsymbol{\sigma}_x^3$.

1.1.4 Basics of quantum error correction

In quantum error correction, one encodes the information in a subspace $\mathscr{C}$, the code space, of a larger Hilbert space. The decoherence channels are described by quantum maps (described by a set of Kraus operators) acting on the code space. These Kraus operators are referred to as the *errors*. The protection by QEC is characterized by the code space $\mathscr{C}$ and the images of this code space through various errors. We start by giving a necessary and sufficient condition for the Kraus operators, to ensure the existence of a recovery operation. Next, through an error discretization theorem, we explain that linear combinations of correctable errors remain correctable by the same code. From this theorem, one infers that an arbitrary single-qubit error can be corrected with a code correcting for bit flips, phase flips, and simultaneous bit flip and phase flip. Finally, we present a well-known example of such a quantum code, the so-called Shor code [80].

1.1.4.1 Quantum error correction condition

Let us consider that a quantum system of interest is subject to a noise map $\mathbb{E}$, represented by a set of Kraus operators (or errors) $\{\mathbf{M}_\mu\}$. The logical information is encoded in a subspace $\mathscr{C}$. Can we find a quantum operation $\mathbb{R}$ that recovers the initial state, i.e $\forall \boldsymbol{\rho} \in \mathscr{C}$, $(\mathbb{R}\circ\mathbb{E})(\boldsymbol{\rho}) = \boldsymbol{\rho}$?

A central theorem in QEC theory addresses this problem by giving a necessary and sufficient condition on the errors $\mathbf{M}_\mu$ (Theorem 10.1 of [57]). There exists a recovery operation $\mathbb{R}$ for the noise map $\mathbb{E}$, if and only if

$$\boldsymbol{\Pi}_{\mathscr{C}}\mathbf{M}_\mu^\dagger\mathbf{M}_\nu\boldsymbol{\Pi}_{\mathscr{C}} = c_{\mu\nu}\boldsymbol{\Pi}_{\mathscr{C}}. \tag{1.2}$$

Here $\boldsymbol{\Pi}_{\mathscr{C}}$ is the projection operator over $\mathscr{C}$ and $c_{\mu\nu} = c_{\nu\mu}^*$ is a complex number. Under this condition, $\{\mathbf{M}_\mu\}$ is a set of *correctable errors* for the code defined by $\mathscr{C}$.

Let us provide an intuitive explanation for this theorem. First, we can choose a more suitable set of Kraus operators $\{\mathbf{E}_\nu\}$ for the map $\mathbb{E}$, such that condition (1.2) becomes $\boldsymbol{\Pi}_{\mathscr{C}}\mathbf{E}_\mu^\dagger\mathbf{E}_\nu\boldsymbol{\Pi}_{\mathscr{C}} = d_\mu\delta_{\mu,\nu}\boldsymbol{\Pi}_{\mathscr{C}}$, with $d_\mu > 0$ and $\sum_\mu d_\mu = 1$. Furthermore, $\delta_{\mu,\nu} = 1$ if and only if $\mu = \nu$ and $\delta_{\mu,\nu} = 0$ otherwise. This change of Kraus operators is justified in the next paragraph. As two distinct errors $\mathbf{E}_\mu$ and $\mathbf{E}_\nu$ satisfy $\boldsymbol{\Pi}_{\mathscr{C}}\mathbf{E}_\mu^\dagger\mathbf{E}_\nu\boldsymbol{\Pi}_{\mathscr{C}} = 0$, they map the code space $\mathscr{C}$ to mutually orthogonal error subspaces $\mathscr{E}_\mu$ and $\mathscr{E}_\nu$. These errors can be unambiguously diagnosed by measuring a set of commuting observables which admit the subspaces $\mathscr{E}_\nu$ as common eigenspaces. In addition, considering an orthonormal basis, $\{|i_L\rangle\}$, of the code space, through the relation $\langle i_L|\frac{\mathbf{E}_\mu^\dagger}{\sqrt{d_\mu}}\frac{\mathbf{E}_\mu}{\sqrt{d_\mu}}|j_L\rangle = \delta_{i,j}$, an error $\mathbf{E}_\mu$ rotates this logical basis to an orthonormal basis of the error subspace $\mathscr{E}_\mu$. This ensures that once an error is diagnosed, one can reverse the operation by applying the inverse unitary. Equivalently, it means that no information about the logical superposition is leaked to the environment through the error channels $\mathbf{E}_\mu$. More precisely, we have $\mathbf{E}_\mu\boldsymbol{\Pi}_{\mathscr{C}} = \sqrt{d_\mu}\mathbf{U}_\mu\boldsymbol{\Pi}_{\mathscr{C}}$, with $\mathbf{U}_\mu$ a unitary operation, and therefore $\boldsymbol{\Pi}_{\mathscr{E}_\mu} = \mathbf{U}_\mu\boldsymbol{\Pi}_{\mathscr{C}}\mathbf{U}_\mu^\dagger$ is the projector on the error subspace $\mathscr{E}_\mu$. The mutual orthogonality of the error subspaces is expressed through the relation $\boldsymbol{\Pi}_{\mathscr{E}_\mu}\boldsymbol{\Pi}_{\mathscr{E}_\nu} = \delta_{\mu,\nu}\boldsymbol{\Pi}_{\mathscr{E}_\mu}$. The quantum operation $\mathbb{R}$ described by the Kraus operators $\{\mathbf{R}_\nu = \mathbf{U}_\nu^\dagger\boldsymbol{\Pi}_{\mathscr{E}_\nu}\}$ is a recovery map for the quantum operation $\mathbb{E}$. Indeed, for an initial state $\boldsymbol{\rho} \in \mathscr{C}$, we have

$$
\begin{aligned}
(\mathbb{R}\circ\mathbb{E})(\boldsymbol{\rho}) &= \sum_{\nu,\mu}\mathbf{R}_\nu\mathbf{E}_\mu\boldsymbol{\rho}\mathbf{E}_\mu^\dagger\mathbf{R}_\nu^\dagger \\
&= \sum_{\nu,\mu} d_\mu\mathbf{U}_\nu^\dagger\boldsymbol{\Pi}_{\mathscr{E}_\nu}\boldsymbol{\Pi}_{\mathscr{E}_\mu}\mathbf{U}_\mu\boldsymbol{\rho}\mathbf{U}_\mu^\dagger\boldsymbol{\Pi}_{\mathscr{E}_\mu}\boldsymbol{\Pi}_{E_\nu}\mathbf{U}_\nu \\
&= \sum_{\nu} d_\nu\mathbf{U}_\nu^\dagger\mathbf{U}_\nu\boldsymbol{\rho}\mathbf{U}_\nu^\dagger\mathbf{U}_\nu = \boldsymbol{\rho}
\end{aligned}
$$

In this paragraph, we justify the existence of a set of operators $\{\mathbf{E}_\nu\}$ for the map $\mathbb{E}$, such that condition (1.2) becomes $\boldsymbol{\Pi}_{\mathscr{C}}\mathbf{E}_\mu^\dagger\mathbf{E}_\nu\boldsymbol{\Pi}_{\mathscr{C}} = d_\mu\delta_{\mu,\nu}\boldsymbol{\Pi}_{\mathscr{C}}$. The hermitian matrix c of eq. (1.2) can be written as $c = pdp^\dagger$, with d a diagonal matrix and p a unitary matrix. We define the operators $\mathbf{E}_\nu = \sum_\mu p_{\mu\nu}\mathbf{M}_\mu$. They satisfy

$$
\boldsymbol{\Pi}_{\mathscr{C}}\mathbf{E}_{\nu_1}^\dagger\mathbf{E}_{\nu_2}\boldsymbol{\Pi}_{\mathscr{C}} = (\sum_{\mu_1,\mu_2} p_{\mu_1\nu_1}^* p_{\mu_2\nu_2} c_{\mu_1\mu_2})\boldsymbol{\Pi}_{\mathscr{C}} = \delta_{\nu_1,\nu_2} d_{\nu_1,\nu_1}\boldsymbol{\Pi}_{\mathscr{C}},
$$

as $d_{\nu_1,\nu_2} = \sum\limits_{\mu_1,\mu_2} p_{\mu_1\nu_1}^* p_{\mu_2\nu_2} c_{\mu_1\mu_2}$ stems from the relations $d = p^\dagger cp$. Following Subsection 1.1.2, the matrix p being unitary, the map $\mathbb{E}$ is equivalently described by the set of Kraus operators $\{\mathbf{E}_\nu\}$.

1.1.4.2 Error discretization

Provided that the logical information is encoded in a code space $\mathscr{C}$, the condition (1.2) states the existence of a recovery operation for a given set of errors. Here we see that, a quantum code can be subject to an infinite number of noise maps, and still remain correctable. It would greatly simplify the design of QEC protocols, if a same correction operation $\mathbb{R}$ could work for various correctable sets of errors. Fortunately, this is the case through the following sufficient condition [57] :

Consider $\{\mathbf{E}_\nu\}$ a set of correctable errors associated to a noise map $\mathbb{E}$, and an associated recovery operation $\mathbb{R}$. Let $\mathbb{F}$ be the noise map represented by the set of errors $\{\mathbf{F}_\mu\}$, where the $\mathbf{F}_\mu$ are linear combinations of the operators $\mathbf{E}_\nu$. Then the set $\{\mathbf{F}_\mu\}$ is a correctable set of errors with the same recovery operation $\mathbb{R}$.

While this statement can be easily proven by inserting into the equation $\mathbb{R} \circ \mathbb{F}(\boldsymbol{\rho}) = \boldsymbol{\rho}$, the relation $\mathbf{F}_\mu = \sum_\nu \lambda_{\mu\nu} \mathbf{E}_\nu$, here we provide a more physical insight into this result. The noise map $\mathbb{F}$ can be represented by a unitary operation U_{SE} acting on the system and an environment E, with $\mathbf{U}_{SE}(|\psi\rangle_S \otimes |g_{\mu_0}\rangle_E) = \sum_\mu (\mathbf{F}_\mu |\psi\rangle_S) \otimes |g_\mu\rangle_E$. Here, we have assumed the initial state of system S to be a pure state for simplicity sakes. By inserting $\mathbf{F}_\mu = \sum_\nu \lambda_{\mu\nu} \mathbf{E}_\nu$, we obtain $\mathbf{U}_{SE}(|\psi\rangle_S \otimes |g_{\nu_0}\rangle_E) = \sum_\nu (\mathbf{E}_\nu |\psi\rangle_S) \otimes |e_\nu\rangle_E$, with the states $|e_\nu\rangle_E = \sum_\mu \lambda_{\mu\nu} |g_\mu\rangle_E$. Note that, the states $|e_\nu\rangle_E$ are not necessarily orthogonal as the matrix $(\lambda_{\mu\nu})$ is not necessarily unitary. The recovery operation $\mathbb{R}$ associated to the error set $\{\mathbf{E}_\nu\}$, can be described by the set of Kraus operators $\mathbf{R}_\nu = \mathbf{U}_\nu^\dagger \boldsymbol{\Pi}_{\mathscr{E}_\nu}$ (see previous subsection). Similarly to the noise map $\mathbb{E}$, the quantum operation $\mathbb{R}$ can be equivalently represented by a unitary operation $\mathbf{U}_{SA}$ acting on the system S and an ancillary system A, such that $\mathbf{U}_{SA}(|\psi\rangle_S \otimes |a_{\mu_0}\rangle_A) = \sum_\mu (\mathbf{R}_\mu |\psi\rangle_S) \otimes |a_\mu\rangle_A$ for all states $|\psi\rangle_S$. Therefore, for a state $|\psi\rangle_S \in \mathscr{C}$, the state after the correction reads

$$\begin{aligned}
\mathbf{U}_{SA}[\mathbf{U}_{SE}(|\psi\rangle_S \otimes |g_{\nu_0}\rangle_E) \otimes |a_{\mu_0}\rangle_A] &= \sum_\nu \mathbf{U}_{SA}[(\mathbf{E}_\nu |\psi\rangle_S \otimes |a_{\mu_0}\rangle_A)] \otimes |e_\nu\rangle_E \\
&= \sum_{\mu,\nu} (\mathbf{U}_\mu^\dagger \boldsymbol{\Pi}_{\mathscr{E}_\mu} \mathbf{E}_\nu |\psi\rangle_S) \otimes |e_\nu\rangle_E \otimes |a_\mu\rangle_A \\
&= |\psi_S\rangle \otimes [\sum_\nu \sqrt{d_\nu} |e_\nu\rangle_E \otimes |a_\nu\rangle_A].
\end{aligned}$$

Here, to obtain the third line from the second one, we have used the fact that $\mathbf{U}_\mu^\dagger \boldsymbol{\Pi}_{\mathscr{E}_\mu} \mathbf{E}_\nu = d_\nu \delta_{\mu,\nu} \boldsymbol{\Pi}_{\mathscr{C}}$. Note that the state of the environment and the ancilla $\sum_\nu \sqrt{d_\nu} |e_\nu\rangle_E \otimes |a_\nu\rangle_A$ does not depend on $|\psi_S\rangle$, which means that no information on this state has leaked out to the environment nor the ancilla.

1.1.4.3 Example: a multi-qubit code

The theory provided in previous two subsections applies to general QEC schemes. In particular, they apply to encodings on a single quantum harmonic oscillator, where the redundancy is insured through the infinite dimensional Hilbert space. An example of such codes, the cat code, is analyzed in detail in Section 1.2. In this subsection, though, we focus on multi-qubit codes similar to three-qubit bit-flip code. As we shall see, the single-qubit errors can be cast into three types of errors.

Here, we study the effect of a noise map defined by the Kraus operators $\{\mathbf{E}_\mu\}$ on a system S composed of n qubits. Let us denote X, Y and Z the standard Pauli matrices, and I the identity on a qubit's Hilbert space. As $\{I,X,Y,Z\}$ forms a basis for the space of linear operators on $\mathbb{C}^2$, the Kraus operators $\mathbf{E}_\mu$ are linear combinations of operators of the Pauli group $G_n = \{I,X,Y,Z\}^{\otimes n}$. In particular, a single-qubit error is a linear combination of the operators I, X_i, Y_j and Z_k acting on a single qubit, where X_i is the operator that acts as X on the qubit i and as the identity on the other qubits (idem for Y_j and Z_k). An error X_k is called a bit-flip error as it maps $|0\rangle \leftrightarrow |1\rangle$, and an error Z_k is a phase-flip error, since it maps $|0\rangle \rightarrow |0\rangle$ and $|1\rangle \rightarrow -|1\rangle$. The error $Y = iZX$ can be seen as a simultaneous bit flip and phase flip.

From the error discretization theorem follows a remarkable corollary. Consider the set of single qubit errors $\{I, X_j, Y_j, Z_j,\ j = 1...n\}$. Let us assume that this set (unnormalized here) is a correctable set of errors and $\mathbb{R}$ a recovery operation for this set. Then any arbitrary single qubit noise map is correctable by the map $\mathbb{R}$. In other words, to protect the information against any kind of noise occurring on a single qubit, it is enough to correct for single phase flips, bit flips and simultaneous bit flips and phase flips. The Shor code [80], presented below, provides such a protection.

One can encode a single logical qubit using nine "physical" qubits. The idea consists in a concatenation of a three-qubit bit-flip code with a three-qubit phase-flip code. First, we group the qubits three by three, and each group encodes a single intermediate logical qubit via the three-qubit bit-flip code. Next, the three intermediate qubits, protected against bit flips, are used to encode a single logical qubit through the three-qubit phase-flip code. The logical states, $|0_L\rangle$ and $|1_L\rangle$, are given by

$$|0_L\rangle = |+\rangle_{1,L} \otimes |+\rangle_{2,L} \otimes |+\rangle_{3,L} = \frac{(|000\rangle + |111\rangle) \otimes (|000\rangle + |111\rangle) \otimes (|000\rangle + |111\rangle)}{2\sqrt{2}}$$

$$|1_L\rangle = |-\rangle_{1,L} \otimes |-\rangle_{2,L} \otimes |-\rangle_{3,L} = \frac{(|000\rangle - |111\rangle) \otimes (|000\rangle - |111\rangle) \otimes (|000\rangle - |111\rangle)}{2\sqrt{2}}$$

Let us study the effect of single bit flips and single phase flips on the code space. The logical qubit is protected against bit flips as it is encoded by intermediate ones which are themselves protected. More precisely, a single bit-flip error occurring on the first three qubits is revealed by measuring the two joint-parties Z_1Z_2 and Z_2Z_3, and so on for the two other groups of three qubits. Hence, single bit flips are revealed by measuring the six two-qubit parities $\{Z_1Z_2, Z_2Z_3, Z_4Z_5, Z_5Z_6, Z_7Z_8, Z_8Z_9\}$. Next, by construction, the logical qubit is protected against the single phase flips of the intermediate logical qubits. Note, however, that a single phase flip occurring on any of the three "physical" qubits, results in a phase flip of the intermediate qubit. These phase flips are identified by the measurement of the operators $X_{1,L}X_{2,L} = X_1X_2X_3X_4X_5X_6$ and $X_{2,L}X_{3,L} = X_4X_5X_6X_7X_8X_9$, where $X_{1,L}$, $X_{2,L}$ and $X_{3,L}$ are the logical X operators of the intermediate qubits. If a phase flip on the first intermediate qubit is diagnosed, the initial state is recovered by applying any of the operators Z_1, Z_2 and Z_3. Finally, note that an error Y_i is diagnosed as a bit flip X_i, and a phase flip $Z_{j,L}$ of the corresponding intermediate qubit. Consequently, such an error is also correctable.

Since the Shor code corrects single qubit errors X_i, Y_i and Z_i, it corrects any arbitrary single qubit errors.

1.1.5 Autonomous QEC

In the previous subsections, we have discussed some general results on QEC. The system, redundantly encoding the logical information, is subject to a noise map $\mathbb{E}$. The initial state is then restored through a recovery procedure represented by the map $\mathbb{R}$. However, we haven't discussed yet how these recovery operations are physically implemented. The subsection 1.1.5.1 introduces the concept of continuous QEC versus discrete QEC. The Subsection 1.1.5.2 presents reservoir engineering as a mean to achieve continuous autonomous QEC, and provides a few examples of existing QEC schemes based on this method. Note that, in this manuscript we consider a correction scheme autonomous, if it does not involve a classical synthesis of a measurement signal in a feedback strategy. This is to be compared to the so-called measurement-based feedback.

1.1.5.1 Continuous QEC vs discrete QEC

So far, we have implicitly adopted a discrete vision of QEC. The system undergoes a noise map, followed by a correction step. The noise map $\mathbb{E}_T$ corresponds to the evolution superoperator over a time duration T of the system: $\boldsymbol{\rho}(t+T) = \mathbb{E}_T(\boldsymbol{\rho})$. Consider that after each time interval T_{error}, one applies a recovery operation $\mathbb{R}$. The state of the system at time $t = nT_{\text{error}}$, is $\boldsymbol{\rho}(nT_{\text{error}}) = [(\mathbb{R}\circ\mathbb{E}_{T_{\text{error}}})\circ\cdots\circ(\mathbb{R}\circ\mathbb{E}_{T_{\text{error}}})](\boldsymbol{\rho}(0))$. Here, the time T_{error} between two successive recovery operations, is assumed to be small enough, so that the error model remains simple enough to be correctable. This recovery operations often involves a projective measurement of some error syndromes followed by an appropriate unitary operation (see Subsection 1.1.4.1). While the above description neglects the finite time needed for the recovery operation, the finite bandwidth of the measurement protocol usually limits the performance. This aspect was carefully analyzed in the experimental work of Kelly et al. [37], where a repetition bit-flip code was realized.

Continuous QEC [1], as opposed to discrete QEC, considers a situation where the recovery operation is applied continuously in time. Continuous QEC was first explored by Ahn et al.

in a measurement-based feedback strategy [1]. In this article, several continuous correction schemes based on existing QEC codes are presented. The error syndromes are continuously monitored through weak measurements, and the corresponding correction is achieved by implementing a time-dependent feedback Hamiltonian. This Hamiltonian, based on the measurement records, continuously steers the system back to the coding subspace. Let us define $\mathbb{R}_t$ the evolution operation on time duration t, resulting from the dynamics of the correction procedure only, while excluding the decoherence channels resulting in $\mathbb{E}_t$. Note that, $\mathbb{R}_t$ represents a recovery operation only for large enough times $t > T_{\text{corr}}$ (larger e.g. than the error syndrome measurement time). The evolution operator $\mathbb{F}_T$ of the continuous QEC scheme, can intuitively be thought as the limit $\mathbb{F}_T = \lim_n (\mathbb{R}_{T/n} \circ \mathbb{E}_{T/n})^n$.

1.1.5.2 Continuous autonomous QEC via reservoir engineering

Reservoir engineering consists of carefully coupling the system we wish to control/manipulate, with a dissipative reservoir. The idea is to transfer the entropy introduced by errors in the system of interest, onto an ancillary system (reservoir). This entropy is next evacuated via the strong dissipation of the ancilla. Several experiments based on this method have led to the continuous stabilization of specific quantum states, in circuit quantum electrodynamics [55, 24, 79, 45] .

In [24], Geerlings et al. demonstrated the continuous stabilization of the ground state of a transmon qubit. In this experiment, a transmon qubit is dispersively coupled with a lossy driven resonator, via a Hamiltonian of the form $-\hbar\chi\boldsymbol{\sigma}_Z\mathbf{a}^\dagger\mathbf{a}/2$. Here, $\boldsymbol{\sigma}_Z$ and $\mathbf{a}$ denote the $Z-$Pauli matrix of the qubit and the annihilation operator of the resonator mode. The transmon spontaneously jumps to the excited state $|e\rangle$ at a rate $\gamma_\uparrow$, while the cavity decay rate κ_c is taken to be much larger than $\gamma_\uparrow$. Through the dispersive coupling, the frequency of the resonator depends on the qubit state, and the qubit frequency depends on the number of photons in the resonator. In this protocol, one applies a drive at frequency ω_c^g, where ω_c^g is the frequency of the cavity when the qubit is in the ground state $|g\rangle$. If the transmon is in $|g\rangle$, the resonator evolves towards a coherent state $|\alpha\rangle$ in a time of order $1/\kappa_c$, where α is given by the ratio between the drive amplitude and the cavity rate κ_c. In this case, the state of the global system is $|g\rangle \otimes |\alpha\rangle$. If the transmon is in the excited state $|e\rangle$, the drive is off-resonant, and the cavity evolves to the vacuum state $|0\rangle$ in a mean time $1/\kappa_c$, leading to the global system state $|e\rangle \otimes |0\rangle$. The state of the transmon is thus imprinted on the state of the resonator. In other words, the cavity realizes a measurement of the qubit state, with the pointer states $|0\rangle$ and $|\alpha\rangle$. Indeed, one could access to the measurement output by looking at the amplitude of the transmitted cavity field, although it is not required by this scheme. Instead, one can regularly apply a fast π-pulse at frequency ω_{ge}^0, where ω_{ge}^0 is the qubit frequency when the cavity is in the vacuum state. More precisely, after a time larger than $1/\kappa_c$, and before the application of the π-pulse, the state of the total system is given by $\boldsymbol{\rho}_{SA} = (1-p)|g\rangle\langle g| \otimes |\alpha\rangle\langle\alpha| + p|e\rangle\langle e| \otimes |0\rangle\langle 0|$, with $0 \leq p \leq 1$. The conditional π-pulse maps $\boldsymbol{\rho}_{SA}$ to the state $|g\rangle \otimes ((1-p)|\alpha\rangle\langle\alpha| + p|0\rangle\langle 0|)$ and next the continuous drive resets the resonator to the state $|\alpha\rangle$ (entropy evacuation). In [24], this reservoir engineering scheme is implemented in a continuous manner, by using a continuous Rabi drive at frequency ω_{ge}^0 instead of π-pulses. As the cavity drive pumps the population on $|g\rangle \otimes |0\rangle$ out to the state $|g\rangle \otimes |\alpha\rangle$ at a rate κ_c, the system is rapidly projected to the steady state $|g\rangle \otimes |\alpha\rangle$. Hence, the entropy introduced by the spontaneous excitations of the transmon at a rate $\gamma_\uparrow$ is evacuated via the resonator at a rate of order $\kappa_c \gg \gamma_\uparrow$.

Inspired from this protocol, Shankar et al. demonstrated the autonomous stabilization of an entangled Bell state by dispersively coupling two transmon qubits to a lossy cavity [79].

Similarly, reservoir engineering QEC schemes use the coupling to an ancillary quantum system to mediate the evacuation of the information entropy created by errors. From Subsection 1.1.4.2, one recalls that the recovery operation involves the use of an ancillary system. More precisely, the effect of a recovery operation is expressed through a unitary operator $\mathbf{U}_{SA}$ on the system S and an ancillary system A, such that

$$\mathbf{U}_{SA}[\sum_\nu(\mathbf{E}_\nu|\psi\rangle_S) \otimes |a_{\mu_0}\rangle_A \otimes |e_\nu\rangle_E] = |\psi_S\rangle \otimes \big(\sum_\mu \sqrt{d_\mu}|a_\mu\rangle_A \otimes |e_\mu\rangle_E\big)$$

Here, the increase of entropy on the system S is expressed through the entangled state $\sum_\nu(\mathbf{E}_\nu|\psi\rangle_S) \otimes |e_\nu\rangle_E$ between S and the environment E. By applying the unitary operation $\mathbf{U}_{SA}$, we have transferred the entropy onto the ancilla, resulting in the creation of the entangled state $\sum_\mu \sqrt{d_\mu}|a_\mu\rangle_A \otimes |e_\mu\rangle_E$. The strong dissipation of the ancilla naturally evacuates the entropy by resetting its state to $|a_{\mu_0}\rangle_A$.

So far, the recovery procedure is not continuous. The discrete operation $\mathbf{U}_{SA}$ corresponds to the conditional π-pulse applied in the above example. The resonator plays the role of the ancilla, and the ancilla state $|a_{\mu_0}\rangle_A$ is the coherent state $|\alpha\rangle$. The operation $\mathbf{U}_{SA}$ and the decay of the ancilla, can be realized in a simultaneous manner as illustrated through the example of [24].

We would like to stress the fact that in a reservoir engineering QEC scheme, error detection and correction are not two distinct steps. Throughout this thesis, we will present several autonomous QEC schemes which illustrate this feature. A few proposals of such protocols can be found in the literature. In [38], Kerckhoff et al. proposed to implement the three-qubit bit-flip (and phase-flip) code in a photonic circuit through an autonomous feedback loop embedded in the system. More precisely, error syndromes are collected through optical beams interacting with the qubits, and then conveyed to two quantum controllers (ancillas) via directional couplings. The beams, combined with the dissipation of the ancillas, drive the controllers to steady states which depend on the error syndromes. Two additional "feedback" beams interact with the controllers, and are injected into the qubit system to drive it back to the code space. Kerckhoff et al. have also presented an extension of this work to the implementation of the 9-qubit Bacon-Shor code [39]. An autonomous QEC scheme based on three-qubit phase-flip code was also proposed in the field of circuit QED by Kapit et al. [36]. In [36], such a scheme is realized by coupling three transmon qubits to three dissipative ancillary qubits. The transmon qubits are two-by-two coupled through well-chosen magnetic fluxes. When the system stepped out of the code space through a single phase flip, it is irreversibly brought back through the dissipation of the ancillas. In Chapter 2, we present another autonomous QEC protocol for three-qubit bit-flip (or phase-flip) code with transmon qubits. As it will be seen, our scheme does not require any directional coupling, nor carefully engineered magnetic fluxes. We will also propose some extensions to the 9-qubit Bacon-Shor code.

1.2 Encoding a qubit in an oscillator : the cat qubits

In the previous section we re-called some general results on quantum error correcting codes, illustrated by a few multi-qubit codes as examples. Instead of using many qubits to provide the redundancy required to protect the encoded information, one can also encode the information in a single harmonic oscillator and benefit from the vastness of the associated Hilbert space. Although other possible encodings exist [26, 52], the focus of this section is on the cat code, which uses superposition of coherent states as the logical states [44]. The cat-code is introduced in Subsection 1.2.1. In particular, we recall the two-component and four-component encoding schemes. We also describe a cat-pumping protocol proposed in [53] and experimentally realized in [45], through which the state of the oscillator is confined to a 2D- or a 4D-manifold spanned by two or four coherent states. Next, in Subsection 1.2.2, we show that this confinement protects the cat qubits from logical phase-flip errors. More precisely, we prove that a wide variety of errors conserving the photon number parity are correctable for the cat codes, and corrected through the pumping. Consequently, the logical phase flips can be efficiently suppressed leaving only bit-flip errors associated to parity jumps.

1.2.1 Principles of cat encoding

1.2.1.1 Two-component cat code

Given a non-zero complex number α, let us consider the coherent states $|\alpha\rangle = e^{-|\alpha|^2}\sum_{n\geq 0}\alpha^n/\sqrt{n!}|n\rangle$ and $|-\alpha\rangle$, and the superposition of these states, i.e the cat states

$$|\mathscr{C}_\alpha^\pm\rangle = \mathscr{N}^\pm(|\alpha\rangle \pm |-\alpha\rangle), \quad \mathscr{N}^\pm = 1/\sqrt{2(1\pm e^{-2|\alpha|^2})}.$$

The state $|\mathscr{C}_\alpha^+\rangle$ ($|\mathscr{C}_\alpha^-\rangle$) is a linear superposition of Fock states with even (resp. odd) photon numbers. As a direct consequence, the cat states $|\mathscr{C}_\alpha^\pm\rangle$ form an orthonormal basis, the cat basis, in which we can encode a logical qubit

$$|0_L\rangle = |\mathscr{C}_\alpha^+\rangle, \quad |1_L\rangle = |\mathscr{C}_\alpha^-\rangle.$$

We define the corresponding Pauli matrices $\boldsymbol{\sigma}_Z^L = |\mathscr{C}_\alpha^+\rangle\langle\mathscr{C}_\alpha^+| - |\mathscr{C}_\alpha^-\rangle\langle\mathscr{C}_\alpha^-|$, $\boldsymbol{\sigma}_X^L = |\mathscr{C}_\alpha^-\rangle\langle\mathscr{C}_\alpha^+| + |\mathscr{C}_\alpha^+\rangle\langle\mathscr{C}_\alpha^-|$ and $\boldsymbol{\sigma}_Y^L = i\boldsymbol{\sigma}_Z^L\boldsymbol{\sigma}_X^L$. Since $|\langle-\alpha|\alpha\rangle|^2 = e^{-2|\alpha|^2}$, the states $|\pm\alpha\rangle$ are quasi-orthogonal for $|\alpha| \geq 2$. Throughout this thesis, we will consider $|\alpha| \gtrsim 2$. In this case, $|\mathscr{C}_\alpha^\pm\rangle \approx (|\alpha\rangle \pm |-\alpha\rangle)/\sqrt{2}$, and the states $|\pm\alpha\rangle$ are approximately the eigenstates of the $\boldsymbol{\sigma}_X^L$ Pauli matrix (see Fig. 1.1a-d).

The two-component cat encodes a single qubit in the 2D-logical space $\mathscr{M}_{2,\alpha} = \text{span}\{|\mathscr{C}_\alpha^\pm\rangle\}$, inside an infinite dimensional Hilbert space of a harmonic oscillator. The protection provided by this code will be thoroughly reviewed in Subsection 1.2.2.

1.2.1.2 Four-component cat code

From the four coherent states $|\pm\alpha\rangle$, $|\pm i\alpha\rangle$, we can define the cat states

$$\begin{aligned}
|\mathscr{C}_\alpha^{(0\text{mod}4)}\rangle &= \mathscr{N}_0(|\mathscr{C}_\alpha^+\rangle + |\mathscr{C}_{i\alpha}^+\rangle), \; |\mathscr{C}_\alpha^{(2\text{mod}4)}\rangle = \mathscr{N}_2(|\mathscr{C}_\alpha^+\rangle - |\mathscr{C}_{i\alpha}^+\rangle),\\
|\mathscr{C}_\alpha^{(1\text{mod}4)}\rangle &= \mathscr{N}_1(|\mathscr{C}_\alpha^-\rangle - i|\mathscr{C}_{i\alpha}^-\rangle), \; |\mathscr{C}_\alpha^{(3\text{mod}4)}\rangle = \mathscr{N}_3(|\mathscr{C}_\alpha^-\rangle + i|\mathscr{C}_{i\alpha}^-\rangle),
\end{aligned}$$

where the normalization constants satisfy $\mathscr{N}_j \approx 1/\sqrt{2}$. The four-component cat state $|\mathscr{C}_\alpha^{(j\text{mod}4)}\rangle$ is a linear superposition of Fock states $|4n+j\rangle$, i.e Fock states with photon numbers $j \mod 4$. As a consequence, these states form an orthonormal basis of the 4D-manifold $\mathscr{M}_{4,\alpha} = \text{span}\{|\alpha\rangle, |-\alpha\rangle, |i\alpha\rangle, |-i\alpha\rangle\}$. This manifold is the direct sum of the even-parity subspace $\mathscr{E}_+ = \text{span}\{|\mathscr{C}_\alpha^{(0\text{mod}4)}\rangle, |\mathscr{C}_\alpha^{(2\text{mod}4)}\rangle\}$ and the odd-parity subspace $\mathscr{E}_- = \text{span}\{|\mathscr{C}_\alpha^{(1\text{mod}4)}\rangle, |\mathscr{C}_\alpha^{(3\text{mod}4)}\rangle\}$. Here, we choose to encode a logical qubit on the even-

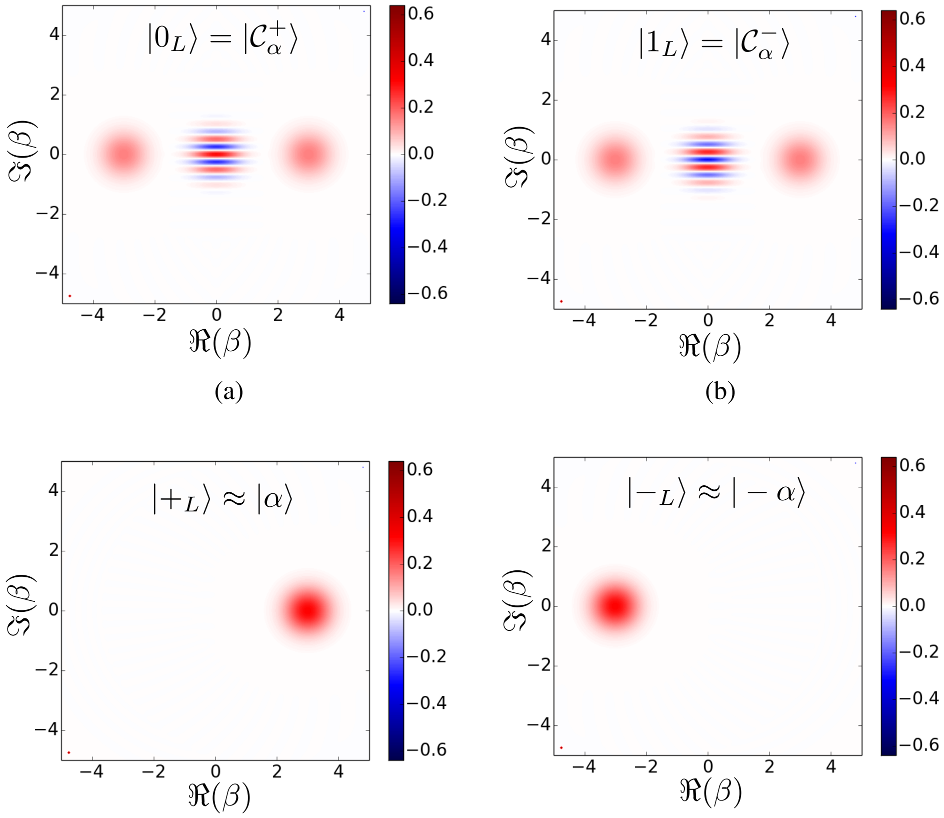

(a) (b) (c) (d)

Fig. 1.1 (a) and (b): Wigner representation of the logical states $|0_L\rangle = |\mathscr{C}_\alpha^+\rangle$ and $|1_L\rangle = |\mathscr{C}_\alpha^-\rangle$ of the two-component cat code, with $\alpha = 3$. The color of the fringe at the center (red or blue), indicates the parity of the cat state (resp. even and odd). (c) and (d): Wigner representation of the logical states $|+_L\rangle = (|0_L\rangle + |1_L\rangle)/\sqrt{2} \approx |\alpha\rangle$ and $|-_L\rangle = (|0_L\rangle - |1_L\rangle)/\sqrt{2} \approx |-\alpha\rangle$.

parity subspace, such that

$$|0_L\rangle = |\mathscr{C}_\alpha^{(0\text{mod}4)}\rangle,\ |1_L\rangle = |\mathscr{C}_\alpha^{(2\text{mod}4)}\rangle.$$

We also define the logical operators

$$\begin{aligned}
\boldsymbol{\sigma}_Z^{\text{even}} &= |\mathscr{C}_\alpha^{(0\text{mod}4)}\rangle\langle\mathscr{C}_\alpha^{(0\text{mod}4)}| - |\mathscr{C}_\alpha^{(2\text{mod}4)}\rangle\langle\mathscr{C}_\alpha^{(2\text{mod}4)}|,\\
\boldsymbol{\sigma}_X^{\text{even}} &= |\mathscr{C}_\alpha^{(0\text{mod}4)}\rangle\langle\mathscr{C}_\alpha^{(2\text{mod}4)}| + |\mathscr{C}_\alpha^{(2\text{mod}4)}\rangle\langle\mathscr{C}_\alpha^{(0\text{mod}4)}|,\\
\boldsymbol{\sigma}_Z^{\text{odd}} &= |\mathscr{C}_\alpha^{(3\text{mod}4)}\rangle\langle\mathscr{C}_\alpha^{(3\text{mod}4)}| - |\mathscr{C}_\alpha^{(1\text{mod}4)}\rangle\langle\mathscr{C}_\alpha^{(1\text{mod}4)}|,\\
\boldsymbol{\sigma}_X^{\text{odd}} &= |\mathscr{C}_\alpha^{(3\text{mod}4)}\rangle\langle\mathscr{C}_\alpha^{(0\text{mod}4)}| + |\mathscr{C}_\alpha^{(1\text{mod}4)}\rangle\langle\mathscr{C}_\alpha^{(2\text{mod}4)}|.
\end{aligned}$$

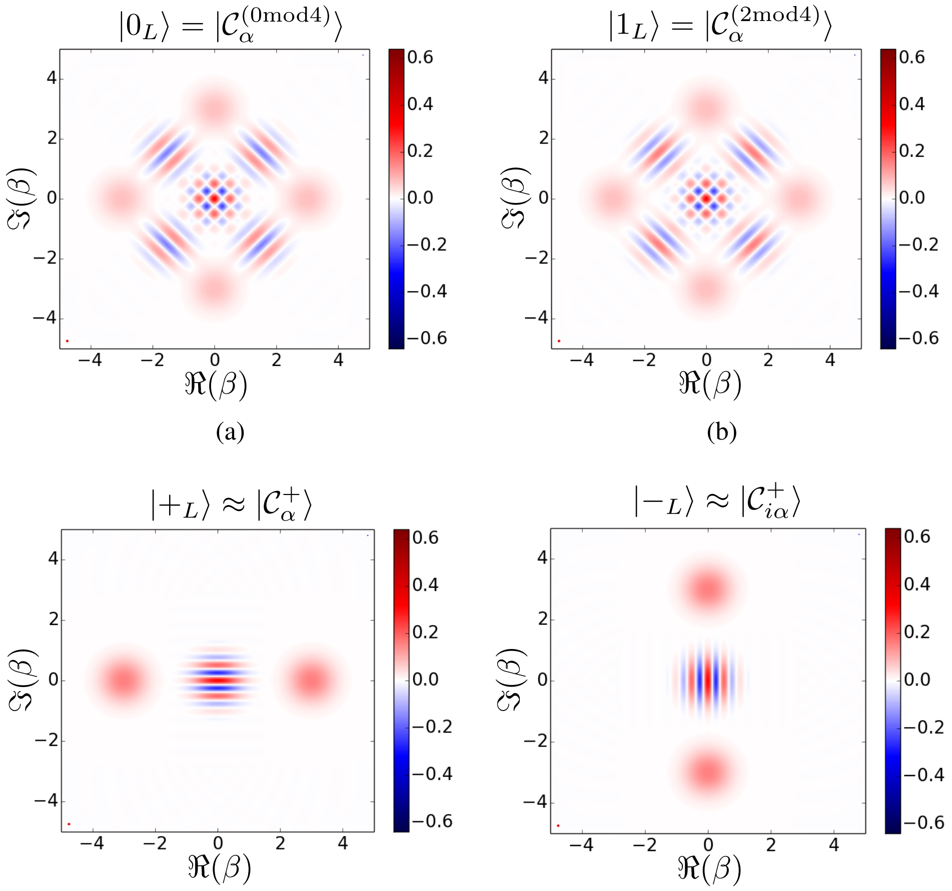

(a) (b) (c) (d)

Fig. 1.2 (a) and (b): Wigner representation of the logical states $|0_L\rangle = |\mathscr{C}_\alpha^{(0\mathrm{mod}4)}\rangle$ and $|1_L\rangle = |\mathscr{C}_\alpha^{(2\mathrm{mod}4)}\rangle$ of the four-component cat code, with $\alpha = 3$. (c) and (d): Wigner representation of the logical states $|+_L\rangle = (|0_L\rangle + |1_L\rangle)/\sqrt{2} \approx |\mathscr{C}_\alpha^{+}\rangle$ and $|-_L\rangle = (|0_L\rangle - |1_L\rangle)/\sqrt{2} \approx |\mathscr{C}_{i\alpha}^{+}\rangle$.

It has been illustrated in [44] that the major photon-loss decay channel of a harmonic oscillator leads to parity jumps in this encoding. More precisely, via the property $\mathbf{a}|\mathscr{C}_\alpha^{(j\mathrm{mod}4)}\rangle = \alpha|\mathscr{C}_\alpha^{((j-1)\mathrm{mod}4)}\rangle$, a single-photon loss maps $\mathscr{E}_+$ to $\mathscr{E}_-$, and $\mathscr{E}_-$ to $\mathscr{E}_+$ while preserving the coherence of the superposition. This jump is revealed by the measurement of the photon number parity, indicating on which subspace ($\mathscr{E}_+$ or $\mathscr{E}_-$) the cat lives. Throughout the Subsection 1.2.2, we will see that such a code can cover a large class of error channels in presence of a 4-photon pumping scheme. Indeed, any reasonable decoherence channel on a harmonic oscillator can be effectively reduced to such parity jumps.

1.2.1.3 Cat pumping

While we have briefly discussed the parity jump effect induced by the photon loss channel, one should note that such a decay also leads to a deterministic relaxation of energy in the harmonic oscillator. Even in presence of photon-number parity measurements, this relaxation would eventually erase the information by steering the oscillator's state to the vacuum state. Indeed, one requires to avoid a significant overlap between the coherent components encoding the quantum information by constantly injecting energy. In [53], Mirrahimi et al. proposed a reservoir engineering scheme, the so-called cat pumping, through which the state of an oscillator can be confined to a 2D-manifold $\mathscr{M}_{2,\alpha} = \text{span}\{|\pm\alpha\rangle\}$ or a 4D-manifold $\mathscr{M}_{4,\alpha} = \text{span}\{|\pm\alpha\rangle, |\pm i\alpha\rangle\}$. More precisely, energy is pumped into the system by exchanging photons in pairs or quadruples. Furthermore, the confinement to the 2D-manifold was experimentally demonstrated in [45]. Here, we start by recalling the effect of single-photon dissipation on an oscillator. Next, we give a description of the cat-pumping schemes and in particular, we provide rigorous proofs of some claims in [53]. In what follows, we choose α real and positive.

Single-photon loss - The evolution of an oscillator state $\boldsymbol{\rho}$, in presence of single-photon loss, is well described by the Lindblad master equation [28] (rotating frame at the oscillator frequency)

$$\frac{d\boldsymbol{\rho}}{dt} = \kappa(\mathbf{a}\boldsymbol{\rho}\mathbf{a}^\dagger - (\mathbf{a}^\dagger\mathbf{a}\boldsymbol{\rho} + \boldsymbol{\rho}\mathbf{a}^\dagger\mathbf{a})/2). \tag{1.3}$$

Throughout this thesis, we use the notation of Lindblad superoperators $\mathscr{D}[\mathbf{O}](\boldsymbol{\rho}) = \mathbf{O}\boldsymbol{\rho}\mathbf{O}^\dagger - (\mathbf{O}^\dagger\mathbf{O}\boldsymbol{\rho} + \boldsymbol{\rho}\mathbf{O}^\dagger\mathbf{O})/2$, with which the master equation takes the more compact form of $\frac{d\boldsymbol{\rho}}{dt} = \mathscr{D}[\sqrt{\kappa}\mathbf{a}](\boldsymbol{\rho})$. This master equation can be written in the Kraus map form,

$$\boldsymbol{\rho}(t+dt) = \sqrt{\kappa dt}\mathbf{a}\boldsymbol{\rho}\sqrt{\kappa dt}\mathbf{a}^\dagger + (\mathbf{I} - \frac{\kappa dt}{2}\mathbf{n})\boldsymbol{\rho}(\mathbf{I} - \frac{\kappa dt}{2}\mathbf{n}) + \mathscr{O}((\bar{n}\kappa dt)^2).$$

where we have defined the photon number operator $\mathbf{n} = \mathbf{a}^\dagger\mathbf{a}$, and the mean photon number $\bar{n} = \text{Tr}(\mathbf{n}\boldsymbol{\rho})$. This Kraus map is associated, approximately, with the set of errors $\{\mathbf{E}_0 = \mathbf{I} - \kappa dt\mathbf{n}/2, \mathbf{E}_1 = \sqrt{\kappa dt}\mathbf{a}\}$. The error $\mathbf{E}_1$ corresponds to the occurrence of a single-photon loss, and induces logical bit flips at a rate $\bar{n}\kappa$, while leaving the system in the coding subspace. If no photon jump has occurred during the time step dt (event $\mathbf{E}_0$ with probability $1-\kappa\bar{n}dt$), the system evolves to the state $\mathbf{E}_0\boldsymbol{\rho}\mathbf{E}_0^\dagger/tr(\mathbf{E}_0\boldsymbol{\rho}\mathbf{E}_0^\dagger)$. This error induces a deterministic decay of the coherent state amplitude. Indeed, at time t, the state of the system initialized in $|\alpha\rangle$, is given by $\boldsymbol{\rho}(t) = |\alpha e^{-\kappa t/2}\rangle\langle\alpha e^{-\kappa t/2}|$. This relaxation takes the oscillator state out of the logical subspace $\mathscr{M}_{2,\alpha}$ (or $\mathscr{M}_{4,\alpha}$) to the subspace $\mathscr{M}_{2,\alpha e^{-\kappa t/2}}$ (or $\mathscr{M}_{4,\alpha e^{-\kappa t/2}}$). Eventually, the overlap of the coherent states $|\pm\alpha e^{-\kappa t/2}\rangle$ becomes significant, and one cannot unambiguously distinguish them. The cat-pumping scheme, described below, prevents this situation from happening.

Cat-pumping scheme - To avoid the deterministic relaxation of the coherent states, one needs to provide some energy to the oscillator. If one drives the oscillator at its resonance frequency, leading to the Hamiltonian $\mathbf{H} = -i\hbar\varepsilon_d(\mathbf{a} - \mathbf{a}^\dagger)$ in the rotating frame, the Lindblad master equation of the driven dissipative system can be written as

$$\frac{d\boldsymbol{\rho}}{dt} = \mathscr{D}[\sqrt{\kappa}(\mathbf{a} - \alpha)](\boldsymbol{\rho}),$$

with $\alpha = 2\varepsilon_d/\kappa$ and $-i\varepsilon_d$ the drive amplitude. Through this evolution equation, the oscillator is driven to the steady state $|\alpha\rangle$. Similarly, the cat pumping protocol confines the oscillator state to the asymptotic manifolds $\mathscr{M}_{2,\alpha}$ or $\mathscr{M}_{4,\alpha}$ via an engineered two- or four-photon driven dissipation. The dynamics of a harmonic oscillator subject to the two-photon process only, is given by

$$\frac{d\boldsymbol{\rho}}{dt} = \mathscr{D}[\sqrt{\kappa_{\mathrm{2ph}}}(\mathbf{a}^2 - \alpha^2)](\boldsymbol{\rho}).$$

Note that $|\pm\alpha\rangle$ are asymptotic states of this dynamics. Furthermore, any superposition of these states is left untouched through this dissipation. Under four-photon driven dissipation, the oscillator dynamics is described by the master equation

$$\frac{d\boldsymbol{\rho}}{dt} = \mathscr{D}[\sqrt{\kappa_{\mathrm{4ph}}}(\mathbf{a}^4 - \alpha^4)](\boldsymbol{\rho}).$$

Similarly, the system state is stabilized to the manifold $\mathscr{M}_{4,\alpha}$.

Let us focus on the two-photon case. Given an initial state $\boldsymbol{\rho}(0)$, one can write the asymptotic state $\boldsymbol{\rho}_f \in \mathscr{M}_{2,\alpha}$ as

$$\boldsymbol{\rho}_f = c_{++}|\mathscr{C}_\alpha^+\rangle\langle\mathscr{C}_\alpha^+| + c_{+-}|\mathscr{C}_\alpha^+\rangle\langle\mathscr{C}_\alpha^-| + c_{-+}|\mathscr{C}_\alpha^-\rangle\langle\mathscr{C}_\alpha^+| + (1 - c_{++})|\mathscr{C}_\alpha^-\rangle\langle\mathscr{C}_\alpha^-|, \tag{1.4}$$

where $c_{++} \geq 0$ and $c_{+-} = c_{-+}^*$. More precisely, these quantities satisfy [53]

$$c_{++} = \mathrm{Tr}(\boldsymbol{\rho}(0)\mathbf{J}_{++}), \quad c_{+-} = \mathrm{Tr}(\boldsymbol{\rho}(0)\mathbf{J}_{+-}).$$

Here, the operators $\mathbf{J}_{++}$ and $\mathbf{J}_{+-}$ are defined by

$$\mathbf{J}_{++} = \sum_{n=0}^{+\infty} |2n\rangle\langle 2n|, \tag{1.5}$$

$$\mathbf{J}_{+-} = \sqrt{\frac{2\alpha^2}{\sinh(2\alpha^2)}} \sum_{q=-\infty}^{+\infty} \frac{(-1)^q}{2q+1} I_q(\alpha^2)\mathbf{J}_{+-}^{(q)}, \tag{1.6}$$

where $I_q(.)$ is the modified Bessel function of the first kind, and $\mathbf{J}_{+-}^{(q)}$ is given by

$$\mathbf{J}_{+-}^{(q)} = \begin{cases} \frac{(\mathbf{a}^\dagger\mathbf{a}-1)!!}{(\mathbf{a}^\dagger\mathbf{a}+2q)!!} J_{++}\mathbf{a}^{2q+1}, & q \geq 0 \\ \\ \mathbf{J}_{++}\mathbf{a}^{2|q|-1}\frac{(\mathbf{a}^\dagger\mathbf{a}-1)!!}{(\mathbf{a}^\dagger\mathbf{a}+2|q|-1)!!}, & q < 0. \end{cases} \tag{1.7}$$

It was illustrated in Fig. 1 of [53], that the system, initialized in the coherent state $\boldsymbol{\rho}(0) = |\gamma\rangle\langle\gamma|$, converges to the state $|\alpha\rangle$ if $\Re(\gamma) > 0$, and to the state $|-\alpha\rangle$ if $\Re(\gamma) < 0$ (the case $\Re(\gamma) \sim 0$ being singular). In the next paragraph, we provide a rigorous proof of this behaviour. Throughout this manuscript, $\Re(.)$ and $\Im(.)$ denote the real and imaginary parts of a complex number.

Recovery operation of the pumping scheme - Given an initial state $\boldsymbol{\rho}(0)$, the system converges, via the two-photon pumping scheme, to an asymptotic state $\boldsymbol{\rho}_f \in \mathscr{M}_{2,\alpha}$. This defines a quantum map $\mathbb{R}_{\text{pump}}$ such that $\boldsymbol{\rho}_f = \mathbb{R}_{\text{pump}}(\boldsymbol{\rho}(0))$. The super-operator $\mathbb{R}_{\text{pump}}$ satisfies the following statements : for all complex number β such that $|\Re(\beta)| < \alpha$,

$$\begin{aligned} \mathbb{R}_{\text{pump}}(|\alpha+\beta\rangle\langle\alpha+\beta|) &= |\alpha\rangle\langle\alpha| + \mathscr{O}(e^{-\alpha^2-|\alpha+\beta|^2+|\beta(2\alpha+\beta)|}), \\ \mathbb{R}_{\text{pump}}(|-\alpha+\beta\rangle\langle-\alpha+\beta|) &= |-\alpha\rangle\langle-\alpha| + \mathscr{O}(e^{-\alpha^2-|\alpha+\beta|^2+|\beta(-2\alpha+\beta)|}) \end{aligned} \tag{1.8}$$

Note that $e^{-\alpha^2-|\alpha+\beta|^2+|\beta(2\alpha+\beta)|} = e^{-\alpha^2-|\alpha+\beta|^2+|(\alpha+\beta)^2-\alpha^2|}$. In particular, for a real negative number β, we have $e^{-\alpha^2-|\alpha+\beta|^2+|\beta(2\alpha+\beta)|} = e^{-2(\alpha-\beta)^2}$. Such a map efficiently suppresses the logical phase flips with the cat amplitude α. Indeed, an error will not result in a phase flip unless it maps the state $|\alpha\rangle$ ($|-\alpha\rangle$) to the left (resp. right) half complex plane (i.e. errors that act locally enough in the phase space of a harmonic oscillator). As it is detailed in Subsection 1.2.2, this operation acts as a recovery operation for the sets of errors that preserve the photon number parity, and that do not displace the state $|\pm\alpha\rangle$ out of their respective half complex plane. Below we provide a proof of the statement (1.8).

Let be β a complex number such that $|\Re(\beta)| < \alpha$. To show that $\mathbb{R}(|\alpha+\beta\rangle\langle\alpha+\beta|) = |\alpha\rangle\langle\alpha| + \mathscr{O}(e^{-\alpha^2-|\alpha+\beta|^2+|\beta(2\alpha+\beta)|})$, we use the quantity $\mathbf{J}_{+-}$ given in eq. (1.5) and conserved by $\mathbb{R}_{\text{pump}}$. The expansion (1.4) of a state $\boldsymbol{\rho}_f \in \mathscr{M}_{2,\alpha}$, can be cast into the form

$$\begin{aligned}\boldsymbol{\rho}_f =& \frac{1}{2}(1+c_{+-}+c_{-+})|\alpha\rangle\langle\alpha| + \frac{1}{2}(1-c_{+-}-c_{-+})|-\alpha\rangle\langle-\alpha| \\ &+ (c_{++}-c_{+-}+c_{-+}-c_{--})|\alpha\rangle\langle-\alpha| + (c_{++}+c_{+-}-c_{-+}-c_{--})|-\alpha\rangle\langle\alpha|.\end{aligned}$$

Therefore, given an arbitrary state $\boldsymbol{\rho}$, the population of $\boldsymbol{\rho}_f = \mathbb{R}_{\text{pump}}(\boldsymbol{\rho})$ on the state $|\pm\alpha\rangle$ is given by $(1 \pm \text{Tr}[\boldsymbol{\rho}\mathbf{J}_X])/2$, where we have defined $\mathbf{J}_X = \mathbf{J}_{+-} + \mathbf{J}_{+-}^\dagger$. The statement (1.8) is then equivalent to

$$\langle\alpha+\beta|\mathbf{J}_X|\alpha+\beta\rangle = 1 + \mathscr{O}(e^{-\alpha^2-|\alpha+\beta|^2+|\beta(2\alpha+\beta)|}) \tag{1.9}$$

$$\langle-\alpha+\beta|\mathbf{J}_X|-\alpha+\beta\rangle = -1 + \mathscr{O}(e^{-\alpha^2-|\alpha+\beta|^2+|\beta(2\alpha+\beta)|}) \tag{1.10}$$

Let us focus on the quantity $\langle\alpha+\beta|\mathbf{J}_X|\alpha+\beta\rangle$. Using equation (A.7) of [53], we have

$$\begin{aligned}\langle\alpha+\beta|\mathbf{J}_X|\alpha+\beta\rangle =& \frac{i\alpha|\alpha+\beta|e^{-|\alpha+\beta|^2-\alpha^2}}{\sqrt{1-e^{-4\alpha^2}}} \\ & \left[\int_0^\pi d\Phi\ [e^{-i(\Phi_b+\Phi)}I_0(|\alpha^2-|\alpha+\beta|^2e^{i2(\Phi_b+\Phi)}|)-c.c]\right]\end{aligned}$$

where $\alpha+\beta = |\alpha+\beta|e^{i\Phi_b}$. Noting that

$$|\alpha^2-|\alpha+\beta|^2e^{i2(\Phi_b+\Phi)}| = \sqrt{\alpha^4+|\alpha+\beta|^4-2\alpha^2|\alpha+\beta|^2\cos(2(\Phi+\Phi_b))},$$

We expand $\cos(2(\Phi+\Phi_b)) = 2\cos^2(\Phi+\Phi_b)-1$, and make the change of variable $\Phi \to u = \cos(\Phi+\Phi_b)$. Note that this is allowed since the function $f(\Phi) = \cos(\Phi+\Phi_b)$ is bijective from the domain $]0,\pi[$ to the domain $]-\cos(\Phi_b),\cos(\Phi_b)[$. Indeed, from the condition $|\Re(\beta)| < \alpha$, one satisfies $\Phi \in]-\frac{\pi}{2},\frac{\pi}{2}[$. This change of variable gives

$$\langle\alpha+\beta|\mathbf{J}_X|\alpha+\beta\rangle = \frac{4\alpha|\alpha+\beta|e^{-|\alpha+\beta|^2-\alpha^2}}{\sqrt{1-e^{-4\alpha^2}}}\int_0^{cos(\Phi_b)} du\, I_0\Big(\sqrt{(\alpha^2+|\alpha+\beta|^2)^2-4\alpha^2|\alpha+\beta|^2u^2}\Big).$$

We do another change of variable $u \to v = \sqrt{(\alpha^2 + |\alpha+\beta|^2)^2 - 4\alpha^2|\alpha+\beta|^2u^2}$ leading to

$$\begin{aligned}
\langle \alpha+\beta|\mathbf{J}_X|\alpha+\beta\rangle =&\mathrm{sign}(\cos(\Phi_b))\frac{2e^{-|\alpha+\beta|^2-\alpha^2}}{\sqrt{1-e^{-4\alpha^2}}}\int\limits_{m(\alpha,|\alpha+\beta|,\Phi_b)}^{m(\alpha,|\alpha+\beta)|,\frac{\pi}{2})}\frac{I_0(v)vdv}{\sqrt{(\alpha^2+|\alpha+\beta|^2)^2-v^2}}\\
=&\mathrm{sign}(\cos(\Phi_b))\frac{2e^{-|\alpha+\beta|^2-\alpha^2}}{\sqrt{1-e^{-4\alpha^2}}}\Bigg[\int\limits_{0}^{m(\alpha,|\alpha+\beta|,\frac{\pi}{2})}\frac{I_0(v)vdv}{\sqrt{(\alpha^2+|\alpha+\beta|^2)^2-v^2}}\\
&-\int\limits_{0}^{m(\alpha,|\alpha+\beta)|,\Phi_b)}\frac{I_0(v)vdv}{\sqrt{(\alpha^2+|\alpha+\beta|^2)^2-v^2}}\Bigg]
\end{aligned}$$

where $m(\alpha,|\alpha+\beta)|,\theta) = \sqrt{(\alpha^2+|\alpha+\beta|^2)^2-4\alpha^2|\alpha+\beta|^2\cos^2(\theta)}$, and $\mathrm{sign}(x) = +1$ if $x > 0$, and $\mathrm{sign}(x) = -1$ if $x < 0$. The condition $|\Re(\beta)| < \alpha$ implies $\cos(\Phi_b) > 0$. Using (2.15.2.6) from [67], the first term gives

$$\frac{2e^{-|\alpha+\beta|^2-\alpha^2}}{\sqrt{1-e^{-4\alpha^2}}}\int\limits_{0}^{m(\alpha,|\alpha+\beta|,\frac{\pi}{2})}\frac{I_0(v)vdv}{\sqrt{(\alpha^2+|\alpha+\beta|^2)^2-v^2}} = \frac{1}{\sqrt{1-e^{-4\alpha^2}}}.$$

The second term is then dominated by $\mathcal{O}(e^{-\alpha^2-|\alpha+\beta|^2+|\beta(2\alpha+\beta)|}/\sqrt{1-e^{-4\alpha^2}})$. Hence, we have

$$\begin{aligned}
\langle \alpha+\beta|\mathbf{J}_X|\alpha+\beta\rangle =&\frac{1}{\sqrt{1-e^{-4\alpha^2}}}(1-\mathcal{O}(e^{-\alpha^2-|\alpha+\beta|^2+|\beta(2\alpha+\beta)|}))\\
>&1-\mathcal{O}(e^{-\alpha^2-|\alpha+\beta|^2+|\beta(2\alpha+\beta)|}).
\end{aligned}$$

From $|\mathrm{Tr}[\boldsymbol{\rho}\mathbf{J}_{+-}]| = |c_{+-}| \leq 1$, we infer that the operator $\mathbf{J}_X$ satisfies, $\forall\boldsymbol{\rho}, |\mathrm{Tr}[\boldsymbol{\rho}\mathbf{J}_X]| \leq 1$. This leads to

$$1-\mathcal{O}(e^{-\alpha^2-|\alpha+\beta|^2+|\beta(2\alpha+\beta)|}) < \langle \alpha+\beta|\mathbf{J}_X|\alpha+\beta\rangle \leq 1.$$

This clearly shows that

$$\langle \alpha+\beta|\mathbf{J}_X|\alpha+\beta\rangle = 1-\mathcal{O}(e^{-\alpha^2-|\alpha+\beta|^2+|\beta(2\alpha+\beta)|}).$$

Similarly, by replacing α by $-\alpha$ in the above derivation, which leads to $\cos(\Phi_b) < 0$, we obtain

$$\langle -\alpha+\beta|\mathbf{J}_X|-\alpha+\beta\rangle = -1+\mathcal{O}(e^{-\alpha^2-|\alpha+\beta|^2+|\beta(-2\alpha+\beta)|}).$$

1.2.2 Synthesis of error protection provided by cat pumping

In the previous subsection, we have shown that the cat-pumping scheme provides a quantum operation $\mathbb{R}_{\text{pump}}$, through which a coherent state $|\gamma\rangle$ is mapped to the state $|\alpha\rangle$ (or $|-\alpha\rangle$), roughly if $\Re(\gamma) > -\alpha$ (resp. $\Re(\gamma) < -\alpha$). In this subsection, we analyze in detail the effect of errors on the two-component or four-component cat codes. Among the sets of errors preserving the photon number parity, we show that a large class of them is correctable for the cat code. In particular, we provide a sufficient condition on these errors to be corrected through the recovery operation $\mathbb{R}_{\text{pump}}$. Next, we illustrate this study by reviewing several types of decoherence channels of a harmonic oscillator.

1.2.2.1 General analysis

Let us consider a general operator $\mathbf{E}(\mathbf{a},\mathbf{a}^\dagger)$ defined on the Hilbert space of a harmonic oscillator. Here, we assume $\mathbf{E}$ to be analytical function of its arguments $\mathbf{a}$ and $\mathbf{a}^\dagger$. We would like to study the effect of such an operator on the code space $\mathscr{M}_{2,\alpha}$. This operator can be written in the form

$$\mathbf{E}(\mathbf{a},\mathbf{a}^\dagger) = \mathbf{F}^I(\mathbf{a}^2,\mathbf{a}^{\dagger 2},\mathbf{a}^\dagger\mathbf{a})\mathbf{I} + \mathbf{F}^{X,-}(\mathbf{a}^2,\mathbf{a}^{\dagger 2},\mathbf{a}^\dagger\mathbf{a})\mathbf{a} + \mathbf{F}^{X,+}(\mathbf{a}^2,\mathbf{a}^{\dagger 2},\mathbf{a}^\dagger\mathbf{a})\mathbf{a}^\dagger,$$

where $\mathbf{F}^I$, $\mathbf{F}^{X,\pm}$, are analytical functions of $\mathbf{a}^2$, $\mathbf{a}^{\dagger 2}$ and $\mathbf{a}^\dagger\mathbf{a}$. In particular, the photon number parity is conserved through the action of such operators. From the relation $\mathbf{a}|\mathscr{C}_\alpha^\pm\rangle = \alpha|\mathscr{C}_\alpha^\mp\rangle$, we infer that $\mathbf{a}\mathbf{\Pi}_{\mathscr{M}_{2,\alpha}} = \alpha\boldsymbol{\sigma}_X^L$ and $\mathbf{a}^2\mathbf{\Pi}_{\mathscr{M}_{2,\alpha}} = \alpha^2\mathbf{\Pi}_{\mathscr{M}_{2,\alpha}}$, where $\mathbf{\Pi}_{\mathscr{M}_{2,\alpha}} = |\mathscr{C}_\alpha^+\rangle\langle\mathscr{C}_\alpha^+| + |\mathscr{C}_\alpha^-\rangle\langle\mathscr{C}_\alpha^-|$ and $\boldsymbol{\sigma}_X^L = |\mathscr{C}_\alpha^+\rangle\langle\mathscr{C}_\alpha^-| + |\mathscr{C}_\alpha^-\rangle\langle\mathscr{C}_\alpha^+|$. Thus, a single photon jump maps the logical subspace onto itself, and acts as a bit-flip $\boldsymbol{\sigma}_X^L$ in the cat basis. As a logical operation cannot be detected by the code, the two-component cat code does not protect against single-photon jumps, or any errors inducing a change in the photon number parity. Based on the same argument, note that the action of the parity-preserving operators $\mathbf{F}^I$, $\mathbf{F}^{X,\pm}$ cannot result in a logical bit-flip inside the coding subspace. As we shall see below, these errors induce at most logical phase flips. Since we are interested in the action of $\mathbf{E}$ on the manifold $\mathscr{M}_{2,\alpha}$, we focus on the operator $\mathbf{E}\mathbf{\Pi}_{\mathscr{M}_{2,\alpha}}$. By writing $\mathbf{a}^\dagger\mathbf{\Pi}_{\mathscr{M}_{2,\alpha}} = \mathbf{a}^\dagger\mathbf{a}^2\mathbf{\Pi}_{\mathscr{M}_{2,\alpha}}/\alpha^2 = \mathbf{a}^\dagger\mathbf{a}\boldsymbol{\sigma}_X^L/\alpha$, the operator $\mathbf{E}(\mathbf{a},\mathbf{a}^\dagger)\mathbf{\Pi}_{\mathscr{M}_{2,\alpha}}$ admits the decomposition

$$\mathbf{E}(\mathbf{a},\mathbf{a}^\dagger)\mathbf{\Pi}_{\mathscr{M}_{2,\alpha}} = \mathbf{F}^I(\mathbf{a}^2,\mathbf{a}^{\dagger 2},\mathbf{a}^\dagger\mathbf{a})\mathbf{\Pi}_{\mathscr{M}_{2,\alpha}} + \mathbf{F}^{X,\alpha}(\mathbf{a}^2,\mathbf{a}^{\dagger 2},\mathbf{a}^\dagger\mathbf{a})\boldsymbol{\sigma}_X^L$$

with $\mathbf{F}^{X,\alpha}(\mathbf{a}^2,\mathbf{a}^{\dagger 2},\mathbf{a}^\dagger\mathbf{a}) = \alpha\mathbf{F}^{X,-}(\mathbf{a}^2,\mathbf{a}^{\dagger 2},\mathbf{a}^\dagger\mathbf{a}) + \mathbf{F}^{X,+}(\mathbf{a}^2,\mathbf{a}^{\dagger 2},\mathbf{a}^\dagger\mathbf{a})\mathbf{a}^\dagger\mathbf{a}/\alpha$. A general error $\mathbf{E}$ acts therefore as a linear combination of a parity-preserving operator (unable to induce logical bit-flips) and the product of a parity-preserving operator with a logical bit-flip. Although the logical bit-flip component cannot be corrected with such a code, we show here that this code is capable of protecting the information against a large class of parity-preserving errors of the type $\mathbf{F}(\mathbf{a}^2,\mathbf{a}^{\dagger 2},\mathbf{a}^\dagger\mathbf{a})$.

Let us consider a noise map $\mathbb{F}$, described by parity-preserving errors $\{\mathbf{F}_k(\mathbf{a}^2,\mathbf{a}^{\dagger 2},\mathbf{a}^\dagger\mathbf{a})\}$. This set of errors is correctable by the cat code if and only if the operators $\mathbf{F}_k$ satisfy the criteria (1.2), i.e

$$\mathbf{\Pi}_{\mathscr{M}_{2,\alpha}}\mathbf{F}_j^\dagger\mathbf{F}_k\mathbf{\Pi}_{\mathscr{M}_{2,\alpha}} = c_{jk}\mathbf{\Pi}_{\mathscr{M}_{2,\alpha}} \tag{1.11}$$

As the operators $\mathbf{F}_k$ are invariant under the transformation $\mathbf{a}\to-\mathbf{a}$, we have the equality $\langle\alpha|\mathbf{F}_j^\dagger\mathbf{F}_k|\alpha\rangle = \langle-\alpha|\mathbf{F}_j^\dagger\mathbf{F}_k|-\alpha\rangle = c_{jk}$. This leads to

$$\mathbf{\Pi}_{\mathscr{M}_{2,\alpha}}\mathbf{F}_j^\dagger\mathbf{F}_k\mathbf{\Pi}_{\mathscr{M}_{2,\alpha}} = c_{jk}\mathbf{\Pi}_{\mathscr{M}_{2,\alpha}} + m_{jk}\boldsymbol{\sigma}_Z^L$$

where $\boldsymbol{\sigma}_Z^L = |\mathscr{C}_\alpha^+\rangle\langle\mathscr{C}_\alpha^+| - |\mathscr{C}_\alpha^-\rangle\langle\mathscr{C}_\alpha^-|$. If one satisfies $m_{jk} := \langle-\alpha|\mathbf{F}_j^\dagger\mathbf{F}_k|\alpha\rangle = \langle\alpha|\mathbf{F}_j^\dagger\mathbf{F}_k|-\alpha\rangle = \mathscr{O}(\varepsilon)$ with ε a small parameter, we can find a recovery map $\mathbb{R}$ such that $\forall\boldsymbol{\rho}\in\mathscr{M}_{2,\alpha}$, $(\mathbb{R}\circ\mathbb{F})(\boldsymbol{\rho}) = \boldsymbol{\rho}+\mathscr{O}(\varepsilon)$. In this case, we say that the noise map $\mathbb{F}$ is (approximately) correctable *up to* $\mathscr{O}(\varepsilon)$ [47]. Roughly, a sufficient condition for this, is that for all j,k, the states $\mathbf{F}_k|\alpha\rangle$ and $\mathbf{F}_j|-\alpha\rangle$ remain far enough, perhaps in the right half and left half planes of the phase space. This can be seen by writing $\langle-\alpha|\mathbf{F}_j^\dagger\mathbf{F}_k|\alpha\rangle = (1/\pi)\int_{\mathbb{C}} d^2\beta\langle-\alpha|\mathbf{F}_j^\dagger|\beta\rangle\langle\beta|\mathbf{F}_k|\alpha\rangle$ and by noting that such a condition ensures the smallness of the quantity $\langle-\alpha|\mathbf{F}_j^\dagger|\beta\rangle\langle\beta|\mathbf{F}_k|\alpha\rangle$ for all $\beta\in\mathbb{C}$. In what follows, we aim to give a rigorous formulation of this statement.

Let us outline the strategy of our analysis. First, given an operator $\mathbf{F}(\mathbf{a}^2,\mathbf{a}^{\dagger 2},\mathbf{a}^\dagger\mathbf{a})$, we decompose $\mathbf{F}\mathbf{\Pi}_{\mathscr{M}_{2,\alpha}}$ as a linear combination of symmetrized displacement operators $\mathbf{D}_\beta+\mathbf{D}_{-\beta}$, where $\mathbf{D}_\beta = e^{\beta\mathbf{a}^\dagger-\beta^*\mathbf{a}}$. We show that these symmetrized displacements, for $|\beta|$ smaller than $|\alpha|$, are correctable errors for the two-component cat code and are corrected by cat pumping. Calling $\mathbb{R}_{\text{pump}}$ the associated recovery map, the noise map $\mathbb{F}$ is also corrected by the same map $\mathbb{R}_{\text{pump}}$.

Error expansion through displacement operators - To characterize the errors $\mathbf{F}(\mathbf{a}^2,\mathbf{a}^{\dagger 2},\mathbf{a}^\dagger\mathbf{a})\mathbf{\Pi}_{\mathscr{M}_{2,\alpha}}$, we consider their expansion on the displacement operators $\mathbf{D}_\beta$,

$$\mathbf{F}(\mathbf{a}^2,\mathbf{a}^{\dagger 2},\mathbf{a}^\dagger\mathbf{a})\mathbf{\Pi}_{\mathscr{M}_{2,\alpha}} = \int\limits_{\beta\in\mathbb{C}} d^2\beta u^\alpha(\beta)\mathbf{D}_\beta\mathbf{\Pi}_{\mathscr{M}_{2,\alpha}},$$

where $u^\alpha(\beta) = \mathrm{Tr}(\mathbf{D}_\beta^\dagger\mathbf{F}\mathbf{\Pi}_{\mathscr{M}_{2,\alpha}})$ is generally defined in the sense of a tempered distribution [71]. As a reminder, the action of a displacement operator $\mathbf{D}_\beta$ on a coherent state $|\gamma\rangle$ is given by $\mathbf{D}_\beta|\gamma\rangle = e^{(\beta\gamma^*-\beta^*\gamma)/2}|\gamma+\beta\rangle$. This expansion was used by Gottesman et al., in [26], to analyze the performance of another type of QEC codes on an oscillator. The fact that $\mathbf{F}$ is a function of $\mathbf{a}^2$, $\mathbf{a}^{\dagger 2}$ and $\mathbf{a}^\dagger\mathbf{a}$, imposes the symmetry $u^\alpha(-\beta) = u^\alpha(\beta)$, leading to

$$\mathbf{F}(\mathbf{a}^2,\mathbf{a}^{\dagger 2},\mathbf{a}^\dagger\mathbf{a})\mathbf{\Pi}_{\mathscr{M}_{2,\alpha}} = \int\limits_{\Re(\beta)\geq 0} d^2\beta u^\alpha(\beta)(\mathbf{D}_\beta + \mathbf{D}_{-\beta})\mathbf{\Pi}_{\mathscr{M}_{2,\alpha}}.$$

The parity-preserving errors are linear combination of the "$\mathbb{Z}_2$-symmetric" displacements $\mathbf{D}_\beta + \mathbf{D}_{-\beta}$. Note that $\mathbf{D}_\beta + \mathbf{D}_{-\beta} = 2\sum_{k\geq 0}(\beta\mathbf{a}^\dagger - \beta^*\mathbf{a})^{2k}/(2k!)$ is only a function of $\mathbf{a}^2$, $\mathbf{a}^{\dagger 2}$ and $\mathbf{a}^\dagger\mathbf{a}$, as expected. The "$\mathbb{Z}_2$-symmetry" property comes from the invariance of the operators $\mathbf{D}_\beta + \mathbf{D}_{-\beta}$ under the transformation $\mathbf{a} \to -\mathbf{a}$. From now on, we consider α real and positive to simplify the derivations.

Protection against $\mathbb{Z}_2$-symmetric displacements - Consider the (unnormalized) set of errors $\{(\mathbf{D}_\beta + \mathbf{D}_{-\beta}), |\Re(\beta)| < R_{\max}\}$. For $R_{\max} < |\alpha|$, this set of errors is correctable *up to* $e^{-2(R_{max}-\alpha)^2}$. More precisely, one can find a recovery operation such that any state $\boldsymbol{\rho} \in \mathscr{M}_{2,\alpha}$ subject to error channels of the form $(\mathbf{D}_\beta + \mathbf{D}_{-\beta}), |\Re(\beta)| < R_{\max}$, can be recovered with a unit fidelity up to $\mathscr{O}(e^{-2(R_{\max}-\alpha)^2})$. Furthermore, this recovery operation is approximately given by the cat-pumping scheme operation $\mathbb{R}_{\text{pump}}$.

Let us first provide an intuitive picture for this result. As the coding subspace is $\mathscr{M}_{2,\alpha} = \text{span}\{|\pm\alpha\rangle\}$, the error subspaces can fill up the rest of the Hilbert space, i.e $\mathscr{H}\setminus\mathscr{M}_{2,\alpha}$. As long as the displaced states $(\mathbf{D}_{\beta_1} + \mathbf{D}_{-\beta_1})|\alpha\rangle$ and $(\mathbf{D}_{\beta_2} + \mathbf{D}_{-\beta_2})|-\alpha\rangle$ remain in the complex right half plane (complex points with positive real part) and left half plane respectively, they will remain orthogonal. This condition is necessary for the existence of a recovery operation that maps $(\mathbf{D}_\beta + \mathbf{D}_{-\beta})|\pm\alpha\rangle$ back to $|\pm\alpha\rangle$ unambiguously.

Proof of protection against $\mathbb{Z}_2$-symmetric displacements - We prove that the errors fullfill the criteria (1.2), which is a necessary and sufficient condition for an error set to be correctable. The operators $\mathbf{D}_\beta + \mathbf{D}_{-\beta}$, with $|\Re(\beta)| < R_{\max} < \alpha$ satisfy

$$\mathbf{\Pi}_{\mathscr{M}_{2,\alpha}}(\mathbf{D}_{\beta_1} + \mathbf{D}_{-\beta_1})^\dagger(\mathbf{D}_{\beta_2} + \mathbf{D}_{-\beta_2})\mathbf{\Pi}_{\mathscr{M}_{2,\alpha}} = c_{\beta_1,\beta_2}\mathbf{\Pi}_{\mathscr{M}_{2,\alpha}} + M\boldsymbol{\sigma}_Z^L$$

where c_{β_1,β_2} is a complex number and

$$M \leq 4e^{-2(\alpha-R_{\max})^2}.$$

More precisely, as $(\mathbf{D}_{\beta_1} + \mathbf{D}_{-\beta_1})^\dagger(\mathbf{D}_{\beta_2} + \mathbf{D}_{-\beta_2})$ depends on $\mathbf{a}^2$, $\mathbf{a}^{\dagger 2}$ and $\mathbf{a}^\dagger\mathbf{a}$, we infer that

$$c_{\beta_1,\beta_2} = \langle\alpha|(\mathbf{D}_{\beta_1} + \mathbf{D}_{-\beta_1})^\dagger(\mathbf{D}_{\beta_2} + \mathbf{D}_{-\beta_2})|\alpha\rangle = \langle-\alpha|(\mathbf{D}_{\beta_1} + \mathbf{D}_{-\beta_1})^\dagger(\mathbf{D}_{\beta_2} + \mathbf{D}_{-\beta_2})|-\alpha\rangle.$$

Besides, the off-diagonal elements read

$$\left|\langle\alpha|(\mathbf{D}_{\beta_1}+\mathbf{D}_{-\beta_1})^\dagger(\mathbf{D}_{\beta_2}+\mathbf{D}_{-\beta_2})|-\alpha\rangle\right| \leq 4e^{-(\max(2\alpha-|\Re(\beta_1)|-|\Re(\beta_2)|,0)^2/2}.$$

The condition $|\Re(\beta_1)|,|\Re(\beta_2)| \leq R_{\max} < \alpha$ leads to the desired result, i.e there exists a recovery map $\mathbb{R}$ for this set of errors. The super-operator $\mathbb{R}$, is, to a very good approximation, given by $\mathbb{R}_{\text{pump}}$. Applying $\mathbb{R}_{\text{pump}}$ to a corrupted state $\boldsymbol{\rho}_{\text{corrupt}} = \mathscr{N}(\mathbf{D}_\beta+\mathbf{D}_{-\beta})|\alpha\rangle\langle\alpha|(\mathbf{D}_\beta+\mathbf{D}_{-\beta})^\dagger$ with $\mathscr{N}$ a normalization constant, leads to $\mathbb{R}_{\text{pump}}(\boldsymbol{\rho}_f) = \mathscr{N}(|\alpha\rangle\langle\alpha|+\mathscr{O}(e^{-\alpha^2-|\alpha+\beta|^2+|(\alpha+\beta)^2-\alpha^2|}))$. Hence, for all initial state $\boldsymbol{\rho}\in\mathscr{M}_{2,\alpha}$, we have

$$\mathrm{Tr}[\boldsymbol{\sigma}_X^L\boldsymbol{\rho}] = \mathrm{Tr}[\boldsymbol{\sigma}_X^L\mathbb{R}_{\text{pump}}(\mathscr{N}(\mathbf{D}_\beta+\mathbf{D}_{-\beta})\boldsymbol{\rho}(\mathbf{D}_\beta+\mathbf{D}_{-\beta})^\dagger)]+\mathscr{O}(e^{-\alpha^2-|\alpha+\beta|^2+|(\alpha+\beta)^2-\alpha^2|}),$$

where $\boldsymbol{\sigma}_X^L = |\alpha\rangle\langle\alpha|-|-\alpha\rangle\langle-\alpha|$. Besides, one has $\mathrm{Tr}[\boldsymbol{\sigma}_Z^L\boldsymbol{\rho}] = \mathrm{Tr}[\boldsymbol{\sigma}_Z^L\mathbb{R}_{\text{pump}}(\mathscr{N}(\mathbf{D}_\beta+\mathbf{D}_{-\beta})\boldsymbol{\rho}(\mathbf{D}_\beta+\mathbf{D}_{-\beta})^\dagger)]$, since $\mathbf{D}_\beta+\mathbf{D}_{-\beta}$ is a parity preserving operator, and the cat-pumping operation $\mathbb{R}_{\text{pump}}$ also preserves the photon number parity. Through a more careful analysis, one can also prove that

$$\mathrm{Tr}[\boldsymbol{\sigma}_Y^L\boldsymbol{\rho}] = \mathrm{Tr}[\boldsymbol{\sigma}_Y^L\mathbb{R}_{\text{pump}}(\mathscr{N}(\mathbf{D}_\beta+\mathbf{D}_{-\beta})\boldsymbol{\rho}(\mathbf{D}_\beta+\mathbf{D}_{-\beta})^\dagger)]+\mathscr{O}(e^{-\alpha^2-|\alpha+\beta|^2+|(\alpha+\beta)^2-\alpha^2|}),$$

where $\boldsymbol{\sigma}_Y^L = i\boldsymbol{\sigma}_Z^L\boldsymbol{\sigma}_X^L$. Therefore, $\mathbb{R}_{\text{pump}}$ satisfies, for β such that $|\Re(\beta)| < R_{\max}$ and for all $\boldsymbol{\rho}\in\mathscr{M}_{2,\alpha}$, $\mathbb{R}_{\text{pump}}(\mathscr{N}(\mathbf{D}_\beta+\mathbf{D}_{-\beta})\boldsymbol{\rho}(\mathbf{D}_\beta+\mathbf{D}_{-\beta})^\dagger)) = \boldsymbol{\rho}+\mathscr{O}(e^{-\alpha^2-|\alpha+\beta|^2+|(\alpha+\beta)^2-\alpha^2|}))$. Note that this results is valid up to $\mathscr{O}(e^{-4\alpha^2})$ due to the quasi orthogonality of $|\alpha\rangle$ and $|-\alpha\rangle$.

As the cat code provides an approximate protection against the set of errors $\{\mathbf{D}_\beta+\mathbf{D}_{-\beta},|\Re(\beta)|<R_{\max}\}$, it also protects the information against any set of linear combination of these errors. This follows from the result on error discretization of Subsection 1.1.4.2. In particular, a set of the parity-preserving errors $\{\mathbf{F}_k(\mathbf{a}^2,\mathbf{a}^{\dagger^2},\mathbf{a}^\dagger\mathbf{a})\}$ is correctable for the two-component cat code if the expansion $\mathbf{F}_k = \int_{\Re(\beta)>0} d^2\beta\, u_k^\alpha(\beta)(\mathbf{D}_\beta+\mathbf{D}_{-\beta})\mathbf{\Pi}_{\mathscr{M}_{2,\alpha}}$ is concentrated on operators $(\mathbf{D}_\beta+\mathbf{D}_{-\beta})$ such that $\Re(\beta)<\alpha$. In simpler words, the states $\mathbf{F}_k(\mathbf{a}^2,\mathbf{a}^{\dagger^2},\mathbf{a}^\dagger\mathbf{a})|\pm\alpha\rangle$ must remain in the right (resp. left) half plane. We can formulate a more precise statement by imposing a condition on the distribution $u_k^\alpha(\beta)$.

Protection against parity-preserving errors - Consider a set of parity-preserving errors $\{\mathbf{F}_k(\mathbf{a}^2,\mathbf{a}^{\dagger^2},\mathbf{a}^\dagger\mathbf{a})\}$. Let us assume that there exists $0<R_\alpha<\alpha$ such that for all $\Re(\beta)>0$,

$$\int_{-\infty}^{\infty} d\Im(\beta)|\langle\alpha\pm\beta|\mathbf{F}_k|\alpha\rangle| \leq Ce^{-(|\Re(\beta)|-R_\alpha)^2/2}, \quad C>0. \tag{1.12}$$

Then applying the recovery operation $\mathbb{R}_{\text{pump}}$ to a state that underwent the noise map $\{\mathbf{F}_k\}$, restores the initial state with fidelity $F \geq 1 - \mathscr{O}(e^{-c(\alpha-R_\alpha)^2})$, with $c = 2/(5+2\sqrt{2}) \approx 1/4$. This bound is not optimal and one should be able to obtain a larger constant c with a more careful analysis.

Proof of the protection against parity-preserving errors - The distribution $u_k^\alpha(\beta) = \mathrm{Tr}(\mathbf{D}_\beta^\dagger \mathbf{F}_k \mathbf{\Pi}_{\mathscr{M}_{2,\alpha}})$ reads

$$\begin{aligned} u_k^\alpha(\beta) &= \langle\alpha|\mathbf{D}_\beta^\dagger\mathbf{F}_k|\alpha\rangle + \langle-\alpha|\mathbf{D}_\beta^\dagger\mathbf{F}_k|-\alpha\rangle \\ &= e^{-i\alpha\Im(\beta)}\langle\alpha+\beta|\mathbf{F}_k|\alpha\rangle + e^{i\alpha\Im(\beta)}\langle-\alpha+\beta|\mathbf{F}_k|-\alpha\rangle \\ &= e^{-i\alpha\Im(\beta)}\langle\alpha+\beta|\mathbf{F}_k|\alpha\rangle + e^{i\alpha\Im(\beta)}\langle\alpha-\beta|\mathbf{F}_k|\alpha\rangle \end{aligned}$$

To go from the second line to the third line, we have used the fact that $\mathbf{F}_k$ is a function of $\mathbf{a}^2$, $\mathbf{a}^{\dagger 2}$ and $\mathbf{a}^\dagger\mathbf{a}$. If $\int d\Im(\beta)|\langle\alpha\pm\beta|\mathbf{F}_k|\alpha\rangle|$ vanishes quickly enough with increasing $\Re(\beta)$, $\int d\Im(\beta)|u_k^\alpha(\beta)|$ will also vanish.

Now, let be $R = \eta R_\alpha + (1-\eta)\alpha$, with $0 < \eta < 1$. The errors $\mathbf{F}_k\mathbf{\Pi}_{\mathscr{M}_{2,\alpha}}$ can be expanded into

$$\begin{aligned} \mathbf{F}_k\mathbf{\Pi}_{\mathscr{M}_{2,\alpha}} &= \int_{\Re(\beta)\geq 0} d^2\beta\, u_k^\alpha(\beta)(\mathbf{D}_\beta + \mathbf{D}_{-\beta}) \\ &= \int_{0\leq\Re(\beta)<R} d^2\beta\, u_k^\alpha(\beta)(\mathbf{D}_\beta + \mathbf{D}_{-\beta}) + \int_{R<\Re(\beta)} d^2\beta\, u_k^\alpha(\beta)(\mathbf{D}_\beta + \mathbf{D}_{-\beta}). \end{aligned}$$

The first term is a linear combination of correctable errors up to $\mathscr{O}(e^{-2(\alpha-R)^2})$, and is therefore correctable up to $\mathscr{O}(e^{-2(\alpha-R)^2})$. The remaining term consists of displacements such that $\Re(\beta) > R$, for which, under the assumption of the statement, one has $\int_{\mathbb{R}} d\Im(\beta)|u_k^\alpha(\beta)| \leq 2Ce^{-(|\Re(\beta)|-R_\alpha)^2/2}$. This leads to

$$\begin{aligned} \left\| \int_{R<\Re(\beta)} d^2\beta\, u_k^\alpha(\beta)(\mathbf{D}_\beta + \mathbf{D}_{-\beta}) \right\| &\leq \int_{R<\Re(\beta)} d^2\beta\, |u_k^\alpha(\beta)| \|(\mathbf{D}_\beta + \mathbf{D}_{-\beta})\| \\ &\leq 4C \int_{R<\Re(\beta)} d\Re(\beta) e^{-(|\Re(\beta)|-R_\alpha)^2/2} \\ &\leq C' e^{-(R-R_\alpha)^2/2}. \end{aligned}$$

Here $\|.\|$ denotes the sup-norm of an operator defined on the Hilbert space of the harmonic oscillator ($\|\mathbf{U}\| = 1$ for $\mathbf{U}$ a unitary operator). The fraction of the state population that undergoes a phase flip due to non-correctable term $\int_{R<\Re(\beta)} d^2\beta\, u_k^\alpha(\beta)(\mathbf{D}_\beta + \mathbf{D}_{-\beta})$ is bounded by $\mathscr{O}(e^{-(R-R_\alpha)^2})$. Let us now optimize the choice of R (and η) by imposing the same exponential behaviour for the two sources of errors, with $2(\alpha - R)^2 = (R - R_\alpha)^2$. This leads to $\eta = 1/(\sqrt{2}+1)$. In this case, applying the recovery operation $\mathbb{R}_{\text{pump}}$ to a state subject to the noise map $\{\mathbf{F}_k\}$ restores the initial state with a unit fidelity up to $\mathscr{O}(e^{-c(\alpha - R_\alpha)^2)})$, with $c = 2/(5+2\sqrt{2}) \approx 1/4$.

1.2.2.2 Examples of decoherence channels

Here, we illustrate the previous analysis with various examples of decoherence channels. First, we focus on energy relaxation via single-photon dissipation, which is generally the dominant decoherence channel of a harmonic oscillator. Next, we study the robustness of the code against various types of errors induced by phase noise. In what follows, we choose α real and positive.

Photon loss channel - As mentioned in Subsection 1.2.1.3, the dynamics of an oscillator subject only to single-photon dissipation at rate κ is well described by the deterministic Lindblad master equation (1.3). For such a master equation the evolution of the system's density matrix $\boldsymbol{\rho}$ over a time interval δt, can be represented by the Kraus map [14]

$$\boldsymbol{\rho}(t+\delta t) = \sum_{k=0}^{\infty} \mathbf{E}_k \boldsymbol{\rho}(t) \mathbf{E}_k^\dagger, \quad \mathbf{E}_k = \sqrt{\frac{(1-e^{-\kappa\delta t})^k}{k!}} e^{-\frac{\kappa\delta t}{2}\mathbf{n}} \mathbf{a}^k, \tag{1.13}$$

where $\mathbf{n} = \mathbf{a}^\dagger \mathbf{a}$ represents the photon number operator. The term $\mathbf{E}_k \boldsymbol{\rho}(t) \mathbf{E}_k^\dagger$ is the state of the system at time $t+\delta t$ if k photon jumps (losses) have occurred within the time interval δt, weighted by the probability of this event. The state of the system $\boldsymbol{\rho}(t+\delta t)$ is then obtained by summing over the number of jumps. The set of errors $\mathbf{E}_k$ can be decomposed into the operators $\mathbf{E}_{2k}$ and $\mathbf{E}_{2k+1}$ involving an even and odd number of photon jumps respectively. Moreover, $\mathbf{E}_{2k+1}$ expands as $\mathbf{E}_{2k+1} = \mathbf{F}_{2k}\mathbf{a}$, where $\mathbf{F}_{2k} = \sqrt{\frac{(1-e^{-\kappa\delta t})^{2k+1}}{(2k+1)!}} e^{-\frac{\kappa\delta t}{2}\mathbf{n}} \mathbf{a}^{2k}$. Since $\mathbf{a}^2 \boldsymbol{\Pi}_{\mathscr{M}_{2,\alpha}} = \alpha^2 \boldsymbol{\Pi}_{\mathscr{M}_{2,\alpha}}$, the operators $\mathbf{E}_{2k}\boldsymbol{\Pi}_{\mathscr{M}_{2,\alpha}}$ read

$$\mathbf{E}_{2k}\boldsymbol{\Pi}_{\mathscr{M}_{2,\alpha}} = \alpha^{2k} \sqrt{\frac{(1-e^{-\kappa\delta t})^{2k}}{(2k)!}} e^{-\frac{\kappa\delta t}{2}\mathbf{n}} \boldsymbol{\Pi}_{\mathscr{M}_{2,\alpha}}.$$

Similarly, we have $\mathbf{F}_{2k}\boldsymbol{\Pi}_{\mathscr{M}_{2,\alpha}} = \alpha^{2k}\sqrt{(1-e^{-\kappa\delta t})^{2k+1}/(2k+1)!} e^{-\frac{\kappa\delta t}{2}\mathbf{n}} \boldsymbol{\Pi}_{\mathscr{M}_{2,\alpha}}$. Noting that

$$\frac{e^{-\kappa\delta t \mathbf{n}/2} |\pm\alpha\rangle}{\| e^{-\kappa\delta t \mathbf{n}/2} |\pm\alpha\rangle \|} = |\pm \alpha e^{-\kappa\delta t/2}\rangle,$$

the operators $\mathbf{E}_{2k}$ and $\mathbf{F}_{2k}$ map the coding subspace to $\mathscr{M}_{2,\alpha e^{-\kappa t/2}}$, while leaving the photon number parity unchanged. For $\beta \in \mathbb{C}$, we have

$$|\langle \alpha \pm \beta | \mathbf{E}_{2k} | \alpha \rangle| < |\langle \alpha \pm \beta | \alpha e^{-\frac{\kappa \delta t}{2}} \rangle| \leq e^{-|\alpha(1-e^{-\kappa\delta t/2}) \mp \Re(\beta)|^2/2} e^{-|\Im(\beta)|^2/2}$$

The condition (1.12) being satisfied with $R_\alpha = \alpha(1-e^{-\frac{\kappa\delta t}{2}})$, it follows that the errors $\mathbf{E}_{2k}$ and $\mathbf{F}_{2k}$ are correctable up to $\mathscr{O}(e^{-c(\alpha e^{-\kappa\delta t/2})^2})$. In other words, the two-component cat code offers the possibility to reduce the errors due to single-photon dissipation to bit-flip errors only, by correcting for the deterministic amplitude decay, up to $\mathscr{O}(e^{-c(\alpha e^{-\kappa\delta t/2})^2})$. In particular, for a given $\kappa\delta t$, increasing the cat amplitude α reduces, exponentially, the logical phase flips induced by energy relaxation.

Unitary errors - A harmonic oscillator can also be subject to unitary errors of the form $\mathbf{E}_\theta = e^{i\theta \mathbf{a}^\dagger \mathbf{a}}$, where θ is a real random variable. Let us quantify the damage of such an error on the logical two-component cat qubit. The matrix elements $|\langle \alpha \pm \beta | \mathbf{E}_\theta | \alpha \rangle|$ read

$$|\langle \alpha \pm \beta | \mathbf{E}_\theta | \alpha \rangle| = |\langle \alpha \pm \beta | \alpha e^{i\theta} \rangle| \leq e^{-|\alpha(1-\cos(\theta)) \pm \Re(\beta)|^2/2} e^{-|-\alpha \sin(\theta) \pm \Im(\beta)|^2/4}$$

One can readily apply the reasoning used in the study of the photon loss channel by replacing $e^{-\kappa\delta t/2}$ with $\cos(\theta)$, leading to $R_\alpha = \alpha(1-\cos(\theta))$ in (1.12). If $\theta > \pi/2$, we have $R_\alpha > \alpha$, which implies that the error $\mathbf{E}_\theta$ is not corrected by the pumping. Indeed, $|\alpha\rangle$ would be mapped to the left half plane (the attraction domain of $|-\alpha\rangle$). The case $\theta < \pi/2$ yields $R_\alpha < \alpha$, which shows that the unitary error $\mathbf{E}_\theta$ is corrected up to $\mathscr{O}(e^{-c(\alpha\cos(\theta))^2})$. These two cases can be cast into a same statement, by saying that the unitary error $\mathbf{E}_\theta$ is corrected up to $\mathscr{O}(e^{-c\max(\alpha\cos(\theta),0)^2})$.

Phase noise due to dispersive coupling to a mode at non-zero temperature- Let us consider that the mode $\mathbf{a}$ is coupled to a mode $\mathbf{b}$ through the cross-Kerr coupling $\mathbf{H}_{\text{int}} = -\hbar\chi \mathbf{a}^\dagger \mathbf{a} \mathbf{b}^\dagger \mathbf{b}$. This mode $\mathbf{b}$, coupled to a non-zero temperature bath, is in the thermal equilibrium $\boldsymbol{\rho}_b^s = \sum_n p_n |n\rangle\langle n|$, associated to the mean photon number $n_{\text{th}} = \sum_n n p_n$. In the expansion $\mathbf{H}_{\text{int}} = -\hbar\chi \mathbf{a}^\dagger \mathbf{a}(\mathbf{b}^\dagger \mathbf{b} - n_{\text{th}}) - \hbar\chi n_{\text{th}} \mathbf{a}^\dagger \mathbf{a}$, we keep only the first term, as the second term induces a deterministic phase rotation that can be taken into account in the cat code pumping. Given an initial state of the form $\boldsymbol{\rho}(0) = \boldsymbol{\rho}_a \otimes \boldsymbol{\rho}_b^s$, the state at time δt is given by $\boldsymbol{\rho}(\delta t) = e^{i\chi\delta t \mathbf{a}^\dagger \mathbf{a}(\mathbf{b}^\dagger \mathbf{b} - n_{\text{th}})} \boldsymbol{\rho}(0) e^{-i\chi\delta t \mathbf{a}^\dagger \mathbf{a}(\mathbf{b}^\dagger \mathbf{b} - n_{\text{th}})}$. The state of the mode $\mathbf{a}$ at time δt reads $\boldsymbol{\rho}_a(\delta t) = \text{Tr}_b[\boldsymbol{\rho}(\delta t)]$, i.e

$$\boldsymbol{\rho}_a(\delta t) = \sum_n p_n e^{i\chi\delta t(n-n_{\text{th}})\mathbf{a}^\dagger \mathbf{a}} \boldsymbol{\rho}_a e^{-i\chi\delta t(n-n_{\text{th}})\mathbf{a}^\dagger \mathbf{a}}.$$

The set of errors associated to this map is the set of unitary errors $\{\mathbf{E}_n = \sqrt{p_n} e^{i\chi\delta t(n-n_{\text{th}})\mathbf{a}^\dagger\mathbf{a}}\}$. From the previous paragraph on unitary errors, it follows that these errors are corrected up to $\mathscr{O}(e^{-c\max(\alpha\cos(\theta_n),0)^2})$ with $\theta_n = \chi\delta t(n-n_{\text{th}})$. One can evaluate the fidelity F to the initial state, after the correction, to be

$$F \sim 1 - \mathscr{O}\left(\sum_n p_n e^{-c\max(\alpha\cos(\chi\delta t(n-n_{\text{th}})),0)^2}\right).$$

In particular, in the limit of large α, the pumping recovery ensures a fidelity exceeding $1-\sum_{n\geq n_c} p_n$. Here, n_c is defined as the minimum integer n such that $\mathbf{E}_n$ is not correctable.

1.2.2.3 Extension to four-photon pumping

Before analyzing the effect of a general error, let us provide a quick overview of the advantage of this code over the two-component cat code. As one satisfies the property $\mathbf{a}|\mathscr{C}_\alpha^{(j\text{mod}4)}\rangle = \alpha|\mathscr{C}_\alpha^{((j-1)\text{mod}4)}\rangle$, a single-photon loss maps $\mathscr{E}_+$ to $\mathscr{E}_-$, and $\mathscr{E}_-$ to $\mathscr{E}_+$ while preserving the coherence of the superposition. This jump is revealed by a change in the photon number parity, indicating on which subspace ($\mathscr{E}_+$ or $\mathscr{E}_-$) the cat lives. Moreover, two consecutive photon losses represented by the jump operator $\mathbf{a}^2$ induce a bit flip on $\mathscr{E}_\pm$. This logical bit-flip is detected via two consecutive flips of the photon number parity. Note that four consecutive photon losses act trivially on $\mathscr{E}_\pm$. Hence, by monitoring of the photon number parity, one can diagnose the occurrence of single-photon loss and correct for it. The two-component cat code does not offer such a protection.

Let us study the effect of an arbitrary analytical function $\mathbf{E}$ of $\mathbf{a}$ and $\mathbf{a}^\dagger$ on the cat qubit. The operator $\mathbf{E}$ can be cast into the form

$$\mathbf{E}(\mathbf{a},\mathbf{a}^\dagger) = \mathbf{F}^{(0)}(\mathbf{a}^4,\mathbf{a}^{\dagger 4},\mathbf{a}^\dagger\mathbf{a}) + \sum_{k=1,2,3} \mathbf{F}^{(-k)}(\mathbf{a}^4,\mathbf{a}^{\dagger 4},\mathbf{a}^\dagger\mathbf{a})\mathbf{a}^k + \mathbf{F}^{(k)}(\mathbf{a}^4,\mathbf{a}^{\dagger 4},\mathbf{a}^\dagger\mathbf{a})\mathbf{a}^{\dagger k}$$

where $\mathbf{F}^{(\pm k)}$ are analytical functions of $\mathbf{a}^4$, $\mathbf{a}^{\dagger 4}$ and $\mathbf{a}^\dagger\mathbf{a}$. Furthermore, the action of $\mathbf{E}$ on the coding 2D-subspace $\mathscr{E}_+$ can be expressed through the operator $\mathbf{E}\mathbf{\Pi}_{\mathscr{E}_+}$ with $\mathbf{\Pi}_{\mathscr{E}_+}$ the projector on $\mathscr{E}_+$. Noting that $\mathbf{a}\mathbf{\Pi}_{\mathscr{E}_+} = \alpha[|\mathscr{C}_\alpha^{(3\text{mod}4)}\rangle\langle\mathscr{C}_\alpha^{(0\text{mod}4)}| + |\mathscr{C}_\alpha^{(1\text{mod}4)}\rangle\langle\mathscr{C}_\alpha^{(2\text{mod}4)}|]$, $\mathbf{a}^2\mathbf{\Pi}_{\mathscr{E}_+} = \alpha^2\boldsymbol{\sigma}_X^{\text{even}}$, and that $\mathbf{a}^{\dagger k}\mathbf{\Pi}_{\mathscr{E}_+} = \mathbf{a}^{\dagger k}(\mathbf{a}/\alpha)^4\mathbf{\Pi}_{\mathscr{E}_+} = \mathbf{a}^{\dagger k}\mathbf{a}^k(\mathbf{a}^{4-k}/\alpha^4)\mathbf{\Pi}_{\mathscr{E}_+}$, we can write $\mathbf{E}\mathbf{\Pi}_{\mathscr{E}_+}$ in the form

$$\mathbf{E}(\mathbf{a},\mathbf{a}^\dagger)\mathbf{\Pi}_{\mathscr{E}_+} = \mathbf{G}_\alpha^{(0)}\mathbf{\Pi}_{\mathscr{E}_+} + \mathbf{G}_\alpha^{(1)}\mathbf{E}_{03,21}^{\mathscr{E}_+\to\mathscr{E}_-} + \mathbf{G}_\alpha^{(2)}\boldsymbol{\sigma}_X^{\text{even}} + \mathbf{G}_\alpha^{(3)}\mathbf{E}_{03,21}^{\mathscr{E}_+\to\mathscr{E}_-}\boldsymbol{\sigma}_X^{\text{even}}.$$

where $\mathbf{E}_{03,21}^{\mathscr{E}_+\to\mathscr{E}_-} = |\mathscr{C}_\alpha^{(3\mathrm{mod}4)}\rangle\langle\mathscr{C}_\alpha^{(0\mathrm{mod}4)}| + |\mathscr{C}_\alpha^{(1\mathrm{mod}4)}\rangle\langle\mathscr{C}_\alpha^{(2\mathrm{mod}4)}|$. Here, the operators $\mathbf{G}_\alpha^{(k)} = \alpha^k\mathbf{F}^{(-k)} + \alpha^{-k}\mathbf{a}^{\dagger 4-k}\mathbf{a}^{4-k}\mathbf{F}^{(4-k)}$, $k = 1,2,3$, and $\mathbf{G}_\alpha^{(0)} = \mathbf{F}^{(0)}$, are $\mathbb{Z}_4$-*parity-preserving operators*, i.e they preserve the photon number parity modulo 4. Under a certain condition similar to (1.12), the sets of $\mathbb{Z}_4$-parity-preserving errors are correctable by the four-component cat code, and corrected through the four-photon cat-pumping operation $\mathbb{R}_{\mathrm{pump}}^{\mathrm{4ph}}$. Besides, the occurrence of the error $\mathbf{E}_{03,21}^{\mathscr{E}_+\to\mathscr{E}_-}$ is revealed through a photon-number parity measurement.

1.3 Plan of the manuscript

In Chapter 2, we design an autonomous QEC scheme based on quantum reservoir engineering adapted to superconducting qubits. First, we focus on a three-qubit bit-flip code, where three transmon qubits are dispersively coupled to a few low-Q resonator modes. By applying only continuous-wave drives of fixed but well-chosen frequencies and amplitudes, we engineer an effective interaction Hamiltonian to evacuate the entropy created by eventual bit-flip errors. We provide a full analytical and numerical study of the protocol, while introducing the main limitations on the achievable error correction rates. In addition, we present two applications that can assess the performances of this scheme. Next, we expose a version of this scheme adapted to the three-qubit phase-flip code. In the last section, we provide some preliminary ideas to achieve a fully autonomous quantum error correction with a 9-qubit Bacon-Shor code.

In the two other chapters, we focus on the cat qubits. In Chapter 3, we propose a scheme to perform continuous and quantum non-demolition measurement of photon-number parity in a microwave cavity. As mentioned in Section 1.2, this corresponds to the error syndrome in the cat code. In our design, we exploit the strongly nonlinear Hamiltonian of a high-impedance Josephson circuit, coupling a high-Q cavity storage cavity mode to a low-Q readout one. In presence of parametric cat pumping, such a non-linear Hamiltonian acts effectively as a parity-type Hamiltonian. More precisely, this is achieved through a projection of the Hamiltonian on the cat manifold, following a quantum Zeno dynamics (QZD) argument. By driving the readout resonator at its resonance, the phase of the reflected/transmitted signal carries the information on the photon number parity of the high-Q mode.

In Chapter 4, we design four continous QEC schemes based on the tools developed in Chapter 3. These protocols offer a protection against phase-flip errors of the logical cat state, together with a first-order protection against the major single-photon loss channel. The first section presents two schemes encoding the information in a single oscillator via the four-component cat code. While one scheme is based on the continuous monitoring of the photon-number parity, another one realizes autonomous QEC by carefully coupling the oscillator to a lossy mode. The second section presents an adaptation of these protection schemes to the three-qubit bit-flip code, using three two-component cat qubits. Note that such a three-mode cat code provides a much stronger protection, as it protects, not only against single-photon loss channel, but against any type of single-mode errors. Indeed, such single-mode errors can only lead to logical bit-flips which are corrected by this encoding.

In this introductory chapter, after recalling basic elements of QEC theory, we have emphasized the difference between discrete QEC and continuous QEC. This was followed by a presentation of reservoir engineering as a method to achieve continuous autonomous QEC. This brief reminder on QEC and reservoir engineering will, in particular, ease the comprehension of Chapter 2 and Chapter 4. The second section of this chapter started with a quick overview of the two- and four-component cat code along with the so-called cat-pumping scheme, through which the corresponding 2D- or 4D-manifolds are stabilized. Next, we have presented a synthesis of the error protection provided by the cat code and the recovery map associated to the cat-pumping protocol. More precisely, we have shown that logical phase flips, under certain conditions, are strongly suppressed in the presence of multi-photon driven dissipation, thus leaving the cat qubits vulnerable to bit flips only. The contents of this section are useful to understand Chapter 3 and Chapter 4. In particular, the results provided in this section can be considered as preliminary results for the QEC schemes of Chapter 4.

Chapter 2

Dissipation-induced continuous quantum error correction for superconducting circuits

Table of contents

2.1 Introduction

A standard measurement-based feedback procedure to perform active QEC consists of probing some observables [57, 25], e.g. multi-qubit parities, in a non-destructive and repeated manner. Analyzing in real-time the measurement output reveals the occurrence of possible errors which could then be corrected by applying an appropriate unitary action in feedback. Recent advances in quantum-limited amplification [13, 8, 29, 74] have opened doors to high-fidelity non-demolition measurement of superconducting qubits and have already led to successful experiments on closed-loop control of such systems [87, 73, 11, 17]. However, the relevant time-scales for these systems imposes important limitations on the complexity of real-time analysis that one can perform on the measurement output. In particular, the finite bandwidth of the amplification procedure, together with the time-consuming data acquisition and post-treatment of the output signal, lead to a latency in the feedback procedure.

Alternatively, the reservoir (dissipation) engineering [65] and the closely related coherent feedback [49] circumvent the necessity of a real-time data acquisition, signal processing and feedback calculation. Coupling the quantum system to be stabilized to a strongly dissipative ancillary quantum system allows one to evacuate the entropy of the main system through the dissipation of the ancillary one. By building the feedback loop into the Hamiltonian, this type of autonomous feedback obviates the need for a complicated external control loop to correct errors. On the experimental side, such autonomous feedback techniques have been used for qubit reset [24], single-qubit state stabilization [55], and the creation [7] and stabilization [42, 79, 48] of states of multipartite quantum systems.

Autonomous Quantum Error Correction (AQEC) with multi-qubit codes has been theoretically investigated in a few recent proposals adapted to quantum photonics systems [38, 39]. The approach of [38, 39] consists in applying an embedded optical feedback loop for the QEC where each qubit is coupled to a different optical resonator, and the directional coupling between these subsystems is ensured through waveguide connections (see Subsection 1.1.5.2 for more details on this proposal). Here instead, we exploit the strong couplings and nonlinearities provided by quantum superconducting circuits to introduce hardware shortcuts and to propose a protocol adapted to state of the art experiments in this context. More precisely, by considering three transmon qubits [40] coupled, in the strong dispersive regime [78], to three (or one in a simplified version) low-Q modes of a single 3D cavity, we propose an AQEC protocol: by applying some appropriate Continuous-Wave (CW) microwave drives, we produce an effective Hamiltonian that evacuates the entropy resulting from bit-flip errors.

The bit-flip correction scheme being only based on the application of CW drives of fixed frequencies, amplitudes and phases (no time-dependence for these parameters), we ensure a strong robustness with respect to small variations of these parameters and require only basic experimental calibrations. While a recent proposal [36, 35] explores the possibility of employing well-controlled magnetic flux to ensure mutual strong couplings between transmon qubits, each one coupled to a separate dissipative degree of freedom, here we base our scheme on simple extensions of recent experiments [79, 45]. In particular, similarly to the recent works [46, 79, 19, 84, 75], our protocol is based on minimal symmetry requirements: we only need a certain linear combination of the dispersive shift strengths to be small. Such a symmetry can be rather easily achieved by rough tuning of the qubits frequencies. Also, compared to the protocols in [38, 39], we avoid any requirement of directional couplings which simplifies the experimental implementation of such a protocol with superconducting circuits. Indeed, ensuring any directionality in the transmission of quantum information, while avoiding corruption with extra noise, necessitates the development of new quantum-limited devices based on Josephson elements and represents, by itself, a significant experimental objective. Finally, by avoiding resonant interactions between the qubits and the low-Q resonators, the qubits remain protected against the Purcell effect.

Next, we propose two possible proof-of-principle experiments that would demonstrate the efficiency of the bit-flip correction scheme. The first protocol aims to demonstrating the conservation of the logical state population, or equivalently the conservation of the $z-$coordinate on the logical Bloch sphere. In a second application, we show that the AQEC scheme can be used to autonomously prepare a GHZ (Greenberger-Horne-Zeilinger) state of three qubits.

Phase-flip correction (instead of bit-flip correction) can be achieved by mapping phase-flip errors to bit-flip errors through $\pi/2$-rotations along the y-axis and correcting for these bit-flip errors. In such a scheme, however, one loses the CW property of the protocol. More interestingly, we show that an equivalent CW AQEC scheme can be realized by replacing the longitudinal dispersive coupling (of the form $\hbar\chi\boldsymbol{\sigma}_z\mathbf{a}^\dagger\mathbf{a}$) by the transverse dispersive coupling (of the form $\hbar\chi^{(x)}\boldsymbol{\sigma}_x\mathbf{a}^\dagger\mathbf{a}$) in the presence of strong Rabi drives on the qubits. This proposal is inspired from a recent experiment [89], in which a transverse dispersive coupling of significant strength was achieved by the mean of CW drives only.

Finally, the three-qubit AQEC, that protects against either bit flips or phase flips, can be used as a building block for the nine-qubit Bacon-Shor code [6]. This code offers a protection against arbitrary single qubit error while requiring the measurement of two-qubit parities only. In the last section of this chapter, we sketch two proposals for the realization of the Bacon-Shor code. These correction schemes are merely drafts, and still require further study. In particular, they should be tested through numerical simulations.

In Section 2.2, we provide the framework of the AQEC scheme. After a brief overview of the idea behind reservoir engineering for QEC, we introduce the considered physical system, together with the required coupling regimes. Section 2.3 provides the AQEC protocol. In Subsection 2.3.1, we present the idea on a simpler case where only one of the three qubits can undergo a bit-flip error. In Subsection 2.3.2, we generalize the idea to the case where the three qubits suffer independently from bit-flip errors. In Subsection 2.3.3, we summarize the ideas and perform numerical simulations that illustrate the performance of the scheme with realistic experimental parameters. In Section 2.4, we expose the limitations of the proposed protocol through the analysis of major decoherence channels created by various possible imperfections. Section 2.5 is devoted to a simplified version of the protocol where we only require the coupling of the three qubits to a single low-Q resonator: this could be considered as the minimal experimental setup required for realizing a bit-flip code. Although the three-qubit bit-flip code does not protect the logical information against phase-flip type errors, we are able to design some experiments to demonstrate the principles of such a protection. More precisely, we show in Section 2.6 how this scheme can be used to conserve the populations (and not phases) of the logical states and more interestingly to autonomously prepare a GHZ state of three qubits. An adaptation of the bit-flip QEC scheme to an autonomous phase-flip correction scheme is discussed in Section 2.7. Finally, in Section 2.8, we propose an extension of the three-qubit QEC scheme to a fully protecting autonmous Bacon-Shor code.

The results of Sections 2.2 through 2.5 have led to a publication in Physical Review A [15].

2.2 Framework of autonomous QEC

2.2.1 Reservoir engineering for QEC

The 3-qubit bit-flip code consists of encoding the logical states $|0\rangle$ and $|1\rangle$ using the states $|000\rangle$ and $|111\rangle$ of three physical qubits. Starting from a superposition in the coding subspace $\mathscr{E}_0 = \text{span}\{|000\rangle, |111\rangle\}$, a single bit-flip error maps the states to one of the *error subspaces* $\mathscr{E}_1 = \text{span}\{|100\rangle, |011\rangle\}$, $\mathscr{E}_2 = \text{span}\{|010\rangle, |101\rangle\}$ or $\mathscr{E}_3 = \text{span}\{|001\rangle, |110\rangle\}$. We can associate to these error processes, the Kraus operators $\mathscr{M}_0 = \sqrt{1-p}\mathbf{I}$, $\mathscr{M}_1 = \sqrt{\frac{p}{3}}\boldsymbol{\sigma}_x^1$, $\mathscr{M}_2 = \sqrt{\frac{p}{3}}\boldsymbol{\sigma}_x^2$ and $\mathscr{M}_3 = \sqrt{\frac{p}{3}}\boldsymbol{\sigma}_x^3$, where $p \ll 1$ is the bit-flip probability for a single physical qubit, $\mathbf{I}$ is the identity on the qubits Hilbert space, and $\boldsymbol{\sigma}_x^k$ is the Pauli matrix along the X axis of the k'th qubit.

In conventional QEC, a measurement of the two-qubit parities would reveal the error subspace the system lives in without leaking out any further information on the superposition between the logical states. The quantum state could then be restored by applying an appropriate quantum gate. Alternatively, in a reservoir engineering scheme, we use the coupling to an ancillary quantum system to mediate the evacuation of the information entropy. More precisely, we design a joint unitary operation U_{SA} between the system (Hilbert space $\mathscr{H}_S$)

and the ancilla (Hilbert space $\mathscr{H}_A$) satisfying

$$\begin{aligned} U_{SA}\left((\mathscr{M}_j|000\rangle_S)\otimes|0\rangle_A\right) &= |000\rangle_S\otimes|j\rangle_A, \\ U_{SA}\left((\mathscr{M}_j|111\rangle_S)\otimes|0\rangle_A\right) &= |111\rangle_S\otimes|j\rangle_A, \quad j=0,1,2,3. \end{aligned}$$

While the system is already mapped back onto the coding subspace $\mathscr{E}_0$, a rapid decay of the ancilla resets its state to $|0\rangle_A$, preparing it for the next run of QEC. Throughout Section 2.3, we propose a QEC scheme along with a possible circuit design (see Section 2.2.2) that implements these steps of unitary operation and ancilla reset. Moreover, using driven damped harmonic oscillators as ancillary system, these operations are performed in a continuous and simultaneous manner.

2.2.2 Physical system

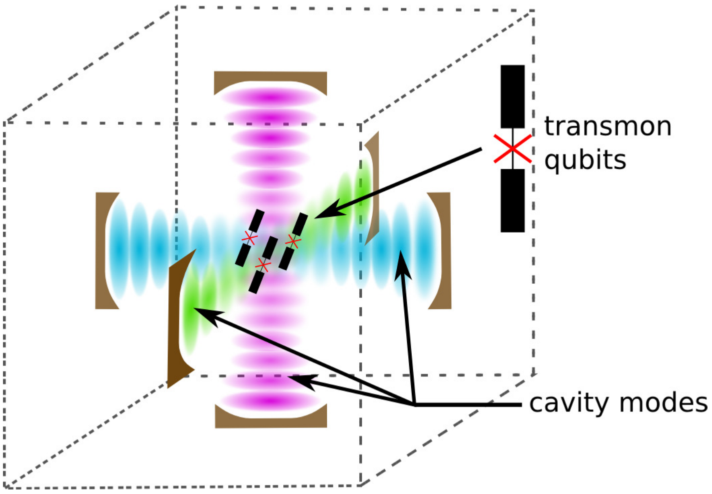

Fig. 2.1 (Color online) A possible physical realization where three transmon qubits are strongly coupled to three low-Q spatial modes of a 3D superconducting cavity. The coupling of the qubits to the modes are designed such that (2.3) and (2.4) are satisfied. External microwave drives may be applied to the cavity, but the output ports of the cavity are not monitored.

We consider three transmon qubits [40] coupled to three low-Q resonators. In Figure 2.1, we present a design where the three qubits are coupled to three spatial modes of a 3D superconducting cavity. While the qubits are used to encode the quantum information, the resonators together play the role of the ancilla. Following the strategy of the previous subsection, we will map the error subspaces $\mathscr{E}_{1,2,3}$ to the three ancilla states $|100\rangle_A$, $|010\rangle_A$

and $|001\rangle_A$, where $|0\rangle_A$ and $|1\rangle_A$ are respectively the vacuum state and the single-photon Fock state of each resonator.

The total Hamiltonian of the driven system can be written in the following form [58],

$$\begin{aligned}\mathbf{H(t)} &= \sum_{k=1}^{3} \hbar\tilde{\omega}_{a_k}\mathbf{a}_k^\dagger\mathbf{a}_k + \sum_{k=1}^{3} \hbar\tilde{\omega}_{b_k}\mathbf{b}_k^\dagger\mathbf{b}_k \\ &- \sum_{k=1}^{3} E_J^k\left(\cos\left(\frac{\mathbf{\Phi}_k}{\phi_0}\right)+\frac{1}{2}\frac{\mathbf{\Phi}_k^2}{\phi_0^2}\right) \\ &+ \sum_{k=1}^{3} \hbar\varepsilon_k^a(t)(\mathbf{a}_k+\mathbf{a}_k^\dagger) + \sum_{k=1}^{3} \hbar\varepsilon_k^b(t)(\mathbf{b}_k+\mathbf{b}_k^\dagger), \qquad (2.1)\end{aligned}$$

where

$$\mathbf{\Phi}_k = \sum_{k'=1}^{3} \phi_{k,k'}^a(\mathbf{a}_{k'}+\mathbf{a}_{k'}^\dagger) + \sum_{k'=1}^{3} \phi_{k,k'}^b(\mathbf{b}_{k'}+\mathbf{b}_{k'}^\dagger).$$

Here we note $\mathbf{a}_k$ (resp. $\mathbf{a}_k^\dagger$) and $\mathbf{b}_k$ (resp. $\mathbf{b}_k^\dagger$) the annihilation (resp. creation) operator of resonator k and qubit k, $\tilde{\omega}_{a_k}$ and $\tilde{\omega}_{b_k}$ the dressed frequencies of resonator k and qubit k respectively, E_J^k the Josephson energy of qubit k, $\phi_0 = \hbar/2e$ the superconducting flux quantum. Some external drives, denoted by $\varepsilon_k^{a,b}(t)$, may also be applied to the resonators and the qubits. The contribution of the Josephson junctions, is given by the cosine terms of the second line, in which we have removed the quadratic part $\mathbf{\Phi}_k^2/2\phi_0^2$ and included it in the terms $\hbar\tilde{\omega}_{a_k}\mathbf{a}_k^\dagger\mathbf{a}_k$ and $\hbar\tilde{\omega}_{b_k}\mathbf{b}_k^\dagger\mathbf{b}_k$.

As it can be seen in the expression of $\mathbf{\Phi}_k$, the dressed modes **a** and **b** participate to the flux across the Josephson junctions. Noting that $\phi_{k,k'}^a \ll \phi_{j,j}^b$, the dressed modes **a** share a much smaller part of the non-linearity than the dressed modes **b**. This is why we refer to the b modes as the qubit modes and the a modes as the cavity modes. Indeed, under the assumption that the drive strengths ε_k^b are much weaker than the anharmonicity of the modes **b**, we can restrict ourselves to the first two levels of the qubit modes $\mathbf{b}_{1,2,3}$.

In the transmon regime $\mid \frac{\mathbf{\Phi}^k}{\phi_0} \mid \ll 1$ and therefore we can neglect higher than fourth order terms in the cosines. In the absence of external drives, the effective Hamiltonian, in the dispersive coupling regime (where the resonance frequencies are well separated), becomes [58]

$$\begin{aligned}
\widetilde{\mathbf{H}}/\hbar = & \sum_{k=1}^{3} \omega_{a_k} \mathbf{a}_k^{\dagger} \mathbf{a}_k + \sum_{k=1}^{3} \frac{\omega_{b_k}}{2} \boldsymbol{\sigma}_z^k \\
& - \sum_{k=1,2,3} \mathbf{a}_k{}^{\dagger} \mathbf{a}_k \left(\frac{\chi_{a_k,b_1}}{2} \boldsymbol{\sigma}_z^1 + \frac{\chi_{a_k,b_2}}{2} \boldsymbol{\sigma}_z^2 + \frac{\chi_{a_k,b_3}}{2} \boldsymbol{\sigma}_z^3 \right) \\
& - \sum_{k} K_{a_k,a_k} \mathbf{a}_k{}^{\dagger 2} \mathbf{a}_k^2 - \sum_{j \neq k} K_{a_k,a_j} \mathbf{a}_j{}^{\dagger} \mathbf{a}_j \mathbf{a}_k{}^{\dagger} \mathbf{a}_k \\
& - \sum_{j \neq k} K_{b_k,b_j} \boldsymbol{\sigma}_z^j \boldsymbol{\sigma}_z^k .
\end{aligned} \tag{2.2}$$

In the above expression, we make use of the renormalized frequencies ω_{a_k} and ω_{b_k} for the resonators modes and for the qubits modes. While the dispersive coupling strengths χ_{a_k,b_j} $(j,k = 1,2,3)$ are the key parameters in our QEC protocol, the other self-Kerr and cross-Kerr terms K_{a_j,a_j}, K_{a_k,a_j} and K_{b_k,b_j} are small compared to these dispersive couplings, as they represent higher order effects. However, as it will be seen later, our QEC protocol is fully insensitive to the contribution of these terms.

Similarly to [46], we consider the strong dispersive coupling regime, where the dispersive shifts χ_{a_k,b_j} are much larger than the qubit and the cavity linewidths:

$$|\chi_{a_k,b_j}| \gg \kappa_{k'}, \gamma_{j'}, \quad j,k,j',k' = 1,2,3, \tag{2.3}$$

where γ_j and κ_k represent, respectively, the linewidths of qubit j and resonator k. An additional symmetry assumption

$$\sum_{j} \chi_{a_k,b_j} = 0 \quad k = 1,2,3,$$

is required to ensure that the QEC protocol does not reveal any information other than the error syndromes. In practice, a finite sum of the dispersive couplings would lead to an extra dephasing between the code states $|000\rangle$ and $|111\rangle$ which could be neglected in the limit

$$|\sum_{j} \chi_{a_k,b_j}| \ll \kappa_k . \tag{2.4}$$

The assumptions (2.3) and (2.4) imply that at least one of the coupling strengths χ_{a_k,b_j} for each resonator k is negative. While this is considered to be a rather hard task for a transmon qubit to change the sign of its dispersive couplings, the above requirement could be relaxed by encoding the quantum information in a different subspace than $\mathrm{span}\{|000\rangle, |111\rangle\}$. Indeed, using the subspace span$\{|100\rangle, |011\rangle\}$ instead, we rather need to satisfy $|\chi_{a_k,b_1} - \chi_{a_k,b_2} - \chi_{a_k,b_3}|$ to be small, which could be satisfied even for positive-valued χ_{a_k,b_j}'s.

2.3 Error Correction Scheme

In this section, we describe in details the error correction scheme using three qubits coupled to three cavities. In a first subsection, we focus on a simple case where only one of the three qubits can undergo a bit-flip and therefore the correction takes place only on this qubit. Next, we will extend the protocol to the case where the three qubits suffer from bit-flips.

2.3.1 Correction on one qubit

Through the rest of this paper, we consider the system in the rotating frame given by the Hamiltonian

$$\mathbf{H}_0/\hbar = \sum_{k=1}^{3} \omega_{a_k} \mathbf{a}_k^\dagger \mathbf{a}_k + \sum_{k=1}^{3} \frac{\omega_{b_k}}{2} \boldsymbol{\sigma}_z^k.$$

The considered errors refer to bit-flips occurring in this rotating frame. In this subsection, we restrict ourselves to the case where such an error only occurs on qubit 1 and at a rate γ_x. Therefore, we need only a single resonator to perform the correction.

Before getting to the details of the scheme, let us provide an intuitive picture (Figure 2.2a). Starting from a superposition state $(c_0|000\rangle + c_1|111\rangle) \in \mathscr{E}_0$ (while the cavity mode is in the vacuum state $|0\rangle_A$), and after an eventual bit-flip error of the first qubit, the system ends up in the state $(c_0|100\rangle + c_1|011\rangle) \in \mathscr{E}_1$. Applying microwave drives of fixed and well-chosen frequencies, we induce an effective transition between the states $|100\rangle \otimes |0\rangle_A$ and $|000\rangle \otimes |1\rangle_A$ and another one between the states $|011\rangle \otimes |0\rangle_A$ and $|111\rangle \otimes |1\rangle_A$. Note that, through the choice of the drive frequencies, these transitions are turned on in a selective manner, only when the three qubits lie in the manifold $\mathscr{E}_1$. Moreover, by fixing the amplitudes of the drives, these transitions which are illustrated by straight-line arrows in Figure 2.2a, will conserve the initial superposition $(c_0|100\rangle + c_1|011\rangle) \otimes |0\rangle_A$ producing the state $(c_0|000\rangle + c_1|111\rangle) \otimes |1\rangle_A$. Now a rapid decay of the ancilla resonator resets its state to the vacuum and projects the three-qubit system to the coding subspace. Through the following paragraphs, we will detail the ingredients of this protocol.

Three-qubit manifold selectivity - We apply two continuous-wave (CW) microwave drives to the resonator at frequencies $\omega_{p_1} = |\omega_{a_1} - \omega_{b_1}|/2$ and $\omega_{p_2} = (\omega_{a_1} + \omega_{b_1})/2$, and amplitudes ε_{p_1} and ε_{p_2}. These drives are far detuned from all resonance frequencies and act as stiff pumps in a parametric procedure. As illustrated in Figure 2.2b (right), two pump photons

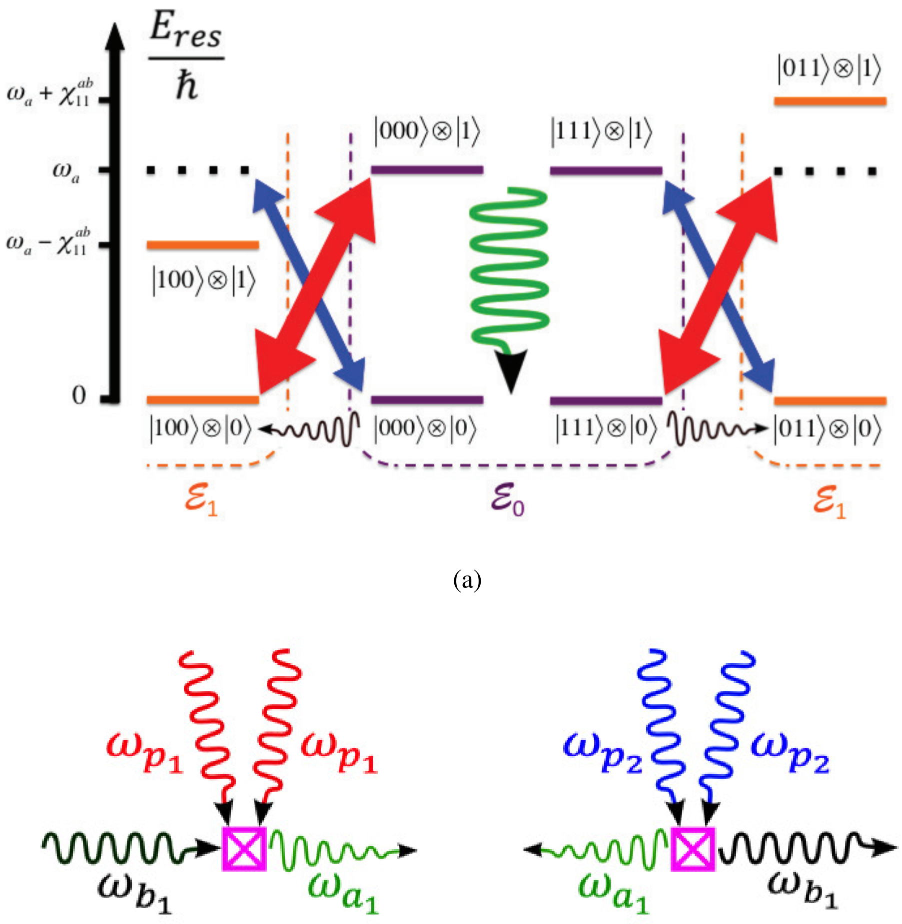

(a)

(b)

Fig. 2.2 (Color online) (a): Energy-level diagram of the resonator only (the qubits energies are not represented here) as a function of the joint-state of the qubits-cavity system. As explained through Subsection 2.3.1, the resonator never gets populated beyond Fock state $|1\rangle_A$ and therefore, we restrict the diagram to the space spanned by Fock states $|0\rangle_A$ and $|1\rangle_A$. Thick red (resp. thin blue) straight-line arrows indicate couplings between two states induced by the pump at frequency ω_{p_1} (resp. ω_{p_2}). Wavy arrow indicates a common decay channel due to the decay of the single photon in the ancillary resonator. (b): Left: Four-wave mixing process induced by the pumps at frequency ω_{p_1} where two pump photons convert a single qubit excitation to a decaying photon of the resonator. Right: Four-wave mixing process induced by the pump at frequency ω_{p_2} where two pump photons create an excitation in both the qubit and the resonator.

at frequency ω_{p_1} convert an excitation in qubit 1 to an excitation of the resonator. In the same way (left on Figure 2.2b), two pump photons at frequency ω_{p_2} create, simultaneously, an excitation both in the qubit and in the resonator. These processes happen in a coherent manner and the oscillation rate and phase can be tuned by adjusting the pumps amplitudes and phases. In particular, we choose these amplitudes and phases to ensure the same rate and phase for both oscillations, leading to an effective Hamiltonian of the form

$$\begin{aligned}\mathbf{H}_{\text{eff}}/\hbar = &-\mathbf{a}_1^\dagger\mathbf{a}_1(\frac{\chi_{a_1,b_1}}{2}\boldsymbol{\sigma}_z^1+\frac{\chi_{a_1,b_2}}{2}\boldsymbol{\sigma}_z^2+\frac{\chi_{a_1,b_3}}{2}\boldsymbol{\sigma}_z^3)\\ &+\frac{\Omega_{p1}}{2}(\boldsymbol{\sigma}_+^1\mathbf{a}_1+h.c.)+\frac{\Omega_{p2}}{2}(\boldsymbol{\sigma}_-^1\mathbf{a}_1+h.c.).\end{aligned} \tag{2.5}$$

Here, the second line of the Hamiltonian is derived from the fourth-order terms of the cosine in (2.2) and after applying a rotating wave approximation (RWA). The Rabi frequency Ω_{p_j} are given by

$$\Omega_{p_j}=\sqrt{K_{a_1,a_1}\chi_{a_1,b_1}}\left|\frac{\varepsilon_1^{a,j}}{\omega_{a_1}-\omega_{p_j}}\right|^2. \tag{2.6}$$

The amplitudes of the pumps $\varepsilon_1^{a,1}$ and $\varepsilon_1^{a,2}$ are chosen such that Ω_{p_1} and Ω_{p_2} are real quantities both equal to Ω_p. Note that, for simplicity sakes, we have neglected the other self-Kerr and cross-Kerr terms K_{a_j,a_k} and K_{b_j,b_k}. We will discuss their effect at the end of the next subsection.

Taking into account the dispersive shifts χ_{a_1,b_j}, the pump tone ω_{p_1} only affects the transition between $|011\rangle\otimes|0\rangle_A$ and $|111\rangle\otimes|1\rangle_A$ (this is satisfied by choosing $\Omega\ll\chi_{a_1,b_1}$). In the same manner, the pump tone ω_{p_2} only affects the transition between $|100\rangle\otimes|0\rangle_A$ and $|000\rangle\otimes|1\rangle_A$. In particular, as illustrated in Figure 2.2a, the manifold $\mathscr{E}_0\otimes|0\rangle_A$ is left untouched: the transitions $|000\rangle\otimes|0\rangle_A\leftrightarrow|100\rangle\otimes|1\rangle_A$ and $|111\rangle\otimes|0\rangle_A\leftrightarrow|011\rangle\otimes|1\rangle_A$ are detuned by $\pm\chi_{a_1,b_1}$ from twice the pump tones. Therefore, the strong dispersive coupling ensured by (2.3) provides the selectivity of the manifold $\mathscr{E}_1$ in the correction procedure.

One can note that, during the correction procedure, the resonator is only populated when the three-qubit system is in the manifold $\mathscr{E}_0$. By the assumption (2.4), in such a case the resonator's frequency is given by ω_{a_1} independently of the states $|000\rangle$ or $|111\rangle$ of the three qubits. This degeneracy ensures that the outgoing photons of the resonator do not reveal any further information about the superposition between these two states.

Finally, the dissipation of the ancilla resonator projects the three-qubit state to the coding subspace $\mathscr{E}_0$ and resets the resonator to its vacuum state. Evacuating the information entropy, this ensures the irreversibility of the transition from $\mathscr{E}_1$ to $\mathscr{E}_0$.

Effective model - Throughout the rest of this subsection, we provide a reduced model and derive an effective correction rate. We start by moving into the rotating frame of $\mathbf{H}_{\text{disp}} = -\mathbf{a}_1^\dagger \mathbf{a}_1 (\frac{\chi_{a_1,b_1}}{2}\boldsymbol{\sigma}_z^1 + \frac{\chi_{a_1,b_2}}{2}\boldsymbol{\sigma}_z^2 + \frac{\chi_{a_1,b_3}}{2}\boldsymbol{\sigma}_z^3)$. The resonance frequencies being well-resolved (2.3), we apply the RWA, removing highly oscillating terms at frequencies of order χ_{jk}^{ab}. Furthermore, choosing $\Omega_p < \kappa_1$, we can adiabatically eliminate the low-Q resonator mode to achieve the following effective master equation (detailed derivation at the end of Section 2.3.1):

$$\frac{d\boldsymbol{\rho}}{dt} = \Gamma_c \mathscr{D}[\mathbf{c}_1](\boldsymbol{\rho}) + \frac{\gamma_x}{2}\mathscr{D}[\boldsymbol{\sigma}_x^1](\boldsymbol{\rho}). \tag{2.7}$$

In this master equation, $\mathscr{D}[\mathbf{o}](\boldsymbol{\rho}) = \mathbf{o}\boldsymbol{\rho}\mathbf{o}^\dagger - 1/2(\mathbf{o}^\dagger\mathbf{o}\boldsymbol{\rho} + \boldsymbol{\rho}\mathbf{o}^\dagger\mathbf{o})$. While the second Lindblad term formulates the bit-flip errors of the qubit 1, the first term represents the effective error correction. Here, the induced correction operator, $\mathbf{c}_1$, is given by

$$\mathbf{c}_1 = |000\rangle\langle 100| + |111\rangle\langle 011| = \boldsymbol{\sigma}_-^1 \mathbf{\Pi}_{|00\rangle}^{23} + \boldsymbol{\sigma}_+^1 \mathbf{\Pi}_{|11\rangle}^{23}.$$

where $\mathbf{\Pi}_{|00\rangle}^{23}$ (resp. $\mathbf{\Pi}_{|11\rangle}^{23}$) is the projection operator of the second and third qubit on the state $|00\rangle$ (resp. $|11\rangle$). Moreover, Γ_c represents the effective correction rate and is well approximated by $\Gamma_c \approx \frac{\Omega_p^2}{\kappa}$.

The simulation of Figure 2.3 illustrates the performance of this correction protocol. Starting from a corrupted state $(|100\rangle - i|011\rangle)/\sqrt{2} \in \mathscr{E}_1$, and neglecting further bit-flip errors ($\gamma_x = 0$), we simulate the system's dynamics before and after the model reduction. By plotting the fidelity $F(t) = \langle\psi_0|\boldsymbol{\rho}(t)|\psi_0\rangle$ with respect to the state $\psi_0 = (|000\rangle - i|111\rangle)/\sqrt{2} \in \mathscr{E}_0$, we observe that the target state is reached after a mean time Γ_c^{-1}. Moreover, the dynamics is well described by the reduced model, which confirms the fact that the correction happens at the predicted rate Γ_c. The deviation of the model before reduction from the reduced one for short time scales could be explained by the fact that the adiabatic elimination of the resonator transforms a second-order process in time (entanglement of the qubits and the resonator followed by resonator's dissipation) into a first-order process (correction process modeled by the dissipation operator $\sqrt{\Gamma_c}\mathbf{c}_1$).

In this paragraph, we give a derivation of the reduced model of eq. (2.7). The Hamiltonian (2.5), in the rotating frame defined by $\mathbf{H}_{\text{disp}} = -\mathbf{a}_1^\dagger \mathbf{a}_1 (\frac{\chi_{a_1,b_1}}{2}\boldsymbol{\sigma}_z^1 + \frac{\chi_{a_1,b_2}}{2}\boldsymbol{\sigma}_z^2 + \frac{\chi_{a_1,b_3}}{2}\boldsymbol{\sigma}_z^3)$ and with $\Omega_p = \Omega_{p_1} = \Omega_{p_2}$, reads

$$\mathbf{H}_{\text{eff}}(t)/\hbar = \frac{\Omega_p}{2}\big(e^{it[\sum_{j=1}^{3} \frac{\chi_{a_1,b_j}}{2}\sigma_Z^j - \chi_{a_1,b_1}(\mathbf{a}_1^\dagger\mathbf{a}_1+1)]}\mathbf{a}_1\boldsymbol{\sigma}_+^1 + e^{it[\sum_{j=1}^{3} \frac{\chi_{a_1,b_j}}{2}\sigma_Z^j + \chi_{a_1,b_1}(\mathbf{a}_1^\dagger\mathbf{a}_1+1)]}\mathbf{a}_1\boldsymbol{\sigma}_-^1 + h.c.\big).$$

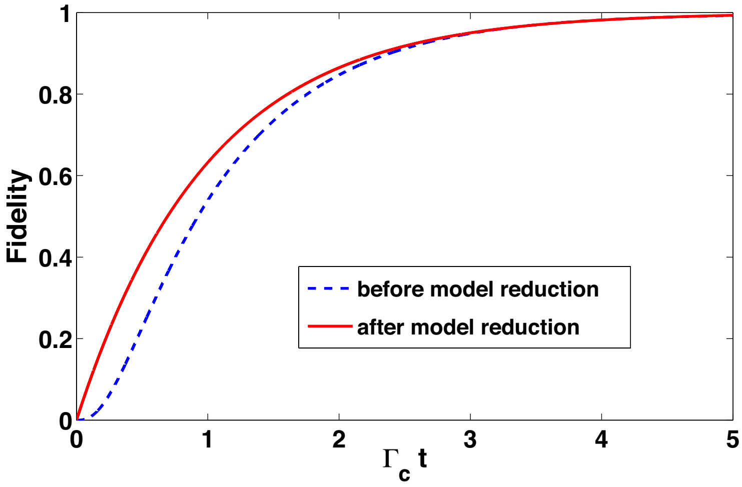

Fig. 2.3 (Color online) Autonomous QEC when the system is initialized in the corrupted state $(|100\rangle - i|011\rangle)/\sqrt{2} \in \mathscr{E}_1$ and no additional errors occur ($\gamma_x = 0$). The dashed blue curve illustrates the fidelity to the state $(|000\rangle - i|111\rangle)/\sqrt{2} \in \mathscr{E}_0$, for the model given by the Hamiltonian (2.5) (before model reduction). The solid red curve represents this fidelity for the reduced model given by (2.7). Other parameters have been set to $\chi_{a_1,b_1} = -20\kappa, \chi_{a_1,b_2} = 10\kappa, \chi_{a_1,b_3} = 10\kappa,$ and $\Omega_p = 0.3\kappa$, giving rise to $\Gamma_c = 0.09\kappa$.

Since $|\chi_{a_1,b_j}| \gg \Omega_p$, we can apply a RWA to this Hamiltonian, which yields

$$\mathbf{H}_{\text{eff}}/\hbar = \frac{\Omega_p}{2}[|0\rangle\langle 1|_A \otimes \mathbf{c}_1^\dagger + |1\rangle\langle 0|_A \otimes \mathbf{c}_1],$$

where the operator $\mathbf{c}_1 = |000\rangle\langle 100| + |111\rangle\langle 011|$ acts on the space of the qubits, and $|j\rangle_A$ denotes the Fock state j of the ancilla resonator. As a reminder, this derivation takes place in the frame where only errors on qubit 1 can occur, such that qubits 2 and 3 remain in the space spanned by the states $|00\rangle_{b_2,b_3}$ and $|11\rangle_{b_2,b_3}$. The master equation of the system reads

$$\begin{aligned} \frac{d\boldsymbol{\rho}}{dt} &= -\frac{i}{\hbar}[\mathbf{H}_{\text{eff}}, \boldsymbol{\rho}] + \frac{\gamma_x^1}{2}\mathscr{D}[\boldsymbol{\sigma}_x^1]\rho + \kappa_1 \mathscr{D}[\mathbf{a}_1]\boldsymbol{\rho}, \\ \mathbf{H}_{\text{eff}}/\hbar &= \frac{\Omega_p}{2}[|0\rangle\langle 1|_A \otimes \mathbf{c}_1^\dagger + |1\rangle\langle 0|_A \otimes \mathbf{c}_1]. \end{aligned} \tag{2.8}$$

Let us define the small parameter $\delta = \Omega_p/\kappa < 1$. The bit-flip rate is assumed to satisfy $\gamma_x^1/\kappa \lesssim \delta^2$. In this dissipative regime, we expect the mean photon number of the resonator to remain close to zero at all time. Thus, we seek a solution $\boldsymbol{\rho}$ of the master equation (2.8) of the form

$$\begin{aligned}\boldsymbol{\rho} = &|0\rangle\langle 0|_A\boldsymbol{\rho}_{00} \\ &+\delta[|1\rangle\langle 0|_A\boldsymbol{\rho}_{10}+|0\rangle\langle 1|_A\boldsymbol{\rho}_{01}] \\ &+\delta^2[|1\rangle\langle 1|_A\boldsymbol{\rho}_{11}+|2\rangle\langle 0|_A\boldsymbol{\rho}_{20}+|0\rangle\langle 2|_A\boldsymbol{\rho}_{02}]+\mathscr{O}(\delta^3),\end{aligned} \tag{2.9}$$

where the operators $\boldsymbol{\rho}_{ij}$ act on the qubits space and satisfy $||\boldsymbol{\rho}_{ij}|| = \mathscr{O}(1)$. Through the adiabatic elimination ([12], Chapter 12), we wish to obtain the reduced dynamics of the qubits given by the reduced density matrix $\boldsymbol{\rho}_s = Tr_A[\boldsymbol{\rho}] = \boldsymbol{\rho}_{00}+\delta^2\boldsymbol{\rho}_{11}+\mathscr{O}(\delta^3)$. Here, $Tr_A[.]$ denotes the partial trace operator with respect to the resonator. Injecting (2.9) into the master equation (2.8) and making the projections $\langle 0|.|0\rangle_A$, $\langle 0|.|1\rangle_A$, $\langle 1|.|0\rangle_A$ and $\langle 1|.|1\rangle_A$, gives respectively

$$\begin{aligned}\frac{1}{\kappa}\frac{d\boldsymbol{\rho}_{00}}{dt} &= -\frac{i\delta^2}{2}(\mathbf{c}_1^\dagger\boldsymbol{\rho}_{10}-\boldsymbol{\rho}_{01}\mathbf{c}_1)+\delta^2\boldsymbol{\rho}_{11}+\delta^2(\boldsymbol{\sigma}_X^1\boldsymbol{\rho}_{00}\boldsymbol{\sigma}_X^1-\boldsymbol{\rho}_{00})+\mathscr{O}(\delta^3) \\ \frac{1}{\kappa}\frac{d\boldsymbol{\rho}_{01}}{dt} &= \frac{i}{2}\boldsymbol{\rho}_{00}\mathbf{c}_1^\dagger-\frac{\boldsymbol{\rho}_{01}}{2}+\mathscr{O}(\delta) \\ \frac{1}{\kappa}\frac{d\boldsymbol{\rho}_{11}}{dt} &= -\frac{i}{2}\boldsymbol{\rho}_{00}(\mathbf{c}_1\boldsymbol{\rho}_{01}-\boldsymbol{\rho}_{10}\mathbf{c}_1^\dagger)-\boldsymbol{\rho}_{11}+\mathscr{O}(\delta)\end{aligned} \tag{2.10}$$

The evolution of $\boldsymbol{\rho}_{01}$ depends on the time-dependent operator $\boldsymbol{\rho}_{00}$. However, the evolution rate of $\boldsymbol{\rho}_{00}$ scales as δ^2 as opposed to $\mathscr{O}(1)$ for $\boldsymbol{\rho}_{01}$. Hence, we can make the adiabatic elimination of the fast dynamics of $\boldsymbol{\rho}_{01}$, and consider that $\boldsymbol{\rho}_{01}$ is constantly in its steady state up to $\mathscr{O}(\delta)$, which gives $\boldsymbol{\rho}_{01} = i\boldsymbol{\rho}_{00}\mathbf{c}_1^\dagger+\mathscr{O}(\delta)$. Similarly, $\boldsymbol{\rho}_{11} = -\frac{i}{2}\boldsymbol{\rho}_{00}(\mathbf{c}_1\boldsymbol{\rho}_{01}-\boldsymbol{\rho}_{10}\mathbf{c}_1^\dagger)+\mathscr{O}(\delta)$. Substituting the expressions of $\boldsymbol{\rho}_{01}$, $\boldsymbol{\rho}_{10}$ and $\boldsymbol{\rho}_{11}$ into the above expression of $\frac{1}{\kappa}\frac{d\boldsymbol{\rho}_{00}}{dt}$ leads to

$$\begin{aligned}\frac{1}{\kappa}\frac{d\boldsymbol{\rho}_s}{dt} =& \frac{1}{\kappa}\frac{d\boldsymbol{\rho}_{00}}{dt}+\mathscr{O}(\delta^3) \\ =& -\frac{\delta^2}{2}[\mathbf{c}_1^\dagger\mathbf{c}_1\boldsymbol{\rho}_{00}+\boldsymbol{\rho}_{00}\mathbf{c}_1^\dagger\mathbf{c}_1]+\delta^2\mathbf{c}_1\boldsymbol{\rho}_{00}\mathbf{c}_1^\dagger+\frac{\gamma_X}{2\kappa}\mathscr{D}[\boldsymbol{\sigma}_X^1](\boldsymbol{\rho}_{00})+\mathscr{O}(\delta^3).\end{aligned} \tag{2.11}$$

This reduced master equation can be written in the more compact form,

$$\frac{d\boldsymbol{\rho}_s}{dt} = \Gamma_c\mathscr{D}[\mathbf{c}_1](\boldsymbol{\rho}_s)+\frac{\gamma_X}{2}\mathscr{D}[\boldsymbol{\sigma}_X^1](\boldsymbol{\rho}_s)+\mathscr{O}(\kappa\delta^3), \tag{2.12}$$

where $\Gamma_c = \delta^2/\kappa = \Omega_p^2/\kappa$.

2.3.2 Correction on three qubits

Now, we consider the case where each qubit j can independently undergo a bit-flip error at a rate of γ_x^j. Similarly to the previous subsection, we apply two pumps at frequencies $\omega_{p_1}^j = (\omega_a^j + \omega_b^j)/2$ and $\omega_{p_2}^j = |\omega_a^j - \omega_b^j|/2$ to the resonators, both associated to each qubit. Following the derivation of (2.5), this leads to the following effective Hamiltonian

$$\begin{aligned}\mathbf{H}_{\text{eff}}/\hbar = &-\sum_{j=1,2,3} \mathbf{a}_j^\dagger \mathbf{a}_j \left(\frac{\chi_{a_j,b_1}}{2}\boldsymbol{\sigma}_z^1 + \frac{\chi_{a_j,b_2}}{2}\boldsymbol{\sigma}_z^2 + \frac{\chi_{a_j,b_3}}{2}\boldsymbol{\sigma}_z^3\right) \\ &+ \frac{\Omega_p^j}{2} \sum_{j=1,2,3} (\boldsymbol{\sigma}_+^j \mathbf{a}_j + h.c.) + \frac{\Omega_p^j}{2} \sum_{j=1,2,3} (\boldsymbol{\sigma}_-^j \mathbf{a}_j + h.c.), \end{aligned} \tag{2.13}$$

where the Ω_p^j's are given by expressions similar to (2.6). It is straightforward from Subsection 2.3.1 that the reduced dynamics is given by

$$\frac{d\boldsymbol{\rho}}{dt} = \sum_{j=1,2,3} \Gamma_c^j \mathscr{D}[\mathbf{c}_j](\boldsymbol{\rho}) + \frac{\gamma_x^j}{2} \mathscr{D}[\boldsymbol{\sigma}_x^j](\boldsymbol{\rho}), \tag{2.14}$$

where

$$\begin{gathered}\mathbf{c}_1 = \boldsymbol{\sigma}_-^1 \boldsymbol{\Pi}_{|00\rangle}^{23} + \boldsymbol{\sigma}_+^1 \boldsymbol{\Pi}_{|11\rangle}^{23}, \; \mathbf{c}_2 = \boldsymbol{\sigma}_-^2 \boldsymbol{\Pi}_{|00\rangle}^{13} + \boldsymbol{\sigma}_+^2 \boldsymbol{\Pi}_{|11\rangle}^{13}, \\ \mathbf{c}_3 = \boldsymbol{\sigma}_-^3 \boldsymbol{\Pi}_{|00\rangle}^{12} + \boldsymbol{\sigma}_+^3 \boldsymbol{\Pi}_{|11\rangle}^{12},\end{gathered}$$

and

$$\Gamma_c^j \approx \frac{|\Omega_p^j|^2}{\kappa_j}.$$

Effect of other self-Kerr and cross-Kerr terms - Through the analysis of Subsections 2.3.1 and 2.3.2, we have neglected the effect of higher order couplings between various modes as presented in the third and fourth lines of Hamiltonian (2.2). Here, we illustrate that these terms can be fully taken into account without any changes in the performance of the protocol. We only require to slightly modify the pump frequencies.

These higher order contributions could be considered in two parts. First, the self-Kerr terms and the cross-Kerr terms between the resonator modes

$$-\sum_k K_{a_k,a_k} {\mathbf{a}_k}^{\dagger 2} \mathbf{a}_k^2 - \sum_{j \neq k} K_{a_j,a_k} {\mathbf{a}_j}^\dagger \mathbf{a}_j {\mathbf{a}_k}^\dagger \mathbf{a}_k$$

do not affect the dynamics. Indeed, the self-Kerr terms vanish as these modes are never populated beyond a single photon. Similarly, the cross-Kerr terms can be neglected since two resonator modes are never populated simultaneously.

Next, the cross-Kerr terms between the qubit modes

$$-\sum_{j\neq k} K_{b_j,b_k} \boldsymbol{\sigma}_z^j \boldsymbol{\sigma}_z^k$$

yield an identical energy shift to each two states in an error subspace $\mathscr{E}_j$. Modifying slightly the pump tones to take into account these energy shifts, we will get the same effective Hamiltonian (modulo the addition of the above self-Kerr and cross-Kerr terms between resonator modes) as in (2.13). More precisely, the modified pump frequencies, associated to qubit 1, are given by

$$\begin{aligned} \tilde{\omega}_{p_1}^1 &= \frac{\omega_{a_1}+\omega_{b_1}}{2} - K_{b_1,b_2} - K_{b_1,b_3}, \\ \tilde{\omega}_{p_2}^1 &= \left| \frac{\omega_{a_1}-\omega_{b_1}}{2} - K_{b_1,b_2} - K_{b_1,b_3} \right|. \end{aligned} \tag{2.15}$$

Similar modifications need to be applied to other pump tones.

2.3.3 Summary of QEC protocol and numerical simulations

Through this subsection, we provide a summary of the requirements for our QEC scheme (presented in previous sections) and we realize numerical simulation to illustrate its performance. We couple three qubits to three low-Q resonator modes as in Figure 2.1 and we assume the following separation of time-scales:

$$\gamma_x^j \ll \kappa_{j'} \ll \chi_{a_k,b_{k'}}, \quad j,k,j',k' = 1,2,3.$$

We further assume the symmetry assumption

$$\sum_{k=1,2,3} \chi_{a_j,b_k} = 0, \quad j = 1,2,3. \tag{2.16}$$

As it will be seen through the next section, this can be relaxed to $\sum_{k=1,2,3} \chi_{a_j,b_k} \sim \gamma_x^j$. Such a symmetry should be achievable by fine tuning the frequencies of the qubits.

Now, we apply six off-resonant CW drives of frequencies $\tilde{\omega}_{p_1,p_2}^j$ given by (2.15) (with adjusted phases and amplitudes), acting as stiff pumps. This yields an effective master equation of the form

$$\begin{aligned}
\frac{d\boldsymbol{\rho}}{dt} &= -\frac{i}{\hbar}[\mathbf{H}_{\text{eff}},\boldsymbol{\rho}] + \sum_{j=1,2,3}\frac{\gamma_x^j}{2}\mathscr{D}[\boldsymbol{\sigma}_x^j]\rho + \sum_{j=1,2,3}\kappa_j\mathscr{D}[\mathbf{a}_j]\boldsymbol{\rho},\\
\mathbf{H}_{\text{eff}}/\hbar &= -\sum_{j=1,2,3}\mathbf{a}_j{}^{\dagger}\mathbf{a}_j\Big(\frac{\chi_{a_j,b_1}}{2}\boldsymbol{\sigma}_z^1 + \frac{\chi_{a_j,b_2}}{2}\boldsymbol{\sigma}_z^2 + \frac{\chi_{a_j,b_3}}{2}\boldsymbol{\sigma}_z^3\Big)\\
&\quad + \sum_{j=1,2,3}\frac{\Omega_p^j}{2}(\boldsymbol{\sigma}_+^j\mathbf{a}_j + h.c.) + \sum_{j=1,2,3}\frac{\Omega_p^j}{2}(\boldsymbol{\sigma}_-^j\mathbf{a}_j + h.c.)\\
&\quad - \sum_j K_{a_j,a_j}\mathbf{a}_j{}^{\dagger 2}\mathbf{a}_j^2 - \sum_{j\neq k}K_{a_j,a_k}\mathbf{a}_j{}^{\dagger}\mathbf{a}_j\mathbf{a}_k{}^{\dagger}\mathbf{a}_k, \qquad (2.17)
\end{aligned}$$

where the Ω_p^j's are given by

$$\Omega_p^j = \sqrt{K_{a_1,a_1}\chi_{a_1,b_1}}\left|\frac{\varepsilon_j^{a,1}}{\omega_a^j - \tilde{\omega}_{p_1}^j}\right|^2 = \sqrt{K_{a_1,a_1}\chi_{a_1,b_1}}\left|\frac{\varepsilon_j^{a,2}}{\omega_a^j - \tilde{\omega}_{p_2}^j}\right|^2.$$

In Figure 2.4, we simulate the above master equation. We fix the decay rates of the low-Q modes to be $\kappa = 500\gamma_x$ and we sweep the dispersive shift strengths χ_{a_j,b_k} and the pump-induced transition rates Ω_p^j (keeping their ratio constant). The system is initialized in $|\psi_0\rangle = (|000\rangle - i|111\rangle)/\sqrt{2}$, the -1 eigenstate of the logical operator $\boldsymbol{\sigma}_y^L = -\boldsymbol{\sigma}_y^1\boldsymbol{\sigma}_y^2\boldsymbol{\sigma}_y^3$. By plotting the fidelity $F(t) = \langle\psi_0|\boldsymbol{\rho}(t)|\psi_0\rangle$ with respect to this initial state (solid lines), we show that the autonomous correction enhances significantly the lifetime of the encoded state. In particular, after a time of order $1/(\gamma_x^1 + \gamma_x^2 + \gamma_x^3)$, we maintain a fidelity in excess of 95%. Besides, we observe that while increasing Ω_p^j improves the correction rate as predicted by formula $\Gamma_c^j = |\Omega_p^j|^2/\kappa$, this rate is saturated when Ω_p^j approaches κ. This corresponds to the fact that the entropy cannot be evacuated at a rate faster than κ. This saturation limit can be enhanced by increasing the decay rate of the low-Q mode while the qubit decay rates remain constant. While in principle this separation of decay rates is usually limited by Purcell effects, in practice we can design Purcell filters to overcome this limitation [45].

We also observe a small but fast decay of the fidelity happening on a short time scale of order Γ_c^{-1}. This effect is due to the fact that the scheme requires a finite time $T_c = \Gamma_c{}^{-1}$ to correct an error, as shown by the reduced master equation (2.7) and illustrated on Figure 2.3. As a consequence, when considering the fidelity at a time t, there is a finite probability of order $3\gamma_x T_c$ that an error has occurred but not been yet corrected. The initial decay of fidelity is explained by this finite probability. This common effect for continuous QEC protocols [62, 1, 77, 34] could be compared to an initial drop of fidelity in a discrete measurement-based QEC protocol when there is a finite delay between the measurement and the correction operation. For a fair comparison to standard measurement-based QEC where

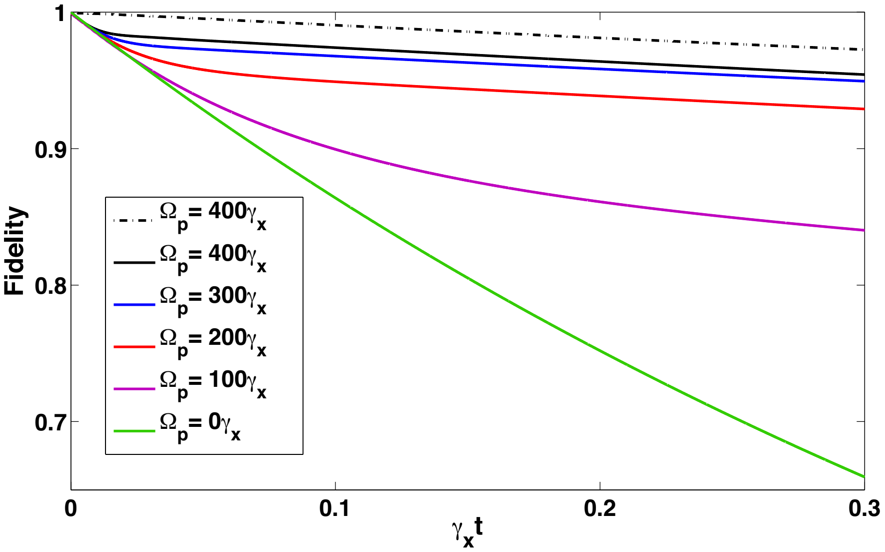

Fig. 2.4 (Color online) Simulation of model (2.17) for the QEC scheme when the system is initialized in the state $(|000\rangle - i|111\rangle)/\sqrt{2} \in \mathscr{E}_0$. The solid curves illustrate the fidelity $F(t) = \langle\psi_0|\boldsymbol{\rho}(t)|\psi_0\rangle$ to the initial state for different values of Ω_p (all Ω_p^j are taken to be identical to Ω_p). The legend respects the monotonic order of the curves. The dashed curve represents the fidelity of the system evaluated after we applied a projective measurement immediately followed by a recovery operation (see Eq. (2.18)). Each qubit suffers from bit-flip errors at a rate $\gamma_x^j = \gamma_x$, and the dissipation rates of the resonators are taken to be equal and set to $\kappa = 500\gamma_x$. The dispersive couplings of qubit 2 and qubit 3, χ_{a_j,b_2} and χ_{a_j,b_3}, $j = 1,2,3$, are chosen to be positive and satisfy $\chi_{a_j,b_2} = \chi_{a_j,b_3} = -\chi_{a_j,b_1}/2$. The coupling strengths of qubit 1, χ_{a_j,b_1}, are equal and swept so as to keep the ratio $\Omega_p/\chi_{a_j,b_1} = 10^{-2}$ constant. The cross-Kerr coefficients between resonators are taken to be $K_{a_j,a_k} = \chi_{a_j,b_k}/100$.

such delay effects are neglected, a different evaluation of performance was proposed in [1]. The fidelity definition

$$F_{\text{alt}}(t) = \langle\psi_0|\left(\boldsymbol{\rho}(t) + \textstyle\sum_{k=1,2,3} \boldsymbol{\sigma}_x^k \boldsymbol{\rho}(t) \boldsymbol{\sigma}_x^k\right)|\psi_0\rangle, \tag{2.18}$$

takes into account the possibility that a single bit-flip error has occurred but not been yet corrected. In practice, such kind of fidelity could correspond to the result of a tomography following a conditioning on a final set of error syndrome measurements [77]. We have plotted in Figure 2.4 (dashed line) this alternative fidelity for the case of $\Omega_p = 400\gamma_x$.

Finally, note that the second order effect of the highly oscillating terms neglected in the RWA of Subsection (2.3.1) induces an extra phase shift between the two logical states. This phase shift is however deterministic and does not corrupt the encoded quantum information.

In the above simulations we take this deterministic phase into account for the calculation of the relative fidelity.

2.4 Effective decoherence rate after QEC

Our first order QEC protocol is not capable of correcting two errors occurring within a time given by the inverse of the correction rate. Instead, it will recover a wrong state inside the coding subspace corresponding to a bit-flip of the logical qubit. This leads to an effective second-order decay rate given by (see [57], Chapter 10)

$$\Gamma_{\mathrm{eff}}^{\mathrm{2nd}} = 3\gamma_x^2/\Gamma_c.$$

This decoherence rate corresponds to the ideal case where all the model reductions of Subsection 2.3.1 are exact. In practice, one needs to take into account further decoherence rates induced by the imperfection of the RWA and the eventual breakdown of symmetry (2.16). Through this section, we present the requirements to reduce the major such effects to the same order as the above effective decoherence rate $\Gamma_{\mathrm{eff}}^{\mathrm{2nd}}$.

2.4.1 Imperfect manifold selectivity

A major requirement for the protocol to perform as predicted, is that the pump tones $\tilde{\omega}_{p_{1,2}}^j$ induce oscillations, only, between the manifolds $\mathscr{E}_j \otimes |0\rangle_j$ ($|0\rangle_j$ corresponds to the vacuum state of resonator j) and $\mathscr{E}_0 \otimes |1\rangle_j$. In particular, the manifold $\mathscr{E}_0 \otimes |0\rangle_j$ should remain untouched. As stated in Subsection 2.3.1, this manifold selectivity is provided by the fact that transitions between $\mathscr{E}_0 \otimes |0\rangle_j$ and $\mathscr{E}_j \otimes |1\rangle_j$ are off-resonant by $\pm\chi_{a_j,b_j}$ (see Figure 2.2a). However, in practice, this undesired manifold $\mathscr{E}_j \otimes |1\rangle_j$ gets slightly populated due to the finite ratio $\chi_{a_j,b_j}/\kappa_j$ between the detuning and the linewidth. This resonator j eventually leaks out its photon carrying information about the logical superposition. This leads to an effective dephasing rate given by

$$\Gamma_{\mathrm{eff}}^{\mathrm{select}} = \sum_{j=1,2,3} \kappa_j \frac{|\Omega_p^j|^2}{|\chi_{a_j,b_j}|^2 + |\kappa_j|^2}. \tag{2.19}$$

This rate could be understood by the fact that the average population of the undesired manifold $\mathscr{E}_j \otimes |1\rangle_j$ due to the detuned pumps is given by $P_{\mathrm{select}}^j = |\Omega_p^j|^2/(|\chi_{a_j,b_j}|^2 + |\kappa_j|^2)$. By the assumption (2.3), any photon loss (occurring at the rate $P_{\mathrm{select}}^j\kappa_j$) fully destroys the phase coherence.

2.4.2 Symmetry breakdown

As stated in Subsection 2.3.1, in order to not leak out any information on a given superposition between the states $|000\rangle$ and $|111\rangle$, we need to ensure a symmetry assumption given by relation (2.16). Here, we assume that such an assumption is not perfectly satisfied and we quantify its major contribution to an induced decoherence rate.

The major effect is due to the fact that whenever the system undergoes a bit-flip (rate γ_x^j), the protocol performs a transition from $\mathscr{E}_j \otimes |0\rangle_j$ to $\mathscr{E}_0 \otimes |1\rangle_j$. The three-qubit system then accumulates a relative phase (rate $\left|\sum_{k=1,2,3} \chi_{a_j,b_k}\right|$) before the photon is lost (time of order $1/\Gamma_c^j$). This induces an effective dephasing rate of order

$$\Gamma_{\text{eff}}^{\text{sym}} \sim \sum_{j=1,2,3} \gamma_x^j \frac{\left|\sum_{k=1,2,3} \chi_{a_j,b_k}\right|}{\Gamma_c^j}. \tag{2.20}$$

To sum up, we provide the requirements to reduce the effect of these imperfection-induced decoherence rates to the same order as the second order bit-flip errors. Increasing the pump powers (Ω_p's of the same order as κ's), we saturate the correction rate Γ_c to a rate of order κ. Then the rate $\Gamma_{\text{eff}}^{\text{select}}$ becomes of the same order as $\Gamma_{\text{eff}}^{\text{2nd}}$, whenever

$$\frac{\kappa_j}{\gamma_x^j} \lesssim \frac{\chi_{a_j,b_j}}{\kappa_j}.$$

Similarly, for the rate $\Gamma_{\text{eff}}^{\text{sym}}$, we need to take

$$\left|\sum_{k=1,2,3} \chi_{a_j,b_k}\right| \lesssim \gamma_x^j.$$

2.5 Towards a simplified implementation

Through this section, we propose a simplified version of the above protocol that only requires the coupling of the three qubits to a single low-Q resonator (Figure 2.5a). As explained through Section 2.3.1, using a single resonator and two CW drives at frequencies $\omega_{p_1} = (\omega_a + \omega_{b_1})/2$ and $\omega_{p_2} = |\omega_a - \omega_{b_1}|/2$, one can autonomously correct bit-flip errors occurring on qubit 1. Here, instead of adding extra resonators (acting as correction channels) for the other qubits, we propose to design an effective Hamiltonian which transfers the errors of the other qubits on this first qubit.

More precisely, we apply two extra CW drives of fixed amplitudes and well-chosen phases at frequencies $\omega_{p_{12}} = |\omega_{b_1} - \omega_{b_2}|/2$ and $\omega_{p_{23}} = |\omega_{b_2} - \omega_{b_3}|/2$ (four stiff pumps in total). These drives acting as stiff pumps induce effective couplings of the form $g_{12}(\boldsymbol{\sigma}_+^1\boldsymbol{\sigma}_-^2 + h.c.) + g_{23}(\boldsymbol{\sigma}_+^2\boldsymbol{\sigma}_-^3 + h.c.)$ to be added to the Hamiltonian (2.5). As illustrated in Figure 2.5b, the first term maps coherently $\mathscr{E}_2$ to $\mathscr{E}_1$ and the second term maps $\mathscr{E}_3$ to $\mathscr{E}_2$. This induces coherent oscillations between the error subspaces $\mathscr{E}_1$, $\mathscr{E}_2$ and $\mathscr{E}_3$. Now taking into account the irreversible correction procedure occurring when the system passes by the manifold $\mathscr{E}_1$ (decay from $\mathscr{E}_1$ to $\mathscr{E}_0$ in Figure 2.5b), we end up correcting all possible errors.

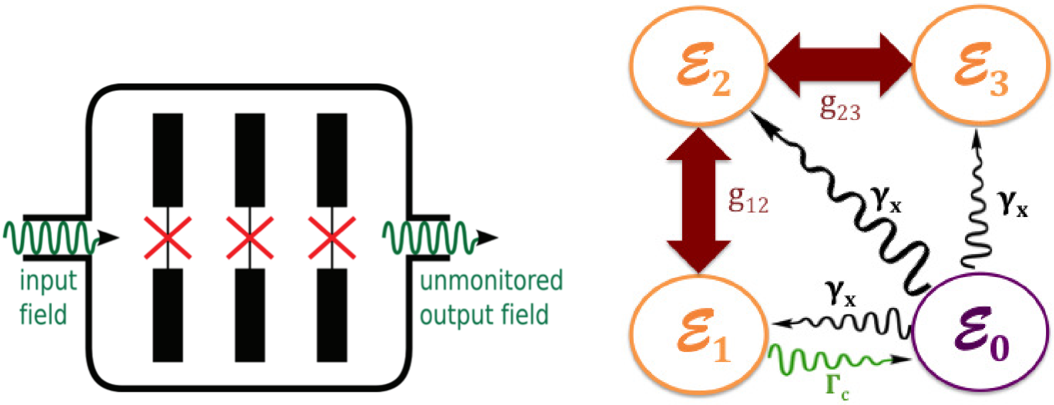

(a) (b)

Fig. 2.5 (Color online) (a) Illustration of the simplified scheme, where three superconducting qubits are coupled to a single resonator. (b) A diagram of the single-resonator scheme. Bit-flip errors occurring at a rate γ_x induce jumps from the coding subspace $\mathscr{E}_0$ to the error subspaces $\mathscr{E}_j$. Applying two stiff pumps on the resonator, any bit-flip error is eventually mapped onto a bit-flip of first qubit, on which correction takes place.

The oscillation rates between the error subspaces, g_{12} and g_{23}, as well as the associated phases can be tuned by the choice of pump amplitudes and phases. The choice of $g_{12} = \Gamma_c/2$ and $g_{23} = -g_{12}/\sqrt{2}$ corresponds to an optimal effective correction rate. In Figure 2.6, we simulate such an error correction scheme based on the use of a single resonator and compare it with the previous case of the correction with three resonators. The master equation simulated is given by

$$\begin{aligned}
\frac{d\boldsymbol{\rho}}{dt} &= -\frac{i}{\hbar}[\mathbf{H}_{\text{eff}}, \boldsymbol{\rho}] + \sum_{j=1,2,3} \frac{\gamma_x^j}{2}\mathscr{D}[\boldsymbol{\sigma}_x^j]\boldsymbol{\rho} + \kappa\mathscr{D}[\mathbf{a}]\boldsymbol{\rho} \\
\mathbf{H}_{\text{eff}}/\hbar &= -\mathbf{a}^\dagger\mathbf{a}\left(\frac{\chi_{a_1,b_1}}{2}\boldsymbol{\sigma}_z^1 + \frac{\chi_{a_1,b_2}}{2}\boldsymbol{\sigma}_z^2 + \frac{\chi_{a_1,b_3}}{2}\boldsymbol{\sigma}_z^3\right) \\
&\quad + \frac{\Omega_p}{2}(\boldsymbol{\sigma}_+^1\mathbf{a} + h.c.) + \frac{\Omega_p}{2}(\boldsymbol{\sigma}_-^1\mathbf{a} + h.c.) \\
&\quad + g_{12}(\boldsymbol{\sigma}_+^1\boldsymbol{\sigma}_-^2 + h.c.) + g_{23}(\boldsymbol{\sigma}_+^2\boldsymbol{\sigma}_-^3 + h.c.). \qquad (2.21)
\end{aligned}$$

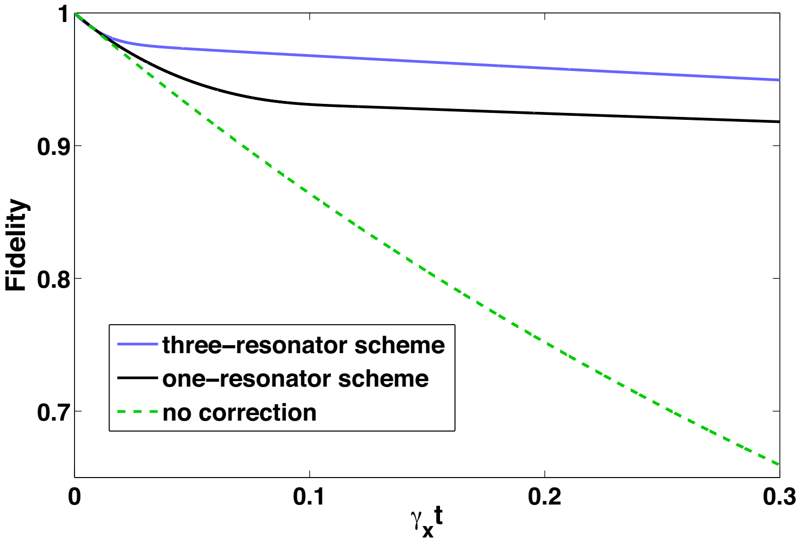

Fig. 2.6 (Color online) QEC protocol using one resonator described by (2.21) when the system is initialized in the state $(|000\rangle - i|111\rangle)/\sqrt{2} \in \mathscr{E}_0$. The black curve shows the fidelity to the initial state achieved with the single-resonator scheme. In comparison, we also plot the fidelity obtained through the three-resonator scheme presented in Section 2.3 represented by the solid blue (upper) line, and the fidelity without any correction (dashed green curve). Each qubit suffers from bit-flip errors at a rate γ_x. The decay rate of all resonators is set to $\kappa = 500\gamma_x$ and the transition rates are all given by $\Omega_p = 300\gamma_x$, $g_{12} = \Gamma_c/2$ and $g_{23} = -g_{12}/\sqrt{2}$. The coupling strengths satisfy $\chi_{a_j,b_2} = \chi_{a_j,b_3} = -\chi_{a_j,b_1}/2$, $j = 1,2,3$, and $\Omega_p/\chi_{a_j,b_1} = 10^{-2}$.

As can be observed in Figure 2.6, the effective correction rate is lower for the case of the simplified protocol. This could be understood by the fact that, at each time, we are only able to correct a single error channel. This is to be compared to the three-resonator protocol, where the three independent error channels are corrected simultaneously. Indeed, the optimal correction rate for this simplified protocol appears to be precisely three times lower than the rate for the three-resonator one. However, for the same reason, the dephasing rate induced by the imperfection in the manifold selectivity (finite ratios $\chi_{a_j,b_k}/\kappa_j$) appears to be at least three times higher for the protocol based on three resonators. This explains the steeper slope of the curve for the three-resonator protocol on the longer time scales.

2.6 Towards proof-of-principle experiments

In the previous sections of this Chapter, we have proposed a quantum error correction scheme adapted to superconducting circuits, that continuously and autonomously corrects for bit-flip errors. The curves of Figs. 2.4 and 2.6 show the protection of an arbitrary state of the logical qubit when the only decay channel for the physical qubits are bit-flip errors. However, transmon qubits suffer from both phase flips and bit flips. More precisely, the errors are generally described by two decoherence channels, the T_1 relaxation represented by the Lindblad super-operator $\frac{1}{T_1}\mathscr{D}[\boldsymbol{\sigma}^-]$, and the pure dephasing corresponding to $\frac{1}{2T_\phi}\mathscr{D}[\boldsymbol{\sigma}_Z]$. While the T_1 decay is composed of both phase-flip and bit-flip errors, the pure dephasing consists only of phase-flip errors. To achieve a full first order protection against both T_1 and T_ϕ decoherence, one also needs to correct for phase-flip errors. This can be done by using a larger number of qubits along with a more complicated encoding, e.g the Bacon-Shor code [6]. We will discuss such an extension in Section 2.8. Here, we propose two possible proof-of-principle experiments, through which one can assess the performances of this three-qubit error correction scheme. Throughout this section, we consider the physical system illustrated in Fig. 2.5a, where three transmon qubits are coupled to a single low-Q resonator.

2.6.1 Conservation of population

Although the scheme does not protect against the phase-flip errors, it corrects for the $\boldsymbol{\sigma}_x$ component of the T_1 decay channels. Indeed, we expect the decoherence channels on the logical qubit to be effectively reduced to phase-flip errors. An arbitrary initial state $c_0|000\rangle + c_1|111\rangle$ will evolve towards the mixed state $|c_0|^2|000\rangle\langle 000| + |c_1|^2|111\rangle\langle 111|$. While the phase between $|000\rangle$ and $|111\rangle$ is lost, the respective population of these states will be conserved. We provide a numerical proof of this result by simulating the following master equation,

$$\begin{aligned}\frac{d\boldsymbol{\rho}}{dt} &= -\frac{i}{\hbar}[\mathbf{H}_{\text{eff}},\boldsymbol{\rho}] + \sum_{j=1,2,3}\frac{1}{T_1}\mathscr{D}[\boldsymbol{\sigma}_-^j]\boldsymbol{\rho} + \frac{1}{2T_\phi}\mathscr{D}[\boldsymbol{\sigma}_z^j]\boldsymbol{\rho} + \kappa\mathscr{D}[\mathbf{a}]\boldsymbol{\rho} \\ \mathbf{H}_{\text{eff}}/\hbar &= -\mathbf{a}^\dagger\mathbf{a}\Big(\frac{\chi_{a_1,b_1}}{2}\boldsymbol{\sigma}_z^1 + \frac{\chi_{a_1,b_2}}{2}\boldsymbol{\sigma}_z^2 + \frac{\chi_{a_1,b_3}}{2}\boldsymbol{\sigma}_z^3\Big) \\ &\quad + \frac{\Omega_p}{2}(\boldsymbol{\sigma}_+^1\mathbf{a} + h.c.) + \frac{\Omega_p}{2}(\boldsymbol{\sigma}_-^1\mathbf{a} + h.c.) \\ &\quad + g_{12}(\boldsymbol{\sigma}_+^1\boldsymbol{\sigma}_-^2 + h.c.) + g_{23}(\boldsymbol{\sigma}_+^2\boldsymbol{\sigma}_-^3 + h.c.).\end{aligned} \tag{2.22}$$

In Fig. 2.7, the population $\langle 000|\rho|000\rangle$ and $\langle 111|\rho|111\rangle$ are represented as a function of time when the system is corrected (blue lines) and it is not (green lines). For both simulations, we set the parameters $1/T_1 = 1/(2T_\phi)$, $\kappa = 500/T_1$, $\chi_{a_1,b_1} = \chi_{a_1,b_2} = -(\chi_{a_1,b_3}/2) = 1.5\ 10^4/T_1$, $g_{12} = \Gamma_c/2$ and $g_{23} = -g_{12}/\sqrt{2}$. The blue curves (resp. green curves) correspond to $\Omega_p = \kappa$ (resp. $\Omega_p = 0$) . The system is initialized in the state $(|000\rangle - 2i|111\rangle)/\sqrt{5}$. While the uncorrected system evolves towards the ground state in a time of order T_1, the state of the corrected system maintains its population on $|000\rangle$ and $|111\rangle$ on a much longer timescale.

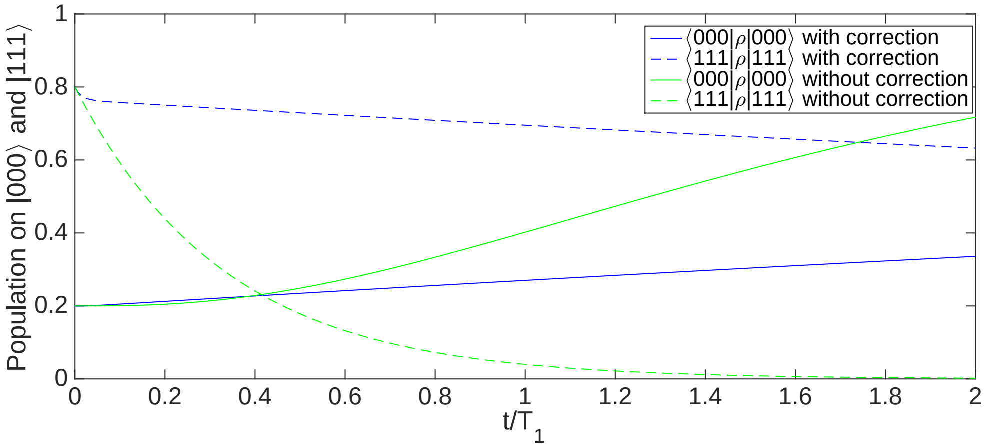

Fig. 2.7 Effect of the QEC protocol on the populations on $|000\rangle$ and $|111\rangle$ for the system described by eq. (2.22). For both simulations, we set the parameters $1/T_1 = 1/(2T_\phi)$, $\kappa = 500/T_1$, $\chi_{a_1,b_1} = \chi_{a_1,b_2} = -(\chi_{a_1,b_3}/2) = 1.5\times 10^4/T_1$, $g_{12} = \Gamma_c/2$ and $g_{23} = -g_{12}/\sqrt{2}$. The blue curves (resp. green curves) correspond to $\Omega_p = \kappa$ (resp. $\Omega_p = 0$), and the system is initialized in the state $(|000\rangle - 2i|111\rangle)/\sqrt{5}$. The correction scheme conserves the populations of the states $|000\rangle$ and $|111\rangle$.

The slow mixing of the populations, that can be observed through the non-zero slopes of the blue curves, are due to second order bit-flip errors. Note that although we accounted for the dephasing errors via the terms $\frac{1}{2T_\phi}\mathscr{D}[\boldsymbol{\sigma}_z^j]\boldsymbol{\rho}$ for a realistic picture, these terms do not affect the curves of Fig. 2.7.

2.6.2 *GHZ*-state preparation

The QEC protocol can be used to prepare a *GHZ*-state $|GHZ\rangle = (|000\rangle + |111\rangle)/\sqrt{2}$. It is enough to initialize the system described by eq. (2.22) in the state $|\phi_0\rangle = (|0\rangle + |1\rangle)(|0\rangle + |1\rangle)(|0\rangle + |1\rangle)/2\sqrt{2}$. The state $|\psi_0\rangle$ can be simply obtained from the ground state $|000\rangle$ by applying a $\pi/2$-rotations along the y-axis on each qubit. We note that $|\psi_0\rangle$ can be written in the form $|\psi_0\rangle = (|GHZ\rangle + \boldsymbol{\sigma}_x^1|GHZ\rangle + \boldsymbol{\sigma}_x^2|GHZ\rangle + \boldsymbol{\sigma}_x^3|GHZ\rangle)/2$. If we assume that the qubits are not subject to errors, then under the correction scheme, each of the states $\boldsymbol{\sigma}_x^j|GHZ\rangle$ is mapped to $|GHZ\rangle$, and $|GHZ\rangle$ is left untouched. Hence, in a time of order $1/\Gamma_c$, $|\psi_0\rangle$ evolves to $|GHZ\rangle$. While the phase-flips induced by the T_1 decay and the pure dephasing would eventually destroy the coherence of the superposition, it is still possible to observe a *GHZ* state in the transient regime. For this, one requires $\Gamma_c \gg 1/T_1, 1/T_\phi$. Fig. 2.8 shows the fidelity of the system state to $|GHZ\rangle$ as a function time, for various values of κT_1 $(T_1 = T_\phi)$. The other parameters are kept fixed with respect to κ. The simulations illustrate a rapid

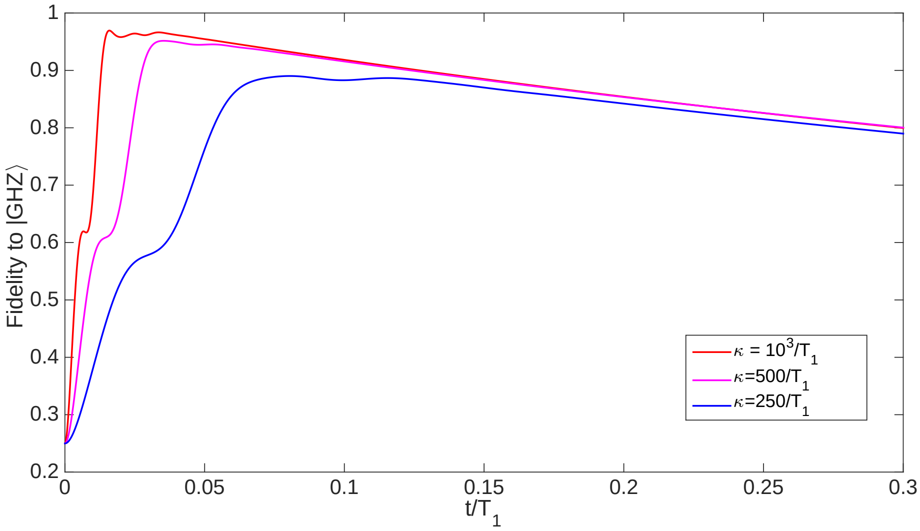

Fig. 2.8 Preparation of the state $|GHZ\rangle = (|000\rangle + |111\rangle)/\sqrt{2}$. The curves corresponds to the fidelity to the state $|GHZ\rangle$ as a function of time for various values of κT_1. The system described by eq. (2.22) is initialized in $|\phi_0\rangle = (|0\rangle + |1\rangle)(|0\rangle + |1\rangle)(|0\rangle + |1\rangle)/2\sqrt{2}$. We fix with respect to κ the following parameters, $\chi_{a_1,b_1} = \chi_{a_1,b_2} = -(\chi_{a_1,b_3}/2) = 30\kappa$, $g_{12} = \Gamma_c$ and $g_{23} = -g_{12}/\sqrt{2}$. Besides, on sets $1/T_1 = 1/(2T_\phi)$.

convergence towards the target state $|GHZ\rangle$. The uncorrected phase-flip errors limit the fidelity, and on a longer time-scale lead to an incoherent mixture of $|000\rangle$ and $|111\rangle$.

2.7 Adaptation to a phase-flip correction scheme

To protect the information against phase-flip errors, a first approach consists of mapping phase-flip errors to bit-flip errors through $\pi/2$-rotations along the y-axis on each qubit, and correcting them applying the bit-flip QEC scheme (see Fig. 2.9). This sequential scheme can be implemented in an autonomous manner. However, one loses the CW property of the protocol. In particular, the correction is not continuous, and phase flips occurring during the correction time are not corrected.

In order to achieve a continuous three-qubit phase-flip correction scheme, we need a Hamiltonian $\mathbf{H}_{\text{eff}}^{(x)}$ of the form $(\boldsymbol{\sigma}_H \otimes \boldsymbol{\sigma}_H \otimes \boldsymbol{\sigma}_H)\mathbf{H}_{\text{eff}}(\boldsymbol{\sigma}_H \otimes \boldsymbol{\sigma}_H \otimes \boldsymbol{\sigma}_H)$, where $\mathbf{H}_{\text{eff}}$ is the Hamiltonian given in eq. (2.13). Here, $\boldsymbol{\sigma}_H$ denotes the Hadamard gate [57], which maps $\boldsymbol{\sigma}_z$ to $\boldsymbol{\sigma}_x$ under the transformation $\boldsymbol{\sigma}_x = \boldsymbol{\sigma}_H\boldsymbol{\sigma}_z\boldsymbol{\sigma}_H$. Hence, we consider a system where three

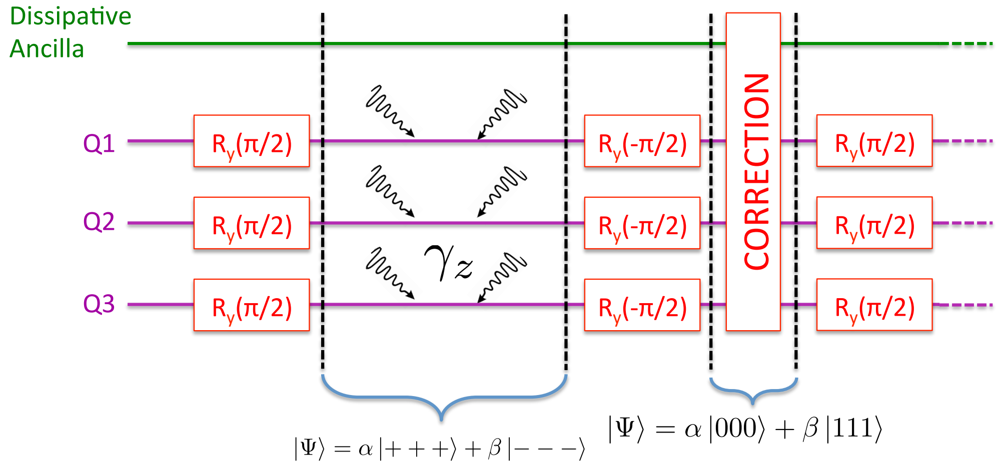

Fig. 2.9 Autonomous (but not continuous) phase-flip correction scheme. The information is encoded via the three-qubit phase-flip code in the states $c_+|{+}{+}{+}\rangle + c_-|{-}{-}{-}\rangle$. Regularly, phase flips are mapped to bit flips through $\pi/2$-rotations along the y-axis on each qubit, and corrected using the bit-flip correction scheme. This correction step ends with $-\pi/2$-rotations along the y-axis to come back in the coding subspace. During the correction phase, the logical information is vulnerable to single phase-flip errors.

resonators are coupled to three transmon qubits, whose Hamiltonian $\mathbf{H}_{\text{eff}}^{(x)}$ reads

$$\begin{aligned}\mathbf{H}_{\text{eff}}^{(x)}/\hbar = &-\sum_{j=1,2,3} \mathbf{a}_j{}^{\dagger}\mathbf{a}_j\Big(\frac{\chi^{(x)}_{a_j,b_1}}{2}\boldsymbol{\sigma}_x^1 + \frac{\chi^{(x)}_{a_j,b_2}}{2}\boldsymbol{\sigma}_x^2 + \frac{\chi^{(x)}_{a_j,b_3}}{2}\boldsymbol{\sigma}_x^3\Big)\\ &+\sum_{j=1,2,3}\frac{\Omega^{(x),j}}{2}\big(\boldsymbol{\sigma}_+^{(x),j}\mathbf{a}_j^{\dagger} + h.c.\big) + \sum_{j=1,2,3}\frac{\Omega^{(x),j}}{2}\big(\boldsymbol{\sigma}_-^{(x),j}\mathbf{a}_j^{\dagger} + h.c.\big)\end{aligned} \tag{2.23}$$

Here, we have introduced the raising (lowering) operators $\boldsymbol{\sigma}_{\pm}^{(x),j} = (\boldsymbol{\sigma}_z^j \mp i\boldsymbol{\sigma}_y^j)/2$ between the eigenstates of $\boldsymbol{\sigma}_x^j$. Note that they satisfy the relation $\boldsymbol{\sigma}_z^j = \boldsymbol{\sigma}_+^{(x),j} + \boldsymbol{\sigma}_-^{(x),j}$. In the regime $|\chi^{(x)}_{a_j,b_1} + \chi^{(x)}_{a_j,b_2} + \chi^{(x)}_{a_j,b_3}| \ll \kappa_j$ and $|\chi^{(x)}_{a_j,b_k}| \gg \kappa_j$, $j = 1,2,3$, one can readily apply the arguments used to prove bit-flip correction scheme and show that this system continuously prevents phase-flip errors from damaging the encoded information. More precisely, an arbitrary state $c_+|{+}{+}{+}\rangle + c_-|{-}{-}{-}\rangle$ is protected against phase-flip errors on single qubit. Below, we briefly discuss a possible construction of such a Hamiltonian with superconducting circuits.

This construction is strongly inspired by [55] and [89]. In Murch et al. [55], the state $|+\rangle$ ($|-\rangle$) of a transmon qubit was stabilized by coupling a low-Q cavity to the transmon, and applying a strong Rabi drive of amplitude $-\Omega_R$ such that $\Omega_R \gg \kappa$, along with a sideband tone detuned from the cavity frequency by $\mp\Omega_R$. Similarly, let us start with a transmon qubit coupled to a low-Q mode. Here, in addition to the strong Rabi drive on the qubit, we propose to simultaneously apply the two sideband drives detuned from the cavity frequency by $-\Omega_R$ and Ω_R, with amplitudes $\varepsilon_{d,-}$ and $\varepsilon_{d,+}$ respectively. Furthermore, we also apply a strong off-resonant drive of amplitude ε_p, detuned from the cavity frequency by $\Delta_p < \Omega_R$. In the frame rotating at both the qubit and the cavity frequencies, the Hamiltonian reads

$$\mathbf{H}/\hbar = -\frac{\Omega_R}{2}\boldsymbol{\sigma}_x - \frac{\chi_{a,b}}{2}\boldsymbol{\sigma}_z\mathbf{a}^\dagger\mathbf{a} + (\varepsilon_{d,+}e^{-i\Omega_R t} + \varepsilon_{d,-}e^{i\Omega_R t} + \varepsilon_p e^{-i\Delta_p t})\mathbf{a}^\dagger + h.c, \tag{2.24}$$

where we have eliminated the terms rotating at frequency of order $\omega_a \gg \Delta_p, \Omega_R$. We remove the drive terms by displacing the field operator, with $\mathbf{a} = \mathbf{d} + \alpha_+ e^{-i\Omega_R t} + \alpha_- e^{i\Omega_R t} + \alpha_p e^{-i\Delta_p t}$. Here, the field amplitudes read $\alpha_\pm = \varepsilon_{d,\pm}/(\pm\Omega_R + i\kappa/2)$ and $\alpha_p = \varepsilon_p/(\Delta_p + i\kappa/2)$. Furthermore, by inserting the expression $\boldsymbol{\sigma}_z = \boldsymbol{\sigma}_+^{(x)} + \boldsymbol{\sigma}_-^{(x)}$ and moving into the rotating frame defined by $-(\Omega_R/2)\boldsymbol{\sigma}_x$, the Hamiltonian (2.24) becomes

$$\begin{aligned}\mathbf{H}/\hbar = -&\frac{\chi_{a,b}}{2}(\boldsymbol{\sigma}_+^{(x)}e^{-i\Omega_R t} + h.c)\\ &[(\mathbf{d}^\dagger + \alpha_+^* e^{i\Omega_R t} + \alpha_-^* e^{-i\Omega_R t} + \alpha_p^* e^{i\Delta_p t})(\mathbf{d} + \alpha_+ e^{-i\Omega_R t} + \alpha_- e^{i\Omega_R t} + \alpha_p e^{-i\Delta_p t})\\ &-(|\alpha_-|^2 + |\alpha_+|^2 + |\alpha_p|^2)].\end{aligned} \tag{2.25}$$

Here, we subtract the AC-stark shift $\chi_{a,b}(|\alpha_-|^2 + |\alpha_+|^2 + |\alpha_p|^2)$ from this Hamiltonian and account for it in the frequency of the Rabi drive. In the regime $\kappa_a, |\alpha_\pm|\chi_{a,b}, |\alpha_p|\chi_{a,b} \ll \Delta_p, \Omega_R, \Omega_R \pm \Delta_p, 2\Omega_R \pm \Delta_p$, one can apply the second order rotating-wave approximation, resulting in the Hamiltonian

$$\begin{aligned}\mathbf{H}/\hbar = &-\frac{\xi}{2}\boldsymbol{\sigma}_x - \frac{\chi_{a,b}^{(x)}}{2}\boldsymbol{\sigma}_x\mathbf{d}^\dagger\mathbf{d} - \frac{\chi_{a,b}^2}{4\Omega_R}\boldsymbol{\sigma}_x\mathbf{d}^{\dagger 2}\mathbf{d}^2\\ &+\big(\frac{\Omega^{(x),+}}{2}\boldsymbol{\sigma}_+^{(x)}\mathbf{d}^\dagger + h.c\big) + \big(\frac{\Omega^{(x),-}}{2}\boldsymbol{\sigma}_-^{(x)}\mathbf{d}^\dagger + h.c\big),\end{aligned} \tag{2.26}$$

The coefficients read

$$\begin{aligned}\Omega^{(x),\pm} =& -\chi_{a,b}\alpha_{\mp}\\ \chi^{(x)}_{a,b} =& \frac{\chi^2_{a,b}}{2}\big[|\alpha_p|^2\big(\frac{1}{\Omega_R+\Delta_p}+\frac{1}{\Omega_R-\Delta_p}\big)+\frac{|\alpha_-|^2+|\alpha_+|^2}{2\Omega_R}+\frac{1}{\Omega_R}\big]\\ \xi =& \big[\chi^{(x)}_{a,b}+\frac{\chi^2_{a,b}}{2}\big(-\frac{1}{\Omega_R}-\frac{2|\alpha_+\alpha_-|^2}{3\Omega_R}\\ &+|\alpha_+\alpha_p|^2\big(\frac{1}{\Delta_p}+\frac{1}{2\Omega_R-\Delta_p}\big)+|\alpha_-\alpha_p|^2\big(-\frac{1}{\Delta_p}+\frac{1}{2\Omega_R+\Delta_p}\big)\big)\big]\end{aligned}$$

A simple adjustment of the drive amplitudes $\varepsilon_\pm$ leads $\alpha_+ = \alpha_- = \alpha_d$ and $\Omega^{(x),+} = \Omega^{(x),-} = \Omega^{(x)}$. The QEC scheme requires the timescale inequality $|\chi^{(x)}_{a,b}| \gg \kappa, |\Omega^{(x)}|$. Indeed, taking $\Omega_R \pm \Delta_p \sim \Omega_R \gg \chi_{a,b}|\alpha_d|$, and $|\alpha_p| \gg |\alpha_d|$, we achieve $|\chi^{(x)}_{a,b}| \gg |\Omega^{(x)}|$. The coefficient expressions simplify to

$$\begin{aligned}\Omega^{(x),\pm} =& -\chi_{a,b}\alpha_d\\ \chi^{(x)}_{a,b} =& \frac{\chi^2_{a,b}}{2}\big[|\alpha_p|^2\big(\frac{1}{\Omega_R+\Delta_p}+\frac{1}{\Omega_R-\Delta_p}\big)+\frac{1}{\Omega_R}\big]\\ \xi =& \frac{\chi^2_{a,b}|\alpha_p|^2}{2}\big[\big(\frac{1}{\Omega_R+\Delta_p}+\frac{1}{\Omega_R-\Delta_p}\big)+|\alpha_d|^2\big(\frac{1}{2\Omega_R-\Delta_p}+\frac{1}{2\Omega_R+\Delta_p}\big)\big]\end{aligned}$$

As $\xi \ll \Omega_R$, the first term of eq. (2.26) only slightly alter the effective Rabi frequency. This change can be taken into account in the sideband tones frequencies. The anharmonic term in $\mathbf{d}^{\dagger 2}\mathbf{d}^2$ does not affect the performances of the QEC scheme, since the Fock states $|n\rangle$ with $n \geq 2$ are never populated. After these simplifications, the effective Hamiltonian of the qubit and the displaced cavity reads

$$\mathbf{H}/\hbar = -\frac{\chi^{(x)}_{a,b}}{2}\boldsymbol{\sigma}_x\mathbf{d}^\dagger\mathbf{d} + \big(\frac{\Omega^{(x),+}}{2}\boldsymbol{\sigma}^{(x)}_+\mathbf{d}^\dagger + h.c\big) + \big(\frac{\Omega^{(x),-}}{2}\boldsymbol{\sigma}^{(x)}_-\mathbf{d}^\dagger + h.c\big). \tag{2.27}$$

Let us come back to the phase-flip protection scheme, which considers three dissipative ancillas coupled to three qubits. Following the method leading to the Hamiltonian (2.27), we apply a strong Rabi drive of amplitude Ω^j_R on each qubit. Also, on each associated cavity, we apply two drives detuned by $\pm\Omega^j_R$. In addition, to obtain the transverse dispersive couplings, we apply a strong off-resonant drive on each cavity detuned by Δ^j_p. The effective Hamiltonian, in the frame rotating at the Rabi frequencies and at the bare cavity frequencies, reads

$$\begin{aligned}\mathbf{H}_{\text{eff}}^{(x)}/\hbar = &-\sum_{j=1,2,3}\mathbf{d}_j{}^{\dagger}\mathbf{d}_j\Big(\frac{\chi^{(x)}_{a_j,b_1}}{2}\boldsymbol{\sigma}_x^1+\frac{\chi^{(x)}_{a_j,b_2}}{2}\boldsymbol{\sigma}_x^2+\frac{\chi^{(x)}_{a_j,b_3}}{2}\boldsymbol{\sigma}_x^3\Big)\\ &+\sum_{j=1,2,3}\frac{\Omega^{(x),j}}{2}(\boldsymbol{\sigma}_+^{(x),j}\mathbf{d}_j^{\dagger}+h.c.)+\sum_{j=1,2,3}\frac{\Omega^{(x),j}}{2}(\boldsymbol{\sigma}_-^{(x),j}\mathbf{d}_j^{\dagger}+h.c.).\end{aligned} \tag{2.28}$$

Experimentally, transverse coupling strengths $\chi^{(x)}_{a,b}$ of a few MHz have been achieved recently [89]. Furthermore, the value of $\chi^{(x)}_{a,b}$ is highly tunable, as it depends on the amplitude of the drives and the detuning of the pump tones from the resonator frequencies. Finally, $\chi^{(x)}_{a,b}$ can take positive or negative values. This flexibility makes the symmetry conditions $|\Sigma\chi^{(x)}_{a_j,b_1}+\chi^{(x)}_{a_j,b_2}+\chi^{(x)}_{a_j,b_3}| \ll \kappa_j,\ j=1,2,3$, much easier to fulfill than in the case of the bit-flip correction scheme.

2.8 Some ideas for extension to Bacon-Shor code

In the previous sections, we have presented an autonomous correction scheme based on the three-qubit bit-flip code. Such a code corrects either single bit flips or single phase flips, but does not offer a complete protection against arbitrary errors on single qubits. A higher number of qubits is required to realize a complete QEC. Actually, the minimal number of qubits required to encode and protect a single logical qubit against single-qubit errors is 5 [57]. Here, we focus on the nine-qubit Bacon-Shor code [6], that offers a protection against arbitrary single qubit errors. The Bacon-Shor codes benefit from the property that, they only require two-qubit joint parity measurements and therefore are compatible with our AQEC scheme.

While Subsection 2.8.1 introduces the Bacon-Shor code, Subsection 2.8.2 sketches two possible protocols to realize this code. These protocols exploit the AQEC scheme presented in the previous sections. We emphasize that the proposed schemes are not finalized nor optimized, and require further study. In particular, these schemes need yet to be tested through extensive numerical simulations taking into account various possible imperfections. Besides, the hardware equipment needed for these scheme is heavy. In Chapter 4, we propose QEC schemes based on the cat codes (introduced in Section 1.2) that appear to be less challenging experimentally.

2.8.1 Introduction to the Bacon-Shor code

As a prerequisite to the description of the Bacon-Shor code, let us briefly introduce the stabilizer formalism in the theory of QEC.

In the three-qubit bit-flip code, the detection of errors is given by the measurement of the commuting joint-parity observables $\boldsymbol{\sigma}_Z^1\boldsymbol{\sigma}_Z^2$ and $\boldsymbol{\sigma}_Z^2\boldsymbol{\sigma}_Z^3$. More precisely, the measurement output indicates on which error subspace the system lives. Another way to formulate this property is that, the Hilbert space $\mathscr{H}$ admits the decomposition $\mathscr{H} = \mathscr{E}_{(1,1)} \oplus \mathscr{E}_{(1,-1)} \oplus \mathscr{E}_{(-1,1)} \oplus \mathscr{E}_{(-1,-1)}$. Here, $\mathscr{E}_{(\pm1,\pm1)}$ are the doubly degenerate common eigenspaces of the commuting $\boldsymbol{\sigma}_Z^1\boldsymbol{\sigma}_Z^2$ and $\boldsymbol{\sigma}_Z^2\boldsymbol{\sigma}_Z^3$ associated to the eigenvalues $(\pm1,\pm1)$. The coding subspace is defined as the stabilized eigenspace $\mathscr{E}_{(1,1)} = \text{span}\{|000\rangle, |111\rangle\}$ of the measurement observables $\boldsymbol{\sigma}_Z^1\boldsymbol{\sigma}_Z^2$ and $\boldsymbol{\sigma}_Z^2\boldsymbol{\sigma}_Z^3$.

One can generalize this to any QEC code consisting of n physical qubits. If $S_1,...,S_p$ are the commuting independent measurement observables of a code (all considered to be tensor products of n Pauli or identity matrices), the Hilbert space expands as $\mathscr{H} = \bigoplus_{\vec{u}\in\mathbb{Z}_p} \mathscr{E}_{\vec{u}}$. Moreover, the dimensions of the subspaces $\mathscr{E}_{\vec{u}}$ are all equal, and given by 2^{n-p}. In such a code, one can in principle encode $n-p$ logical independent qubits. This is the case of the three-qubit bit-flip code, consisting of $n=3$ physical qubits and $p=2$ measurement observables, and the Steane code [81], for which one has $n=7$ and $p=6$. As a logical operation on the encoded qubit should not disturb the error syndrome $\vec{u}$, the logical operators $\boldsymbol{\sigma}_{x,L}^i$ and $\boldsymbol{\sigma}_{z,L}^j$ of these independent qubits should commute with all the stabilizers S_m, and also satisfy the commutation relations $[\boldsymbol{\sigma}_{x,L}^i, \boldsymbol{\sigma}_{z,L}^j] = 0$ for $i \neq j$.

Alternatively, one can choose to encode a fewer qubits, say $k < n-p$ qubits, and leave $n-p-k$ gauge degrees of freedom. The eigenspaces $\mathscr{E}_{\vec{u}}$ can be correspondingly decomposed as $\mathscr{E}_{\vec{u}} = \mathscr{L}_{\vec{u}} \otimes \mathscr{T}_{\vec{u}}$, where the logical qubits live on the subspaces $\mathscr{L}_{\vec{u}}$ and the $n-p-k$ other qubits (the so-called gauge qubits) live on $\mathscr{T}_{\vec{u}}$. Let us consider we have measured the error syndrome $\vec{u}$. The system state $\boldsymbol{\rho}$ lives in $\mathscr{E}_{\vec{u}}$, and can be written in the form $\boldsymbol{\rho} = \boldsymbol{\rho}_{\mathscr{L}_{\vec{u}}} \otimes \boldsymbol{\rho}_{\mathscr{T}_{\vec{u}}}$, with $\boldsymbol{\rho}_{\mathscr{L}_{\vec{u}}} \in \mathscr{L}_{\vec{u}}$ and $\boldsymbol{\rho}_{\mathscr{T}_{\vec{u}}} \in \mathscr{T}_{\vec{u}}$. The logical information is contained in the state $\boldsymbol{\rho}_{\mathscr{L}_{\vec{u}}}$, while one can completely disregard the state $\boldsymbol{\rho}_{\mathscr{T}_{\vec{u}}}$ of the gauge qubits. As a direct consequence, the logical operators of the gauge qubits provide a set of operators that can be applied or measured without disturbing the logical information nor the measurement observables. This defines the class of subsystem codes [6].

The Bacon-Shor code belongs to the latter class of code. Here, we focus on the 9-qubit Bacon-Shor code, although it can be generalized to a lattice of size $n \times n$ qubits. The qubits are represented on a 3×3-lattice, as depicted in Fig. 2.10a. Here, $X_{i,j}$ and $Z_{i,j}$ define the logical operators of the physical qubit $Q_{i,j}$. The error syndromes are given by the observables

$\{L_X^{1,2} = X_{1,*}X_{2,*},\ L_X^{2,3} = X_{2,*}X_{3,*},\ L_Z^{1,2} = Z_{*,1}Z_{*,2},\ L_Z^{2,3} = Z_{*,2}Z_{*,3},\}$, where we have defined $X_{i,*} = X_{i,1}X_{i,2}X_{i,3}$ and $Z_{*,j} = Z_{1,j}Z_{2,j}Z_{3,j}$. Note that the elements of the group generated by these observables $\mathscr{S} = \langle L_X^{1,2},\ L_X^{2,3},\ L_Z^{1,2},\ L_Z^{2,3}\rangle$, also stabilizes the coding subspace. $\mathscr{S}$ is called the stabilizer of the code. A representation of $L_X^{1,2}$ and $L_Z^{1,2}$ is given in Fig. 2.10a. Here, we have $n = 9$ qubits for $p = 4$ measurement observables, leading to $n - p = 5$ independent degrees of freedom. The 9-qubit Bacon-Shor code encodes only a single logical qubit, thus leaving 4 gauge qubits. The set of logical operators for the one logical qubit is $\mathscr{L} = \{X_L^k = X_{k,*},\ Z_L^j = Z_{*,j}\}$ (illustration in Fig 2.10b). For all k and j, one has $X_L^k Z_L^j = -Z_L^j X_L^k$, which shows that solely one independent qubit is defined by these operators. The operators acting non-trivially on the four gauge qubit subspaces $\mathscr{T}_{\vec{u}}$, can be drawn from the group $\mathscr{G}$ generated by adjacent-row X operators $X_{i,j}X_{i+1,j}$ and adjacent-column Z operators $Z_{i,j}Z_{i,j+1}$, i.e the group $\mathscr{G} = \langle X_{i,j}X_{i+1,j},\ Z_{i,j}Z_{i,j+1}\rangle$. A set of four logical operators of $\mathscr{G}$ defining four independent gauge qubits is illustrated in Fig 2.10c. As the elements of the set $\mathscr{L}$ and the group $\mathscr{G}$ commute with those of the stabilizer $\mathscr{S}$, their application does not disturb the error syndromes. Moreover, as the operators of $\mathscr{L}$ commute with the elements of $\mathscr{G}$, the operators of $\mathscr{G}$ leave intact the encoded logical qubit (and vice-versa).

Let us consider a single bit-flip error occurs on the qubit $Q_{1,2}$ through the operation $X_{1,2}$. The resulting error syndrome is $(L_X^{1,2} = 1,\ L_X^{2,3} = 1,\ L_Z^{1,2} = -1,\ L_Z^{2,3} = -1)$, indicating a single bit-flip on one of the qubits of the second column. The initial logical qubit state can be recovered by flipping any of the qubits of the second column. Indeed, in this case, the overall operation is either the identity I, or $X_{1,2}X_{2,2}$, or $X_{1,2}X_{3,2}$. Since the two latter pairs of X operators are elements of $\mathscr{G}$, such global operation at most disturbs the gauge qubits while leaving the logical qubit state untouched. A similar analysis holds for phase-flip errors. By correcting for both single phase flips and single bit flips, the nine-qubit Bacon-Shor offers a protection against arbitrary single qubit errors.

Although the error syndromes are given by the joint measurement of six qubit parities $L_{X(Z)}^{i,i+1}$, one needs only to measure two-qubit parities to obtain the error syndromes. This stems from the property that $\mathscr{S} \subset \mathscr{G}$. Indeed, $L_X^{i,i+1}$ and $L_Z^{j,j+1}$ are products of elements of $\mathscr{G}$, since $L_X^{i,i+1} = (X_{i,1}X_{i+1,1})(X_{i,2}X_{i+1,2})(X_{i,3}X_{i+1,3})$ and $L_Z^{j,j+1} = Z_{*,j}Z_{*,j+1} = (Z_{1,j}Z_{1,j+1})(Z_{2,j}Z_{2,j+1})(Z_{3,j}Z_{3,j+1})$.

2.8.2 The autonomous Bacon-Shor code

Here, we discuss two possible designs for the realization of the Bacon-Shor code. As we shall see, these protocols exploit the three-qubit bit-flip code presented in the previous sections. In this Subsection, we focus on the correction of single bit-flip errors. Phase-flip correction

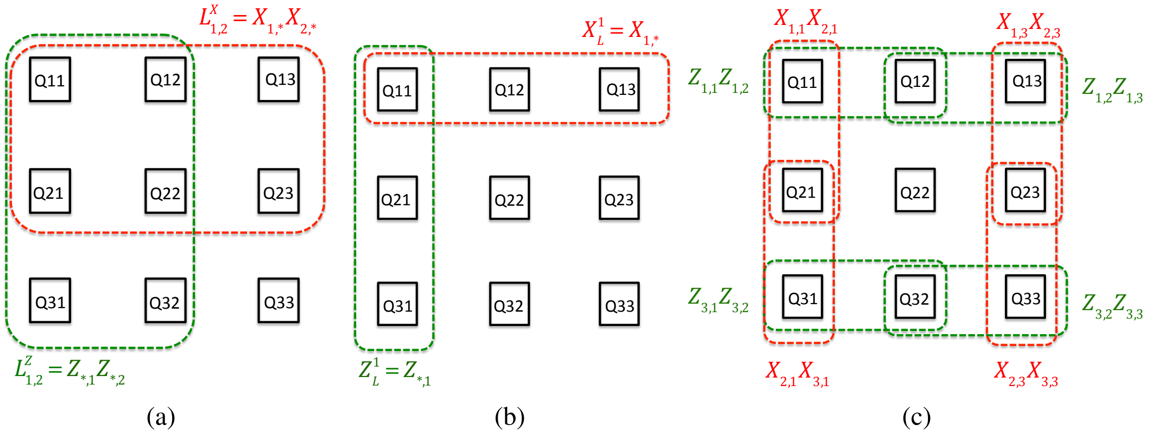

Fig. 2.10 Illustration of the nine-qubit Bacon-Shor code (a) : Two syndrome operators $L_X^{1,2}$ and $L_Z^{1,2}$ are represented. (b) : Logical operators X_L^1 and Z_L^1 acting on the encoded qubit. (c) : Four pairs of gauge operators drawn in $\mathscr{G}$ defining four independent gauge qubits.

is achieved by mapping phase-flip errors to bit-flip errors through $\pi/2$-rotations around the y-axis and correcting for these bit-flip errors. Although phase flips and bit flips are corrected in a sequential and alternating manner, each of the correction steps (bit-flip or phase-flip) is realized in a continuous and autonomous manner. It would be interesting to explore the possibility of extending these ideas towards a fully continuous AQEC scheme.

Let us consider the logical encoding introduced in Subsection 2.8.1 and illustrated in Fig. 2.10a. We would like to apply the bit-flip AQEC scheme developed earlier in this Chapter. As mentioned in the previous subsection, the measurement of $L_Z^{1,2}$ and $L_Z^{2,3}$ indicates on which column a bit-flip has possibly occurred, and the error recovery can be done by bit-flipping any of the three qubits of the same column. Hence, one can freely decide to execute the recovery operations on qubits of the third row only (for example), i.e on the qubits $Q_{3,1}$, $Q_{3,2}$ and $Q_{3,3}$. Besides, one has $L_Z^{1,2} = Z_L^1 Z_L^2$ and $L_Z^{2,3} = Z_L^2 Z_L^3$, meaning that the error syndromes are given by the joint parities of the logical operators Z_L^j. This is in complete analogy with the three-qubit bit-flip code, where the error syndromes result from the measurement of the two-qubit parities Z_1Z_2 and Z_2Z_3, and where each of the operators Z_j also acts as the logical operator Z_L on the three-qubit system. Since we can restrict the bit-flip corrections on the three qubits of the third row, the difference with the three-qubit bit flip scheme resides in the observables conditioning the correction. Indeed, instead of depending upon the "physical" two-qubit parities $Z_{3,1}Z_{3,2}$ and $Z_{3,2}Z_{3,3}$, one looks at the joint parities of logical qubits $Z_L^1 Z_L^2$ and $Z_L^2 Z_L^3$, thus accounting for the state of the physical qubits of the first and second rows. Here, we show that an appropriate application of the gauge operators $X_{i,j}X_{i+1,j}$ depending on the value of two-qubit parities $Z_{i,j}Z_{i,j+1}$ (also gauge operators), leads effectively to $L_Z^{1,2} = Z_{3,1}Z_{3,2}$ and $L_Z^{2,3} = Z_{3,2}Z_{3,3}$. This means that the joint parities between the physical qubits $Q_{3,1}$ and $Q_{3,2}$ (resp. $Q_{3,2}$ and $Q_{3,3}$), is equivalent to logical parities $Z_L^1 Z_L^2$ (resp. $Z_L^2 Z_L^3$). In this case, the error recovery can be done by simply applying the three-qubit scheme to the third row.

Here we provide a more precise explanation of the above claim. The observables $L_Z^{1,2}$ and $L_Z^{2,3}$ are products of gauge operators: e.g. $L_Z^{1,2}$ expands as $L_Z^{1,2} = (Z_{1,1}Z_{1,2}) * (Z_{2,1}Z_{2,2}) * (Z_{3,1}Z_{3,2})$. The relation $L_Z^{1,2} = Z_{3,1}Z_{3,2}$ is equivalent to having $(Z_{1,1}Z_{1,2}) * (Z_{2,1}Z_{2,2}) = 1$. A sufficient condition to satisfy the latter equality is to fix the gauge operators $Z_{1,1}Z_{1,2} = 1$ and $Z_{2,1}Z_{2,2} = 1$. Note that imposing these equalities only affects the gauge qubits. Let us consider that $Z_{2,1}Z_{2,2} = -1$. One can flip the sign of this equality by bit-flipping any of the two qubits, for instance by applying $X_{1,1}$. In order to make this operation harmless to the logical information while leaving untouched the other gauge operator $Z_{1,1}Z_{1,2}$, it should be followed by an operation $X_{3,1}$, so that the overall operation $X_{1,1}X_{3,1}$ acts on the gauge qubits only. In Subsection 2.8.2.1, we design a scheme in which the correction is achieved by continuously stabilizing the two-qubit parities to 1 via reservoir engineering. Alternatively, one can also directly condition the correction on the third row upon the two-qubit parities without stabilizing them. This approach is described in Subsection 2.8.2.2.

2.8.2.1 Bacon-Shor code through two-qubit parities stabilization

We propose to realize the continuous stabilization of the two-qubit parities to +1 through an engineered coupling with lossy resonators. The physical system consists of 9 transmon qubits dispersively coupled to five lossy cavities A_{Z_i}, $i = 1,2,3,4,C$. As illustrated in Fig. 2.11a, each cavity A_{Z_i} is coupled to two row-adjacent qubits, while the cavity A_{Z_C} is coupled to the three qubits of the third row. The strong dissipation on the resonators A_{Z_i} will allow the fast stabilization of the joint-parity of the two qubits to which the resonator is coupled. On a longer timescale, the autonomous three-qubit bit-flip scheme, realized on the three qubits of the third row through the coupling with the cavity A_{Z_C}, stabilizes the observables $Z_{3,1}Z_{3,2} = 1$ and $Z_{3,2}Z_{3,3} = 1$ by applying the operation $X_{3,1}$, $X_{3,2}$ or $X_{3,3}$.

Let us focus on the resonator A_{Z_1}. It is strongly coupled to $Q_{1,1}$ and $Q_{1,2}$. It is also parametrically coupled to qubit $Q_{3,1}$, through the Hamiltonian

$$\mathbf{H}_{Z_1}/\hbar = -\frac{1}{2}\mathbf{a}_{Z_1}{}^{\dagger}\mathbf{a}_{Z_1}(\chi_{Q_{1,1}}^{A_{Z_1}}\boldsymbol{\sigma}_Z^{1,1} + \chi_{Q_{1,2}}^{A_{Z_1}}\boldsymbol{\sigma}_Z^{1,2}) + \frac{\Omega_Z^1}{2}(\mathbf{a}_{Z_1} + \mathbf{a}_{Z_1}{}^{\dagger})\boldsymbol{\sigma}_X^{1,1}\boldsymbol{\sigma}_X^{3,1}.$$

This Hamiltonian could be realized with Josephson circuits via the application of four pump tones. We consider the following timescale separations $|\chi_{Q_{1,1}}^{A_{Z_1}}| \gg \kappa_{Z_1} \gtrsim \Omega_Z^1 \gg \gamma_x$, where γ_x denotes bit-flip rate for each qubit and κ_{Z_1} denotes the decay rate of cavity A_{Z_1}. In addition,

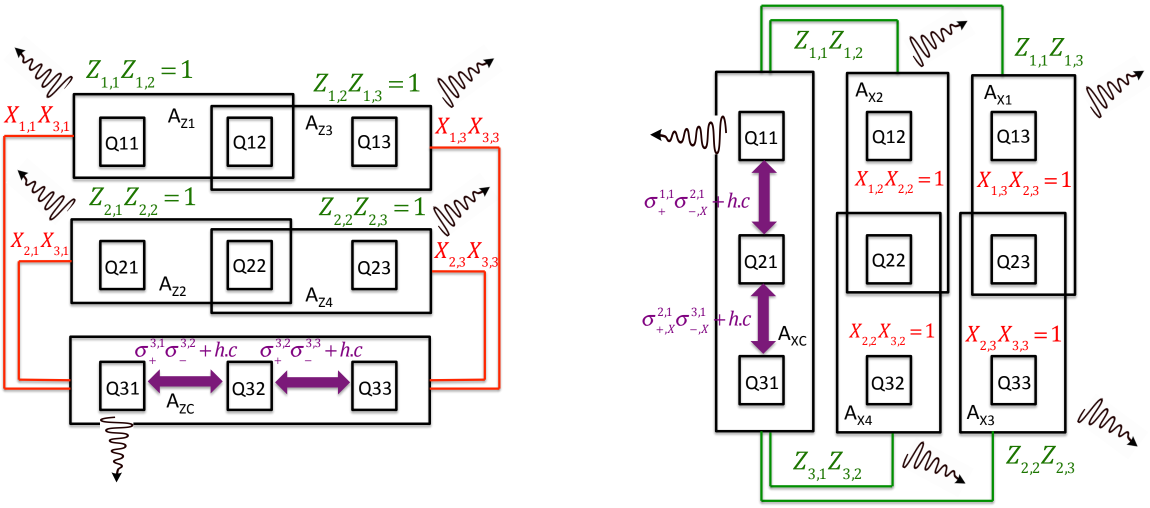

Bit flip correction step
Recovery operation : $X_{3,1}$or $X_{3,2}$or $X_{3,3}$

(a)

Phase flip correction step
Recovery operation : $Z_{1,1}$or $Z_{2,1}$or $Z_{3,1}$

(b)

Fig. 2.11 Bacon-Shor code through the continuous stabilization of the two-qubit parities to +1 (a): Bit-flip correction step. Each of the four lossy cavities A_{Z_i} are coupled to two transmons, while the cavity A_{Z_C} is coupled to the three qubits of the third row. Under the application of pump tones of well-chosen frequencies, we continuously stabilize the gauge operators $Z_{1,1}Z_{1,2} = 1$ and $Z_{2,1}Z_{2,2} = 1$, $Z_{1,2}Z_{1,3} = 1$ and $Z_{2,2}Z_{2,3} = 1$, in order to obtain the reduced error syndromes $L_Z^{1,2} = Z_{3,1}Z_{3,2}$ and $L_Z^{2,3} = Z_{3,2}Z_{3,3}$. This operation amounts to continuously transferring bit flips onto qubits of the third row. These errors are corrected via the three-qubit bit-flip scheme using the dissipative resonator A_{Z_C}. (b): Phase-flip correction step. The qubits are coupled to five other cavities A_{X_i} and A_{X_C} in a similar manner than for the bit-flip correction step, but with a different orientation. Phase flips are mapped to bit-flips by applying $\pi/2$-rotation around the $y-$axis on each qubit, and corrected through the same protocol used for bit-flips.

we assume the symmetries $\chi_{Q_{1,2}}^{A_{Z_1}} = -\chi_{Q_{1,1}}^{A_{Z_1}} = -\chi_{Z_1}$. This yields the Hamiltonian

$$\mathbf{H}_{Z_1}/\hbar = -\frac{\chi_{Z_1}}{2}\mathbf{a}_{Z_1}{}^{\dagger}\mathbf{a}_{Z_1}(\boldsymbol{\sigma}_Z^{1,1} - \boldsymbol{\sigma}_Z^{1,2}) + \frac{\Omega_Z^1}{2}\mathbf{a}_{Z_1}{}^{\dagger}\boldsymbol{\sigma}_X^{1,1}\boldsymbol{\sigma}_X^{3,1}. \tag{2.29}$$

In the following analysis, we note $\{O = \pm 1\}$ the ± 1-eigenspace of the Pauli operator O, and $\{O_1 = \pm 1,\ O_2 = \pm 1\}$ is the common $(\pm 1, \pm 1)$-eigenspace of two commuting Pauli operators O_1 and O_2. Combined with the dissipation on cavity A_{Z_1}, the Hamiltonian (2.29) autonomously stabilizes the gauge operator $Z_{1,1}Z_{1,2}$ to $+1$, through the operation $X_{1,1}X_{3,1}$, at an optimal rate $\kappa_{Z_1}/2$. Indeed, $Z_{1,1}Z_{1,2} = -1$ implies that $\chi_{Z_1}(\boldsymbol{\sigma}_Z^{1,1} - \boldsymbol{\sigma}_Z^{1,2}) \approx \pm 2\chi_{Q_{1,1}}^{A_{Z_1}}$, and $Z_{1,1}Z_{1,2} = 1$ corresponds to $|\chi_{Z_1}(\boldsymbol{\sigma}_Z^{1,1} - \boldsymbol{\sigma}_Z^{1,2})| = 0$. Hence, while the transition

$\{Z_{1,1}Z_{1,2}=1\}\otimes|0\rangle_{A_{Z_1}} \to \{Z_{1,1}Z_{1,2}=-1\}\otimes|1\rangle_{A_{Z_1}}$ is detuned by $|\pm 2\chi_{Q_{1,1}}^{A_{Z_1}}| \gg \kappa_{Z_1}$, the manifold $\{Z_{1,1}Z_{1,2}=-1\}\otimes|0\rangle_{A_{Z_1}}$ is resonantly coupled to $\{Z_{1,1}Z_{1,2}=1\}\otimes|1\rangle_{A_{Z_1}}$. The dissipation on the cavity A_{Z_1} projects the system to the manifold $\{Z_{1,1}Z_{1,2}=1\}\otimes|0\rangle_{A_{Z_1}}$. Similarly, the cavities A_Z^i, $i=2,3,4$, stabilize the gauge operators $Z_{2,1}Z_{2,2}$, $Z_{1,2}Z_{1,3}$ and $Z_{2,2}Z_{2,3}$ to 1, through the Hamiltonians $\mathbf{H}_{Z_i}$.

The cavity A_{Z_C} is coupled to the qubits of the third row, $Q_{3,1}$, $Q_{3,2}$ and $Q_{3,3}$, so as to realize the three-qubit AQEC scheme. As expressed in eq. (2.21), the associated Hamiltonian reads

$$\begin{aligned}\mathbf{H}_{Z_C}/\hbar = & -\frac{1}{2}\chi_Z^{\text{corr}}\mathbf{a}_{Z_C}{}^{\dagger}\mathbf{a}_{Z_C}(\boldsymbol{\sigma}_Z^{3,1}-2\boldsymbol{\sigma}_Z^{3,2}+\boldsymbol{\sigma}_Z^{3,3}) \\ & +\frac{g_{1,2}}{2}(\boldsymbol{\sigma}_+^{3,1}\boldsymbol{\sigma}_-^{3,2}+h.c)+\frac{g_{2,3}}{2}(\boldsymbol{\sigma}_+^{3,2}\boldsymbol{\sigma}_-^{3,3}+h.c)+(\frac{\Omega_1}{2}\mathbf{a}_{Z_C}{}^{\dagger}\boldsymbol{\sigma}_X^{3,1}+h.c).\end{aligned}$$

The associated correction rate $\Gamma_Z^C \sim \kappa_{A_C}/6$ should be lower than the stabilization rate of the gauge operators, i.e $\Gamma_C^Z \ll \kappa_Z^j$. This condition ensures that the correction on the third row occurs only when the four gauge operators $Z_{1,1}Z_{1,2}$, $Z_{2,1}Z_{2,2}$, $Z_{1,2}Z_{1,3}$ and $Z_{2,2}Z_{2,3}$ are set to 1. This can be understood through quantum Zeno dynamics [20]. Indeed, under the fast stabilization of these operators, the dynamics is confined to the manifold defined by $\{Z_{1,1}Z_{1,2}=1,\ Z_{2,1}Z_{2,2}=1,\ Z_{1,2}Z_{1,3}=1,\ Z_{2,2}Z_{2,3}=1\}$ to first order in Γ_C^Z/κ_Z^j. The effective values of the observables $L_Z^{1,2}$ and $L_Z^{2,3}$ on this manifold, are given by $Z_{3,1}Z_{3,2}$ and $Z_{3,2}Z_{3,3}$ respectively.

The effect of the terms $\frac{g_{1,2}}{2}(\boldsymbol{\sigma}_+^{3,1}\boldsymbol{\sigma}_-^{3,2}+h.c)+\frac{g_{2,3}}{2}(\boldsymbol{\sigma}_+^{3,2}\boldsymbol{\sigma}_-^{3,3}+h.c)$ is to transfer a potential error on the third row to the qubit $Q_{3,1}$, or equivalently, to map the error subspaces $\{Z_{3,1}Z_{3,2}=1,\ Z_{3,2}Z_{3,3}=-1\}$ and $\{Z_{3,1}Z_{3,2}=-1,\ Z_{3,2}Z_{3,3}=-1\}$ to the subspace $\{Z_{3,1}Z_{3,2}=-1,\ Z_{3,2}Z_{3,3}=1\}$. Indeed, one can express $\boldsymbol{\sigma}_+^{3,1}\boldsymbol{\sigma}_-^{3,2}+h.c=\boldsymbol{\sigma}_x^{3,1}\boldsymbol{\sigma}_x^{3,2}(1-\boldsymbol{\sigma}_z^{3,1}\boldsymbol{\sigma}_z^{3,2})$. As $(1-\boldsymbol{\sigma}_z^{3,1}\boldsymbol{\sigma}_z^{3,2})$ is an operator acting on the gauge qubits, the term $\boldsymbol{\sigma}_+^{3,1}\boldsymbol{\sigma}_-^{3,2}+h.c$ acts as $X_{3,1}X_{3,2}$ on the logical system only if $Z_{3,1}Z_{3,2}=-1$. A similar analysis holds for $\boldsymbol{\sigma}_+^{3,2}\boldsymbol{\sigma}_-^{3,3}+h.c$. Eventually, the corrupted system ends up in the subspace $\{Z_{3,1}Z_{3,2}=-1, Z_{3,1}Z_{3,2}=1\}$, and the correct state is recovered by bit-flipping the qubit $Q_{3,1}$.

To summarize, the Hamiltonian of the system for bit-flip correction step reads

$$\mathbf{H}_Z=\mathbf{H}_{Z_1}+\mathbf{H}_{Z_2}+\mathbf{H}_{Z_3}+\mathbf{H}_{Z_4}+\mathbf{H}_{Z_C}$$

This protocol requires the timescales to satisfy $|\chi_{Z_i}| \gg \kappa_{Z_i} \gg \kappa_{Z_C} \gg \gamma_x$.

The correction of phase flips is achieved in a similar way. Five other cavities, A_{X_i}, $i=1,2,3,4$, and A_{Z_C}, are coupled to the qubits in a horizontal manner, as depicted in Fig. 2.11b.

Phase flips are mapped to bit-flips by applying $\pi/2$-rotation around the $y-$axis on each qubit, and corrected through the same protocol used for bit-flips.

2.8.2.2 Autonomous correction conditioned on the two-qubit parities

The scheme presented in the previous subsection consists continuously fixing each of the four gauge operators $Z_{1,1}Z_{1,2}$, $Z_{2,1}Z_{2,2}$, $Z_{1,2}Z_{1,3}$ and $Z_{2,2}Z_{2,3}$ to 1, and apply the 3-qubit bit flip correction scheme on qubits of the third row. Here, instead, we adopt the strategy to condition the correction on qubits of the third row upon these two-qubit parities set to 1, while continuously applying Rabi drive on the four gauge qubits (as defined in Fig. 2.10c).

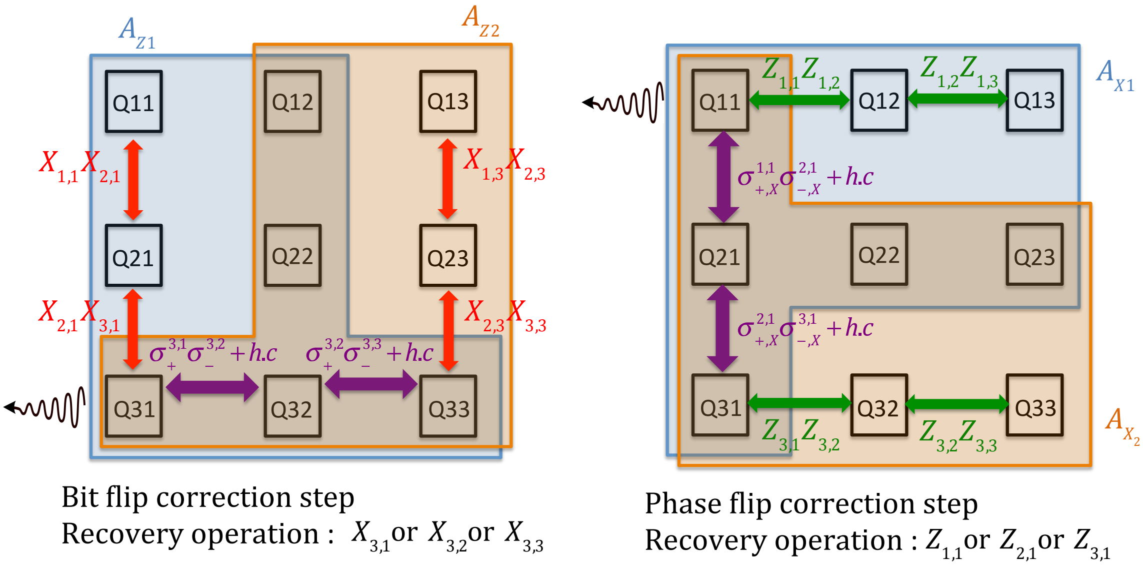

(a) (b)

Fig. 2.12 Bacon-Shor code, where the correction on qubits of a single row (or column) is conditioned on having four-qubit joint operators set to +1. (a): Bit-flip correction step. Two lossy cavities are dispersively coupled to the qubits in the colored corresponding regions. The two-qubit interactions (red arrows), induced by pump tones, map an error that has occurred on qubits of the first and second rows onto qubits of the third row. The correction on qubits of the third row, is conditioned on having $Z_{1,1}Z_{1,2} = Z_{2,1}Z_{2,2} = Z_{1,2}Z_{1,3} = Z_{2,2}Z_{2,3} = 1$, leading to effective syndrome operators $L_Z^{1,2} = Z_{3,1}Z_{3,2}$ and $L_Z^{2,3} = Z_{3,2}Z_{3,3}$. (b): Phase-flip correction step. The design is the same than the bit-flip setup (a), but with a different orientation. Phase flips are mapped to bit-flips by applying $\pi/2$-rotation around the $y-$axis on each qubit, and corrected through the same protocol used for bit-flips.

For this scenario, we consider the physical system represented in Fig. 2.12a, where the dissipative resonator A_{Z_1} (A_{Z_2}) is dispersively coupled to the qubits

$Q_{1,1}$, $Q_{1,2}$, $Q_{2,1}$, $Q_{2,2}$, $Q_{3,1}$, $Q_{3,2}$, $Q_{3,3}$ (resp. $Q_{1,2}$, $Q_{1,3}$, $Q_{2,2}$, $Q_{2,3}$, $Q_{3,1}$, $Q_{3,2}$, $Q_{3,3}$). Let us consider the following Hamiltonian

$$\begin{aligned}\frac{\mathbf{H}_Z}{\hbar} = &-\frac{1}{2}\mathbf{a}_{Z_1}{}^\dagger\mathbf{a}_{Z_1}[\chi_{A_{Z_{1,1}}}(\boldsymbol{\sigma}_Z^{1,1}-\boldsymbol{\sigma}_Z^{1,2})+\chi_{A_{Z_{1,2}}}(-\boldsymbol{\sigma}_Z^{2,1}+\boldsymbol{\sigma}_Z^{2,2})+\chi_{A_{Z_1}}^{\mathrm{corr}}(\boldsymbol{\sigma}_Z^{3,1}-2\boldsymbol{\sigma}_Z^{3,2}+\boldsymbol{\sigma}_Z^{3,3})]\\
&-\frac{1}{2}\mathbf{a}_{Z_2}{}^\dagger\mathbf{a}_{Z_2}[\chi_{A_{Z_{2,1}}}(-\boldsymbol{\sigma}_Z^{1,2}+\boldsymbol{\sigma}_Z^{1,3})+\chi_{A_{Z_{2,2}}}(\boldsymbol{\sigma}_Z^{2,2}-\boldsymbol{\sigma}_Z^{2,3})+\chi_{A_{Z_2}}^{\mathrm{corr}}(\boldsymbol{\sigma}_Z^{3,1}-2\boldsymbol{\sigma}_Z^{3,2}+\boldsymbol{\sigma}_Z^{3,3})]\\
&+\frac{g_{1,2}}{2}(\boldsymbol{\sigma}_+^{3,1}\boldsymbol{\sigma}_-^{3,2}+h.c)+\frac{g_{2,3}}{2}(\boldsymbol{\sigma}_+^{3,2}\boldsymbol{\sigma}_-^{3,3}+h.c)+(\frac{\Omega_1}{2}\mathbf{a}_{Z_1}{}^\dagger\mathbf{a}_{Z_2}{}^\dagger\boldsymbol{\sigma}_X^{3,1}+h.c)\\
&+\frac{\Omega_X^{11,21}}{2}\boldsymbol{\sigma}_X^{1,1}\boldsymbol{\sigma}_X^{2,1}+\frac{\Omega_X^{21,31}}{2}\boldsymbol{\sigma}_X^{2,1}\boldsymbol{\sigma}_X^{3,1}+\frac{\Omega_X^{13,23}}{2}\boldsymbol{\sigma}_X^{1,3}\boldsymbol{\sigma}_X^{2,3}+\frac{\Omega_X^{23,33}}{2}\boldsymbol{\sigma}_X^{2,3}\boldsymbol{\sigma}_X^{3,3}.\end{aligned}\tag{2.30}$$

We consider the timescale $\chi_{A_{Z_{j,k}}} \sim \chi_{A_{Z_j}}^{\mathrm{corr}} \gg \kappa_Z \gtrsim \Omega_1 \gtrsim g_{k,k+1} \gtrsim \Omega_X \gg \gamma_x$, $j,k = 1,2$, with κ_Z the dissipation rate of the resonators A_{Z_1} and A_{Z_2}.

The first three lines consist of a modified version of the three-qubit AQEC protocol. For $\chi_{A_{Z_1}}^{\mathrm{corr}} = \frac{5}{4}\chi_{A_{Z_{1,1}}}$ and $\chi_{A_{Z_{1,2}}} = 2\chi_{A_{Z_{1,1}}}$, the dispersive shift on cavity A_{Z_1} takes the form $(2n_1+3n_2+5n_{\mathrm{corr}})\chi_{A_{Z_{1,1}}}$ with $|n_1|,|n_2|,|n_{\mathrm{corr}}| = 0,1$. We obtain a zero dispersive shift only for $n_1 = 0$, $n_2 = 0$, $n_{\mathrm{corr}} = 0$, corresponding to the situation

$$\begin{aligned}\boldsymbol{\sigma}_Z^{1,1}-\boldsymbol{\sigma}_Z^{1,2} &= 0\\ -\boldsymbol{\sigma}_Z^{2,1}+\boldsymbol{\sigma}_Z^{2,2} &= 0\\ \boldsymbol{\sigma}_Z^{3,1}-2\boldsymbol{\sigma}_Z^{3,2}+\boldsymbol{\sigma}_Z^{3,3} &= 0,\end{aligned}$$

which is equivalent to

$$\begin{aligned}Z_{1,1}Z_{1,2} &= 1\\ Z_{2,1}Z_{2,2} &= 1\\ Z_{3,1}Z_{3,2} &= 1,\\ Z_{3,2}Z_{3,3} &= 1.\end{aligned}$$

Similarly, for $\chi_{A_{Z_2}}^{\mathrm{corr}} = \frac{5}{4}\chi_{A_{Z_{2,1}}}$ and $\chi_{A_{Z_{2,2}}} = 2\chi_{A_{Z_{2,1}}}$, a zero frequency shift on the resonator A_{Z_2} is conditioned on having

$$\begin{aligned}Z_{1,2}Z_{1,3} &= 1\\ Z_{2,2}Z_{2,3} &= 1\\ Z_{3,1}Z_{3,2} &= 1,\\ Z_{3,2}Z_{3,3} &= 1.\end{aligned}$$

As explained in the previous subsection, the terms $\frac{g_{1,2}}{2}(\boldsymbol{\sigma}_+^{3,1}\boldsymbol{\sigma}_-^{3,2}+h.c)+\frac{g_{2,3}}{2}(\boldsymbol{\sigma}_+^{3,2}\boldsymbol{\sigma}_-^{3,3}+h.c)$ transfer a potential error from the qubits $Q_{3,2}$ and $Q_{3,3}$ onto the qubit $Q_{3,1}$. In other words, it maps the error subspaces $\{Z_{3,1}Z_{3,2}=1,\ Z_{3,2}Z_{3,3}=-1\}$ and $\{Z_{3,1}Z_{3,2}=-1,\ Z_{3,2}Z_{3,3}=-1\}$ to the subspace $\{Z_{3,1}Z_{3,2}=-1,\ Z_{3,2}Z_{3,3}=1\}$. Besides, the manifolds $\{Z_{3,1}Z_{3,2}=-1,\ Z_{3,2}Z_{3,3}=1\}\otimes|0\rangle_{A_{Z_1}}\otimes|0\rangle_{A_{Z_2}}$ and $\{Z_{3,1}Z_{3,2}=1,\ Z_{3,2}Z_{3,3}=1\}\otimes|1\rangle_{A_{Z_1}}\otimes|1\rangle_{A_{Z_2}}$ are coupled by the interaction term $\frac{\Omega_1}{2}\mathbf{a}_{Z_1}{}^\dagger\mathbf{a}_{Z_2}{}^\dagger\boldsymbol{\sigma}_X^{3,1}+h.c.$ This transition is resonant only if the four two-qubit parities $Z_{1,1}Z_{1,2}$, $Z_{2,1}Z_{2,2}$, $Z_{1,2}Z_{1,3}$ and $Z_{2,2}Z_{2,3}$ are set to 1. A quick decay of the resonators A_{Z_1} and A_{Z_2} projects the system to the manifold $\{Z_{3,1}Z_{3,2}=1,\ Z_{3,2}Z_{3,3}=1,\ Z_{1,1}Z_{1,2}=1,\ Z_{2,1}Z_{2,2}=1,\ Z_{1,2}Z_{1,3}=1,\ Z_{2,2}Z_{2,3}=1\}\otimes|0\rangle_{A_{Z_1}}\otimes|0\rangle_{A_{Z_2}}$. Hence the correction on the third row, described by the terms of the third line of eq. (2.30), is conditioned upon having $Z_{1,1}Z_{1,2}=Z_{2,1}Z_{2,2}=Z_{1,2}Z_{1,3}=Z_{2,2}Z_{2,3}=1$. As explained for the three-qubit correction scheme, the timescales of the system should satisfy $\chi_{A_{Z_j}}\gg\kappa_Z\gtrsim\Omega_1\gtrsim g_{k,k+1}\gg\gamma_x$, $j=1,2$.

Let us consider the hamiltonian obtained by removing the fourth line of eq. (2.30), i.e

$$\begin{aligned}\mathbf{H}_Z/\hbar=&-\frac{1}{2}\mathbf{a}_{Z_1}{}^\dagger\mathbf{a}_{Z_1}[\chi_{A_{Z_1}}(\boldsymbol{\sigma}_Z^{1,1}-\boldsymbol{\sigma}_Z^{1,2}-\boldsymbol{\sigma}_Z^{2,1}+\boldsymbol{\sigma}_Z^{2,2})+\chi_{A_{Z_1}}^{\mathrm{corr}}(\boldsymbol{\sigma}_Z^{3,1}-2\boldsymbol{\sigma}_Z^{3,2}+\boldsymbol{\sigma}_Z^{3,3})]\\&-\frac{1}{2}\mathbf{a}_{Z_2}{}^\dagger\mathbf{a}_{Z_2}[\chi_{A_{Z_2}}(-\boldsymbol{\sigma}_Z^{1,2}+\boldsymbol{\sigma}_Z^{1,3}+\boldsymbol{\sigma}_Z^{2,2}-\boldsymbol{\sigma}_Z^{2,3})+\chi_{A_{Z_2}}^{\mathrm{corr}}(\boldsymbol{\sigma}_Z^{3,1}-2\boldsymbol{\sigma}_Z^{3,2}+\boldsymbol{\sigma}_Z^{3,3})]\\&+(\frac{g_{1,2}}{2}\boldsymbol{\sigma}_+^{3,1}\boldsymbol{\sigma}_-^{3,2}+h.c)+(\frac{g_{2,3}}{2}\boldsymbol{\sigma}_+^{3,2}\boldsymbol{\sigma}_-^{3,3}+h.c)+(\frac{\Omega_1}{2}\mathbf{a}_{Z_1}{}^\dagger\mathbf{a}_{Z_2}{}^\dagger\boldsymbol{\sigma}_X^{3,1}+h.c).\end{aligned}$$

If an error occurs on the third row, it will disturb the operators $Z_{3,1}Z_{3,2}$ and $Z_{3,2}Z_{3,3}$ while leaving untouched the operators $Z_{1,1}Z_{1,2}$, $Z_{2,1}Z_{2,2}$, $Z_{1,2}Z_{1,3}$ and $Z_{2,2}Z_{2,3}$ (initially set to 1), and will therefore be corrected. If a bit flip occurs on the first or second row, the system will remain on the manifold $\{Z_{3,1}Z_{3,2}=1, Z_{3,2}Z_{3,3}=1\}$. However, the values of $Z_{1,1}Z_{1,2}$, $Z_{2,1}Z_{2,2}$, $Z_{1,2}Z_{1,3}$ and $Z_{2,2}Z_{2,3}$ will change, and the scheme won't correct for this error. Now, suppose we add the two-qubit interaction terms described in fourth line of eq. (2.30). Through these terms, errors occurring on the first and second row are continuously mapped on the third row. Indeed, the term $(\Omega_X^{11,21}/2)\boldsymbol{\sigma}_X^{1,1}\boldsymbol{\sigma}_X^{2,1}$ maps the subspace $\{Z_{1,1}Z_{1,2}=-1,\ Z_{2,1}Z_{2,2}=1\}$ to $\{Z_{1,1}Z_{1,2}=1,\ Z_{2,1}Z_{2,2}=-1\}$, while the term $(\Omega_X^{21,31}/2)\boldsymbol{\sigma}_X^{2,1}\boldsymbol{\sigma}_X^{3,1}$ couples the two manifolds $\{Z_{2,1}Z_{2,2}=-1, Z_{3,1}Z_{3,2}=1\}$ and $\{Z_{2,1}Z_{2,2}=1, Z_{3,1}Z_{3,2}=-1\}$. A similar analysis holds for the interaction terms acting on qubits of third column. Hence, errors occurring on the first and second row are continuously transfered on the third row. As explained above, the resulting bit flips on the third row are corrected through the first three lines of the Hamiltonian in eq. (2.30). Since the corresponding terms $\boldsymbol{\sigma}_X^{i,j}\boldsymbol{\sigma}_X^{i+1,j}$ are gauge operators, their application does not disturb the logical information nor the error syndromes L_{Z_1} and L_{Z_2}. Ideally, the Rabi frequency should be lower than the correction rate $\kappa_Z/6$. This leads to the timescale requirement

$$\chi_{A_{Z_j}} \gg \kappa_Z \gtrsim \Omega_1 \gtrsim G > \Omega_X \gg \gamma_x, \quad j = 1, 2.$$

The correction of phase flips is achieved in a similar way. Two other cavities are coupled to the qubits in a horizontal manner, as illustrated in Fig. 2.12b. Phase flips are mapped to bit-flips by applying $\pi/2$-rotation around the $y-$axis on each qubit, and corrected through the same protocol used for bit-flips.

2.9 Conclusion

In conclusion, we have presented a quantum error correction scheme adapted to superconducting circuits that does not require any external feedback loop, but works in an autonomous way through quantum reservoir engineering. The scheme protects a logical qubit encoded in the three-qubit code against bit-flip errors, using three transmon qubits dispersively coupled to three low-Q resonators. We exploit the strong nonlinearity of the Josephson elements to directly build the feedback loop into the Hamiltonian thus avoiding any need in a directional (non-reciprocal) transmission of quantum information. We have shown that by applying continuous-wave microwave drives of appropriate and fixed frequencies and amplitudes to this system, the lifetime of an encoded quantum state can be significantly enhanced. Numerical simulations realized with currently achievable parameters predict a fidelity to the initial state higher than 95% after a time of the same order as the lifetime of the unprotected system. Besides, we have analytically determined that for the scheme to be efficient, we need only certain ratios to be large in addition to a basic symmetry requirement. The hardware equipment needed for the correction scheme can be reduced through the use of an alternative scheme, which requires to couple three transmon qubits to only one low-Q resonator at the cost of a slightly smaller correction efficiency.

This bit-flip correction protocol can be adapted to correct for phase flips by mapping the bit flips to phase flips through $\pi/2$-rotation around the $y-$axis on each qubit. Alternatively, one can directly create the corresponding physical Hamiltonian, involving a dispersive shift on the cavity depending on the transverse component of the qubits.

Finally, taking the bit-flip QEC scheme as a building block, we have sketched some ideas to extend the AQEC to Bacon-Shor codes for correcting arbitrary single-qubit errors. These preliminary ideas however require an extensive study along with numerical simulations. They also represent important experimental challenges. In the next chapters, we present an alternative approach to AQEC encoding the information in harmonic oscillators. This approach should lead to significant hardware shortcuts for a fully protected logical qubit.

Chapter 3

Continuous quantum non-demolition measurement of parity-type observables for cat-qubits

Table of contents

3.1 Motivations and objectives

Cat-codes have recently proven to be a strong and versatile tool to perform quantum information processing. By encoding a qubit in a superposition of coherent states of a harmonic oscillator, one benefits from the redundancy provided by the infinite dimensional Hilbert space of the system to realize an error correction (QEC) protocol. In a set of theoretical and experimental results, various aspects of encoding [43, 88], manipulation [53, 2, 30, 91], error syndrome measurement [82] and full quantum error correction [44, 59] with these states have been explored. Most spectacularly, a recent experiment [59] demonstrated an enhancement of the error-corrected cat-code's lifetime with respect to all system components. The performance of the error correction is however limited by uncorrected error channels such as deterministic relaxation of the coherent states amplitude, dephasing induced by cavity's inherited anharmonicity, and most significantly the propagating errors from the ancillary transmon [40] used for error syndrome measurements.

In an effort towards a fault-tolerant and scalable architecture for quantum information processing, Mirrahimi et al. recently proposed a framework based on non-linear drives and dissipations to dynamically protect a degenerate manifold spanned by two or four coherent states against some of these error channels [53]. Indeed, by engineering a non-linear coupling to a driven bath where the exchange of photons occurs mainly in pairs (or quadruples) of photons, one can stabilize a manifold spanned by two (resp. four) coherent states $\mathscr{M}_{2,\alpha} = \text{span}\{|\pm\alpha\rangle\}$ (resp. $\mathscr{M}_{4,\alpha} = \text{span}\{|\pm\alpha\rangle, |\pm i\alpha\rangle\}$). In Section 1.2, we have proved that this stabilization strongly suppresses the phase-flip errors of a logical qubit given by $|0\rangle_L = |\mathscr{C}_\alpha^+\rangle, |1\rangle_L = |\mathscr{C}_\alpha^-\rangle$ (resp. $|0\rangle_L = |\mathscr{C}_\alpha^{(0\text{mod}4)}\rangle, |1\rangle_L = |\mathscr{C}_\alpha^{(2\text{mod}4)}\rangle$). We remind the following definitions,

$$
\begin{aligned}
&|\mathscr{C}_\alpha^\pm\rangle = \mathscr{N}_\pm(|\alpha\rangle \pm |-\alpha\rangle),\\
&|\mathscr{C}_\alpha^{(0\text{mod}4)}\rangle = \mathscr{N}_0(|\mathscr{C}_\alpha^+\rangle + |\mathscr{C}_{i\alpha}^+\rangle),\ |\mathscr{C}_\alpha^{(2\text{mod}4)}\rangle = \mathscr{N}_2(|\mathscr{C}_\alpha^+\rangle - |\mathscr{C}_{i\alpha}^+\rangle),\\
&|\mathscr{C}_\alpha^{(1\text{mod}4)}\rangle = \mathscr{N}_1(|\mathscr{C}_\alpha^-\rangle - i|\mathscr{C}_{i\alpha}^-\rangle),\ |\mathscr{C}_\alpha^{(3\text{mod}4)}\rangle = \mathscr{N}_3(|\mathscr{C}_\alpha^-\rangle + i|\mathscr{C}_{i\alpha}^-\rangle),
\end{aligned}
$$

where $\mathscr{N}_\pm, \mathscr{N}_{0,1,2,3}$ are normalization constants near $1/\sqrt{2}$. One therefore deals with logical qubits that are only susceptible to bit-flip errors, but on which one can perform a universal set of logical gates (see [53, 2]). Such bit-flip errors can next be suppressed to first order by photon-number parity measurements as in [59]. Also, one can achieve higher-order correction through a register of such logical qubits (susceptible to highly biased noise) [3] and performing joint parity measurements between adjacent ones.

While initial experiments with two-photon driven dissipation [45] illustrate the viability of such a framework, many theoretical and experimental improvements are required in order to achieve a fully fault-tolerant architecture. One very important improvement concerns the quantum non-demolition (QND) measurement protocols. Indeed, a central requirement for all above proposals is the ability to measure observables such as photon number parity of a cavity mode, or joint parity of two cavity modes. Such single-mode or two-mode photon number parity measurements have been performed using an ancillary transmon and a Ramsey interferometry type scheme [10, 82, 91]. They however suffer from an important degree of non fault-tolerance and represent the main limitation in QEC [59]. In the present Chapter, we propose a new framework to perform QND measurement of various important parity-type observables which could be integrated in a fault-tolerant architecture.

The current measurement schemes [82, 91] are based on a dispersive coupling of the cavity mode to a transmon through a Hamiltonian of the form $-\hbar\chi|e\rangle\langle e|\mathbf{a}^\dagger\mathbf{a}$. The parity measurement is performed by initializing the transmon in the superposition $(|g\rangle+|e\rangle)/\sqrt{2}$ and waiting for a time π/χ. The $|e\rangle$ state of transmon will therefore acquire a π phase only for odd cavity Fock states. A measurement of the transmon, distinguishing between $(|g\rangle+|e\rangle)/\sqrt{2}$ and $(|g\rangle-|e\rangle)/\sqrt{2}$ will indicate the photon number parity. Nevertheless, a T_1 error of the transmon during the evolution will propagate to the cavity mode inducing photon dephasing. Indeed, such a measurement protocol is not fault-tolerant as the eigenstates of the measured observable (here parity cat states) get entangled to the ancillary system during the measurement protocol, making them vulnerable to the ancilla's errors (here T_1 errors): a cat state $|\mathscr{C}_\alpha^\pm\rangle$ evolves to $(|\mathscr{C}_\alpha^\pm\rangle\otimes|g\rangle+|\mathscr{C}_{\alpha e^{-i\chi t}}^\pm\rangle\otimes|e\rangle)/\sqrt{2}$. A fault-tolerant parity measurement could be for instance achieved through an effective Hamiltonian of the form $\hbar\chi|e\rangle\langle e|\cos(\pi\mathbf{a}^\dagger\mathbf{a})$. A cat state $|\mathscr{C}_\alpha^\pm\rangle$ would then evolve to $|\mathscr{C}_\alpha^\pm\rangle\otimes(|g\rangle+e^{\pm i\chi t}|e\rangle)/\sqrt{2}$, without entangling to the transmon.

While the engineering of a highly degenerate Hamiltonian of the form $\hbar\chi\cos(\pi\mathbf{a}^\dagger\mathbf{a})$ seems to be a complicated task, we show here that in presence of two-photon or four-photon driven dissipation, it could be effectively achieved with the help of quantum Zeno dynamics (QZD) [20]. By confining the dynamics to the manifold $\mathscr{M}_{2,\alpha}$, a physical Hamiltonian $\mathbf{H}$ acts as a projected Hamiltonian $\mathbf{H}_{\mathscr{M}_{2,\alpha}}=\Pi_{\mathscr{M}_{2,\alpha}}\mathbf{H}\Pi_{\mathscr{M}_{2,\alpha}}$, where $\Pi_{\mathscr{M}_{2,\alpha}}$ represents the projector on $\mathscr{M}_{2,\alpha}$. More precisely to achieve an effective parity Hamiltonian, one requires a physical Hamiltonian $\mathbf{H}$ satisfying

$$\mathbf{H}_{\mathscr{M}_{2,\alpha}}=\hbar\chi\Pi_{\mathscr{M}_{2,\alpha}}\cos(\pi\mathbf{a}^\dagger\mathbf{a})\Pi_{\mathscr{M}_{2,\alpha}}=\hbar\chi\boldsymbol{\sigma}_z^L,$$

where $\boldsymbol{\sigma}_z^L$ is the Pauli operator along the z-axis of the logical qubit defined by $\{|\mathscr{C}_\alpha^\pm\rangle\}$ and well-approximated by $|\alpha\rangle\langle-\alpha|+|-\alpha\rangle\langle\alpha|$. This means that $\mathbf{H}$ should couple the two coherent states $|\pm\alpha\rangle$. In the context of quantum superconducting circuits, such a

Hamiltonian can be achieved by strongly coupling a high impedance cavity mode to a Josephson junction [50, 64].

The construction of $\boldsymbol{\sigma}_z^L$-type hamiltonian, as well as similar parity-type Hamiltonians, such as the joint parity of two modes subjected to two-photon process, or the parity of a single mode under four-photon process, is detailed in Section 3.2. In Section 3.3, we develop a scheme to continuously measure these parity-type observables in a QND manner. These measurement protocols are based on the off-resonant coupling between the oscillators and a readout mode. While the main results of this Chapter are presented in these two sections, Sections 3.4 and 3.5 develop non-trivial points concerning the derivations and the limitations of these results. The last three sections present some extensions of these results. In particular, Section 3.7 illustrates the possibility to adapt this measurement scheme to non-dissipative cases, and Section 3.8 generalizes the construction of $\mathbb{Z}_2$-parity observables to build $\mathbb{Z}_n$ parity-like Hamiltonians.

The results of this chapter have led to a submitted publication in collaboration with Michel Devoret and Clarke Smith at Yale university [16].

3.2 Construction of parity-type observables

3.2.1 Two-component case

In this section, the systems are subject to two photon driven dissipation.

3.2.1.1 Single-parity observable $\boldsymbol{\sigma}_z^L$

Considering a cavity mode with frequency ω_a coupled capacitively to a Josephson junction (JJ), and assuming that other modes (including the junction mode) are never excited, the effective Hamiltonian in the interaction picture will be of the form

$$\mathbf{H}_{\text{int}}(t) = -\frac{E_J}{2}(\mathbf{D}[c(t)] + \mathbf{D}^\dagger[c(t)]), \quad c(t) = i\varphi_a e^{i\omega_a t}.$$

Here E_J is the effective Josephson energy and $\varphi_a = \sqrt{Z_a/2R_Q}$, where Z_a is the impedance of the cavity mode seen by the junction, and $R_Q = (2e)^2/\hbar$ is the superconducting resistance quantum. Moreover, $\mathbf{D}[c(t)]$ is the displacement operator defined by $\mathbf{D}[c(t)] = e^{c(t)\mathbf{a}^\dagger - c(t)^*\mathbf{a}}$. Clearly, for $\varphi_a \approx 2\alpha$, this Hamiltonian couples the two coherent states $|\pm\alpha\rangle$. While a practical realization of such a high impedance cavity mode is discussed later, we provide here a more precise analysis of the effective Hamiltonian.

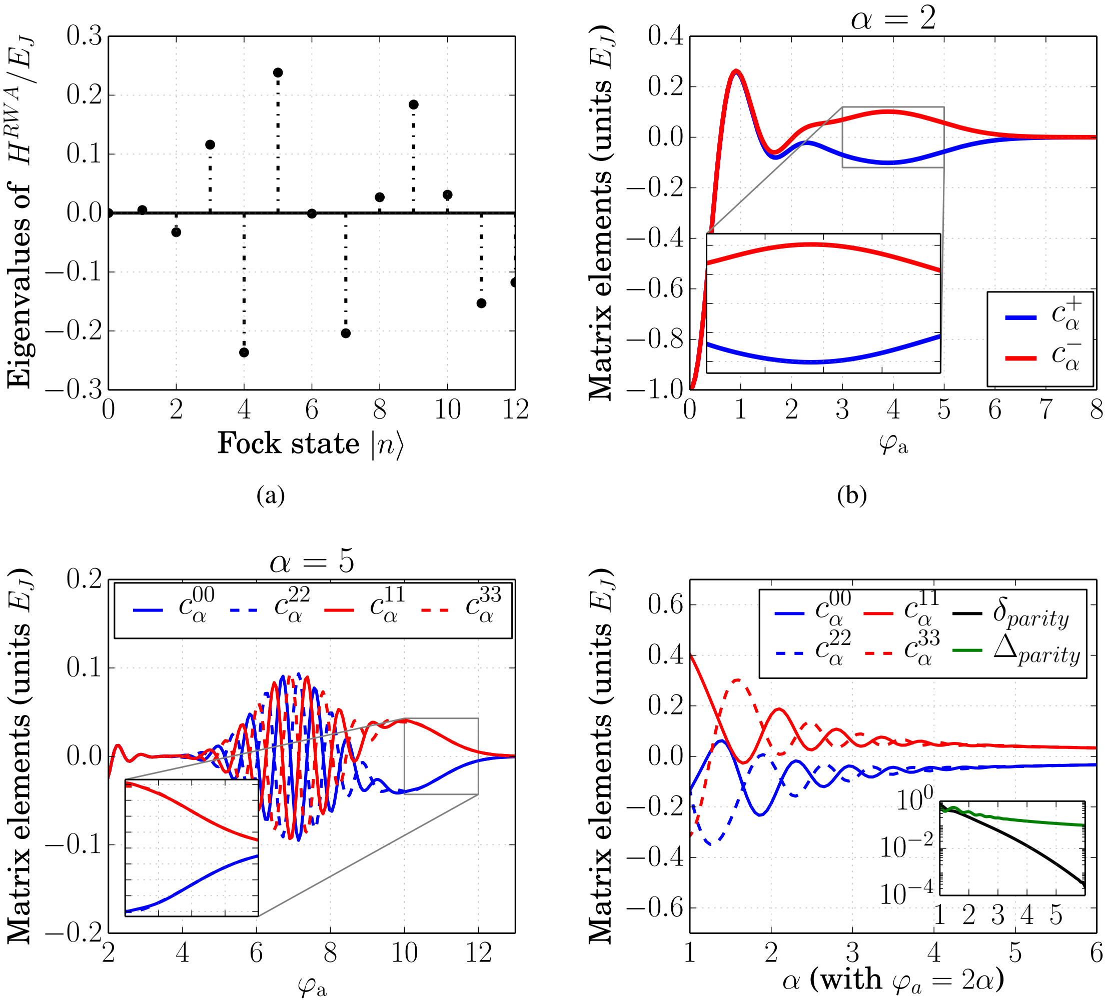
Eigenvalues of H^{RWA}/E_J
Fock state $|n\rangle$
$\alpha = 2$
Matrix elements (units E_J)
c_α^+
c_α^-
φ_a
$\alpha = 5$
Matrix elements (units E_J)
c_α^{00}
c_α^{22}
c_α^{11}
c_α^{33}
φ_a
Matrix elements (units E_J)
c_α^{00}
c_α^{11}
δ_{parity}
c_α^{22}
c_α^{33}
Δ_{parity}
10^0
10^{-2}
10^{-4}
α (with $\varphi_a = 2\alpha$)

(a)

(b)

(c)

(d)

Fig. 3.1 *(previous page)* (a) Eigenvalues of $\mathbf{H}^{\mathrm{RWA}}/E_J$ in (3.1), associated to the Fock states $|j\rangle,\ j=0,\cdots,14$. The zero-point phase fluctuation φ_a is set to 4. While for a precise parity hamilitonian, we expect the eigenvalues to alternate between $+1$ and -1, we observe here that for a coherent state $|\alpha\rangle$ with $|\alpha|=\varphi_a/2=2$, it nearly acts as a parity Hamiltonian. This can be observed through the sign alternance around the Fock state $\bar{n}=4$. Indeed, in presence of two-photon or four-photon driven dissipation, this Hamiltonian is projected on the cat states basis and effectively acts as parity. These projected Hamiltonians are presented in plots (b) and (c). (b) Matrix elements of projected Hamiltonian for the two-photon driven dissipation, $c_\alpha^\pm = \langle\mathscr{C}_\alpha^\pm|\mathbf{H}^{\mathrm{RWA}}|\mathscr{C}_\alpha^\pm\rangle$ as a function of φ_a (α being set to 2) plotted in units of E_J. The other two matrix elements $\langle\mathscr{C}_\alpha^\mp|\mathbf{H}^{\mathrm{RWA}}|\mathscr{C}_\alpha^\pm\rangle\equiv 0$ as the Hamiltonian is diagonal in the Fock states basis and does not couple even and odd manifolds. Furthermore, as underlined in the inset, $c_\alpha^\pm$ take opposite values for $3<\varphi_a<5$, which indicates that the projected Hamiltonian acts as the $\boldsymbol{\sigma}_Z$ Pauli operator in the logical basis $|\mathscr{C}_\alpha^\pm\rangle$. (c) Matrix elements of projected Hamiltonian for the four-photon driven dissipation, $c_\alpha^{jj}=\langle\mathscr{C}_\alpha^{(j\mathrm{mod}4)}|\mathbf{H}^{\mathrm{RWA}}|\mathscr{C}_\alpha^{(j\mathrm{mod}4)}\rangle$ as a function of φ_a (α being set to 5) plotted in units of E_J. The off-diagonal matrix elements are zero as the Hamiltonian conserves the photon number. The larger value of α compared to two-photon process is to ensure the degeneracy within parity subspaces (see plot (d)). Varying φ_a, we observe three different regimes: for $\varphi_a<4$, the Hamiltonian is fully degenerate in the cat subspace and acts as the identity; for $4<\varphi_a<9$, the Hamiltonian is non-degenerate and distinguishes the four cat states; for $9<\varphi_a<12$ which corresponds to a window around 2α, the Hamiltonian is degenerate in each parity subspace. This is the regime that we explore to ensure a parity measurement for 4-photon process. (d) We study the effect of the cat amplitude $|\alpha|$ on the parity-subspace degeneracy for the 4-photon process. Fixing $\varphi_a=2\alpha$, we observe that for $\alpha<4$, we deal with a non-degenerate Hamiltonian which explains the choice of $\alpha=5$ in plot (c). The inset illustrates that while the parity Hamiltonian strength $\Delta_{\mathrm{parity}}=\sqrt{(c_\alpha^{00}-c_\alpha^{11})^2+(c_\alpha^{22}-c_\alpha^{33})^2}$ decreases in $1/|\alpha|$, the parity subspace non-degeneracy $\delta_{\mathrm{parity}}=\sqrt{(c_\alpha^{00}-c_\alpha^{22})^2+(c_\alpha^{11}-c_\alpha^{33})^2}$ is suppressed exponentially in $|\alpha|^2$.

In the limit $\hbar\omega_a \gg E_J$, we can apply a rotating-wave approximation (RWA) to $\mathbf{H}_{\mathrm{int}}(t)$ [27, 86, 31], leading to the Hamiltonian

$$\mathbf{H}^{\mathrm{RWA}} = -E_J e^{-\frac{\varphi_a^2}{2}} \sum_n L_n(\varphi_a^2)|n\rangle\langle n|, \tag{3.1}$$

where $L_n(.)$ is the Laguerre polynomial of order n. In the presence of two-photon loss, the effective Hamiltonian of the system, given by $\mathbf{H}^{\mathrm{RWA}}_{\mathscr{M}_{2,\alpha}}$, follows a remarkable result. Under the condition

$$\varphi_a \approx 2|\alpha|, \tag{3.2}$$

the Hamiltonian takes the form of the parity Hamiltonian, i.e

$$\begin{aligned}\mathbf{H}^{\mathrm{RWA}}_{\mathscr{M}_{2,\alpha}} &= -\frac{\hbar\Omega_a}{2}[|\mathscr{C}^{+}_{\alpha}\rangle\langle\mathscr{C}^{+}_{\alpha}| - |\mathscr{C}^{-}_{\alpha}\rangle\langle\mathscr{C}^{-}_{\alpha}|] + \mathscr{O}(E_J e^{-\frac{\varphi_a^2}{2}}) \\ &= -\frac{\hbar\Omega_a}{2}\boldsymbol{\sigma}^L_z + \mathscr{O}(E_J e^{-\frac{\varphi_a^2}{2}}),\end{aligned} \tag{3.3}$$

where Ω_a is a function of E_J, φ_a and α. It is well approximated by (see Section 3.5.1.1)

$$\Omega_a = \frac{E_J}{\hbar}\frac{e^{-\frac{1}{2}(\varphi_a - 2|\alpha|)^2}}{\sqrt{\pi|\alpha|\varphi_a}}. \tag{3.4}$$

A precise analytical derivation of the above result is carried in Section 3.5.1.1.

In Fig. 3.1a, we plot, for $\varphi_a = 4$, the eigenvalues of $\mathbf{H}^{\mathrm{RWA}}/E_J$ associated to various Fock states. Following the above arguments, $\mathbf{H}^{\mathrm{RWA}}$ acts, for $\alpha \approx 2$, as a parity Hamiltonian on $\mathscr{M}_{2,\alpha}$. This can be understood through the observation of alternating signs for the eigenvalues of $\mathbf{H}^{\mathrm{RWA}}$ around the Fock state $|\bar{n} = 4\rangle$ corresponding to the average photon number in the coherent state $|\alpha\rangle$. Although the parity operator $\cos(\pi\mathbf{a}^\dagger\mathbf{a})$ requires also its eigenvalues to have the same module, this sign alternance is sufficient for having a parity Hamiltonian under two-photon loss. In Fig. 3.1b, we fix $\alpha = 2$ and we plot the diagonal matrix elements $c^{\pm}_{\alpha} = \langle\mathscr{C}^{\pm}_{\alpha}|\mathbf{H}^{\mathrm{RWA}}|\mathscr{C}^{\pm}_{\alpha}\rangle$ as a function of φ_a and in units of E_J. Note that, the off-diagonal terms $\langle\mathscr{C}^{\pm}_{\alpha}|\mathbf{H}^{\mathrm{RWA}}|\mathscr{C}^{\mp}_{\alpha}\rangle \equiv 0$ as H^{RWA} is diagonal in the Fock states basis and does not couple even and odd manifolds. For $\varphi_a < 1.5$, c^{+}_{α} and c^{-}_{α} are roughly equal, meaning that the Hamiltonian $\mathbf{H}^{\mathrm{RWA}}_{\mathscr{M}_{2,\alpha}}$ acts as the identity on $\mathscr{M}_{2,\alpha}$. At larger values of φ_a, c^{+}_{α} and c^{-}_{α} differ from each other. In particular, as shown in the inset of Fig. 3.1b, around $\varphi_a = 4 = 2|\alpha|$, c^{+}_{α} and c^{-}_{α} take opposite values. In this case, $\mathbf{H}^{\mathrm{RWA}}_{\mathscr{M}_{2,\alpha}}$ becomes proportional to $\boldsymbol{\sigma}^L_z$.

3.2.1.2 Joint-parity observable $\boldsymbol{\sigma}^{a,L}_z \otimes \boldsymbol{\sigma}^{b,L}_z$

From the construction of a single-mode parity Hamiltonian, acting as a $\boldsymbol{\sigma}^L_z$ Pauli operator in the logical basis, stems an immediate route to build a joint-parity Hamiltonian of two cavity modes **a** and **b** both subject to two-photon dissipation. Considering two cavity modes **a** and **b** coupled to a Josephson junction, the interaction Hamiltonian reads $\mathbf{H}_{int}(t) = -E_J\cos[\varphi_a(\mathbf{a}e^{-i\omega_a t} + c.c) + \varphi_b(\mathbf{b}e^{-i\omega_b t} + c.c)]$. The mode frequencies ω_a and ω_b are off-resonant so that we can apply the rotating wave approximation (more precisely, one needs to choose these frequencies in a way to avoid also high-order resonances)

$$\mathbf{H}^{\mathrm{RWA}} = -E_J e^{-\frac{\varphi_a^2+\varphi_b^2}{2}} \sum_{n_a,n_b} L_{n_a}(\varphi_a^2) L_{n_b}(\varphi_b^2) |n_a, n_b\rangle\langle n_a, n_b|. \tag{3.5}$$

Similarly to the single-mode case, if both **a** and **b** are high-impedance modes and are subject to two-photon loss, one can choose $|\alpha| \approx \varphi_a/2$ and $|\beta| \approx \varphi_b/2$, such that the confined Hamiltonian takes the form

$$\mathbf{H}^{\mathrm{RWA}}_{\mathscr{M}_{2,\alpha,\beta}} = -\frac{\hbar\Omega_{a,b}}{2} \boldsymbol{\sigma}_Z^{a,L} \otimes \boldsymbol{\sigma}_Z^{b,L}, \tag{3.6}$$

where $\Omega_{a,b} = \hbar\Omega_a\Omega_b/2E_J$, $\boldsymbol{\sigma}_Z^{a(b),L} = |\mathscr{C}^+_{\alpha(\beta)}\rangle\langle\mathscr{C}^+_{\alpha(\beta)}| - |\mathscr{C}^-_{\alpha(\beta)}\rangle\langle\mathscr{C}^-_{\alpha(\beta)}|$.

3.2.2 Four-component case

We have seen that under two-photon loss, the Hamiltonian $\mathbf{H}^{\mathrm{RWA}}$ acts as a parity Hamiltonian. Remarkably, this result also holds in the presence of four-photon loss, where the dynamics is confined to the larger manifold $\mathscr{M}_{4,\alpha} = \mathscr{M}_{2,\alpha} \oplus \mathscr{M}_{2,i\alpha}$. More precisely, for $\varphi_a \approx 2|\alpha|$, the projection of $\mathbf{H}^{\mathrm{RWA}}$ on $\mathscr{M}_{4,\alpha}$ satisfies $\mathbf{H}^{\mathrm{RWA}}_{\mathscr{M}_{4,\alpha}} = -\hbar\Omega_a/2\ (\Pi_{\mathscr{M}_{4,\alpha}} \cos(\pi\mathbf{a}^\dagger\mathbf{a})\Pi_{\mathscr{M}_{4,\alpha}} + O(e^{-\xi|\alpha|^2}))$, with $\xi = (\sqrt{2}-1)^2 \approx 0.17$ (see Section 3.5.1.2). The undesired term that scales as $e^{-\xi|\alpha|^2}$ lifts the degeneracy within the parity subspaces. This non-degeneracy is however suppressed exponentially with cat size $|\alpha|^2$, while the effective Hamiltonian strength decreases only linearly in $|\alpha|^{-1}$. Therefore for large enough α's we still achieve an effective parity Hamiltonian. This is illustrated in Fig. 3.1d, where we plot the diagonal matrix elements $c_\alpha^{jj} = \langle\mathscr{C}_\alpha^{j\mathrm{mod}4}|\mathbf{H}^{\mathrm{RWA}}|\mathscr{C}_\alpha^{j\mathrm{mod}4}\rangle$. As shown in the inset, the non-degeneracy vanishes rapidly and around values of $|\alpha| = 4$, $\mathbf{H}^{\mathrm{RWA}}_{\mathscr{M}_{4,\alpha}}$ is well-approximated by a parity Hamiltonian. The perfect degeneracy, for cat states of smaller amplitude, can also be achieved by introducing more junctions providing more degrees of freedom (see Section 3.6 for more details). Similarly to Fig. 3.1b, in Fig. 3.1c, we fix $\alpha = 5$ (for which, as analyzed in Fig. 3.1d, the parity subspace degeneracy is ensured) and we plot the diagonal matrix elements c_α^{jj} as a function of φ_a and in units of E_J. As shown in the inset, around $\varphi_a = 10 = 2|\alpha|$, we achieve an effective Hamiltonian of the form $\boldsymbol{\pi}_{4\mathrm{ph}} = |\mathscr{C}_\alpha^{(0\mathrm{mod}4)}\rangle\langle\mathscr{C}_\alpha^{(0\mathrm{mod}4)}| + |\mathscr{C}_\alpha^{(2\mathrm{mod}4)}\rangle\langle\mathscr{C}_\alpha^{(2\mathrm{mod}4)}| - |\mathscr{C}_\alpha^{(1\mathrm{mod}4)}\rangle\langle\mathscr{C}_\alpha^{(1\mathrm{mod}4)}| - |\mathscr{C}_\alpha^{(3\mathrm{mod}4)}\rangle\langle\mathscr{C}_\alpha^{(3\mathrm{mod}4)}|$.

3.3 Continuous measurement of the parity-type observables $\boldsymbol{\sigma}_z^{a,L}$, $\boldsymbol{\sigma}_z^{a,L} \otimes \boldsymbol{\sigma}_z^{b,L}$ and $\boldsymbol{\pi}_{\mathrm{4ph}}$

3.3.1 Measurement protocol

Following the same idea as in the usual dispersive measurements of superconducting qubits [90], one can perform a continuous quantum non-demolition measurement of the above observables, $\boldsymbol{\sigma}_Z^L$ and $\boldsymbol{\sigma}_Z^L \otimes \boldsymbol{\sigma}_Z^L$ for the two-photon dissipation scheme, and $\boldsymbol{\pi}_{\mathrm{4ph}}$ for the four-photon dissipation. This can be done by coupling an extra off-resonant readout mode to the same junction (see Figs. 3.2a and 3.2c). This mode is then driven at its resonance and the measurement outcome is imprinted on the phase or/and the amplitude of the reflected signal. More precisely, by coupling a driven readout mode $\mathbf{c}$ to the junction, and in the case of $\varphi_c \sqrt{n_c} \ll 1$ (here n_c denotes the average number of readout photons and this requirement is equivalent to assuming $n_c \ll n_{\mathrm{crit}}$, the critical number for dispersive approximation [22]), we achieve the following effective Hamiltonians:

$$\begin{aligned}
\mathbf{H}^{\mathrm{disp}}_{\mathscr{M}_{2,\alpha}} &\approx -\frac{\hbar\widetilde{\Omega}_a}{2}\boldsymbol{\sigma}_Z^a + \frac{\hbar\chi_a}{2}\boldsymbol{\sigma}_Z^a\mathbf{c}^\dagger\mathbf{c} + \mathbf{H}_{\mathrm{drive}}(t), \\
\mathbf{H}^{\mathrm{disp}}_{\mathscr{M}_{2,\alpha,\beta}} &\approx -\frac{\hbar\widetilde{\Omega}_{a,b}}{2}\boldsymbol{\sigma}_Z^a\boldsymbol{\sigma}_Z^b + \frac{\hbar\chi_{a,b}}{2}\boldsymbol{\sigma}_Z^a\boldsymbol{\sigma}_Z^b\mathbf{c}^\dagger\mathbf{c} + \mathbf{H}_{\mathrm{drive}}(t), \\
\mathbf{H}^{\mathrm{disp}}_{\mathscr{M}_{4,\alpha}} &\approx -\frac{\hbar\widetilde{\Omega}_a}{2}\boldsymbol{\pi}_{\mathrm{4ph}} + \frac{\hbar\chi_a}{2}\boldsymbol{\pi}_{\mathrm{4ph}}\mathbf{c}^\dagger\mathbf{c} + \mathbf{H}_{\mathrm{drive}}(t).
\end{aligned} \tag{3.7}$$

Here $\mathbf{H}_{\mathrm{drive}}(t) = \hbar(\varepsilon_c(t)\mathbf{c}^\dagger + \varepsilon_c^*(t)\mathbf{c})$, $\widetilde{\Omega}_a = e^{-\varphi_c^2/2}\Omega_a$, $\widetilde{\Omega}_{a,b} = e^{-\varphi_c^2/2}\Omega_{a,b}$, $\chi_a = \widetilde{\Omega}_a\phi_c^2$, $\chi_{a,b} = \widetilde{\Omega}_{a,b}\phi_c^2$.

The first terms in the above Hamiltonians simply induce deterministic rotations in the associated parity subspaces, whereas the second terms correspond to frequency pulls on mode $\mathbf{c}$ that depend on the values of associated observables. By driving the mode $\mathbf{c}$ at resonance, so that $\mathbf{H}_{\mathrm{drive}}$ is time-independent, the measurement outcome is imprinted on the phase of the pointer coherent state.

3.3.2 Measurement rates

Taking κ_c to be the dissipation rate of $\mathbf{c}$ induced by its coupling to a readout transmission line, the measurement rate is optimal when $\kappa_c = \chi_a$ ($\chi_{a,b}$ for joint-parity measurement) [23]. This optimal rates Γ_m^a (single mode in two- and four-component case) and $\Gamma_m^{a,b}$ (two modes

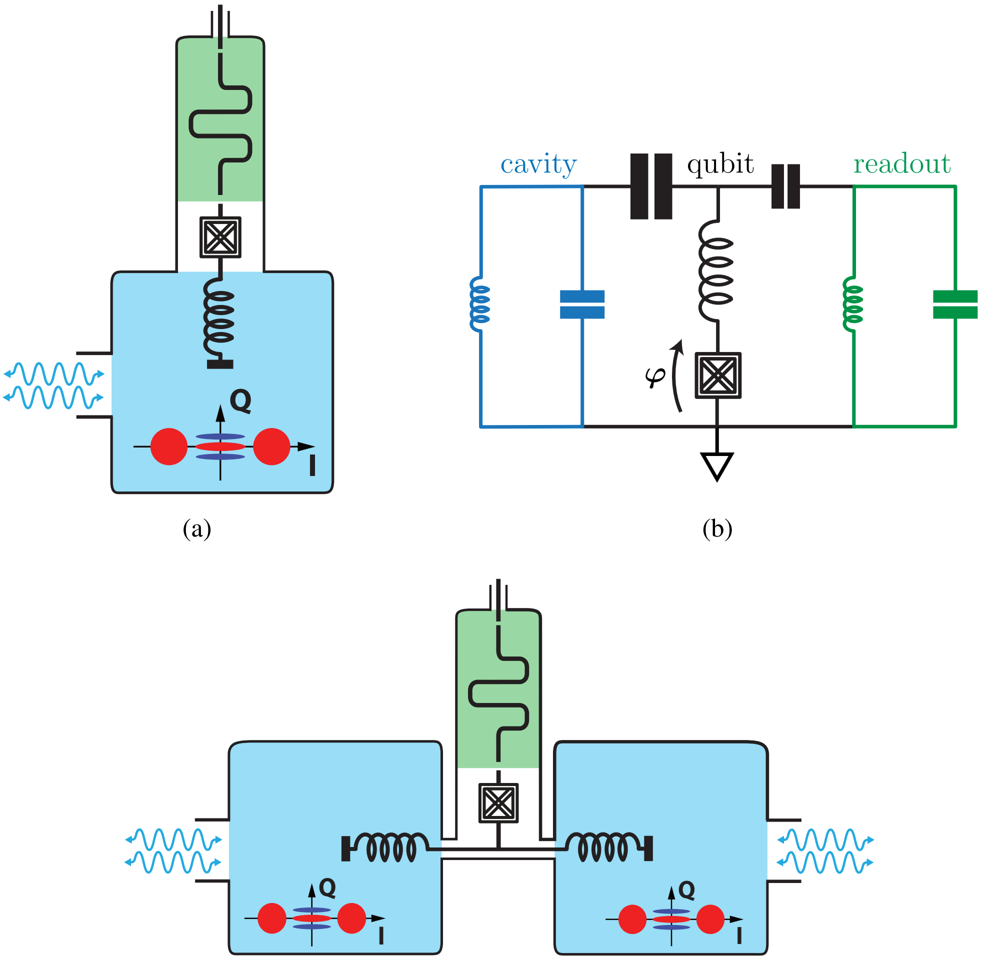

(a)

(b)

(c)

Fig. 3.2 (a) Possible physical realization of a single-mode continuous parity measurement in presence of two-photon driven dissipation. In such a realization, similarly to [85], on one side we mediate a two-photon dissipation of the storage high-Q cavity mode and on the other side we couple to a low-Q readout mode through a high-impedance Josephson circuit. (b) Electrical circuit equivalent to the experimental schematic in Fig. 3.2a without the two-photon driven dissipation. The cavity (blue) and readout (green) modes are modeled by LC oscillators, and are capacitively coupled to an high impedance qubit mode. This qubit mode consists of a large superinductance, formed from an array of large Josephson junctions (as in the fluxonium), in series with a nonlinear circuit element, depicted as a cross-hatched box. (c) Design extension to the case of joint-parity measurements between two high-Q cavity modes under two-photon driven dissipation, inspired from [91]. Here, the coupling between the high-Q modes is ensured through high-impedance elements.

in two-component case) are given by (see Fig. 3.3)

$$\begin{aligned}
\Gamma_m^a &= \bar{n}_c\chi_a = \bar{n}_c\phi_c^2 e^{-\frac{\varphi_c^2}{2}}\frac{E_J}{\hbar}\frac{e^{-\frac{1}{2}(\varphi_a-2|\alpha|)^2}}{\sqrt{\pi|\alpha|\varphi_a}}, \\
\Gamma_m^{a,b} &= \bar{n}_c\chi_{a,b} = \bar{n}_c\phi_c^2 e^{-\frac{\varphi_c^2}{2}}\frac{E_J}{\hbar}\frac{e^{-\frac{1}{2}(\varphi_a-2|\alpha|)^2-\frac{1}{2}(\varphi_b-2|\beta|)^2}}{2\pi\sqrt{|\alpha\beta|\varphi_a\varphi_b}}.
\end{aligned} \tag{3.8}$$

3.3.3 Towards an experimental realization

Practical realization of a high impedance cavity mode, satisfying Eq. 2, poses a notable challenge. To see this, note that Eq. 2 for $\alpha = 2$ requires an impedance $Z_a = 32R_Q$, where $R_Q = (2e)^2/\hbar$ is the superconducting resistance quantum. For comparison, typical superconducting cavities have impedances $0.1R_Q < Z_a < R_Q$ [60, 70]. However, much larger impedances $Z \sim 8R_Q$ have been produced using devices comprising superinductances (fabricated from arrays of large Josephson junctions), such as in the fluxonium qubit [51, 64].

In our proposed experimental system (see Figs. 3.2a,3.2b), a fluxonium-based qubit mode composed of a superinductance in series with a nonlinear circuit element is capacitively coupled to two cavities. This nonlinear circuit element is assumed to have a Josephson junction-like Hamiltonian of the form

$$\mathbf{H}_{\mathrm{el}} = 4E_C\mathbf{n}^2 - E_J\cos\mu\boldsymbol{\varphi},$$

where $\mathbf{n}$ is the number of Cooper pairs across the element, $\boldsymbol{\varphi}$ is the superconducting phase, E_C is the charging energy, E_J is the Josephson energy, and μ is an integer-valued parameter determined by the implementation. It may be worthwhile to realize $\mu > 1$, and this could be achieved by circuits similar to those proposed by Brooks et al. [9] and Ioffe et al. [33]. This transforms the effective cavity impedance according to $Z_a \to \mu^2 Z_a$, making Eq. 2 much easier to satisfy. The details of this strategy will be described in a forthcoming publication.

3.3.4 Performance and limitations

Let us now study the limitations of such a measurement protocol. Here we have made a few approximations and the main limitations are due to second order effects. The first one concerns the rotating wave approximation. Indeed, dealing with high-impedance modes one needs to be extra cautious about higher order terms in the cosine. While in the single-mode case, such second-order effects lead to a slight modification of the measurement rate, in the two-mode case, they could lead to a small dephasing within the parity subspaces, as

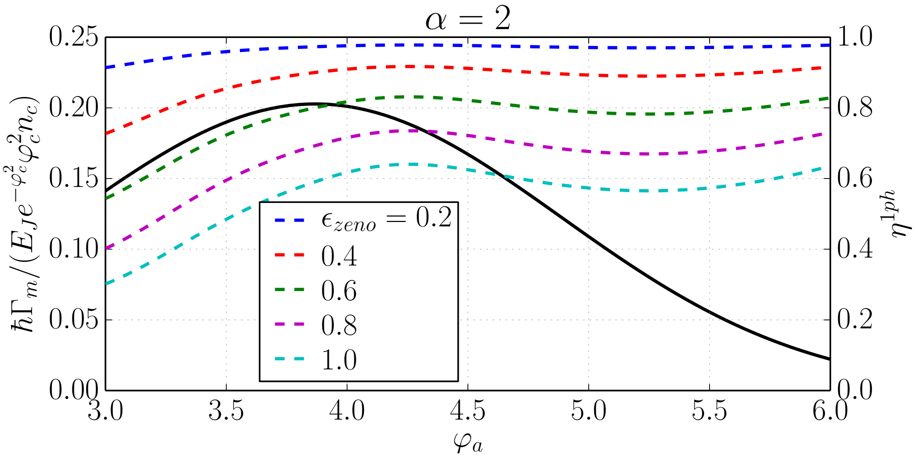

Fig. 3.3 The left axis corresponding to the black straight curve illustrates the measurement rate in the single-mode case (see eq. (3.8)) in units of $E_J/\hbar$ and renormalized by the parameters of the readout mode (zero point fluctuations and number of photons). Fixing $\alpha = 2$ and varying φ_a, we observe an optimal measurement rate around $\varphi_a = 2\alpha$. The right axis, corresponding to the colored dashed curves, illustrate the efficiency of the measurement limited by the higher order Zeno effects. Here, we fix $\varphi_c = .1$ and the number of readout photons $n_c = 1$ and we plot $\eta_{1\text{ph}} = \Gamma_m^{1\text{ph}}/(\Gamma_m^{1\text{ph}} + \Gamma_Z)$. The measurement rate $\Gamma_m^{1\text{ph}}$ is given by (3.8) and the extra dephasing rate Γ_Z, induced by higher-order Zeno effects, is calculated through the simulation of the master equation (3.9). Varying φ_a, we observe that this efficiency achieves a local optimum near $\varphi_a = 2\alpha$ corresponding to the optimum point of the measurement rate Γ_m. Also, by decreasing the Zeno parameter $\varepsilon_{\text{zeno}} = E_J/\hbar\kappa_{2\text{ph}}$, this higher-order effect can be suppressed.

shown in Section 3.4.2. These effects could be minimized by a careful choice of resonance frequencies.

A more important limitation concerns the Zeno approximation. We have considered that under the two-photon process, the confined dynamics is given by the projected Hamiltonian $\mathbf{H}^{\text{RWA}}_{\mathscr{M}_{2,\alpha}}$. This corresponds to a first order Zeno dynamics approximation in $\varepsilon_{\text{zeno}} = E_J/\hbar\kappa_{2\text{ph}}$ [4, 5]. The second order correction in $\varepsilon_{\text{zeno}}$ induces a dephasing in the basis $\{|\mathscr{C}_\alpha^{\pm}\rangle\}$ occurring at a rate $\Gamma_Z = r(\alpha, \varphi_a)\varepsilon_{\text{zeno}}^2\kappa_{2\text{ph}}$, where the numerical factor $r(\alpha, \varphi_a)$ can be derived from [5]. This could be seen as an inefficiency in the measurement, where a constant part (independent of the number of readout photons) of the measurement signal is lost through the two-photon decay channel. Here, we analyze numerically this second order effect by simulating the master equation

$$\begin{aligned}\frac{d\boldsymbol{\rho}}{dt} &= -\frac{i}{\hbar}[\mathbf{H}^{\mathrm{RWA}}, \boldsymbol{\rho}] + \kappa_{2\mathrm{ph}}\mathbf{D}[\mathbf{a}^2 - \alpha^2](\rho) \\ \boldsymbol{\rho}(0) &= \frac{1}{2}(|\mathscr{C}_\alpha^+\rangle + |\mathscr{C}_\alpha^-\rangle)(\langle\mathscr{C}_\alpha^+| + \langle\mathscr{C}_\alpha^-|),\end{aligned} \tag{3.9}$$

where the single mode Hamiltonian, $\mathbf{H}^{\mathrm{RWA}}$, is given by (3.1). Taking $\alpha = 2$, and varying φ_a and the Zeno parameter $\varepsilon_{\mathrm{zeno}}$, we look at the decay of purity with time. This corresponds to a dephasing due to higher order Zeno dynamics well-approximated by Γ_Z. We illustrate in Fig. 3.3 (dashed lines corresponding to the right axis) the value of $\eta_{1\mathrm{ph}} = \Gamma_m^{1\mathrm{ph}}/(\Gamma_m^{1\mathrm{ph}} + \Gamma_Z)$ corresponding to the measurement efficiency when the number of readout photons is fixed to $n_c = 1$. Indeed, as Γ_Z does not depend on the number of readout photons while Γ_m increases linearly in n_c, this efficiency improves for higher number of readout photons. We observe that for a given Zeno parameter $\varepsilon_{\mathrm{zeno}}$, the point $\varphi_a \approx 2\alpha$ corresponding to the optimal measurement rate Γ_m, is also a local optimum of the efficiency. We do not account for the readout mode **c** in these simulations, as it does not contribute to higher-order Zeno approximations and therefore to Γ_Z. Note that, this measurement inefficiency is the only detrimental effect of such higher-order dynamics. As the Hamiltonian $\mathbf{H}^{\mathrm{RWA}}$ is diagonal in the Fock states basis, it does not change the parity and therefore do not lead to any bit-flip type error of the logical qubit.

We can perform a similar analysis for the two-mode joint-parity measurement protocol. While higher order Zeno dynamics cannot lead to any change of photon number parities (Hamiltonian being diagonal in the Fock states basis), in principle, it can lead to a dephasing for each logical qubit. However, it can be seen that, up to a very good approximation (exponentially precise in $|\alpha|^2$), such a dephasing occurs in a correlated manner, giving rise to a dissipation channel of the form $\boldsymbol{\sigma}_Z^a \otimes \boldsymbol{\sigma}_Z^b + \mathscr{O}(e^{-c|\alpha|^2})$, $c > 0$. This effect is studied in detail in Section 3.5.2. This means that such higher order effects do not induce any decoherence within a given joint-parity subspace. Therefore starting from $c_{++}|\mathscr{C}_\alpha^+, \mathscr{C}_\alpha^+\rangle + c_{--}|\mathscr{C}_\alpha^-, \mathscr{C}_\alpha^-\rangle + c_{+-}|\mathscr{C}_\alpha^+, \mathscr{C}_\alpha^-\rangle + c_{-+}|\mathscr{C}_\alpha^-, \mathscr{C}_\alpha^+\rangle$, the measurement will project the state on one of the two parity states $c_{++}|\mathscr{C}_\alpha^+, \mathscr{C}_\alpha^+\rangle + c_{--}|\mathscr{C}_\alpha^-, \mathscr{C}_\alpha^-\rangle$ or $c_{+-}|\mathscr{C}_\alpha^+, \mathscr{C}_\alpha^-\rangle + c_{-+}|\mathscr{C}_\alpha^-, \mathscr{C}_\alpha^+\rangle$ without affecting the purity of these states. We thus deal with a quantum non-demolition measurement (with non-unit efficiency) of joint parity.

3.4 The Rotating-Wave Approximation (RWA) : Derivation and validity

3.4.1 Derivation of the Hamiltonian $\mathbf{H}^{\text{RWA}}$: one-mode case and two-mode case

In the case of a single cavity mode coupled to a Josephson junction, the Hamiltonian in the interaction picture reads $\mathbf{H}_{\text{int}}(t) = -E_J\cos(\varphi_a(\mathbf{a}e^{-i\omega_a t} + \mathbf{a}^\dagger e^{i\omega_a t})) = -E_J/2(\mathscr{D}[c_a(t)] + \mathscr{D}[-c_a(t)])$, where $c_a(t) = i\varphi_a e^{i\omega_a t}$. We can expand the displacement operator,

$$\mathscr{D}[c_a(t)] = \sum_{l_a=0}^{\infty}\mathbf{A}(l_a)(-\mathbf{a}e^{-i\omega_a t})^{l_a} + \sum_{l_a=1}^{\infty}(\mathbf{a}^\dagger e^{i\omega_a t})^{l_a}\mathbf{A}(l_a), \tag{3.10}$$

where $\mathbf{A}(l_a) = \varphi_a^{l_a}e^{-\frac{\varphi_a^2}{2}}\sum\limits_{n_a=0}\frac{n_a!}{(n_a+l_a)!}L_n^{(l_a)}(\varphi_a^2)|n_a\rangle\langle n_a|$ is a hermitian operator [31]. Here, $L_n^{(l_a)}$ is the generalized Laguerre polynomial of order n and parameter l_a. The first order RWA, given by the formula $\mathbf{H}^{\text{RWA},1} = \overline{\mathbf{H}(t)}$ where $\overline{\mathbf{H}(t)} = \lim\limits_{T\to\infty}\frac{1}{T}\int_0^T\mathbf{H}(t)dt$, reads in our case,

$$\mathbf{H}^{\text{RWA},1} = -E_J e^{-\frac{\varphi_a^2}{2}}\sum_n L_n(\varphi_a^2)|n\rangle\langle n|. \tag{3.11}$$

In the two-mode case, the Hamiltonian reads in the interaction picture $\mathbf{H}_{\text{int}}(t) = -E_J/2(\mathscr{D}[c_a(t)]\mathscr{D}[c_b(t)] + h.c.)$, where $c_a(t) = i\varphi_a e^{i\omega_a t}$ and $c_b(t) = i\varphi_b e^{i\omega_b t}$, i.e

$$\begin{aligned}\mathbf{H}_{\text{int}}(t) = -\frac{E_J}{2}\big[&\big(\sum_{l_a=0}^{\infty}\mathbf{A}(l_a)(-\mathbf{a}e^{-i\omega_a t})^{l_a} + \sum_{l_a=1}^{\infty}(\mathbf{a}^\dagger e^{i\omega_a t})^{l_a}\mathbf{A}(l_a)\big)\\ &\big(\sum_{l_b=0}^{\infty}\mathbf{B}(l_b)(-\mathbf{b}e^{-i\omega_b t})^{l_b} + \sum_{l_b=1}^{\infty}(\mathbf{b}^\dagger e^{i\omega_b t})^{l_b}\mathbf{B}(l_b)\big)\\ &+h.c.\big]\end{aligned} \tag{3.12}$$

Similarly to $\mathbf{A}(l_a)$, we have defined $\mathbf{B}(l_b) = \varphi_b^{l_b}e^{-\frac{\varphi_b^2}{2}}\sum\limits_{n_b=0}\frac{n_b!}{(n_b+l_b)!}L_n^{(l_b)}(\varphi_b^2)|n_b\rangle\langle n_b|$. The frequencies ω_a and ω_b are taken to be incommensurate, meaning that $l_a\omega_a \neq l_b\omega_b$ for all l_a, $l_b > 0$. In practice, we require that the modes are sufficiently off resonant to avoid high order photon exchange terms. Under this assumption, the only non-rotating term corresponds to $l_a = 0$ and $l_b = 0$, which leads to

$$\mathbf{H}^{\mathrm{RWA},1} = -E_J e^{-\frac{\varphi_a^2+\varphi_b^2}{2}} \sum_{n_a,n_b} L_{n_a}(\varphi_a^2) L_{n_b}(\varphi_b^2) |n_a,n_b\rangle\langle n_a,n_b|. \tag{3.13}$$

As mentioned in Section 3.3.4, some of the high order terms eventually approach resonances. This effect, which is accounted for in the second order RWA, is studied in section 3.4.2.

3.4.2 Validity of the RWA

As we consider high impedance modes, we need to be careful about the validity of the RWA. Indeed, non resonant high order terms in the development of the cosine (see expressions (3.10) and (3.12)) have larger amplitudes than in the case of low impedance modes, and can affect the dynamics throughout higher order interaction terms. The effect of these terms can be evaluated though the second order correction of the RWA, resulting in the Hamiltonian $\mathbf{H}^{\mathrm{RWA},2}$, given by the following expression [54, 76]

$$\mathbf{H}^{\mathrm{RWA},2} = \mathbf{H}^{\mathrm{RWA},1} - i\overline{(\mathbf{H}(t) - \mathbf{H}^{\mathrm{RWA},1}) \int_0^t du(\mathbf{H}(u) - \mathbf{H}^{\mathrm{RWA},1})}. \tag{3.14}$$

The Hamiltonian remains diagonal in the Fock states basis at the second order, so that the second order correction induces at most a shift of the Hamiltonian eigenvalues. In the two-photon process for the single-mode case, this merely leads to a small modification of the measurement rate Γ_m. Moreover, as the smallest frequency of non-secular terms is given by $\omega_a \gg E_J$ (see expression (3.10)), this shift is small relatively to the eigenvalues.

In the case of two modes **a** and **b** with incommensurate frequencies ω_a and ω_b, the second order Hamiltonian $\mathbf{H}^{\mathrm{RWA},2}$ is also diagonal in the Fock states basis. As a direct consequence, its projection $\mathbf{H}^{\mathrm{RWA},2}_{\mathcal{M}_{2,\alpha,\beta}}$ on the manifold $\mathcal{M}_{2,\alpha,\beta}$ is a linear combination of the operators $\mathbf{I}_a \otimes \mathbf{I}_b, \boldsymbol{\sigma}_Z^a \otimes \mathbf{I}_b, \mathbf{I}_a \otimes \boldsymbol{\sigma}_Z^b$ and $\boldsymbol{\sigma}_Z^a \otimes \boldsymbol{\sigma}_Z^b$, where $\mathbf{I}_{a(b)}$ is defined as the identity on $\mathcal{M}_{2,\alpha(\beta)}$. Unlike in the single-mode case where this energy shift merely modifies the measurement rate, here it can also lead to an unwanted dephasing within the parity subspaces. Indeed, while for the first order RWA, $\mathbf{H}^{\mathrm{RWA},1}_{\mathcal{M}_{2,\alpha,\beta}} \propto \boldsymbol{\sigma}_Z^a \otimes \boldsymbol{\sigma}_Z^b$, the projection $\mathbf{H}^{\mathrm{RWA},2}_{\mathcal{M}_{2,\alpha,\beta}}$ of the second order Hamiltonian $\mathbf{H}^{\mathrm{RWA},2}$ on the manifold $\mathcal{M}_{2,\alpha,\beta}$ can acquire non-zero components on $\boldsymbol{\sigma}_Z^a \otimes \mathbf{I}_b$ and $\mathbf{I}_a \otimes \boldsymbol{\sigma}_Z^b$. The measurement would therefore lead to a dephasing in two-qubit parity subspaces. Besides, the second order energy shifts for this second order approximation can, in principle, be large with respect to single-mode case. This is due to the fact that some high order terms in l_a and l_b (see expression (3.12)) become close to resonance. By inserting the expression of $\mathbf{H}(t)$ given in eq. (3.12) into eq. (3.14), we derive $\mathbf{H}^{\mathrm{RWA},2}$

$$\begin{aligned}\mathbf{H}^{\mathrm{RWA},2} = &-E_J\mathbf{H}^{\mathrm{RWA},1}\\ &+E_J^2\sum_{l_a,l_b\geq 0,\ (l_a,l_b)\neq(0,0)}\frac{(1+(-1)^{l_a+l_b})}{2(l_a\omega_a+l_b\omega_b)}[(\mathbf{a}^{\dagger l_a}\mathbf{A}(l_a)^2\mathbf{a}^{l_a})(\mathbf{b}^{\dagger l_b}\mathbf{B}(l_b)^2\mathbf{b}^{l_b})\\ &-(\mathbf{A}(l_a)\mathbf{a}^{l_a}\mathbf{a}^{\dagger l_a}\mathbf{A}(l_a))(\mathbf{B}(l_b)\mathbf{b}^{l_b}\mathbf{b}^{\dagger l_b}\mathbf{B}(l_b))]\\ &+E_J^2\sum_{l_a,l_b\geq 1}\frac{((-1)^{l_a}+(-1)^{l_b})}{2(l_a\omega_a-l_b\omega_b)}[(\mathbf{a}^{\dagger l_a}\mathbf{A}(l_a)^2\mathbf{a}^{l_a})(\mathbf{B}(l_b)\mathbf{b}^{l_b}\mathbf{b}^{\dagger l_b}\mathbf{B}(l_b))\\ &-(\mathbf{A}(l_a)\mathbf{a}^{l_a}\mathbf{a}^{\dagger l_a}\mathbf{A}(l_a))(\mathbf{b}^{\dagger l_b}\mathbf{B}(l_b)^2\mathbf{b}^{l_b})],\end{aligned}$$

where $\mathbf{A}(l_a)$ and $\mathbf{B}(l_b)$ are introduced in Section 3.4.1. The ratios $\Gamma_\phi^\pm/\Gamma_m$, where Γ_ϕ^+ (Γ_ϕ^-) is the measurement induced dephasing within the even (resp. odd) joint parity subspace, quantify how much the quantum state is disturbed during a parity measurement, and can be evaluated through

$$\begin{aligned}\Gamma_\phi^+ &= \left|\langle\mathscr{C}_\alpha^+,\mathscr{C}_\beta^+|\mathbf{H}^{\mathrm{RWA},2}|\mathscr{C}_\alpha^+,\mathscr{C}_\beta^+\rangle-\langle\mathscr{C}_\alpha^-,\mathscr{C}_\beta^-|\mathbf{H}^{\mathrm{RWA},2}|\mathscr{C}_\alpha^-,\mathscr{C}_\beta^-\rangle\right|/\hbar\\ \Gamma_\phi^- &= \left|\langle\mathscr{C}_\alpha^+,\mathscr{C}_\beta^-|\mathbf{H}^{\mathrm{RWA},2}|\mathscr{C}_\alpha^+,\mathscr{C}_\beta^-\rangle-\langle\mathscr{C}_\alpha^-,\mathscr{C}_\beta^+|\mathbf{H}^{\mathrm{RWA},2}|\mathscr{C}_\alpha^-,\mathscr{C}_\beta^+\rangle\right|/\hbar\\ \Gamma_m &= \Big|\langle\mathscr{C}_\alpha^+,\mathscr{C}_\beta^+|\mathbf{H}^{\mathrm{RWA},2}|\mathscr{C}_\alpha^+,\mathscr{C}_\beta^+\rangle+\langle\mathscr{C}_\alpha^-,\mathscr{C}_\beta^-|\mathbf{H}^{\mathrm{RWA},2}|\mathscr{C}_\alpha^-,\mathscr{C}_\beta^-\rangle\\ &\quad-\langle\mathscr{C}_\alpha^+,\mathscr{C}_\beta^-|\mathbf{H}^{\mathrm{RWA},2}|\mathscr{C}_\alpha^+,\mathscr{C}_\beta^-\rangle-\langle\mathscr{C}_\alpha^-,\mathscr{C}_\beta^+|\mathbf{H}^{\mathrm{RWA},2}|\mathscr{C}_\alpha^-,\mathscr{C}_\beta^+\rangle\Big|/\hbar.\end{aligned}$$

As a numerical example, we set the mode frequencies to $\omega_a/2\pi = 9.10\mathrm{GHz}$ and $\omega_b/2\pi = 7.5\mathrm{GHz}$, the Josphson energy $E_J/\hbar = 300\mathrm{MHz}$, the cat amplitudes $\alpha=\beta=2$, the parameters $\varphi_a=\varphi_b=2\alpha$. We find that $\Gamma_\phi^+/\Gamma_m\sim 10^{-3}$ and $\Gamma_\phi^-/\Gamma_m\sim 5\times 10^{-3}$, while the measurement rate $\Gamma_m/2\pi$ can be as high as 1MHz (see Fig. 3.3).

3.5 Zeno dynamics approximation : first order and second order corrections

3.5.1 First order Zeno dynamics approximation

3.5.1.1 Two-photon process : Derivation of the effective Hamiltonian $\mathbf{H}^{\mathrm{RWA}}_{\mathscr{M}_{2,\alpha}}$

Under two-photon driven dissipation, the state of the oscillator is confined to the manifold $\mathscr{M}_{2,\alpha}=\mathrm{span}\{|\mathscr{C}_\alpha^\pm\rangle\}$. The dynamics in the first order approximation in $\varepsilon_{\mathrm{zeno}} = E_J/\hbar\kappa_{\mathrm{2ph}}$, is given by the projection $\mathbf{H}^{\text{RWA}}_{\mathscr{M}_{2,\alpha}}$ of the Hamiltonian $\mathbf{H}_{\text{RWA}}$ on $\mathscr{M}_{2,\alpha}$. Since $\mathbf{H}_{\text{RWA}}$ is diagonal in the Fock states basis, the off-diagonal matrix elements $\langle\mathscr{C}^{\pm}_{\alpha}|\mathbf{H}_{\text{RWA}}|\mathscr{C}^{\mp}_{\alpha}\rangle$ are identically zero. The diagonal matrix elements $c^{\pm}_{\alpha} = \langle\mathscr{C}^{\pm}_{\alpha}|\mathbf{H}_{\text{RWA}}|\mathscr{C}^{\pm}_{\alpha}\rangle$ satisfy

$$\begin{aligned} c^{\pm}_{\alpha} &= -E_J e^{-\frac{\varphi_a^2}{2}-|\alpha|^2}\sum_{n\geq 0}\frac{|\alpha|^{2n}}{n!}L_n(\varphi_a^2) \mp E_J e^{-\frac{\varphi_a^2}{2}-|\alpha|^2}\sum_{n\geq 0}\frac{(-|\alpha|^2)^n}{n!}L_n(\varphi_a^2) \\ &= -E_J e^{-\frac{\varphi_a^2}{2}}[J_0(2|\alpha|\varphi_a) \pm e^{-2|\alpha|^2}I_0(2|\alpha|\varphi_a)], \end{aligned} \tag{3.15}$$

where $J_0(.)$ and $I_0(.)$ are respectively the Bessel function and the modified Bessel function, both of the first kind. To derive the second line of eq. (3.15), we applied the identity (5.1.16) of [83]. As we have $|J_0(2|\alpha|\varphi_a)| \leq 1$, the first term is bounded by $E_J e^{-\frac{\varphi_a^2}{2}}$. Note that this ensures the symmetry $c^{+}_{\alpha} = -c^{-}_{\alpha} + \mathscr{O}(E_J e^{-\frac{\varphi_a^2}{2}})$. Using the asymptotic expansion (29.7) of [41] for I_0 leads to $e^{-\frac{\varphi_a^2}{2}}e^{-2|\alpha|^2}I_0(2|\alpha|\varphi_a) = e^{-\frac{1}{2}(\varphi_a-2|\alpha|)^2}[1+F(2|\alpha|\varphi_a)]/\sqrt{4\pi|\alpha|\varphi_a}$, with F satisfying $|F(2|\alpha|\varphi_a)| < (16|\alpha|\varphi_a)^{-1}$. Hence, the Hamiltonian $\mathbf{H}^{\text{RWA}}_{\mathscr{M}_{2,\alpha}}$ reads

$$\begin{aligned} \mathbf{H}^{\text{RWA}}_{\mathscr{M}_{2,\alpha}} &= -\frac{\hbar\Omega_a}{2}[|\mathscr{C}^{+}_{\alpha}\rangle\langle\mathscr{C}^{+}_{\alpha}| - |\mathscr{C}^{-}_{\alpha}\rangle\langle\mathscr{C}^{-}_{\alpha}|] + \mathscr{O}(E_J e^{-\frac{\varphi_a^2}{2}}) \\ &= -\frac{\hbar\Omega_a}{2}\boldsymbol{\sigma}^L_z + \mathscr{O}(E_J e^{-\frac{\varphi_a^2}{2}}), \\ \Omega_a &= \frac{E_J}{\hbar}\frac{e^{-\frac{1}{2}(\varphi_a-2|\alpha|)^2}}{\sqrt{\pi|\alpha|\varphi_a}}[1+F(2|\alpha|\varphi_a)]. \end{aligned}$$

Note that in the regime we consider, we typically have $\varphi_a = 2|\alpha| = 4$. It leads to $|F(2|\alpha|\varphi_a)| < 1/64$, so that Ω_a is well approximated by

$$\Omega_a \approx \frac{E_J}{\hbar}\frac{e^{-\frac{1}{2}(\varphi_a-2|\alpha|)^2}}{\sqrt{\pi|\alpha|\varphi_a}}.$$

3.5.1.2 Four-photon process : Derivation of the effective Hamiltonian $\mathbf{H}^{\mathbf{RWA}}_{\mathscr{M}_{4,\alpha}}$

Under four-photon driven dissipation, the state is confined to the manifold $\mathscr{M}_{4,\alpha} = \text{span}\{|\mathscr{C}^{(\text{jmod4})}_{\alpha}\rangle,\ j = 0,1,2,3\}$, and the effective Hamiltonian is given by the projection $\mathbf{H}^{\text{RWA}}_{\mathscr{M}_{4,\alpha}}$ of the physical Hamiltonian $\mathbf{H}_{\text{RWA}}$ on the 4D-manifold $\mathscr{M}_{4,\alpha}$ (first order approximation in $\varepsilon_{\text{zeno}} = E_J/\hbar\kappa_{4\text{ph}}$). Since $\mathbf{H}_{\text{RWA}}$ is diagonal in the Fock states basis, its projection $\mathbf{H}^{\text{RWA}}_{\mathscr{M}_{4,\alpha}}$ is also diagonal in the basis $\{|\mathscr{C}^{(\text{jmod4})}_{\alpha}\rangle\}$ (as the expansion of $|\mathscr{C}^{(\text{jmod4})}_{\alpha}\rangle$ includes only Fock states n such that $n\ mod\ 4 = j$). The diagonal matrix elements

$c_\alpha^{jj} = \langle \mathscr{C}_\alpha^{(\mathrm{jmod4})} | \mathbf{H}_{\mathrm{RWA}} | \mathscr{C}_\alpha^{(\mathrm{jmod4})} \rangle$ read

$$c_\alpha^{jj} = (-1)^{j+1}\frac{\hbar\Omega_a}{2} + \frac{i^j}{2}[\langle i\alpha|\mathbf{H}_{\mathrm{RWA}}|\alpha\rangle + (-1)^j \langle i\alpha|\mathbf{H}_{\mathrm{RWA}}|-\alpha\rangle], \quad j=0,1,2,3$$

In the above expression, the first term comes from the coupling of $|\alpha\rangle$ and $|-\alpha\rangle$, and the coupling of $|i\alpha\rangle$ and $|-i\alpha\rangle$. This corresponds to the desired parity-like term. Note that its amplitude is given by $\hbar\Omega_a/2$, as in the case of $\mathbf{H}^{\mathrm{RWA}}_{\mathscr{M}_{2,\alpha}}$. The second term, resulting from the coupling of the states $|\pm\alpha\rangle$ and $|\pm i\alpha\rangle$ through $\mathbf{H}_{\mathrm{RWA}}$, lifts the degeneracy within the parity subspace. This undesired term can be evaluated, as we have

$$\begin{aligned}\langle i\alpha|\mathbf{H}_{\mathrm{RWA}}|\alpha\rangle &= -E_J e^{-\varphi_a^2-(1+i)|\alpha|^2} I_0(2e^{i\frac{\pi}{4}}|\alpha|\varphi_a)\\ &\approx -E_J e^{-\frac{1}{2}(\varphi_a-\sqrt{2}|\alpha|)^2}\frac{e^{i[-\frac{\pi}{8}+|\alpha|(|\alpha|-\sqrt{2}\varphi_a)]}}{\sqrt{4\pi|\alpha|\varphi_a}},\end{aligned}$$

and $\langle i\alpha|\mathbf{H}_{\mathrm{RWA}}|-\alpha\rangle = (\langle\alpha|\mathbf{H}_{\mathrm{RWA}}|i\alpha\rangle)^\dagger$. Hence, the diagonal matrix elements read

$$\begin{aligned}c_\alpha^{jj} &= -\frac{\hbar\Omega_a}{2} + (-1)^{\frac{j}{2}}\frac{e^{-\frac{1}{2}(\varphi_a-\sqrt{2}|\alpha|)^2}}{\sqrt{4\pi|\alpha|\varphi_a}}\cos\big(|\alpha|(|\alpha|-\sqrt{2}\varphi_a)-\frac{\pi}{8}\big), \quad j=0,2\\ c_\alpha^{jj} &= \frac{\hbar\Omega_a}{2} + (-1)^{\frac{j-1}{2}}\frac{e^{-\frac{1}{2}(\varphi_a-\sqrt{2}|\alpha|)^2}}{\sqrt{4\pi|\alpha|\varphi_a}}\sin\big(|\alpha|(|\alpha|-\sqrt{2}\varphi_a)-\frac{\pi}{8}\big), \quad j=1,3.\end{aligned}$$

Under the condition $\varphi_a = 2|\alpha|$, the second terms scale as $e^{-|(\sqrt{2}-1)\alpha|^2}|\alpha|^{-1}$, and the ratio of the second and the first terms simply scales as $e^{-|(\sqrt{2}-1)\alpha|^2}$. Note that $(\sqrt{2}-1)^2 \approx 0.17$, which explains the necessity to consider larger cat amplitude α to obtain a parity Hamiltonian (see Fig. 3.1d).

3.5.2 Second order Zeno dynamics approximation for two modes under two-photon driven dissipation

In this section, we study the effect of the second order Zeno dynamics approximation for the case of two modes **a** and **b**, both subjected to two-photon driven dissipation and the two mode Hamiltonian $\mathbf{H}_{\mathrm{RWA}}$ given by eq. (3.13), with $\varphi_a \approx 2|\alpha|$ and $\varphi_b \approx 2|\beta|$. While the first order Zeno dynamics approximation in $\varepsilon_{\mathrm{zeno}}$ corresponds to a modification of the Hamiltonian part of the dynamics ($\mathbf{H}_{\mathrm{RWA}}$ acts as a projected Hamiltonian on the manifold $\mathscr{M}_{2,\alpha,\beta}$), the second order correction arises in the form of dissipation channels described by Lindblad operators acting on $\mathscr{M}_{2,\alpha,\beta}$. As the Hamiltonian $\mathbf{H}_{\mathrm{RWA}}$ is diagonal in the Fock state basis, these Lindblad operators are linear combinations of $\mathbf{I}_a \otimes \mathbf{I}_b$, $\boldsymbol{\sigma}_a \otimes \mathbf{I}_b$, $\mathbf{I}_a \otimes \boldsymbol{\sigma}_b$ and $\boldsymbol{\sigma}_a \otimes \boldsymbol{\sigma}_b$. Indeed, the Hamiltonian $\mathbf{H}_{\mathrm{RWA}}$ cannot induce any change of single-mode parities. It, therefore, cannot induce bit-flip type errors on logical qubits. While the correlated phase-flips occuring through the operator $\boldsymbol{\sigma}_a \otimes \boldsymbol{\sigma}_b$ reduce the efficiency of the measurement without affecting the state of the system (see Section 3.3.4), independent phase-flips induced by the operators $\boldsymbol{\sigma}_a \otimes \mathbf{I}_b$ and $\mathbf{I}_a \otimes \boldsymbol{\sigma}_b$ lead to an unwanted dephasing within the parity subspaces. In what follows, we show numerical evidence that the induced dephasing rate γ_{ind} decreases exponentially with the cats amplitudes $|\alpha|$ and $|\beta|$. For simplicity sakes, we set $\alpha = \beta$.

It is useful to note that phase-flips in the basis $\{|\mathscr{C}_\alpha^{\pm}\rangle\}$ corresponds to bit-flips in the basis $\{|\pm\alpha\rangle\}$. Thus, under independent phase-flips, the state $|\alpha,\alpha\rangle$ will evolve towards a mixture of the states $|\alpha,\alpha\rangle$, $|-\alpha,\alpha\rangle$, $|\alpha,-\alpha\rangle$ and $|-\alpha,-\alpha\rangle$, whereas correlated phase-flips will map $|\alpha,\alpha\rangle$ to a mixture of the states $|\alpha,\alpha\rangle$ and $|-\alpha,-\alpha\rangle$. Initializing the two-mode system in the state $|\alpha,\alpha\rangle$ and letting it evolve for a fixed time $T_{\mathrm{2ph}} = (\kappa_{\mathrm{2ph}})^{-1} \gg \gamma_{\mathrm{ind}}^{-1}$, where $\kappa_{\mathrm{2ph}} = \min(\kappa_{\mathrm{2ph}}^a, \kappa_{\mathrm{2ph}}^b)$, the final state population on the manifold $\mathrm{span}\{|-\alpha,\alpha\rangle, |\alpha,-\alpha\rangle\}$ directly yields the quantity $\gamma_{\mathrm{ind}}/\kappa_{\mathrm{2ph}}$. However, simulating the full two-mode master equation for high values of $|\alpha|$, e.g $|\alpha| = 4$, requires important computational resources due to the high dimensionality of the Hilbert space. We propose a different semi-analytical approach to circumvent this difficulty.

The idea is to analytically derive the second order corrective terms acting on the reduced manifold $\mathscr{M}_{2,\alpha,\alpha}$. As stated in [5], these terms take the form of Lindblad operators $\mathbf{C}_{a,\mu}$ and $\mathbf{C}_{b,\mu}$, given by $\mathbf{C}_{j,\mu} = \mathbf{M}_\mu \mathbf{R_j}$, with $\mathbf{R}_j = 2\mathbf{L}_j(\mathbf{L}_a^\dagger \mathbf{L}_a + \mathbf{L}_b^\dagger \mathbf{L}_b)^{-1} \mathbf{H}_{\mathrm{RWA}} \mathbf{\Pi}_{\mathscr{M}_{2,\alpha,\alpha}}$. Here, we have used the operators $\mathbf{L}_a = \sqrt{\kappa_{\mathrm{2ph}}}(\mathbf{a}^2 - \alpha^2)$, $\mathbf{L}_b = \sqrt{\kappa_{\mathrm{2ph}}}(\mathbf{b}^2 - \alpha^2)$, and the projector $\mathbf{\Pi}_{\mathscr{M}_{2,\alpha,\alpha}}$ on the manifold $\mathscr{M}_{2,\alpha,\alpha}$. The inverse operation in $(\mathbf{L}_a^\dagger \mathbf{L}_a + \mathbf{L}_b^\dagger \mathbf{L}_b)^{-1}$ is understood here as the Moore-Penrose pseudo-inverse [63]. Finally, $\{\mathbf{M}_\mu\}$ corresponds to a set of Kraus operators such that, for any initial state ρ, $\mathscr{L}_{2,\alpha,\alpha}(\rho) = \sum_\mu \mathbf{M}_\mu \rho \mathbf{M}_\mu^\dagger$ is the steady state of the system subject to two-photon process. Here, the operator $\mathbf{R}_j$ arises from the part of $\mathbf{H}_{\mathrm{RWA}}$ which differs from the parity operator. Indeed, if $\mathbf{H}_{\mathrm{RWA}}$ were the photon-number parity operator, it would stabilize the manifold $\mathscr{M}_{2,\alpha,\alpha}$, leading to $(\mathbf{L}_a^\dagger \mathbf{L}_a + \mathbf{L}_b^\dagger \mathbf{L}_b)^{-1} \mathbf{H}_{\mathrm{RWA}} \mathbf{\Pi}_{\mathscr{M}_{2,\alpha,\alpha}} = (\mathbf{L}_a^\dagger \mathbf{L}_a + \mathbf{L}_b^\dagger \mathbf{L}_b)^{-1} \mathbf{\Pi}_{\mathscr{M}_{2,\alpha,\alpha}} \mathbf{H}_{\mathrm{RWA}} \mathbf{\Pi}_{\mathscr{M}_{2,\alpha,\alpha}} = 0$ and thus $\mathbf{R}_j = 0$. Note that evaluating the application of the Kraus map $\mathscr{L}_{2,\alpha,\alpha}$ to a state $\boldsymbol{\rho}$ only requires the calculation of the nine quantities $\langle \mathbf{J}_{r1,r2} \rangle_{\boldsymbol{\rho}} = \mathrm{tr}(\boldsymbol{\rho} \mathbf{J}_{r1,r2})$, with $\mathbf{J}_{r1,r2} = \mathbf{J}_{r1} \otimes \mathbf{J}_{r2}$ and $(r1,r2) \in \{(++,++),(++,--),(--,++),(++,+-),(--,+-),(+-,++),(+-,--),(+-,+-),(+-,-+)\}$, and where the single mode operators $\mathbf{J}_{++}$ and $\mathbf{J}_{+-}$ are defined in eq. (1.5)

In the second order Zeno dynamics approximation, the reduced master equation reads

$$\begin{aligned}\frac{d\boldsymbol{\rho}_{\text{2nd}}}{dt} =& -i[\mathbf{H}_{\mathscr{M}_{2,\alpha,\alpha}}/\hbar, \boldsymbol{\rho}_{\text{2nd}}] \\ &+ \sum_{\mu;j=a,b} \mathbf{M}_\mu \mathbf{R_j} \boldsymbol{\rho}_{\text{2nd}} \mathbf{R_j^\dagger} \mathbf{M}_\mu^\dagger - \frac{\mathbf{1}}{\mathbf{2}}(\mathbf{R_j^\dagger} \mathbf{M}_\mu^\dagger \mathbf{M}_\mu \mathbf{R_j} \boldsymbol{\rho}_{\text{2nd}} + \boldsymbol{\rho}_{\text{2nd}} \mathbf{R_j^\dagger} \mathbf{M}_\mu^\dagger \mathbf{M}_\mu \mathbf{R_j}) \\ =& -i[\mathbf{H}_{\mathscr{M}_{2,\alpha,\alpha}}/\hbar, \boldsymbol{\rho}_{\text{2nd}}] + \sum_{j=a,b} \mathscr{L}_{\mathscr{M}_{2,\alpha,\alpha}}(\mathbf{R}_j \boldsymbol{\rho}_{\text{2nd}} \mathbf{R}_j^\dagger) - \frac{1}{2}(\mathbf{R}_j^\dagger \mathbf{R}_j \boldsymbol{\rho}_{\text{2nd}} + \boldsymbol{\rho}_{\text{2nd}} \mathbf{R}_j^\dagger \mathbf{R}_j)\end{aligned}$$

Here, we study the second order correction $\mathscr{R}_{\text{2nd}}(\boldsymbol{\rho}_{\text{2nd}}) = \sum_{j=a,b} \mathscr{L}_{\mathscr{M}_{2,\alpha,\alpha}}(\mathbf{R}_j \boldsymbol{\rho}_{\text{2nd}} \mathbf{R}_j^\dagger) - \frac{1}{2}(\mathbf{R}_j^\dagger \mathbf{R}_j \boldsymbol{\rho}_{\text{2nd}} + \boldsymbol{\rho}_{\text{2nd}} \mathbf{R}_j^\dagger \mathbf{R}_j)$. The rate γ_{ind} is well estimated by

$$\gamma_{\text{ind}} \sim \text{tr}[(|-\alpha,\alpha\rangle\langle-\alpha,\alpha| + |\alpha,-\alpha\rangle\langle\alpha,-\alpha|)\mathscr{R}_{\text{2nd}}(|\alpha,\alpha\rangle\langle\alpha,\alpha|)]. \tag{3.16}$$

In Fig. 3.4, we numerically calculate the above expression for $\varepsilon_{\text{zeno}} = 1$. We clearly observe an exponential suppression of γ_{ind} with the cats amplitude $|\alpha|$.

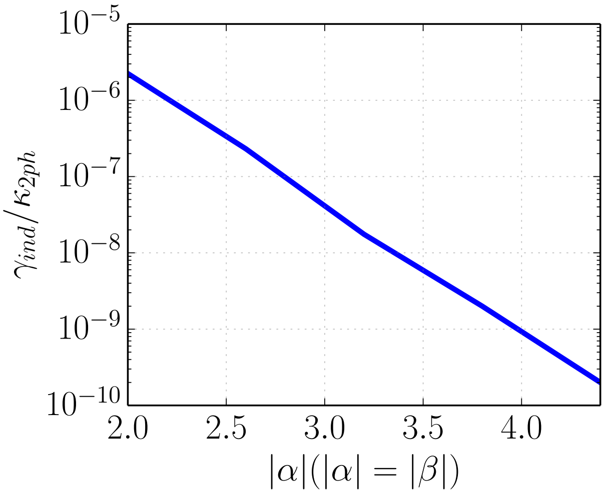

Fig. 3.4 Numerical estimation of undesired dephasing γ_{ind} (see eq. (3.16)) within the two-mode parity subspaces, for $\varepsilon_{\text{zeno}} = 1$. This dephasing rate, induced by second order correction to Zeno dynamics, is exponentially suppressed with $|\alpha|$.

This exponential suppression can be understood through the study of the jump operators $\mathbf{R}_j$. We first focus on a single mode case, where the dissipation part is given $\mathscr{R}_{\text{2nd}}(\boldsymbol{\rho}_{\text{2nd}}) = \mathscr{L}_{\mathscr{M}_{2,\alpha}}(\mathbf{R}\boldsymbol{\rho}_{\text{2nd}}\mathbf{R}^\dagger) - \frac{1}{2}(\mathbf{R}^\dagger\mathbf{R}\boldsymbol{\rho}_{\text{2nd}} + \boldsymbol{\rho}_{\text{2nd}}\mathbf{R}^\dagger\mathbf{R})$, $\mathbf{R} = 2\mathbf{L}_a(\mathbf{L}_a^\dagger\mathbf{L}_a)^{-1}\mathbf{H}_{\text{RWA}}\boldsymbol{\Pi}_{\mathscr{M}_{2,\alpha,\alpha}}$ and $\mathbf{H}_{\text{RWA}}$ is given in eq. (3.11). The state $|\alpha\rangle$ is mapped through a jump to the state $|\psi_R\rangle = \mathbf{R}|\alpha\rangle/||\mathbf{R}|\alpha\rangle||$. The first row of Fig. 3.5 shows the Husimi Q functions $Q(\gamma) = \frac{1}{\pi}|\langle\gamma|\psi_R\rangle|^2$ for $\alpha = 2,3,4,5$. While the states population is concentrated around $|-\alpha\rangle$, it presents a dip precisely at $-\alpha$. This dip simply indicates that the dissipation term arises from the component of $\mathbf{H}_{\rm RWA}$ which differs from the parity Hamiltonian. The Q functions of the projected states $\mathscr{L}_{\mathscr{M}_{2,\alpha}}(|\psi_R\rangle\langle\psi_R|)$, represented in second row of Fig. 3.5, show a quick suppression of the final population on the state $|\alpha\rangle$. This means that the second order Zeno effect only leads to a $\boldsymbol{\sigma}_z$ jump and not a combination of $\mathbf{I}$ and $\boldsymbol{\sigma}_z$. Similarly, in the two-mode case, the jumps are necessarily of the form $\boldsymbol{\sigma}_z^a \otimes \boldsymbol{\sigma}_z^b$.

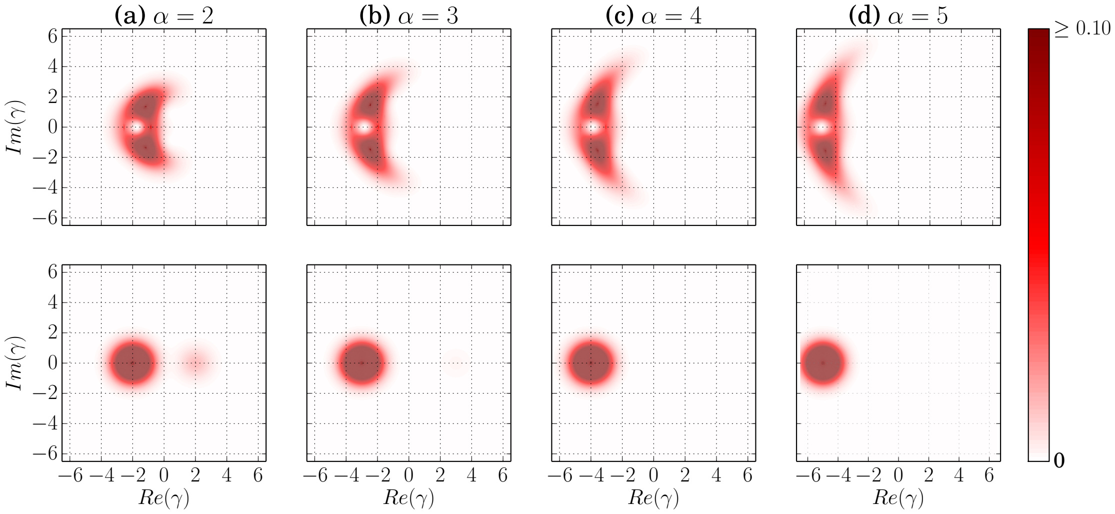

Fig. 3.5 The first row shows the Husimi Q functions $Q(\gamma) = \frac{1}{\pi}|\langle\gamma|\psi_R\rangle|^2$ of the state $|\psi_R\rangle = \mathbf{R}|\alpha\rangle/||\mathbf{R}|\alpha\rangle||$, where $\mathbf{R}$ is the single mode jump operator defined in Section 3.5.2. The different figures correspond to the various values of $\alpha = 2,3,4,5$, from left to right. While the states population is concentrated around $|-\alpha\rangle$, it presents a dip precisely at $-\alpha$. This dip simply indicates that the dissipation term arises from the component of $\mathbf{H}_{\rm RWA}$ which differs from the parity Hamiltonian. For the same values of α, the second row shows the Q functions of the projected states $\mathscr{L}_{\mathscr{M}_{2,\alpha}}(|\psi_R\rangle\langle\psi_R|)$. We observe a rapid suppression of the population on $|\alpha\rangle$ with the amplitude α. As numerically estimated in Fig. 3.4, this suppression is exponential.

3.5.3 Second order Zeno dynamics approximation for a single mode under four-photon driven dissipation

Similarly, in the case of a single mode subjected to four-photon driven dissipation and the single-mode Hamiltonian $\mathbf{H}_{\rm RWA}$ given in eq. (3.11), additional dissipation channels result from the second order Zeno dynamics approximation. More precisely, the associated Lindblad operators, diagonal in the basis $\{|\mathscr{C}_\alpha^{(\text{jmod}4)}\rangle\}$, are linear combinations of the operators

$\mathbf{I}_{\mathscr{M}_{4,\alpha}}$, $\boldsymbol{\pi}_{4\mathrm{ph}}$, $\boldsymbol{\sigma}_Z^{even}$ and $\boldsymbol{\sigma}_Z^{odd}$, with $\boldsymbol{\sigma}_Z^{even} = |\mathscr{C}_\alpha^{(0\mathrm{mod}4)}\rangle\langle\mathscr{C}_\alpha^{(0\mathrm{mod}4)}| - |\mathscr{C}_\alpha^{(2\mathrm{mod}4)}\rangle\langle\mathscr{C}_\alpha^{(2\mathrm{mod}4)}|$ and $\boldsymbol{\sigma}_Z^{odd} = |\mathscr{C}_\alpha^{(3\mathrm{mod}4)}\rangle\langle\mathscr{C}_\alpha^{(3\mathrm{mod}4)}| - |\mathscr{C}_\alpha^{(1\mathrm{mod}4)}\rangle\langle\mathscr{C}_\alpha^{(1\mathrm{mod}4)}|$. The phase flips between states of different parity subspaces, occurring through the operator $\boldsymbol{\pi}_{4\mathrm{ph}}$, only reduces the measurement efficiency. However, the phase flips induced by the operator $\boldsymbol{\sigma}_Z^{even}$ ($\boldsymbol{\sigma}_Z^{odd}$) lead to an undesired dephasing within the even-parity subspace span$\{|\mathscr{C}_\alpha^{(0\mathrm{mod}4)}\rangle, |\mathscr{C}_\alpha^{(2\mathrm{mod}4)}\rangle\}$ (resp. odd-parity subspace span$\{|\mathscr{C}_\alpha^{(3\mathrm{mod}4)}\rangle, |\mathscr{C}_\alpha^{(1\mathrm{mod}4)}\rangle\}$). Here, we numerically prove that these induced dephasing rates $\gamma_{4\mathrm{ph}}^{even/odd}$ decrease exponentially with the cat amplitude $|\alpha|$.

While the focus is on phase flips occurring within the even-parity manifold, a similar analysis holds for the odd-parity manifold. From the definitions $|\mathscr{C}_\alpha^{(0\mathrm{mod}4)}\rangle = \mathscr{N}_0(|\mathscr{C}_\alpha^+\rangle + |\mathscr{C}_{i\alpha}^+\rangle)$ and $|\mathscr{C}_\alpha^{(2\mathrm{mod}4)}\rangle = \mathscr{N}_2(|\mathscr{C}_\alpha^+\rangle - |\mathscr{C}_{i\alpha}^+\rangle)$, we note that phase flips in the basis span$\{|\mathscr{C}_\alpha^{(0\mathrm{mod}4)}\rangle, |\mathscr{C}_\alpha^{(2\mathrm{mod}4)}\rangle\}$ correspond to bit flips in the basis span$\{|\mathscr{C}_\alpha^+\rangle, |\mathscr{C}_{i\alpha}^+\rangle\}$, up to a normalization factor due to the quasi-orthogonality of the coherent states $|\pm\alpha\rangle$ and $|\pm i\alpha\rangle$. Initializing the oscillator in the state $|\mathscr{C}_\alpha^+\rangle$, the dephasing rate $\gamma_{4\mathrm{ph}}^{even}$ corresponds to the population leakage rate from the state $|\mathscr{C}_\alpha^+\rangle$ towards the state $|\mathscr{C}_{i\alpha}^+\rangle$. As in the two-mode case, we estimate $\gamma_{4\mathrm{ph}}^{even}$ by directly evaluating the second order correction. In the second order Zeno dynamics approximation, the master equation of the system becomes

$$\frac{d\boldsymbol{\rho}_{2\mathrm{nd}}}{dt} = -i[\mathbf{H}_{\mathscr{M}_{4,\alpha}}/\hbar, \boldsymbol{\rho}_{2\mathrm{nd}}] + \mathscr{L}_{\mathscr{M}_{4,\alpha}}(\mathbf{R}\boldsymbol{\rho}_{2\mathrm{nd}}\mathbf{R}^\dagger) - \frac{1}{2}(\mathbf{R}^\dagger\mathbf{R}\boldsymbol{\rho}_{2\mathrm{nd}} + \boldsymbol{\rho}_{2\mathrm{nd}}\mathbf{R}^\dagger\mathbf{R}).$$

where $\mathbf{R} = 2\mathbf{L}(\mathbf{L}^\dagger\mathbf{L})^{-1}\mathbf{H}^{\mathrm{RWA}}\boldsymbol{\Pi}_{\mathscr{M}_{4,\alpha}}$ and $\mathbf{L} = \sqrt{\kappa_{4\mathrm{ph}}}(\mathbf{a}^4 - \alpha^4)$. Also, $\mathscr{L}_{4,\alpha}(\rho)$ is the steady state of the system subject to four-photon process when initialized in ρ. We call the second order correction $\mathscr{R}_{2\mathrm{nd}}(\boldsymbol{\rho}_{2\mathrm{nd}}) = \mathscr{L}_{\mathscr{M}_{4,\alpha}}(\mathbf{R}\boldsymbol{\rho}_{2\mathrm{nd}}\mathbf{R}^\dagger) - \frac{1}{2}(\mathbf{R}^\dagger\mathbf{R}\boldsymbol{\rho}_{2\mathrm{nd}} + \boldsymbol{\rho}_{2\mathrm{nd}}\mathbf{R}^\dagger\mathbf{R})$. Following a reasoning similar to that of the previous subsection, an estimation of the rate $\gamma_{4\mathrm{ph}}^{even}$ is

$$\gamma_{4\mathrm{ph}}^{even} \sim \langle\mathscr{C}_{i\alpha}^+|\mathscr{R}_{2\mathrm{nd}}(|\mathscr{C}_\alpha^+\rangle\langle\mathscr{C}_\alpha^+|)|\mathscr{C}_{i\alpha}^+\rangle. \tag{3.17}$$

Using this estimation, Fig. 3.6 shows the behaviour of $\gamma_{4\mathrm{ph}}^{even}$ as a function of $|\alpha|$, for $E_J/(\hbar\kappa_{4\mathrm{ph}}) = 1$. The dephasing rate decays exponentially with the cat amplitude $|\alpha|$. Note that the estimation of the asymptotic state $\mathscr{L}_{\mathscr{M}_{4,\alpha}}(\mathbf{R}|\mathscr{C}_\alpha^+\rangle\langle\mathscr{C}_\alpha^+|\mathbf{R}^\dagger)$ was necessary to evaluate $\gamma_{4\mathrm{ph}}^{even}$. In Subsection 3.5.2, the asymptotic state $\mathscr{L}_{\mathscr{M}_{2,\alpha,\alpha}}(\mathbf{R}|\alpha,\alpha\rangle\langle\alpha,\alpha|\mathbf{R}^\dagger)$ was obtained by calculating several conserved quantities conserved through the two-photon dissipative dynamics, thus avoiding the need for simulating the master equation. To our knowledge, the corresponding conserved quantities under four-photon driven dissipation, have not been derived yet. Here, instead, the asymptotic state $\mathscr{L}_{\mathscr{M}_{4,\alpha}}(\mathbf{R}|\mathscr{C}_\alpha^+\rangle\langle\mathscr{C}_\alpha^+|\mathbf{R}^\dagger)$, was obtained by simulating the following system,

$$\begin{aligned}\frac{d\boldsymbol{\rho}}{dt} &= \mathscr{D}[\mathbf{a}^4-\alpha^4](\boldsymbol{\rho})\\ \boldsymbol{\rho}(0) &= \mathscr{N}\mathbf{R}|\mathscr{C}_\alpha^+\rangle\langle\mathscr{C}_\alpha^+|\mathbf{R}^\dagger, \quad \mathscr{N}=||\mathbf{R}|\mathscr{C}_\alpha^+\rangle||^{-2}.\end{aligned}$$

The simulation stops when the convergence criteria $(1-\mathrm{tr}[\boldsymbol{\Pi}_{\mathscr{M}_{4,\alpha}}\boldsymbol{\rho}])<10^{-3}$ is fulfilled. Note that this criteria is generally reached at $t \ll 1/\kappa_{4\mathrm{ph}}$. This method yields a relative imprecision of 10^{-3} on the value $\gamma_{4\mathrm{ph}}^{even}$.

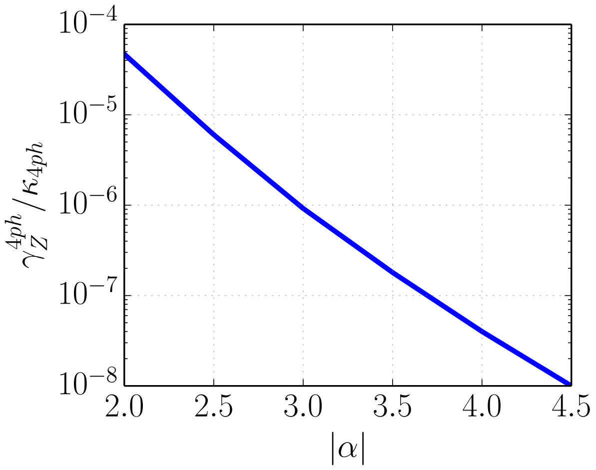

Fig. 3.6 Numerical estimation of undesired dephasing $\gamma_{4\mathrm{ph}}^{even}$ (see eq. (3.17)) within the even-parity subspace span$\{|\mathscr{C}_\alpha^{(0\mathrm{mod}4)}\rangle, |\mathscr{C}_\alpha^{(2\mathrm{mod}4)}\rangle\}$, for $\varepsilon_{\mathrm{zeno}}=1$. This dephasing rate, induced by second order correction to Zeno dynamics, is exponentially suppressed with $|\alpha|$.

Let us provide an intuitive explanation for the exponential suppression of the rate $\gamma_{4\mathrm{ph}}^{even}$, through the study of the jump operator $\mathbf{R}$. This operator maps the state $|\alpha\rangle$ to the state $|\psi_R\rangle = \mathbf{R}|\alpha\rangle/||\mathbf{R}|\alpha\rangle||$. The first row of Fig. 3.7 shows the Husimi Q functions $Q(\gamma)=\frac{1}{\pi}|\langle\gamma|\psi_R\rangle|^2$ for $\alpha = 2,3,4,5$. While the states population is concentrated around $|-\alpha\rangle$, it presents a dip precisely at $-\alpha$. This dip simply indicates that the dissipation term arises from the component of $\mathbf{H}_{\mathrm{RWA}}$ which differs from the parity Hamiltonian. The Q functions of the projected states $\mathscr{L}_{\mathscr{M}_{4,\alpha}}(|\psi_R\rangle\langle\psi_R|)$, represented in the second row of Fig. 3.7, show a quick suppression of the final population on the state $|\alpha\rangle$. We also observe a slower suppression of the final state population on the states $|\pm i\alpha\rangle$, corresponding to a decrease of $\gamma_{4\mathrm{ph}}^{even}$ and $\gamma_{4\mathrm{ph}}^{odd}$.

This means that for large $|\alpha|$, the second order Zeno effect only leads to $\boldsymbol{\pi}_{4\mathrm{ph}}$ jumps instead of combinations of $\mathbf{I}_{\mathscr{M}_{4,\alpha}}$, $\boldsymbol{\pi}_{4\mathrm{ph}}$, $\boldsymbol{\sigma}_Z^{even}$ and $\boldsymbol{\sigma}_Z^{odd}$. The unwanted induced dephasing for small values of $|\alpha|$, is closely related to the non-degeneracy of the Hamiltonian $\mathbf{H}_{\mathscr{M}_{4,\alpha}}^{\mathrm{RWA}}$.

Indeed, these spurious features are both due to unwanted couplings between the states $|\pm\alpha\rangle$ and the states $|\pm i\alpha\rangle$ through the Hamiltonian $\mathbf{H}^{\mathrm{RWA}}$.

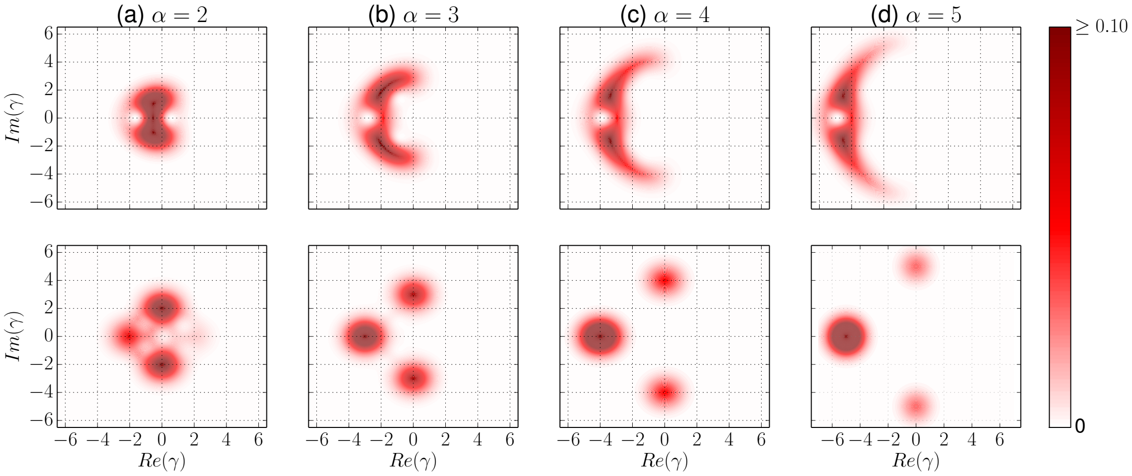

Fig. 3.7 The first row shows the Husimi Q functions $Q(\gamma) = \frac{1}{\pi}|\langle\gamma|\psi_R\rangle|^2$ of the state $|\psi_R\rangle = \mathbf{R}|\alpha\rangle/||\mathbf{R}|\alpha\rangle||$, where $\mathbf{R}$ is the single mode jump operator defined in Section 3.5.3. The different figures correspond to the various values of $\alpha = 2,3,4,5$, from left to right. While the states population is concentrated around $|-\alpha\rangle$, it presents a dip precisely at $-\alpha$. This dip simply indicates that the dissipation term arises from the component of $\mathbf{H}_{\mathrm{RWA}}$ which differs from the parity Hamiltonian. For the same values of α, the second row shows the Q functions of the projected states $\mathscr{L}_{\mathscr{M}_{4,\alpha}}(|\psi_R\rangle\langle\psi_R|)$. We observe a rapid suppression of the population on $|\alpha\rangle$ with the amplitude α, and a slower decay of the population on $|\pm i\alpha\rangle$. As numerically estimated in Fig. 3.6, this suppression is exponential.

3.6 Perfect degeneracy using three junctions

It was pointed out that the projection of the Hamiltonian $\mathbf{H}^{\mathrm{RWA},1}$ on the 4D-subspace $\mathscr{M}_{\alpha,4}$ does not lead to an exact parity Hamiltonian. More precisely, we have $\mathbf{H}^{\mathrm{RWA}}_{\mathscr{M}_{4,\alpha}} \propto \Pi_{\mathscr{M}_{4,\alpha}} \cos(\pi\mathbf{a}^\dagger\mathbf{a})\Pi_{\mathscr{M}_{4,\alpha}} + O(e^{-\xi|\alpha|^2})$. While $\mathbf{H}^{\mathrm{RWA}}_{\mathscr{M}_{4,\alpha}}$ approaches the parity Hamiltonian exponentially with the cat size $|\alpha|^2$, the parity subspace are non-degenerate for small $|\alpha|$ (see Section 3.5.1.2). This non-degeneracy is illustrated in Figure 3.1c. Here, we show that one can make the parity subspace exactly degenerate by capacitively coupling a high impedance cavity mode to three Josephson junctions instead of a single one. Considering the Hamiltonian of such a system, we move to the rotating frame and apply the RWA, leading to

$$\mathbf{H}^{\mathrm{RWA}} = \mathbf{H}^{\mathrm{RWA}}_1 + \mathbf{H}^{\mathrm{RWA}}_2 + \mathbf{H}^{\mathrm{RWA}}_3, \quad \mathbf{H}^{\mathrm{RWA}}_k = -E_{J,k}\sum_n e^{-\frac{\varphi^2_{a,k}}{2}} L_n(\varphi^2_{a,k})|n\rangle\langle n|. \tag{3.18}$$

$E_{J,i}$ is the Josephson energy of junction i, and $\varphi_{a,i} = \sqrt{\pi e^2 Z_{a,i}/h}$ where $Z_{a,i}$ is the impedance of the cavity mode seen by junction i. We define $c_k^{jj} = \langle \mathscr{C}_\alpha^{(j \bmod 4)} | \mathbf{H}_k^{\mathrm{RWA}} | \mathscr{C}_\alpha^{(j \bmod 4)} \rangle$, $j = 0,1,2,3$, and $k = 1,2,3$. We then note $\Delta_k^{0,2} = c_k^{22} - c_k^{00}$ and $\Delta_k^{3,1} = c_k^{11} - c_k^{33}$, $k = 1,2,3$. The parity subspaces are degenerate if one has

$$\begin{aligned} \sum_{k=1,2,3} E_{J,k}\Delta_k^{0,2} &= 0 \\ \sum_{k=1,2,3} E_{J,k}\Delta_k^{3,1} &= 0 \\ E_{J,k} &> 0. \end{aligned} \tag{3.19}$$

We think of the Josephson energies $E_{J,k}$ as the variables of the system as they can be effectively adjusted using SQUID architecture, while the $\phi_{a,k}$ are parameters of the system. The system only needs a rough tuning of the parameters $\phi_{a,k}$. In Fig. 3.8, the red domains indicate the existence of a solution $(E_{J,1}, E_{J,2}, E_{J,3})$ for the above system by as we vary $\phi_{a,2}$ and $\phi_{a,3}$ from $0.5|\alpha|$ to $2.5|\alpha|$, having set $\phi_{a,1} = 2|\alpha|$ and $|\alpha| = 2$. The system requires a rough tuning of $\phi_{a,2}$ and $\phi_{a,3}$ and a fine tuning of the Josephson energies to achieve perfect degeneracy of the parity subspaces.

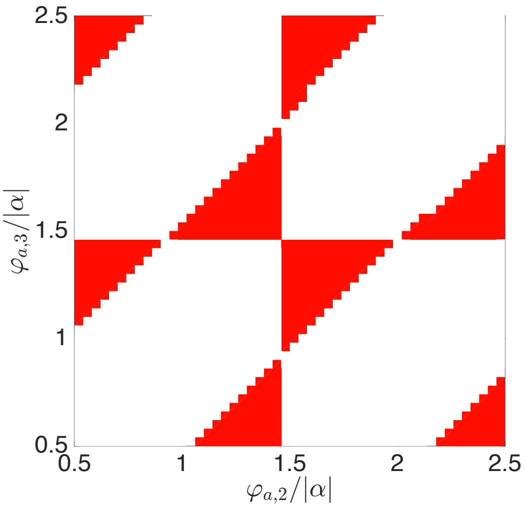

Fig. 3.8 By choosing $\phi_{a,1} = 2|\alpha|$ and $|\alpha| = 2$, we indicate in red the domains of $\phi_{a,2}$ and $\phi_{a,3}$ (in units of $|\alpha|$) for which the Hamiltonian $\mathbf{H}^{\mathrm{RWA}}$, given by 3.18, can potentially act as a perfect parity Hamiltonian on $\mathscr{M}_{4,\alpha}$. More precisely, one can carefully choose the Josephson energies $E_{J,1}$, $E_{J,2}$ and $E_{J,3}$, such that the parity subspaces of $\mathbf{H}^{\mathrm{RWA}}_{\mathscr{M}_{4,\alpha}}$ are degenerate.

3.7 Parity measurement in non-dissipative scheme

While the focus of this chapter is on Zeno dynamics induced by multi-photon driven dissipation, the scheme could also be adapted to non-dissipative cases such as [68]. Indeed, in presence of strong Kerr type non-linearities, the Hamiltonian perturbation due to high-impedance coupling to a Josephson junction results in the creation of a parity Hamiltonian. More precisely, considering a cavity subject to strong self-Kerr effect on which one applies a two-photon drive, the Hamiltonian was shown to satisfy in the interaction picture [68]

$$\mathbf{H}_0 = -\hbar K(\mathbf{a}^{\dagger 2} - \frac{\mathscr{E}_p^*}{K})(\mathbf{a}^2 - \frac{\mathscr{E}_p}{K}). \tag{3.20}$$

Here, K is the self-Kerr coefficient, and $\mathscr{E}_p$ is the two-photon drive strengths. We define $\mathscr{M}_k,\ k \geq 0$ the eigenspaces of $\mathbf{H}_0$ associated to the eigenvalues $\lambda_0 > \cdots > \lambda_k > \cdots$. The eigenspace $\mathscr{M}_0$, associated to $\lambda_0 = 0$, is doubly degenerate and reads $\mathscr{M}_0 = \text{span}\{|\mathscr{C}_\alpha^\pm\rangle\}$, with $\alpha = (\mathscr{E}_p/K)^{\frac{1}{2}}$. Note moreover that, there is a gap of order $4\hbar|\mathscr{E}_p|$ between this eigenvalue and the next one λ_1. Let us add the Hamiltonian term $\mathbf{H}_1 = -E_J e^{-\varphi_a^2/2} \sum L_n(\varphi_a^2)|n\rangle\langle n|$, so that the total Hamiltonian reads $\mathbf{H} = \mathbf{H}_0 + \mathbf{H}_1$. We are interested in the regime where $\mathbf{H}_1$ is a pertubation compared to $\mathbf{H}_0$, i.e $||\mathbf{H}_1|| \ll \hbar|\mathscr{E}_p|$. In this case, $\mathbf{H}_1$ does not induce transitions between $\mathscr{M}_0$ and the other eigenspaces $\mathscr{M}_k,\ k \geq 1$. It, however, lifts the degeneracy of $\mathscr{M}_0$, leading to two non-degenerate eigenstates approximately given by $|\mathscr{C}_\alpha^+\rangle$ and $|\mathscr{C}_\alpha^-\rangle$. This implies that we have achieved an effective $\boldsymbol{\sigma}_z$ Hamiltonian on the logical basis of cat states. Let us provide a numerical illustration by simulating the Schrödinger equation

$$\begin{aligned}\frac{d|\psi\rangle}{dt} &= -i\frac{\mathbf{H}}{\hbar}|\psi\rangle \\ \mathbf{H} &= -\hbar K(\mathbf{a}^{\dagger 2} - \frac{\mathscr{E}_p^*}{K})(\mathbf{a}^2 - \frac{\mathscr{E}_p}{K}) - E_J e^{-\varphi_a^2/2} \sum L_n(\varphi_a^2)|n\rangle\langle n|\end{aligned} \tag{3.21}$$

Here we set $\varphi_a = 2\alpha = 4$. We initialize the system in the state $|\alpha\rangle$, and plot the Wigner functions at different times $(T = 0, \Omega_a^{\text{eff}}/3\pi, \Omega_a^{\text{eff}}/2\pi, \Omega_a^{\text{eff}}/\pi)$ from left to right in Fig. 3.9e-(l). The Rabi frequency Ω_a^{eff} is defined as $\Omega_a^{\text{eff}} = 2\pi/T_R$ with T_R the time needed for a complete Rabi oscillation. The first row illustrates the system evolution for $E_J/\hbar|\mathscr{E}_p| = 0.25$, while the second corresponds to $E_J/\hbar|\mathscr{E}_p| = 12.5$ respectively. In the case $E_J/\hbar|\mathscr{E}_p| = 0.25$, we observe a very neat Rabi oscillation between $|\alpha\rangle$ and $|\alpha\rangle$, which indicates an effective Hamiltonian $-\hbar\Omega_a^{\text{eff}}\boldsymbol{\sigma}_z/2$. For $E_J/\hbar|\mathscr{E}_p| = 12.5$, the system state still ends up in the left half plane, but the final state is distorted, indicating a coupling between $|\pm\alpha\rangle$ with higher energy states of $\mathbf{H}_0$. Note that the effective Rabi frequency Ω_a^{eff} depends on $E_J/\hbar K$, while it converges towards Ω_a for small values of $E_J/\hbar|\mathscr{E}_p|$.

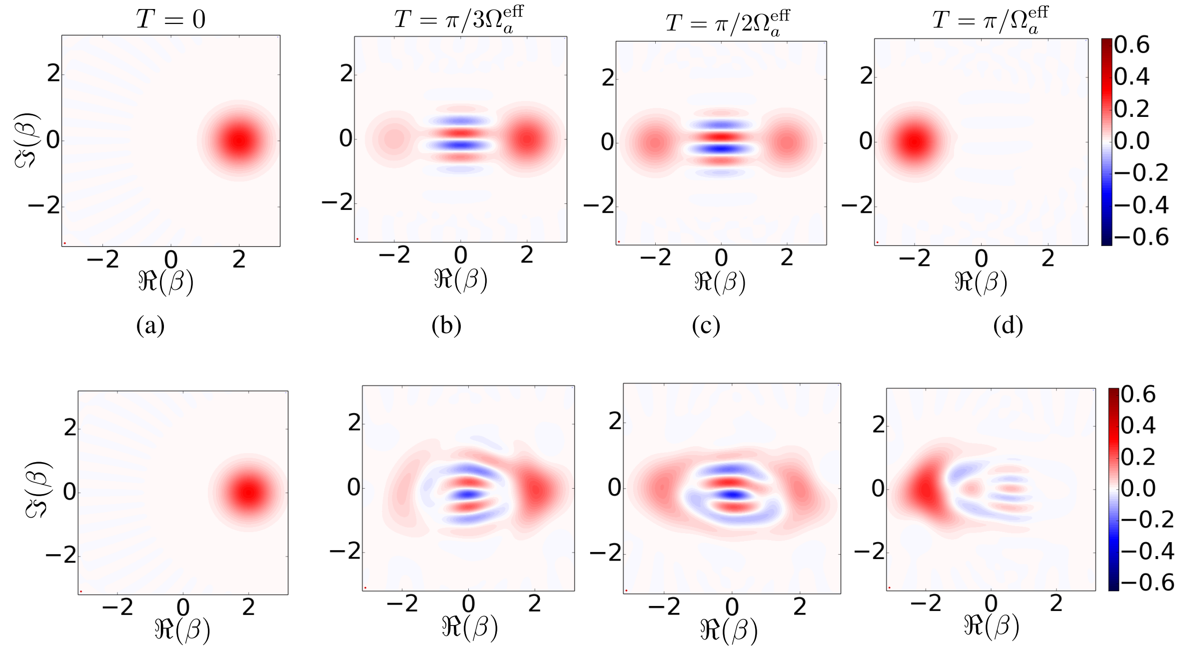

(a) (b) (c) (d)

(e) (f) (g) (h)

Fig. 3.9 (a)-(d) : Simulation of the non-dissipative system (3.21), where the harmonic oscillator is subject to a perturbative Hamiltonian $\mathbf{H}_1 = -E_J e^{-\varphi_a^2/2} \sum L_n(\varphi_a^2)|n\rangle\langle n|$ in the presence of the strong Kerr-type Hamiltonian $\mathbf{H}_0 = -\hbar K(\mathbf{a}^{\dagger 2} - \frac{\mathscr{E}_p^*}{K})(\mathbf{a}^2 - \frac{\mathscr{E}_p}{K})$. The parameters satisfy $\varphi_a = 2\alpha = 4$ and $E_J/\hbar|\mathscr{E}_p| = 0.25$. We initialize the system in $|\alpha\rangle$, and plot the Wigner function of the state at times $T = 0, \Omega_a^{\mathrm{eff}}/3\pi, \Omega_a^{\mathrm{eff}}/2\pi, \Omega_a^{\mathrm{eff}}/\pi$, from left to right. The system undergoes $\pi-$Rabi oscillation between the states $|\alpha\rangle$ and $|-\alpha\rangle$, which demonstrates the presence of an effective Hamiltonian $-\hbar\Omega_a^{\mathrm{eff}}\boldsymbol{\sigma}_z/2$. The frequency Ω_a^{eff} is defined as $\Omega_a^{\mathrm{eff}} = 2\pi/T_R$, where T_R is the time needed for a complete Rabi oscillation. (e)-(h) : Same as first row, with $E_J/\hbar|\mathscr{E}_p| = 12.5$. Although the oscillator is mapped to the left half plane, the final state substantially differs from $|-\alpha\rangle$. This distortion results from the coupling between the states $|\pm\alpha\rangle$ and higher energy states of $\mathbf{H}_0$ through $\mathbf{H}_1$ due to large $E_J/\hbar|\mathscr{E}_p|$.

3.8 Extension : from a $\mathbb{Z}_2$-parity Hamiltonian to a $\mathbb{Z}_n$-parity Hamiltonian

We have focused on obtaining a $\mathbb{Z}_2$-parity Hamiltonian under two-photon (or four-photon) driven dissipation, i.e a physical Hamiltonian $\mathbf{H}$ satisfying $\mathbf{H}_{\mathscr{M}_{2(4),\alpha}} \propto \mathbf{\Pi}_{\mathscr{M}_{2(4),\alpha}} \cos(\pi\mathbf{a}^\dagger\mathbf{a})\mathbf{\Pi}_{\mathscr{M}_{2(4),\alpha}}$. More precisely, under two-photon process, we have designed schemes to measure, in a continuous and QND manner, the observable $\boldsymbol{\sigma}_Z^a = |\mathscr{C}_\alpha^+\rangle\langle\mathscr{C}_\alpha^+| - |\mathscr{C}_\alpha^-\rangle\langle\mathscr{C}_\alpha^-|$ for a single-mode under two-photon process. Under four-photon driven dissipation, we have proposed a measurement scheme for the observable $\boldsymbol{\pi}_{4\mathrm{ph}} = |\mathscr{C}_\alpha^{(0\mathrm{mod}4)}\rangle\langle\mathscr{C}_\alpha^{(0\mathrm{mod}4)}| + |\mathscr{C}_\alpha^{(2\mathrm{mod}4)}\rangle\langle\mathscr{C}_\alpha^{(2\mathrm{mod}4)}| - |\mathscr{C}_\alpha^{(1\mathrm{mod}4)}\rangle\langle\mathscr{C}_\alpha^{(1\mathrm{mod}4)}| - |\mathscr{C}_\alpha^{(3\mathrm{mod}4)}\rangle\langle\mathscr{C}_\alpha^{(3\mathrm{mod}4)}|$. More generally, under the q-photon driven dissipation induced by the Lindblad operator $\sqrt{\kappa_q}(\mathbf{a}^q - \alpha^q)$, the oscillator state is confined to the manifold $\mathscr{M}_{q,\alpha} = \mathrm{span}\{|\alpha e^{\frac{2i\pi p}{q}}\rangle,\ p = 0,...,q-1\}$. Considering the same single mode Hamiltonian $\mathbf{H}^{\mathrm{RWA}}$ given in eq. (3.11), we show that $\mathbf{H}^{\mathrm{RWA}}$ can act as the operator $\cos(\frac{m\pi}{q}\mathbf{a}^\dagger\mathbf{a})$ for an appropriate choice of φ_a. This operator with $0 \leq m \leq q-1$ corresponds to generalized parity-type observables on $\mathscr{M}_{q,\alpha}$.

Let us first define another basis of the manifold $\mathscr{M}_{q,\alpha}$, the set of the q-component cat states $\{|\mathscr{C}_\alpha^{(k \mod q)}\rangle = \frac{1}{\sqrt{q}}\sum_{p=0}^{q-1} e^{-\frac{2ipk\pi}{q}}|\alpha e^{\frac{2ip\pi}{q}}\rangle,\ k = 0,...,q-1\}$ [28]. Note that the expansion of the state $|\mathscr{C}_\alpha^{(k \mod q)}\rangle$ contains only Fock states $|m\rangle$ such that $m \equiv k (\mathrm{mod}\ q)$. With similar arguments used to derive $\mathbf{H}^{\mathrm{RWA}}_{\mathscr{M}_{2(4),\alpha}}$, the single mode Hamiltonian $\mathbf{H}^{\mathrm{RWA}}$ given by eq. (3.11) acts as the projected Hamiltonian on $\mathscr{M}_{q,\alpha}$ and its projection is diagonal in the cat states basis. For any $\varphi_a > 0$, the matrix elements $c^{kk}_{\alpha,q} = \langle\mathscr{C}_\alpha^{(k \mod q)}|\mathbf{H}^{\mathrm{RWA}}|\mathscr{C}_\alpha^{(k \mod q)}\rangle$ read

$$c^{kk}_{\alpha,q} = -\frac{E_J}{\sqrt{4\pi\varphi_a|\alpha|}}\sum_{m=0}^{q-1} e^{-\frac{1}{2}(\varphi_a - 2|\alpha|\sin(\frac{m\pi}{q}))^2}\cos(k\frac{m\pi}{q} + \theta_{m,q}), \tag{3.22}$$

where $\theta_{m,q} = 2|\alpha|\cos(\frac{m\pi}{q})[\varphi_a - |\alpha|\sin(\frac{m\pi}{q})] - \frac{\pi}{4} - \frac{m\pi}{2q}$. Thus, if one sets $\varphi_a = 2|\alpha|\sin(\frac{m_0\pi}{q})$, the matrix elements $c^{kk}_{\alpha,q}$ read

$$c^{kk}_{\alpha,q} = -\frac{E_J}{\sqrt{4\pi\varphi_a|\alpha|}}[\cos(k\frac{m_0\pi}{q} + \theta_{m_0,q}) + \mathscr{O}(e^{-2|\alpha|^2(\sin\frac{(m_0+1)\pi}{q} - \sin\frac{m_0\pi}{q})^2})], \tag{3.23}$$

with $\theta_{m_0,q} = |\alpha^2|\sin(\frac{2m_0\pi}{q}) - \frac{\pi}{4} - \frac{m_0\pi}{2q}$.

In Fig. 3.10a, the matrix elements $c^{kk}_{\alpha,q}$ are represented as a function of φ_a in the case $\alpha = 5$ and $q = 4$ (Fig. 3.10a). Around the values $\varphi_a = 2|\alpha|\sin(\frac{m_0\pi}{4})$, the spectrum exhibits the expected behaviours. For $m_0 = 2$ ($\varphi_a = 2|\alpha|$), the spectrum of the Hamiltonian $\mathbf{H}_{\mathscr{M}_{4,\alpha}}$ consists in two degenerate eigenspaces, grouping the states by their photon number modulo 2. For $m_0 = 1$ ($\varphi_a = \sqrt{2}|\alpha|$), the spectrum of the Hamiltonian $\mathbf{H}_{\mathscr{M}_{4,\alpha}}$ is fully non-degenerate, resulting in a distinction of the states according to their photon number modulo 4. In the case $\alpha = 7$ and $q = 6$ (Fig. 3.10b), the stabilized manifold is generated by the states $|\mathscr{C}_\alpha^{(k \mod 6)}\rangle$, $k = 0,...,5$. Setting the parameter $m_0 = 3$ ($\varphi_a = 2|\alpha|$), $\mathbf{H}_{\mathscr{M}_{4,\alpha}}$ gives a parity Hamiltonian (photon number modulo 2). For $m_0 = 2$ ($\varphi_a = \sqrt{3}|\alpha|$), there are three degenerate eigenspaces representing the states photon number modulo 3. Finally, the case $m_0 = 1$ ($\varphi_a = |\alpha|$) yields a fully non-degenerate Hamiltonian, which allows a spectral distinction of the states indexed by the photon number modulo 6.

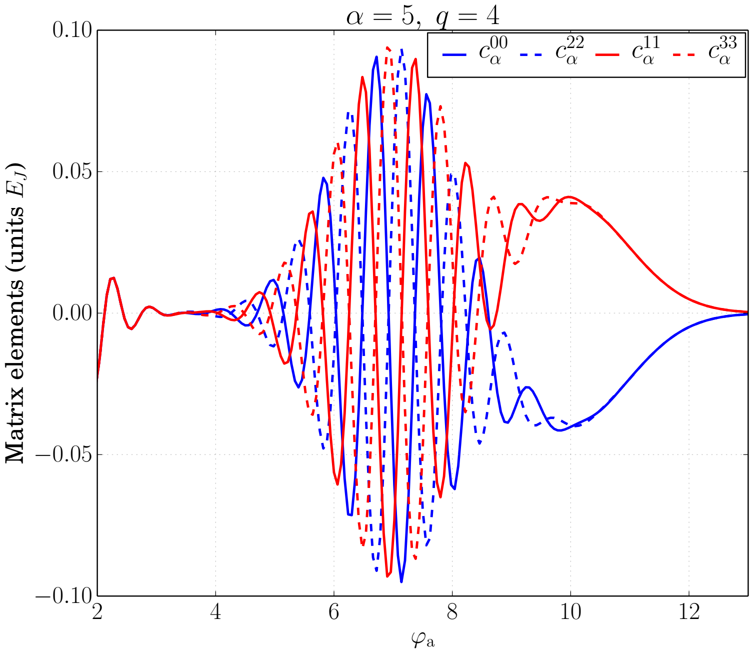
$\alpha = 5,\ q = 4$
c_α^{00}
c_α^{22}
c_α^{11}
c_α^{33}
Matrix elements (units E_J)
0.10
0.05
0.00
−0.05
−0.10
2
4
6
8
10
12
φ_a

(a)

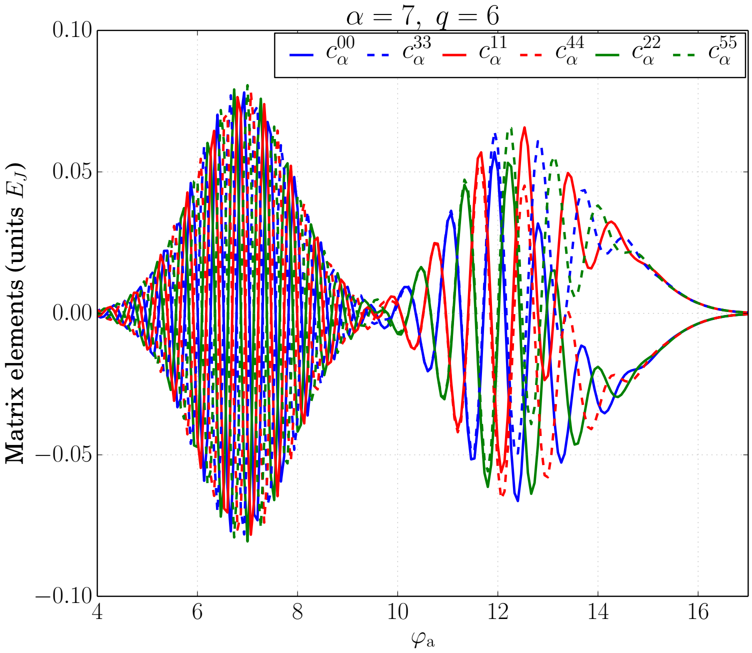
$\alpha = 7,\ q = 6$
c_α^{00}
c_α^{33}
c_α^{11}
c_α^{44}
c_α^{22}
c_α^{55}
Matrix elements (units E_J)
0.10
0.05
0.00
−0.05
−0.10
4
6
8
10
12
14
16
φ_a

(b)

Fig. 3.10 *(previous page)* (a) : Diagonal matrix elements $c^{kk}_{\alpha=5,q=4} = \langle \mathscr{C}^{(k \mod 4)}_{\alpha=5} | \mathbf{H}^{\mathrm{RWA}} | \mathscr{C}^{(k \mod 4)}_{\alpha=5} \rangle$ as given by eq. (3.22), plotted as a function of φ_a. For $\varphi_a \approx 2|\alpha|$ which corresponds to $m_0 = 2$ in eq. (3.23), one has $c^{00}_{\alpha,4} = c^{22}_{\alpha,4} = -c^{11}_{\alpha,4} = -c^{33}_{\alpha,4}$, so that $\mathbf{H}^{\mathrm{RWA}}$ acts as a $\mathbb{Z}_2$-parity Hamiltonian on $\mathscr{M}_{4,\alpha}$. For $\varphi_a \approx \sqrt{2}|\alpha|$ ($m_0 = 1$), the Hamiltonian $\mathbf{H}_{\mathscr{M}_{4,\alpha}}$ is fully non-degenerate for most values of φ_a around $\sqrt{2}|\alpha|$, which allows the measurement of the photon number modulo 4. (b) : Diagonal matrix elements $c^{kk}_{\alpha=7,q=6} = \langle \mathscr{C}^{(k \mod 6)}_{\alpha=7} | \mathbf{H}^{\mathrm{RWA}} | \mathscr{C}^{(k \mod 6)}_{\alpha=7} \rangle$ as given by eq. (3.22), plotted as a function of φ_a. For $\varphi_a \approx 2|\alpha|$ (corresponds to $m_0 = 3$ in eq. (3.23)), $\mathbf{H}^{\mathrm{RWA}}$ acts almost as a $\mathbb{Z}_2$-parity Hamiltonian on $\mathscr{M}_{6,\alpha}$. The degeneracy within the parity subspaces is lifted because of the second term of eq. (3.23). For $\varphi_a \approx \sqrt{3}|\alpha|$ ($m_0 = 2$), one has $c^{00}_{\alpha,6} = c^{33}_{\alpha,6}$, $c^{11}_{\alpha,6} = c^{44}_{\alpha,6}$ and $c^{11}_{\alpha,6} = c^{44}_{\alpha,6}$, meaning that the Hamiltonian distinguish the states according to their photon number modulo 3. For $\varphi_a \approx |\alpha|$ ($m_0 = 1$), the Hamiltonian $\mathbf{H}_{\mathscr{M}_{6,\alpha}}$ is fully non-degenerate except for a discrete set of values of φ_a, and allows the measurement of the photon number modulo 6.

3.9 Summary

We have shown how to achieve continuous quantum non-demolition measurement of three parity-type observables for harmonic oscillators. We focus on the case of multi-photon driven dissipative systems previously introduced for universal quantum computation with cat-qubits [53]. The three observables consist of $\boldsymbol{\sigma}^a_Z = |\mathscr{C}^+_\alpha\rangle\langle\mathscr{C}^+_\alpha| - |\mathscr{C}^-_\alpha\rangle\langle\mathscr{C}^-_\alpha|$ for a single-mode under two-photon process, joint-parity $\boldsymbol{\sigma}^a_Z \otimes \boldsymbol{\sigma}^b_Z$ for two modes under two-photon process, and $\boldsymbol{\pi}_{4\mathrm{ph}} = |\mathscr{C}^{(0\mathrm{mod}4)}_\alpha\rangle\langle\mathscr{C}^{(0\mathrm{mod}4)}_\alpha| + |\mathscr{C}^{(2\mathrm{mod}4)}_\alpha\rangle\langle\mathscr{C}^{(2\mathrm{mod}4)}_\alpha| - |\mathscr{C}^{(1\mathrm{mod}4)}_\alpha\rangle\langle\mathscr{C}^{(1\mathrm{mod}4)}_\alpha| - |\mathscr{C}^{(3\mathrm{mod}4)}_\alpha\rangle\langle\mathscr{C}^{(3\mathrm{mod}4)}_\alpha|$ under four-photon process. The continuous and QND measurement of these observables play a central role towards scalable fault-tolerant architectures for universal quantum computation. We also propose a possible implementation of these measurements through the high-impedance coupling of the cavity mode(s) to a Josephson junction. While the focus of this Chapter is on Zeno dynamics induced by multi-photon driven dissipation, the scheme can be adapted to non-dissipative cases such as [68]. Indeed, in presence of strong Kerr type non-linearities, the Hamiltonian perturbation due to high-impedance coupling to a Josephson junction results in the creation of a parity Hamiltonian.

In the next Chapter, we will see that these measurement schemes can be used to design continous quantum error correction protocols. These protocols, based on the cat code, protect the logical information against dephasing errors and first order single-photon losses.

Chapter 4

Fully protected information using cat qubits

4.1 Introduction

In a recent work [53], Mirrahimi et al. proposed to dynamically confine the state of an oscillator to a degenerate manifold spanned by two or four coherent states. Through this stabilization, a logical qubit, encoded by $|0\rangle_L = |\mathscr{C}_\alpha^+\rangle, |1\rangle_L = |\mathscr{C}_\alpha^-\rangle$ (or $|0\rangle_L = |\mathscr{C}_\alpha^{(0\text{mod}4)}\rangle, |1\rangle_L = |\mathscr{C}_\alpha^{(2\text{mod}4)}\rangle$), is protected against a wide class of dephasing errors. More precisely, in Section 1.2, we have shown that this stabilization suppresses the phase-flip errors exponentially in $|\alpha|^2$. The resulting cat qubits remain susceptible to logical bit-flips only, mainly induced by single-photon losses.

The protection against bit-flips requires the measurement of various photon number parities. Indeed, whether the strategy follows the four-component cat code as in [59] or the three-qubit bit-flip code with two-component cat qubits, the detection of a single-photon loss requires the measurement of either the photon number parity of one mode or the joint photon number parity of two modes. However, the current measurement schemes [82, 91], based on a dispersive coupling of the cavity mode with a transmon through a Hamiltonian of the form $-\hbar\chi|e\rangle\langle e|\mathbf{a}^\dagger\mathbf{a}$, do not work in presence of two (or four)-photon driven dissipation. The multi-photon pumping must be turned off during the measurement, leaving the cat qubit vulnerable to dephasing errors. In addition, the propagating T_1 errors of the transmon used for the syndrome measurement, constitutes an important source of dephasing. In the previous chapter, we have developed a continuous and QND measurement scheme of parity-type observables for multi-photon driven dissipative systems. More precisely, the three observables consist of $\boldsymbol{\sigma}_Z^a = |\mathscr{C}_\alpha^+\rangle\langle\mathscr{C}_\alpha^+| - |\mathscr{C}_\alpha^-\rangle\langle\mathscr{C}_\alpha^-|$ for a single-mode under two-photon process, joint-parity $\boldsymbol{\sigma}_Z^a \otimes \boldsymbol{\sigma}_Z^b$ for two modes under two-photon process, and $\boldsymbol{\pi}_{\rm 4ph} = |\mathscr{C}_\alpha^{(0 \rm mod 4)}\rangle\langle\mathscr{C}_\alpha^{(0 \rm mod 4)}| + |\mathscr{C}_\alpha^{(2 \rm mod 4)}\rangle\langle\mathscr{C}_\alpha^{(2 \rm mod 4)}| - |\mathscr{C}_\alpha^{(1 \rm mod 4)}\rangle\langle\mathscr{C}_\alpha^{(1 \rm mod 4)}| - |\mathscr{C}_\alpha^{(3 \rm mod 4)}\rangle\langle\mathscr{C}_\alpha^{(3 \rm mod 4)}|$ under four-photon process.

In this chapter, by combining the inherent protection against dephasing errors in the presence of multi-photon driven dissipation, and the set of tools developed to measure the qubits $\boldsymbol{\sigma}_Z$-type observables, we propose several schemes that provide a completely protected logical qubit against phase-flips and first order single-photon losses. While Section 4.2 exposes two protocols encoding the information in a single oscillator via the four-component cat code, Section 4.3 presents an adaptation of these protection schemes to the three-qubit bit-flip code, using three two-component cat qubits. These schemes, based on the application of CW drives only, are robust against the variation of small parameters, and require only basic experimental calibration.

4.2 QEC with four-component cat code

In general, the redundancy required by a quantum error correcting code is provided by the use of multiple qubits. It is for example the case of the three-qubit bit-flip code which was considered in Chapter 2. However, one can avoid using multiple modes by exploiting the vastness of the Hilbert space of a single resonator with the four-component cat code. As a reminder, the information is encoded in the 4D-manifold $\mathscr{M}_{4,\alpha} = \text{span}\{\mathscr{C}_\alpha^{(j \rm mod 4)},\ j = 0,1,2,3\}$, such that $|0\rangle_L = |\mathscr{C}_\alpha^{(0 \rm mod 4)}\rangle, |1\rangle_L = |\mathscr{C}_\alpha^{(2 \rm mod 4)}\rangle$. Here, the resonator state is confined to the manifold $\mathscr{M}_{4,\alpha}$ via four-photon driven dissipation, so that the dephasing errors are suppressed, and one deals with a qubit susceptible to errors induced by single-photon losses only. Let us define the even-parity subspace $\mathscr{E}_+ = \text{span}\{|\mathscr{C}_\alpha^{(0 \rm mod 4)}\rangle, |\mathscr{C}_\alpha^{(2 \rm mod 4)}\rangle\}$ and the odd-parity subspace $\mathscr{E}_- = \text{span}\{|\mathscr{C}_\alpha^{(1 \rm mod 4)}\rangle, |\mathscr{C}_\alpha^{(3 \rm mod 4)}\rangle\}$. As one satisfies the property $\mathbf{a}|\mathscr{C}_\alpha^{(j \rm mod 4)}\rangle = \alpha|\mathscr{C}_\alpha^{((j-1) \rm mod 4)}\rangle$, a single-photon loss maps $\mathscr{E}_+$ to $\mathscr{E}_-$, and $\mathscr{E}_-$ to $\mathscr{E}_+$ while preserving the coherence of the superposition. This jump is revealed by a change in the photon number parity, indicating on which subspace ($\mathscr{E}_+$ or $\mathscr{E}_-$) the cat lives. Moreover, two consecutive photon losses represented by the jump operator $\mathbf{a}^2$ induce a bit flip on $\mathscr{E}_+$. This logical bit-flip is detected via two consecutive flips of the photon number parity. Note that four consecutive photon losses act trivially on $\mathscr{E}_\pm$. Hence, by monitoring the evolution of the error syndrome, one can follow the cyclic evolution of the cat state. In Subsection 4.2.1, we propose a protection scheme based on the continuous and quantum non-demolition measurement of the photon number parity developed in Chapter 3. Unlike the experimental work by Ofek et al. [59], which demonstrated an enhancement of the qubit lifetime based on the sequential measurement of the photon number parity, our scheme is compatible with the protection against dephasing errors. Secondly, Subsection 4.2.2 provides an autonomous QEC protocol via reservoir engineering.

4.2.1 Protection of the information via continuous monitoring of the error syndrome

The simple monitoring of the error syndrome is sufficient to prevent single-photon losses from damaging the four-component cat qubit. Rather than using an ancillary transmon for the error syndrome measurement that would require to turn off the four-photon pumping, here the error syndrome is continuously measured in a QND manner. The scheme setup is depicted in Fig. 4.1a, where a high-Q mode, subjected to four-photon driven dissipation, is coupled to an extra off-resonant readout mode. By driving the readout mode at its bare resonance frequency and monitoring the phase/amplitude of the output field, we collect information about the parity state of the resonator (see Subsection 3.3). As a reminder, the effective Hamiltonian of the system (also given in eq. (3.7)) reads

$$\mathbf{H}^{\mathrm{disp}}_{\mathscr{M}_{4,\alpha}} \approx -\frac{\hbar\widetilde{\Omega}_a}{2}\boldsymbol{\pi}_{4\mathrm{ph}} + \frac{\hbar\chi_a}{2}\boldsymbol{\pi}_{4\mathrm{ph}}\mathbf{c}^\dagger\mathbf{c} + \hbar(\varepsilon_c(t)\mathbf{c}^\dagger + \varepsilon_c^*(t)\mathbf{c}).$$

The above Hamiltonian is doubly degenerate on each parity subspace $\mathscr{E}_+$ and $\mathscr{E}_-$. This ensures the QNDness of the syndrome measurement, as no information is leaked about the value of the logical operators $\boldsymbol{\sigma}_Z^{\mathrm{even}} = |\mathscr{C}_\alpha^{(0\mathrm{mod}4)}\rangle\langle\mathscr{C}_\alpha^{(0\mathrm{mod}4)}| - |\mathscr{C}_\alpha^{(2\mathrm{mod}4)}\rangle\langle\mathscr{C}_\alpha^{(2\mathrm{mod}4)}|$ and $\boldsymbol{\sigma}_Z^{\mathrm{odd}} = |\mathscr{C}_\alpha^{(3\mathrm{mod}4)}\rangle\langle\mathscr{C}_\alpha^{(3\mathrm{mod}4)}| - |\mathscr{C}_\alpha^{(1\mathrm{mod}4)}\rangle\langle\mathscr{C}_\alpha^{(1\mathrm{mod}4)}|$. However, the spectrum of the projected Hamiltonian $\mathbf{H}^{\mathrm{disp}}_{\mathscr{M}_{4,\alpha}}$ is non-degenerate for small values of $|\alpha|$, e.g $|\alpha| \sim 2$. To obtain such two-fold degeneracy, one should consider either larger cat amplitude $|\alpha| \gtrsim 5$, or the three-junction circuit exposed in Section 3.6. We provide in table 4.1 a summary of the expected performances of the protocol.

Required timescales	$\kappa_{4\mathrm{ph}} \gg \Omega_a > \chi_a \sim \kappa_c \gg \kappa_a$
Corrected errors	
First order single-photon losses	detection rate $\Gamma_m = \bar{n}_c \chi_a$ i.e $\Gamma_m = \bar{n}_c \phi_c^2 e^{-\frac{\varphi_c^2}{2}} \frac{E_{J,\pi}}{\hbar} \frac{e^{-\frac{1}{2}(\varphi_a - 2\|\alpha\|)^2}}{\sqrt{\pi\|\alpha\|\varphi_a}}$
Failure modes	
Second order photon losses	bit-flip rate $\Gamma_{\mathrm{eff}}^{2nd} = (\|\alpha\|^2 \kappa_a)^2 / 2\Gamma_m$
Second order Zeno dynamics approximation	dephasing rate $\Gamma_{\mathrm{eff}}^{\mathrm{Zeno}} = F(\|\alpha\|) \frac{E_J^2}{\hbar^2 \kappa_{4\mathrm{ph}}}$, where $f(\|\alpha\|) = \mathscr{O}(e^{-c\|\alpha\|}),\ c > 0$

Table 4.1 Performances of the four-component cat QEC scheme realized through the continuous measurement of error syndromes.

4.2.2 Autonomous quantum error correction via reservoir engineering

Instead of actively measuring the error syndromes to keep track of the photon jumps, one can directly build a feedback loop into the system via reservoir engineering to evacuate the entropy created by errors. By coupling the oscillator with a dissipative system, we show that one can shape the spectral density of the environment seen by the oscillator so as to stabilize one of the 2D-parity subspace $\mathscr{E}_\pm$ and ensure a protection against single-photon loss. As dephasing errors are efficiently suppressed through four-photon process, it realizes a completely protected qubit. Moreover, the scheme uses only continuous-wave drives and no output field is monitored.

As the ingredients of this reservoir engineering scheme resemble those of the three-qubit bit-flip correction protocol exposed in Chapter 2, we choose to organize this section in a similar way while often referring to Chapter 2 for details that have already been discussed. We start by giving a description of the physical system, followed by a detailed presentation of the correction scheme. Next, we illustrate and discuss the performances of the scheme through numerical simulations, and we analyze the limitations of this protocol.

4.2.2.1 Physical System

Here, the oscillator **a** encoding the logical qubit is coupled to a dissipative mode **c** through a Josephson junction embedded in a transmission line (Josephson energy E_J). In order to

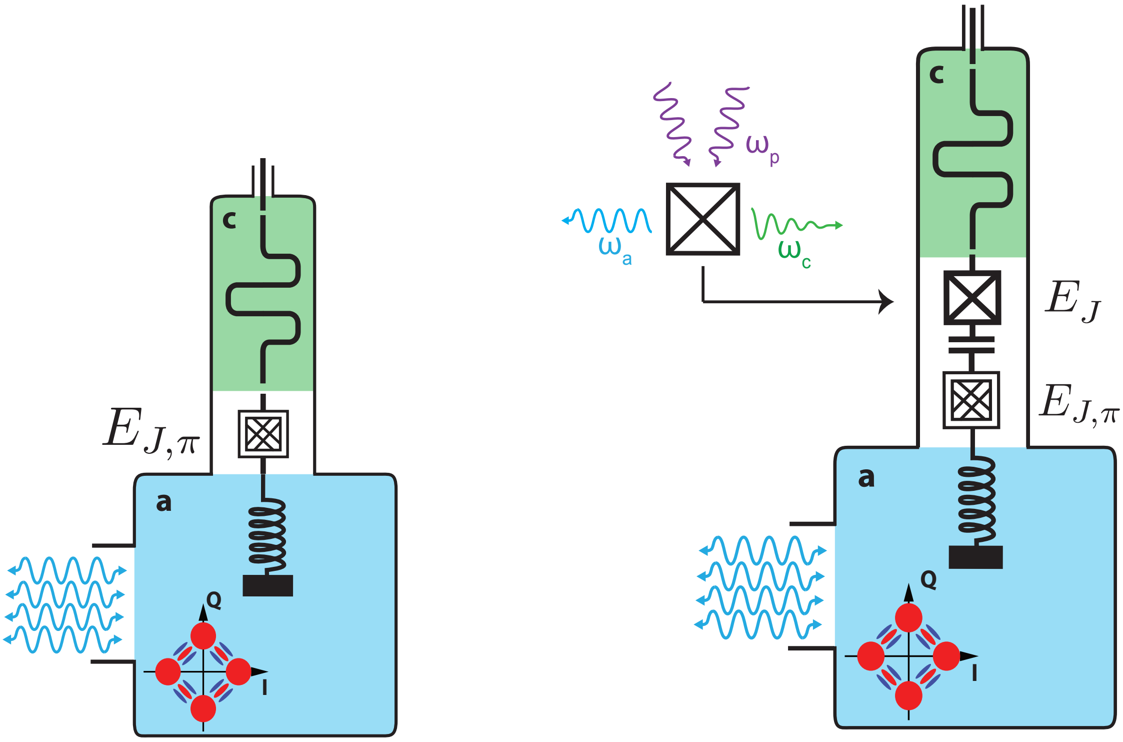

(a) (b)

Fig. 4.1 (a) Possible physical realization of the four-component cat QEC scheme through the continuous monitoring of the oscillator parity state in presence of four-photon driven dissipation. While the four-photon exchange process is realized through one port of the cavity, on the other side the cavity is coupled to a low-Q readout mode **c** through a high-impedance Josephson circuit. (b) Design for an autonomous QEC scheme based on the four-component cat code in presence of four-photon process. The entropy created by eventual photon losses on the cavity mode **a** is evacuated through a dissipative mode **c**. Here, in comparison with the design (a), the low-Q mode **c** is coupled to the high-impedance Josephson circuit via a simple Josephson junction.

create a parity-type Hamiltonian acting on the mode **a**, another high-impedance Josephson circuit is strongly coupled to the mode **a** creating an effective parity type Hamiltonian. A representation of the system is depicted in Fig. 4.1b. By assuming that the junction modes never get excited, one can neglect their contribution to the Hamiltonian. The total

Hamiltonian of the driven system takes the following form [58],

$$\begin{aligned}
\mathbf{H} =& \hbar\tilde{\omega}_a \mathbf{a}^\dagger \mathbf{a} + \hbar\tilde{\omega}_c \mathbf{c}^\dagger \mathbf{c} - E_J\big(\cos(\frac{\mathbf{\Phi}}{\phi_0}) + \frac{1}{2}\frac{\mathbf{\Phi}^2}{\phi_0^2}\big) - E_{J,\pi}\big(\cos(\frac{\mathbf{\Phi}_{\boldsymbol{\pi}}}{\phi_0}) + \frac{1}{2}\frac{\mathbf{\Phi}_{\boldsymbol{\pi}}^2}{\phi_0^2}\big) \\
&+ \hbar\varepsilon^a(t)(\mathbf{a}+\mathbf{a}^\dagger) + \hbar\varepsilon^c(t)(\mathbf{c}+\mathbf{c}^\dagger), \\
\frac{\mathbf{\Phi}}{\phi_0} =& \varphi_a(\mathbf{a}+\mathbf{a}^\dagger) + \varphi_c(\mathbf{c}+\mathbf{c}^\dagger) \\
\frac{\mathbf{\Phi}_{\boldsymbol{\pi}}}{\phi_0} =& \varphi_{a,\pi}(\mathbf{a}+\mathbf{a}^\dagger) + \varphi_{c,\pi}(\mathbf{c}+\mathbf{c}^\dagger)
\end{aligned} \tag{4.1}$$

The dressed frequencies $\tilde{\omega}_a$ and $\tilde{\omega}_c$, are taken to be sufficiently far from each other to avoid resonances between the modes. The terms $\varepsilon^{a(c)}(t)$ denotes some external drives that might be applied to the modes. Similarly to the previous chapter, we consider the high-impedance regime $\varphi_{a,\pi} \approx 2|\alpha|$. Here, the Hamiltonian is a small perturbation relatively to the four-photon driven dissipation acting on mode **a**. Let us move in the interaction frame, rotating at the renormalized mode frequencies (by Lamb and Stark shifts) ω_a and ω_c. If no external drive is applied, the effective interaction Hamiltonian reads (see Section 3.3)

$$\mathbf{H}_{\mathscr{M}_{4,\alpha}}/\hbar = -\frac{\Omega_a}{2}\boldsymbol{\pi}^a_{4ph} + \frac{\chi_a}{2}\boldsymbol{\pi}^a_{4ph}\mathbf{c}^\dagger\mathbf{c}. \tag{4.2}$$

In this expression, we have assumed that the projected Hamiltonian is two-fold degenerate on the parity subspaces $\mathscr{E}_\pm$. While this degeneracy is ensured for large values of $|\alpha|$ (see Section 3.2.2), we show in Subsection 4.2.2.3 that a fine tuning of $|\alpha|$ allows the autonomous scheme to work with smaller $|\alpha| \sim 2$. In this subsection and the next, to facilitate the description of the correction scheme, we consider that the projected Hamiltonian is two-fold degenerate on the parity subspaces and described by $\boldsymbol{\pi}^a_{4ph}$. The two terms of eq. (4.2) arise from the coupling through the high-impedance Josephson circuit, and the expressions of Ω_a and χ_a can be found in eq. (3.7). In particular, we have $\chi_a \ll \Omega_a$. Since we consider the usual regime $\varphi_c, \varphi_{c,\pi} \ll 1$, we have neglected the anharmonic terms induced by the junctions on the mode **c**. The other self-Kerr and cross-Kerr terms of the mode **a** are also neglected, as their effect is suppressed under the four-photon process. Indeed, their projections on the $\mathscr{M}_{4,\alpha}$ act as the identity.

In this correction protocol, we require the timescales of the system to satisfy

$$\kappa_{\text{4ph}} \gg \Omega_a \gg \kappa_c \gg \kappa_a, \tag{4.3}$$

where $\kappa_{a(c)}$ are the dissipation rates of the modes, and κ_{4ph} is the four-photon driven dissipation rate. The condition $\kappa_{\text{4ph}} \gg \Omega_a$ implies that the dynamics of mode **a** is well approximated by its projection on the manifold $\mathscr{M}_{4,\alpha}$ through quantum Zeno dynamics. The timescale inequality $\Omega_a \gg \kappa_c \gg \kappa_a$ leads to well-resolved spectral lines corresponding to each parity-subspaces. More precisely, the linewidths of the system are small enough, so that the total energy strongly depends on the parity states of mode **a**. In this regime, one can selectively address the transitions between the system states. A similar regime was used in the experimental work by Murch et al. [55], to stabilize the states $|\pm\rangle$ of a transmon through an engineered coupling with the environment.

4.2.2.2 Correction scheme

In this subsection, we first give a global picture of the scheme, followed by a more detailed description. Next, we derive a reduced model, providing an expression of the correction rate.

Global picture - Starting from an initial state $c_0|\mathscr{C}_\alpha^{(0\mathrm{mod}4)}\rangle + c_2|\mathscr{C}_\alpha^{(2\mathrm{mod}4)}\rangle \in \mathscr{E}_+$, while the mode **c** is in the vacuum state $|0\rangle_c$, a single-photon loss sends the system to the state $c_0|\mathscr{C}_\alpha^{(3\mathrm{mod}4)}\rangle + c_2|\mathscr{C}_\alpha^{(1\mathrm{mod}4)}\rangle \in \mathscr{E}_-$ (black wavy arrows Fig. 4.2a, Fig.4.2b). Through the application of a pump tone at a well-chosen frequency, we create a resonant interaction term of the form $g\tilde{\mathbf{a}}^\dagger\mathbf{c}^\dagger + h.c$, where $\tilde{\mathbf{a}}^\dagger = \mathbf{\Pi}_{\mathscr{M}_{4,\alpha}}\mathbf{a}^\dagger\mathbf{\Pi}_{\mathscr{M}_{4,\alpha}}$. Unlike the annihilation operator **a** which maps the manifold $\mathscr{M}_{4,\alpha}$ onto itself, the operator $\mathbf{a}^\dagger$ slightly distorts the coherent states $|\pm\alpha\rangle, |\pm i\alpha\rangle$. However, the Zeno dynamics corrects for this dephasing (in phase space) and yields the effective operator $\tilde{\mathbf{a}}^\dagger$. This interaction term induces an effective transition between the states $(c_0|\mathscr{C}_\alpha^{(3\mathrm{mod}4)}\rangle + c_2|\mathscr{C}_\alpha^{(1\mathrm{mod}4)}\rangle)\otimes|0\rangle_c$ and $(c_0|\mathscr{C}_\alpha^{(0\mathrm{mod}4)}\rangle + c_2|\mathscr{C}_\alpha^{(2\mathrm{mod}4)}\rangle)\otimes|1\rangle_c$ (purple straight-line arrows). Because of the spectral signature of the parity state, this transition is turned on only when the system lies in the manifold $\mathscr{E}_-\otimes|0\rangle_c$. The quick decay of the dissipative resonator resets its state to vacuum and projects the mode **a** to the initial state $c_0|\mathscr{C}_\alpha^{(0\mathrm{mod}4)}\rangle + c_2|\mathscr{C}_\alpha^{(2\mathrm{mod}4)}\rangle$ (green wavy arrows). Hence, a single-photon loss is detected and corrected by the injection of a photon. The overall operation on mode **a** is $\mathbf{a}^\dagger\mathbf{a}$, whose projection on the manifold $\mathscr{M}_{4,\alpha}$ acts as the identity.

Detailed construction - The application of a pump tone at frequency $\omega_p = (\omega_a+\omega_c)/2+\Delta$, with $\Delta = -\Omega_a$, leads to an effective interaction Hamiltonian of the form

$$\mathbf{H}_{\mathscr{M}_{4,\alpha}}/\hbar = -\frac{\Omega_a}{2}\boldsymbol{\pi}^a_{4ph} - \Delta\mathbf{c}^\dagger\mathbf{c} + \big(\frac{g}{2}\tilde{\mathbf{a}}^\dagger\mathbf{c}^\dagger + \frac{g^*}{2}\tilde{\mathbf{a}}\mathbf{c}\big). \tag{4.4}$$

In the regime $\Omega_a \gg \kappa_c \gtrsim |g\alpha|$, this engineered Hamiltonian effectively corrects for single-photon losses. The last term of the above equation is achieved through the four-wave mixing property of the junction with Josephson energy E_J. More precisely, two pump photons create, simultaneously, an excitation in both modes **a** and **c** (see interaction diagram of Fig. 4.1b). By setting $\Delta = -\Omega_a$, the pump tone only affects the transition between the subspaces $\mathscr{E}_-\otimes|0\rangle_c$

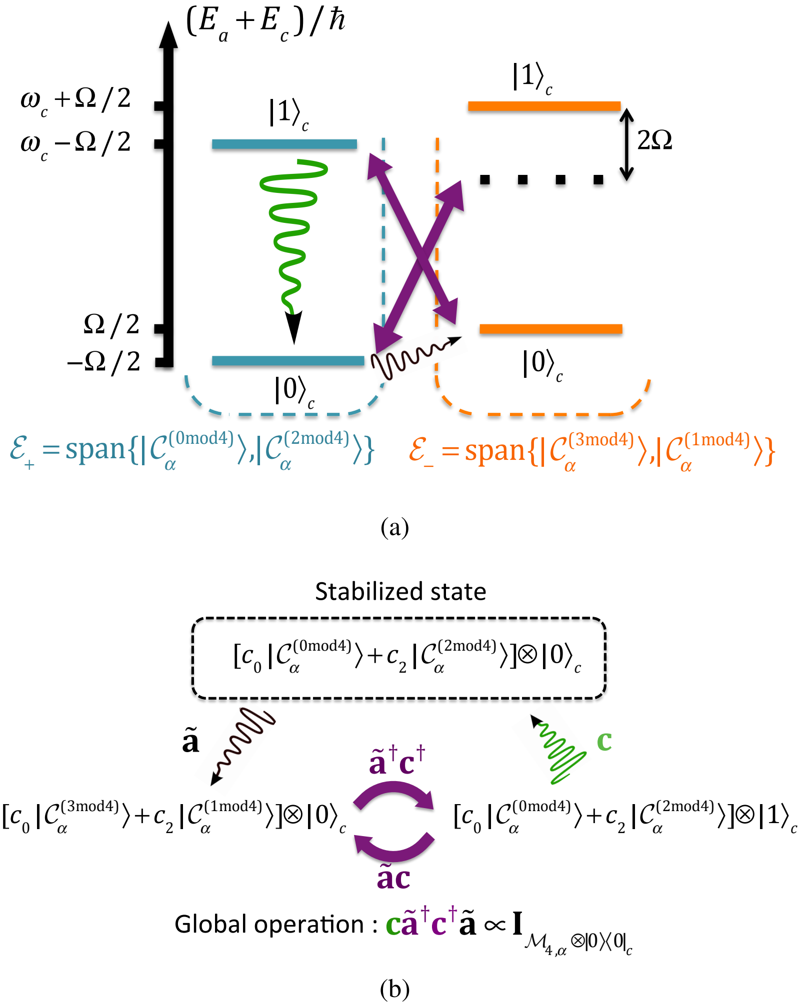

Fig. 4.2 (a): Energy-level diagram of the system in the rotating frame of $\hbar\omega_a\mathbf{a}^\dagger\mathbf{a}$ as a function of the joint-state of the cat qubit and the dissipative mode **c**, illustrating the stabilization of the manifold $\mathscr{E}_+\otimes|0\rangle_c$. As explained in Subsection 4.2.2.2, the mode **c** never gets populated beyond Fock state $|1\rangle_c$, so that one can restrict the energy diagram to the subspace spanned by the Fock states $|0\rangle_c$ and $|1\rangle_c$. The purple straight-line arrows indicate the coupling between two states due to the pump tone at frequency ω_p. The black wavy arrow represents the single-photon dissipation on mode **a**, while the green wavy arrows indicates the photon losses on the ancillary mode **c**. (b): Detailed effect of the error and the correction procedure on an arbitrary initial state in $\mathscr{E}_+$. We used the same symbols as in Fig. 4.2a. The overall operation, i.e error followed by correction, acts trivially on the manifold $\mathscr{M}_{4,\alpha}\otimes|0\rangle_c$

and $\mathscr{E}_+\otimes|1\rangle_c$. Indeed, the transition between the subspaces $\mathscr{E}_+\otimes|0\rangle_c$ and $\mathscr{E}_-\otimes|1\rangle_c$ is detuned by $2\Omega_a\gg\kappa_c$, leaving the subspace $\mathscr{E}_+\otimes|0\rangle_c$ untouched. The dissipation of the ancilla projects the oscillator **a** to the even-parity subspace $\mathscr{E}_+$ and resets the ancilla to its vacuum state, ensuring therefore the irreversibility of the transition from $\mathscr{E}_-$ to $\mathscr{E}_+$. Note that one can also choose to stabilize $\mathscr{E}_-$ by fixing $\Delta = \Omega_a$.

Let us sketch the derivation of the Hamiltonian (4.4). By applying a pump tone at frequency $\omega_p = (\omega_a + \omega_b)/2 + \Delta$, with $\Delta \sim \Omega_a \ll \omega_a, \omega_b$, we obtain the Hamiltonian

$$\mathbf{H}_{\mathscr{M}_{4,\alpha}}/\hbar = -\frac{\Omega_a}{2}\boldsymbol{\pi}^a_{4ph} + (-\Delta + \frac{\chi_a}{2}\boldsymbol{\pi}^a_{4ph})\mathbf{c}^\dagger\mathbf{c} + \big((\frac{g^\pi}{2}\boldsymbol{\pi}^a_{4ph} + \frac{g}{2})\tilde{\mathbf{a}}^\dagger\mathbf{c}^\dagger + h.c\big) \tag{4.5}$$

Here, the coefficients g^π and g read

$$g^\pi = i\frac{\Omega_a\varphi^3_{c,\pi}\varepsilon^{c\,2}_p}{|\alpha|(\omega_c - \omega_p)^2}, \quad g = -\frac{E_J\varphi_a\varphi_c^3\varepsilon^{c\,2}_p}{\hbar(\omega_c - \omega_p)^2},$$

where ε^c_p is the pump amplitude. By setting $\Delta = -\Omega_a + \chi_a/2$, the pump tone resonantly drive the transition between the subspaces $\mathscr{E}_- \otimes |0\rangle_c$ and $\mathscr{E}_+ \otimes |1\rangle_c$. As explained in the description of the scheme, as a result of the strong dissipation rate of mode **c**, the Fock states $|n\rangle_c$ with $n \geq 2$ are never populated. Since a non-zero value of χ_a only weakly affects the detuning $2(\Omega_a - \chi_a/2) \approx 2\Omega_a \gg \kappa_c$ of the off-resonant transition between the subspaces $\mathscr{E}_+ \otimes |0\rangle_c$ and $\mathscr{E}_- \otimes |1\rangle_c$, one can remove the dispersive coupling term $\frac{\hbar\chi_a}{2}\boldsymbol{\pi}^a_{4ph}\mathbf{c}^\dagger\mathbf{c}$ and simply account for the frequency shift $\chi_a/2$ in the value of Δ. This amounts to fixing $\chi_a = 0$, leading to $\Delta = -\Omega_a$.

Note that the interaction strength $\frac{g^\pi}{2}\boldsymbol{\pi}^a_{4ph} + \frac{g}{2}$ depends on the parity state. This non-trivial feature comes from the participation of mode **c** in the flux across the high-impedance Josephson circuit. More precisely, it results from the projection on the manifold $\mathscr{M}_{4,\alpha}$ of the interaction term $iE_{J,\pi}\varphi_c^3(\varepsilon^c_p/(\omega_c - \omega_p)^2)\mathbf{a}^\dagger\mathbf{c}^\dagger\mathbf{A}(1) + h.c$, with $\mathbf{A}(l) = \varphi_a^l e^{-\frac{\varphi_a^2}{2}} \sum\limits_{n_a=0} \frac{n_a!}{(n_a+l)!}L_n^{(l)}(\varphi_a^2)|n_a\rangle\langle n_a|$ (obtained after the rotating-wave approximation). This dependency on the parity state does not affect the performance of the scheme since the system always lies in one of the parity subspace. Indeed, the correction step from $\mathscr{E}_-$ to $\mathscr{E}_+$ occurs through an interaction strength of $\frac{g+g^\pi}{2} = \frac{g^+}{2}$. For simplicity sakes, we set $g^\pi = 0$ in what follows, leading to $g^+ = g$.

After these simplifications, the interaction Hamiltonian takes the form (4.4) with $\Delta = -\Omega_a$.

Effective model - Similarly to Section 2.3.1, an effective correction rate can be derived from a reduced model. Let us move into the rotating frame of $-\frac{\hbar\Omega_a}{2}\boldsymbol{\pi}^a_{4ph} - \Delta\mathbf{c}^\dagger\mathbf{c}$. In the regime $\Omega_a \gg \kappa_c$, the resonance frequencies are well resolved. Hence, for $|g\alpha| < \kappa_c$, one can safely make a RWA and remove the oscillating terms at frequencies of order Ω_a. Moreover, one can also adiabatically eliminate the dissipative mode [12] and obtain the following master equation on the state $\boldsymbol{\rho}$ of mode $\mathbf{a}$

$$\begin{aligned}\frac{d\boldsymbol{\rho}}{dt} &= \Gamma_c \mathscr{D}[\mathbf{r}](\boldsymbol{\rho}) + \kappa_{\mathbf{a}} \mathscr{D}[\mathbf{a}](\boldsymbol{\rho}),\\ \mathbf{r} &= \frac{\tilde{\mathbf{a}}^\dagger}{\alpha^*}\boldsymbol{\Pi}_{\mathscr{E}_-} = |\mathscr{C}_\alpha^{(0\mathrm{mod}4)}\rangle\langle\mathscr{C}_\alpha^{(3\mathrm{mod}4)}| + |\mathscr{C}_\alpha^{(2\mathrm{mod}4)}\rangle\langle\mathscr{C}_\alpha^{(1\mathrm{mod}4)}|,\end{aligned} \tag{4.6}$$

where $\tilde{\mathbf{a}}^\dagger = \boldsymbol{\Pi}_{\mathscr{M}_{4,\alpha}}\mathbf{a}^\dagger\boldsymbol{\Pi}_{\mathscr{M}_{4,\alpha}}$, and $\boldsymbol{\Pi}_{\mathscr{M}_{4,\alpha}}$ ($\boldsymbol{\Pi}_{\mathscr{E}_-}$) is the projector on the subspace $\mathscr{M}_{4,\alpha}$ (resp. $\mathscr{E}_-$). This model reduction provides the following expression for the correction rate, $\Gamma_c \approx |\alpha g|^2/\kappa_c$, valid for $|\alpha g| \ll \kappa_c$.

4.2.2.3 Non-degeneracy within parity subspace : small cat size

In eq. (4.4) we presented the effective Hamiltonian under strong four-photon process, given by the projection of the physical Hamiltonian on the manifold $\mathscr{M}_{4,\alpha}$. However, we wish to simulate the full unprojected system along with the four-photon driven-dissipation in order to account for the decoherence rates that may arise due to these approximations. The simulation of this strongly nonlinear dissipation, represented by the Lindblad operator $\sqrt{\kappa_{\mathrm{4ph}}}(\mathbf{a}^4 - \alpha^4)$, requires a large truncation of the Hilbert space and relatively short time steps (compared to the simulation time of order κ_a^{-1}). For large values of α, this leads to important numerical challenges. We therefore focus on the simulation with smaller values of $|\alpha|$, such as $|\alpha| \sim 2$.

Note however that, for small cat amplitudes $|\alpha| \sim 2$, the projection of the Hamiltonian $\mathbf{H}^{\mathrm{RWA}}(\varphi_{a,\pi})$ on $\mathscr{M}_{4,\alpha}$ is not exactly two-fold degenerate on each parity subspace (see Subsection 3.2.2). As a reminder, $\mathbf{H}^{\mathrm{RWA}}(\varphi_{a,\pi})$ reads

$$\mathbf{H}^{\mathrm{RWA}}(\varphi_{a,\pi}) = -E_{J,\pi} e^{-\varphi_{a,\pi}^2/2} \sum_n L_n(\varphi_{a,\pi}) |n\rangle\langle n|_a \tag{4.7}$$

Indeed, in eq. (4.4), the operator $\boldsymbol{\pi}_{4ph}$ should be replaced with $\boldsymbol{\pi}_{4ph} \to \boldsymbol{\pi}_{4ph} + (\delta^+/\Omega_a)\boldsymbol{\sigma}_Z^{\mathrm{even}} + (\delta^-/\Omega_a)\boldsymbol{\sigma}_Z^{\mathrm{odd}}$. These additional terms can be seen as effective qubit frequencies in each of the parity subspaces. For general values of $\varphi_{a,\pi}$ around $2|\alpha|$, one can have $|\delta^+ - \delta^-| > \kappa_c$, as illustrated on Fig. 4.3a. This degeneracy lift leads to a strong limitation in the correction procedure. Indeed, in this case, the transitions $|\mathscr{C}_\alpha^{(3\mathrm{mod}4)}\rangle \otimes |0\rangle_c \leftrightarrow |\mathscr{C}_\alpha^{(0\mathrm{mod}4)}\rangle \otimes |1\rangle_c$ and $|\mathscr{C}_\alpha^{(1\mathrm{mod}4)}\rangle \otimes |0\rangle_c \leftrightarrow |\mathscr{C}_\alpha^{(2\mathrm{mod}4)}\rangle \otimes |1\rangle_c$ cannot be both resonant as they are energetically different, although both induced by the same interaction term $g\mathbf{a}^\dagger\mathbf{c}^\dagger + g^*\mathbf{ac}$. Here, we show that by carefully choosing the value of $\varphi_{a,\pi}$ around $2|\alpha|$, one can set the two effective qubit frequencies to be the same, i.e $\delta^+ = \delta^-$. This ensures the resonance condition for both transitions. Moreover, the deterministic phase rotations induced by the terms $\delta^+\boldsymbol{\sigma}_Z^{\text{even}} + \delta^-\boldsymbol{\sigma}_Z^{\text{odd}}$, are the same in both parity subspaces, so that no random phase is acquired during the correction procedure.

In Fig. 4.3a, the frequencies δ^+ and δ^- are plotted as a function of $\varphi_{a,\pi}/|\alpha|$ in units of Ω_a, for $\alpha = \sqrt{6}$. We observe that several values of $\varphi_{a,\pi}$ lead to $\delta^+ = \delta^-$, one of which is close to $2|\alpha|$. Alternatively, one can fix $\varphi_{a,\pi}$ and vary $|\alpha|$ around $\varphi_{a,\pi}/2$ to reach $\delta^+ = \delta^-$, as shown in Fig. 4.3b. In the case $\delta^+ = \delta^-$, the spectrum of mode **a** remains non-degenerate on each parity subspace, yielding four distinct energy levels represented on Fig.4.4. Nevertheless, the same pump tone resonantly drives the two transitions $|\mathscr{C}_\alpha^{(3\text{mod}4)}\rangle \rightarrow |\mathscr{C}_\alpha^{(0\text{mod}4)}\rangle$ and $|\mathscr{C}_\alpha^{(1\text{mod}4)}\rangle \rightarrow |\mathscr{C}_\alpha^{(2\text{mod}4)}\rangle$ (solid purple arrows in Fig. 4.4) through the same term $g\tilde{\mathbf{a}}^\dagger\mathbf{c}^\dagger + h.c.$ The emitted photon in mode **c**, whose decay ensures the irreversibility of such transition, does not carry any information on the logical superposition. In practice, one only needs to satisfy $|\delta^+ - \delta^-| \ll \kappa_c$, as κ_c is the spectral width of these transitions. This symmetry condition is very similar to the relation expressed in eq. (2.4) required for the autonomous correction scheme exposed in Chapter 2. In this case, the effective Hamiltonian of eq. (4.4) reads

$$\mathbf{H}_{\mathscr{M}_{4,\alpha}}/\hbar = -\frac{\Omega_a}{2}\boldsymbol{\pi}^a_{4ph} - \frac{\delta}{2}(\boldsymbol{\sigma}_Z^{even} + \boldsymbol{\sigma}_Z^{odd}) - \Delta\mathbf{c}^\dagger\mathbf{c} + \left(\frac{g}{2}\tilde{\mathbf{a}}^\dagger\mathbf{c}^\dagger + \frac{g^*}{2}\tilde{\mathbf{a}}\mathbf{c}\right).$$

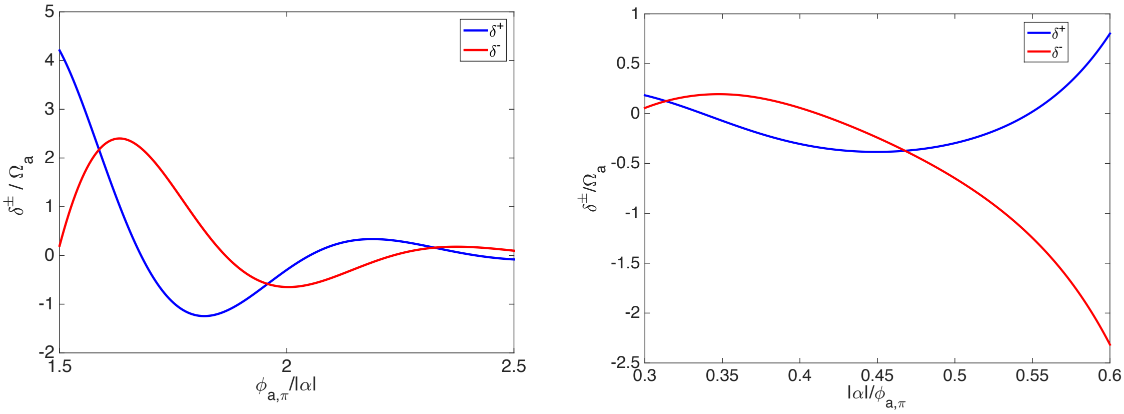

(a)

(b)

Fig. 4.3 (a) Behaviour of the effective qubit frequencies $\delta^\pm$ defined by $\delta^+ = \langle\mathscr{C}_\alpha^{(0\text{mod}4)}|\mathbf{H}^{\text{RWA}}(\varphi_{a,\pi})|\mathscr{C}_\alpha^{(0\text{mod}4)}\rangle - \langle\mathscr{C}_\alpha^{(2\text{mod}4)}|\mathbf{H}^{\text{RWA}}(\varphi_{a,\pi})|\mathscr{C}_\alpha^{(2\text{mod}4)}\rangle$ and $\delta^- = \langle\mathscr{C}_\alpha^{(3\text{mod}4)}|\mathbf{H}^{\text{RWA}}(\varphi_{a,\pi})|\mathscr{C}_\alpha^{(3\text{mod}4)}\rangle - \langle\mathscr{C}_\alpha^{(1\text{mod}4)}|\mathbf{H}^{\text{RWA}}(\varphi_{a,\pi})|\mathscr{C}_\alpha^{(1\text{mod}4)}\rangle$ (see eq. (4.7) for the expression of $\mathbf{H}^{\text{RWA}}(\varphi_{a,\pi})$), as a function of $\varphi_{a,\pi}$. The curves are plotted in units of Ω_a, for $\alpha = \sqrt{6}$. A few specific values of $\varphi_{a,\pi}$ lead to $\delta^+ = \delta^-$. (b) Inversely, $\varphi_{a,\pi}$ is set to $\varphi_{a,\pi} = 2\sqrt{6}$ and plot $\delta^\pm$ as a function of $|\alpha|$, in units of Ω_a. Similarly, the curves cross at a couple of points.

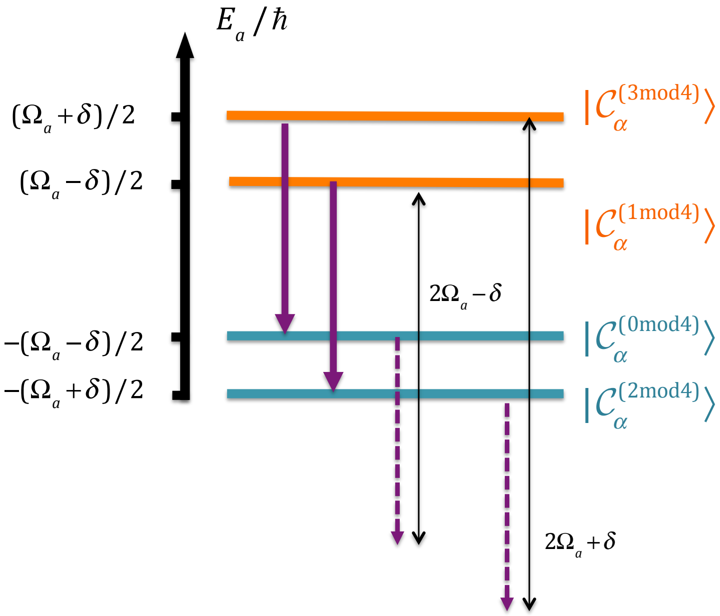

Fig. 4.4 Energy-level diagram of the high-Q mode **a** only (the energy and the states of mode **c** are not represented here), in the non-degenerate case corresponding to small $|\alpha|$, with $\delta^+ = \delta^- = \delta$. Here we represent the four possible transitions $|\mathscr{C}_\alpha^{(j\mathrm{mod}4)}\rangle \rightarrow |\mathscr{C}_\alpha^{((j+1)\mathrm{mod}4)}\rangle$ induced by the term $g\tilde{\mathbf{a}}^\dagger\mathbf{c}^\dagger + h.c$ (one-sided purple arrows of the same length). The irreversibility of these transitions is ensured by the decay of mode **c** (not represented here). The two solid-line arrows indicate the transitions resonantly addressed by the pump, while the dotted-line arrows represent off-resonant transitions whose detuning is quantified and corresponds to the thin black arrows.

4.2.2.4 Numerical simulations

In what follows, we work out the non-degeneracy issue as suggested in Subsection 4.2.2.3 by using the working value of $\varphi_{a,\pi}$ which is close to $2.4|\alpha|$. The master equation reads

$$\begin{aligned}\frac{d\boldsymbol{\rho}}{dt} &= -\frac{i}{\hbar}[\mathbf{H},\boldsymbol{\rho}] + \kappa_{4\mathrm{ph}}\mathscr{D}[\mathbf{a}^4-\alpha^4](\boldsymbol{\rho}) + \kappa_a\mathscr{D}[\mathbf{a}](\boldsymbol{\rho}) + \kappa_c\mathscr{D}[\mathbf{c}](\boldsymbol{\rho}),\\ \mathbf{H} &= \mathbf{H}^{\mathrm{RWA}}(\varphi_{a,\pi}) - \hbar\Delta\mathbf{c}^\dagger\mathbf{c} + \Big(\frac{\hbar g}{2}\mathbf{a}^\dagger\mathbf{c}^\dagger + h.c\Big),\end{aligned} \tag{4.9}$$

where $\mathbf{H}^{\text{RWA}}(\varphi_{a,\pi})$ and Δ read

$$\begin{aligned}\mathbf{H}^{\text{RWA}}(\varphi_{a,\pi}) &= -E_{J,\pi}e^{-\frac{\varphi_{a,\pi}^2}{2}}\sum_n L_n(\varphi_{a,\pi})|n\rangle\langle n|_a \\ \Delta = -\Omega_a &= \langle\mathscr{C}_\alpha^{(0\text{mod}4)}|\mathbf{H}^{\text{RWA}}/\hbar|\mathscr{C}_\alpha^{(0\text{mod}4)}\rangle - \langle\mathscr{C}_\alpha^{(3\text{mod}4)}|\mathbf{H}^{\text{RWA}}/\hbar|\mathscr{C}_\alpha^{(3\text{mod}4)}\rangle \\ &= \langle\mathscr{C}_\alpha^{(2\text{mod}4)}|\mathbf{H}^{\text{RWA}}/\hbar|\mathscr{C}_\alpha^{(2\text{mod}4)}\rangle - \langle\mathscr{C}_\alpha^{(1\text{mod}4)}|\mathbf{H}^{\text{RWA}}/\hbar|\mathscr{C}_\alpha^{(1\text{mod}4)}\rangle\end{aligned}$$

The system is simulated in the regime $\kappa_{4\text{ph}} > E_{J,\pi}/\hbar \gg \kappa_c \gg \kappa_a$, and the correction performances of the scheme are illustrated in Figs. 4.5a and 4.5b, for $\alpha = 2.4$. In both simulations, we look at the various fidelities in the frame rotating at the effective qubit frequencies, defined by the Hamiltonian $\mathbf{H}_R/\hbar = \delta(\boldsymbol{\sigma}_Z^{\text{even}} + \boldsymbol{\sigma}_Z^{\text{odd}})/2$.

In Fig. 4.5a, we initialize the oscillator in a corrupted state $(|\mathscr{C}_\alpha^{(3\text{mod}4)}\rangle - i|\mathscr{C}_\alpha^{(1\text{mod}4)}\rangle)/\sqrt{2} \in \mathscr{E}_-$ and the ancilla in the vacuum state, while neglecting further single-photon losses on mode $\mathbf{a}$ ($\kappa_a = 0$). We simulate the evolution of the system before and after the model reduction, corresponding respectively to the master equations (4.9) and (4.6). The curves represent the time evolution of the fidelity $F(t) = \langle\psi_0|\boldsymbol{\rho}_a|\psi_0\rangle$ with respect to the state $|\psi_0\rangle = (|\mathscr{C}_\alpha^{(0\text{mod}4)}\rangle - i|\mathscr{C}_\alpha^{(2\text{mod}4)}\rangle)/\sqrt{2} \in \mathscr{E}_+$. For the case before the model reduction, in our definition of the fidelity, we discard the state of the ancilla by taking the partial trace with respect to the mode $\mathbf{c}$, $\rho_a = \text{Tr}_c(\rho)$. In both cases, the oscillator recovers the state $|\psi_0\rangle$ in a time of order $1/\Gamma_c$. However the correction rates of the two curves differ by a small factor. We attribute this difference to the saturation of the correction rate, as we have set a high value $|g\alpha| = 0.8\kappa_c$, whereas the approximation $\Gamma_c \approx |\alpha g|^2/\kappa_c$ holds for $|g\alpha| \ll \kappa_c$. Besides, the asymptotic value of the fidelity for the system before model reduction appears to be less than unity. The reasons for this limitation, necessarily induced by the correction protocol itself as we have set $\kappa_a = 0$, are analyzed in Subsection 4.2.2.5.

Next, we include the dissipation of mode $\mathbf{a}$, simulating the full master equation (4.9). We initialize the system in the even-parity state $(|\mathscr{C}_\alpha^{(0\text{mod}4)}\rangle - i|\mathscr{C}_\alpha^{(2\text{mod}4)}\rangle) \otimes |0\rangle_c/\sqrt{2}$, and plot the fidelity to the initial state as a function of time in Fig. 4.5b. Here, while sweeping the values of the ratio κ_c/κ_a, the ratios $E_{J,\pi}/\hbar\kappa_c = 12$ and $\hbar\kappa_{4\text{ph}}/E_{J,\pi} = 5$ are kept constant. For comparison, the dashed-line illustrates the fidelity of an uncorrected system. At small timescale, we observe a quick decay due to the finite correction time of the procedure. This characteristic effect of continuous QEC, was already encountered in Chapter 2, Subsection 2.3.3. At longer timescales, the curves show a gentler slope, indicating an enhancement of the qubit lifetime. This reduced slope eventually gets saturated because of other sources of decoherence induced by the protocol, whose strengths are proportional to the constant ratios $E_{J,\pi}/\hbar\kappa_c$ and $\hbar\kappa_{4\text{ph}}/E_{J,\pi}$, and do not depend on κ_c/κ_a (see next Subsection).

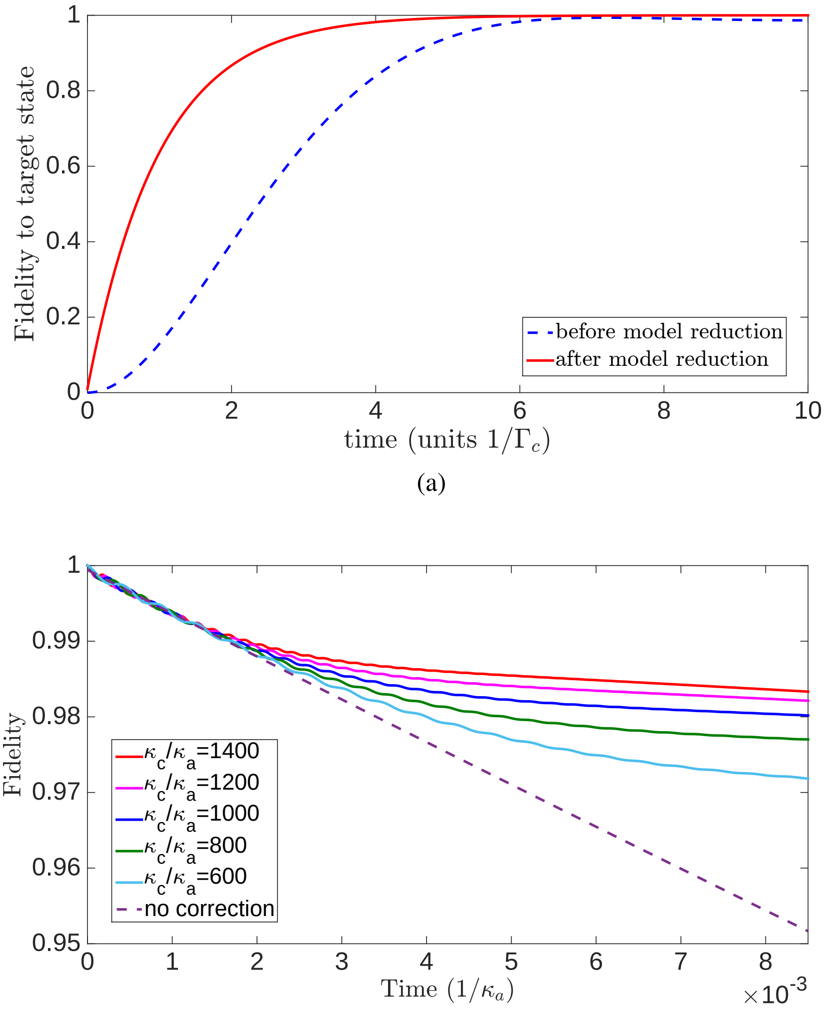

(a)

(b)

Fig. 4.5 (a): Correction performance of the scheme when the system is initialized in a corrupted state $(\mathbf{a}|\psi_0\rangle/||\mathbf{a}|\psi_0\rangle||) \in \mathscr{E}_-$, with $|\psi_0\rangle = (|\mathscr{C}_\alpha^{(0\text{mod}4)}\rangle - i|\mathscr{C}_\alpha^{(2\text{mod}4)}\rangle)/\sqrt{2} \in \mathscr{E}_+$, and further photon losses on mode **a** are neglected ($\kappa_a = 0$). The blue dashed-line corresponds the evolution of the fidelity $\langle\psi_0|\boldsymbol{\rho}_a(t)|\psi_0\rangle$ for the system before the elimination of mode **c**, and was obtained using the full master equation (4.9). The red solid line shows the behaviour of the fidelity in the case of the reduced system ruled by the master equation Eq. (4.6). The parameters of the simulation are set to $\alpha = 2.4$, $|\alpha g| = 0.75\kappa_c$, $\kappa_{4\text{ph}} \approx 20\kappa_c$, $E_{J,\pi} = 10\kappa_c$, leading to the definition $\Gamma_c = 0.56\kappa_c$. (b): Simulation of the model (4.9) when the system is initialized in the state $|\psi_0\rangle = (|\mathscr{C}_\alpha^{(0\text{mod}4)}\rangle - i|\mathscr{C}_\alpha^{(2\text{mod}4)}\rangle)/\sqrt{2} \in \mathscr{E}_+$. The evolution of the fidelity $F(t) = \langle\psi_0|\boldsymbol{\rho}_a(t)|\psi_0\rangle$ is plotted for different values of the ratio κ_c/κ_a, while the ratios $E_{J,\pi}/\kappa_c = 12$ and $\kappa_{4\text{ph}}/E_{J,\pi} = 5$ are kept constant. The other parameters are fixed to $\alpha = 2.4$, $|\alpha g| = 0.8\kappa_c$. The curves show an improvement of the qubit lifetime with the ratio κ_c/κ_a, in comparison with the uncorrected system (dotted-line).

4.2.2.5 Limitations of the scheme

We will first start by showing numerically that the scheme stabilizes the coding subspace $\mathscr{E}_+$ and next, we will study the effective decoherence channels inside this manifold. We simulate the system obtained by projecting the master equation (4.9) on the manifold $\mathscr{M}_{4,\alpha}$

$$\begin{aligned} \frac{d\boldsymbol{\rho}}{dt} &= -\frac{i}{\hbar}[\mathbf{H}_{\mathscr{M}_{4,\alpha}},\boldsymbol{\rho}] + \kappa_a \mathscr{D}[\mathbf{a}](\boldsymbol{\rho}) + \kappa_c \mathscr{D}[\mathbf{c}](\boldsymbol{\rho}), \\ \mathbf{H}_{\mathscr{M}_{4,\alpha}} &= \boldsymbol{\Pi}_{\mathscr{M}_{4,\alpha}}[\mathbf{H}^{\mathrm{RWA}}(\varphi_{a,\pi}) - \hbar\Delta \mathbf{c}^\dagger \mathbf{c} + \big(\frac{\hbar g}{2}\mathbf{a}^\dagger \mathbf{c}^\dagger + h.c\big)]\boldsymbol{\Pi}_{\mathscr{M}_{4,\alpha}}. \end{aligned} \tag{4.10}$$

This corresponds to the first order Zeno dynamics approximation. The system is initialized in $(|\mathscr{C}_\alpha^{(0\mathrm{mod}4)}\rangle - i|\mathscr{C}_\alpha^{(2\mathrm{mod}4)}\rangle)\otimes|0\rangle_c/\sqrt{2}\in\mathscr{E}_+$. In Fig. 4.6, we plot the population on the even-parity subspace $\mathscr{E}_+$ as a function of time, while sweeping the values of the ratio $E_{J,\pi}/\hbar\kappa_c$ or equivalently Ω_a/κ_c. The population on $\mathscr{E}_+$ quickly converges to its asymptotic value. Increasing the ratio Ω_a/κ_c, these asymptotic values saturate to an upper bound approximately given by $1-2|\alpha|^2\kappa_a/\kappa_c$. This behaviour, due to the finite correction time, indicates that a fraction $2|\alpha|^2\kappa_a/\kappa_c$ of the state population is not still corrected. Although the first order Zeno approximation was applied, we would still observe a stabilization of the subspace $\mathscr{E}_+$ with a simulation of the full master equation (4.9). Indeed, since the Hamiltonian $\mathbf{H}^{\mathrm{RWA}}(\varphi_{a,\pi})$ commutes with the photon number operator $\mathbf{a}^\dagger\mathbf{a}$, it does not induce any change of the parity state.

Even though we have shown that the scheme stabilizes the parity subspace $\mathscr{E}_+$, it does not mean that the coherent superpositions between the logical states $|\mathscr{C}_\alpha^{(0\mathrm{mod}4)}\rangle$ and $|\mathscr{C}_\alpha^{(2\mathrm{mod}4)}\rangle$ are preserved. Here, we expose the effective decoherence channels within the 2D-manifold $\mathscr{E}_+$. As emphasized in the previous subsections, the timescales should satisfy $\kappa_{4\mathrm{ph}}\gg\Omega_a\gg\kappa_c\gg\kappa_a$. This regime consists of three inequalities, $\kappa_{4\mathrm{ph}}\gg\Omega_a$, $\Omega_a\gg\kappa_c$, and $\kappa_c\gg\kappa_a$, and each of the finite ratios $\Omega_a/\kappa_{4\mathrm{ph}}$, κ_c/Ω_a and κ_a/κ_c, is a source of decoherence. Note that the parameter g does not appear here. We fix the ratio $|\alpha g|/\kappa_c = 0.75$, so that the correction rate Γ_c saturates to $\Gamma_c\approx\kappa_c/2$. Another remark concerning Ω_a, is that the ratio $\hbar\Omega_a/E_{J,\pi}$, given by eq. (3.4), depends on $\varphi_{a,\pi}$ and $|\alpha|$ only. More precisely, $\varphi_{a,\pi}\approx 2|\alpha|$ leads to $\hbar\Omega_a/E_{J,\pi}\approx(|\alpha|\sqrt{2\pi})^{-1}$. In the following analysis, we use alternatively $E_{J,\pi}/\hbar$ or Ω_a.

Second-order errors - First, two single-photon losses occurring within a time window smaller than the inverse of the correction rate Γ_c^{-1}, are not seen by the correction protocol, and result in a logical bit-flip error. This yields a decoherence rate

$$\Gamma_{\mathrm{eff}}^{2nd} = (|\alpha|^2\kappa_a)^2/\Gamma_c. \tag{4.11}$$

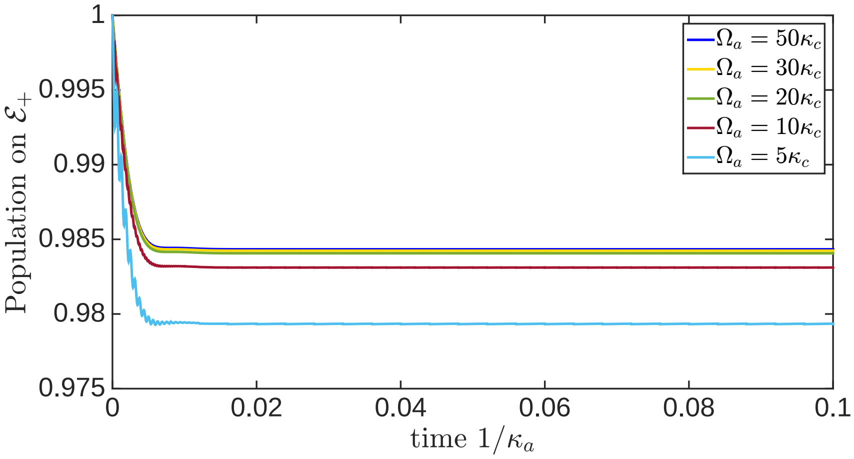

Fig. 4.6 Stabilization of the even-parity manifold $\mathscr{E}_+$ through the QEC scheme modeled by the master equation (4.10). The system is initialized in the state $(|\mathscr{C}_\alpha^{(0\text{mod}4)}\rangle - i|\mathscr{C}_\alpha^{(2\text{mod}4)}\rangle)/\sqrt{2}$, and the evolution of the population on the subspace $\mathscr{E}_+$ are plotted for various values of the ratio Ω_a/κ_c. The asymptotic values of the populations are bounded by approximately $1-2|\alpha|^2\kappa_a/\kappa_c$. The parameters of the simulation are $\alpha = 2.4$ and $\kappa_a/\kappa_c = 10^{-3}$.

The value $|g\alpha|/\kappa_c = 0.75$ gives $\Gamma_{\text{eff}}^{2nd} \approx 2(|\alpha|^2\kappa_a)^2/\kappa_c$.

Imperfect manifold selectivity - Similarly to the AQEC scheme of Chapter 2, where the pumps were required to leave the correct subspace span$\{|000\rangle, |111\rangle\} \otimes |0\rangle_c$ untouched, here we need to avoid any coupling between the subspaces $\mathscr{E}_+ \otimes |0\rangle_c$ and $\mathscr{E}_- \otimes |1\rangle_c$. However, due to the finite ratio Ω_a/κ_c, a fraction of the population on $\mathscr{E}_+ \otimes |0\rangle_c$ is sent to $\mathscr{E}_- \otimes |1\rangle_c$ through the addition of a photon in both modes (operator $\mathbf{a}^\dagger\mathbf{c}^\dagger$). The dissipation on mode $\mathbf{c}$ eventually projects the system on the subspace $\mathscr{E}_- \otimes \{|0\rangle_c\}$. In response, the autonomous correction procedure maps the system to $\mathscr{E}_+ \otimes \{|0\rangle_c\}$ via the insertion of a photon on mode $\mathbf{a}$. The overall operation on mode $\mathbf{a}$, given by $\tilde{\mathbf{a}}^{\dagger 2} = (\mathbf{\Pi}_{\mathscr{M}_{4,\alpha}}\mathbf{a}^\dagger\mathbf{\Pi}_{\mathscr{M}_{4,\alpha}})^2$, is a logical bit-flip. The induced decoherence rate $\Gamma_{\text{eff}}^{\text{select}}$ is given by

$$\Gamma_{\text{eff}}^{\text{select}} = \frac{|\alpha g|^2}{4\Omega_a^2 + \kappa_c^2}\kappa_c. \tag{4.12}$$

Fig. 4.7a corresponds to the same simulation studied in Fig. 4.6 (master equation Eq. (4.10)), but shows the fidelity to the initial state $(|\mathscr{C}_\alpha^{(0\text{mod}4)}\rangle - i|\mathscr{C}_\alpha^{(2\text{mod}4)}\rangle) \otimes |0\rangle_c/\sqrt{2}$ instead of the population on the even-parity manifold. Since master equation (4.10) is obtained in the first order Zeno dynamics approximation, the decoherence due to second order Zeno dynamics approximation is out of the picture (see paragraph below). In the absence of second order Zeno dynamics correction, we expect the effective decay rate of the fidelity to be given by $\Gamma_{\text{eff}}^{\text{2nd}} + \Gamma_{\text{eff}}^{\text{select}}$. After a quick initial decay due to a finite correction time, the fidelity exhibits a slower decay rate. As one increases the ratio Ω_a/κ_c, one suppresses $\Gamma_{\text{eff}}^{\text{select}}$ and the decay rate converges towards $\Gamma_{\text{eff}}^{\text{2nd}}$. This effect is illustrated in Fig. 4.7b, where the solid line indicates the estimation of the decay rate (obtained from the slopes of the curves in Fig. 4.7a) as a function of the ratio Ω_a/κ_c. In comparison, the dashed-line represents the expected behaviour of this decoherence rate, given by $\Gamma_{\text{eff}}^{\text{2nd}}+\Gamma_{\text{eff}}^{\text{select}}$, and derived from Eqs. (4.11) and (4.12).

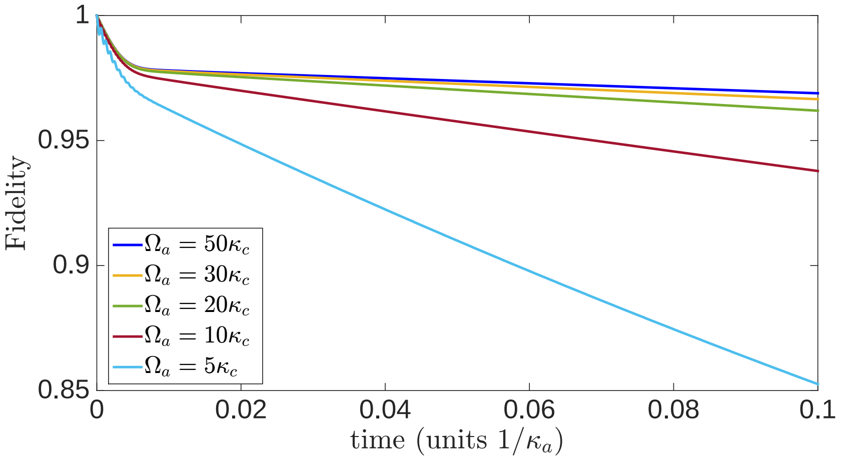

(a)

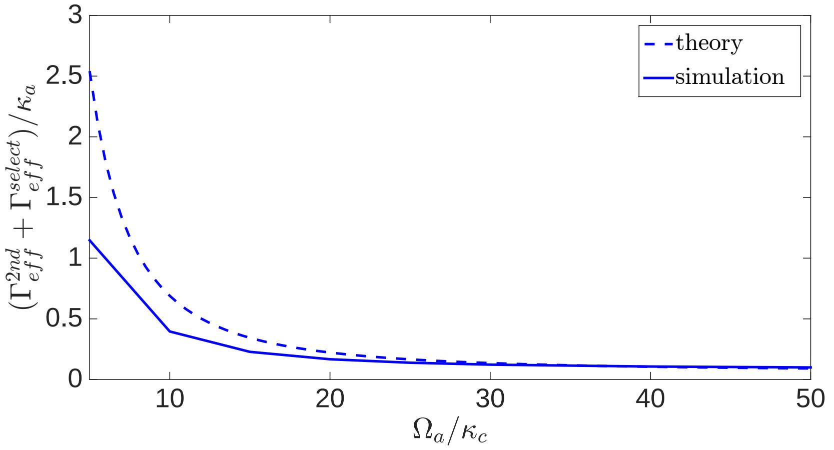

(b)

Fig. 4.7 (a) Decoherence channel induced by the imperfect manifold selectivity due to the finite ratio Ω_a/κ_c. The simulated system is identical to that of Fig. 4.6, and the curves show the evolution of the fidelity to the initial state $(|\mathscr{C}_\alpha^{(0\text{mod}4)}\rangle - i|\mathscr{C}_\alpha^{(2\text{mod}4)}\rangle)/\sqrt{2}$ for several values of Ω_a/κ_c. (b) The decay rate of the fidelities in Fig. (a) is plotted as a function of the ratio Ω_a/κ_c (solid line). This decoherence rate, given by $\Gamma_{\text{eff}}^{\text{2nd}}+\Gamma_{\text{eff}}^{\text{select}}$, decreases towards the finite value $\Gamma_{\text{eff}}^{\text{2nd}}$. The dashed-line indicates the theoretically expected behaviour.

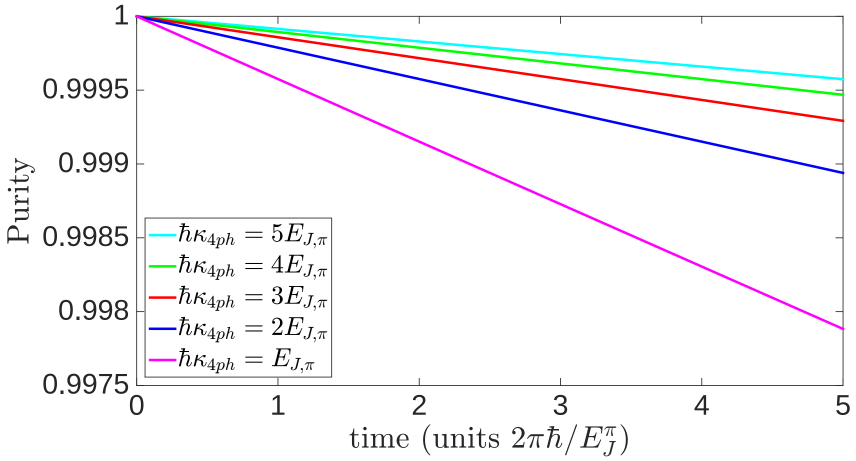

Fig. 4.8 Second order effect of Zeno dynamics approximation. The simulated system (4.13) consists of the mode **a** only, subjected to the parity-type Hamiltonian and the four-photon driven dissipation, and initialized in the state $(|\mathscr{C}_\alpha^{(0\text{mod}4)}\rangle - i|\mathscr{C}_\alpha^{(2\text{mod}4)}\rangle)/\sqrt{2}$. The evolution of the purity is plotted for various values of $(\hbar\kappa_{4\text{ph}})/E_{J,\pi}$.

Second order effect of Zeno dynamics approximation - While the first order Zeno dynamics approximation in $E_{J,\pi}/(\hbar\kappa_{4\text{ph}})$ (or $\sqrt{2\pi}|\alpha|\Omega_a/\kappa_{4\text{ph}}$) corresponds to a modification of the Hamiltonian part of the dynamics ($\mathbf{H}_{\text{RWA}}$ acts as a projected Hamiltonian on the manifold $\mathscr{M}_{4,\alpha}$), the second order correction leads to a form of dissipation described by Lindblad operators acting on $\mathscr{M}_{4,\alpha}$. These decoherence channels, studied in Subsection 3.5.3, induce a dephasing rate $\Gamma_{\text{eff}}^{\text{Zeno}} = f(|\alpha|)E_{J,\pi}{}^2/(\hbar^2\kappa_{4\text{ph}})$, with $f(|\alpha|) = \mathscr{O}(e^{-c|\alpha|})$, $c > 0$. In Fig. 4.8, we plot the evolution of the purity $\sqrt{Tr(\boldsymbol{\rho}^2)}$ of the system initialized in the state $(|\mathscr{C}_\alpha^{(0\text{mod}4)}\rangle - i|\mathscr{C}_\alpha^{(2\text{mod}4)}\rangle)/\sqrt{2}$ for various values of the ratio $(\hbar\kappa_{4\text{ph}})/E_{J,\pi}$. This is done by simulating the master equation

$$\frac{d\boldsymbol{\rho}}{dt} = -\frac{i}{\hbar}[\mathbf{H}^{\text{RWA}}(\varphi_{a,\pi}), \boldsymbol{\rho}] + \kappa_{4\text{ph}}\mathscr{D}[\mathbf{a}^4 - \alpha^4](\boldsymbol{\rho}),$$
$$\mathbf{H}^{\text{RWA}}(\varphi_{a,\pi}) = -E_{J,\pi}e^{-\frac{\varphi_{a,\pi}^2}{2}}\sum_n L_n(\varphi_{a,\pi})|n\rangle\langle n|_a \tag{4.13}$$

The decoherence rate $\Gamma_{\text{eff}}^{\text{Zeno}}$ corresponds to the slopes of the straight lines in Fig. 4.8. Note that we have not included the dynamics of the mode **c**, as it does not affect the decoherence rate $\Gamma_{\text{eff}}^{\text{Zeno}}$.

The performances of this correction scheme are summarized in table 4.2.

Required timescales	$\kappa_{4\text{ph}} \gg \Omega_a \gg \kappa_c \gtrsim \lvert\alpha g\rvert \gg \kappa_a$
Corrected errors	
First order single-photon losses (and gains)	correction rate $\Gamma_c \approx \frac{\lvert\alpha g\rvert^2}{\kappa_c} \lesssim \kappa_c/2$ optimal for $\lvert\alpha g\rvert \approx 0.8\kappa_c$
Effective decoherence rates	
Second order photon loss	decoherence rate $\Gamma_{\text{eff}}^{2nd} = (\lvert\alpha\rvert^2\kappa_a)^2/\Gamma_c.$
Imperfect manifold selectivity	decoherence rate $\Gamma_{\text{eff}}^{\text{select}} = \frac{\lvert\alpha g\rvert^2}{4\Omega_a^2+\kappa_c^2}\kappa_c \approx \frac{1}{16}\frac{\kappa_c^2}{\Omega_a^2}\kappa_c$
Second order Zeno dynamics approximation	dephasing rate $\Gamma_{\text{eff}}^{\text{Zeno}} = f(\lvert\alpha\rvert)\frac{E_{J,\pi}^2}{\hbar^2\kappa_{4\text{ph}}} = f(\lvert\alpha\rvert)\frac{\Omega_a^2}{2\pi\lvert\alpha\rvert^2\kappa_{4\text{ph}}}$ where $f(\lvert\alpha\rvert) = \mathscr{O}(e^{-c\lvert\alpha\rvert})$, $c > 0$

Table 4.2 Summary of the performances of the AQEC scheme using the four-component cat code.

4.3 Three-qubit bit-flip code with two-component cat qubits

In this section, we focus on using the three-qubit bit-flip code with two-component cat qubits, to detect or correct for single-photon losses. Here, the logical states are defined by $|0_L\rangle = |\mathscr{C}_\alpha^+,\mathscr{C}_\alpha^+,\mathscr{C}_\alpha^+\rangle$ and $|1_L\rangle = |\mathscr{C}_\alpha^-,\mathscr{C}_\alpha^-,\mathscr{C}_\alpha^-\rangle$. Starting from a superposition in the *coding subspace* $\mathscr{E}_0 = \text{span}\{|\mathscr{C}_\alpha^+,\mathscr{C}_\alpha^+,\mathscr{C}_\alpha^+,\rangle, |\mathscr{C}_\alpha^-,\mathscr{C}_\alpha^-,\mathscr{C}_\alpha^-\rangle\}$, a single-photon loss maps the states to one of the *error subspaces* $\mathscr{E}_1 = \text{span}\{|\mathscr{C}_\alpha^-,\mathscr{C}_\alpha^+,\mathscr{C}_\alpha^+\rangle, |\mathscr{C}_\alpha^+,\mathscr{C}_\alpha^-,\mathscr{C}_\alpha^-\rangle\}$, $\mathscr{E}_2 = \text{span}\{|\mathscr{C}_\alpha^+,\mathscr{C}_\alpha^-,\mathscr{C}_\alpha^+\rangle, |\mathscr{C}_\alpha^-,\mathscr{C}_\alpha^+,\mathscr{C}_\alpha^-\rangle\}$ or $\mathscr{E}_3 = \text{span}\{|\mathscr{C}_\alpha^+,\mathscr{C}_\alpha^+,\mathscr{C}_\alpha^-\rangle, |\mathscr{C}_\alpha^-,\mathscr{C}_\alpha^-,\mathscr{C}_\alpha^+\rangle\}$. The occurrence of a single-photon loss is revealed by the measurement of the joint-parities $\boldsymbol{\sigma}_Z^1\boldsymbol{\sigma}_Z^2$ and $\boldsymbol{\sigma}_Z^2\boldsymbol{\sigma}_Z^3$. More precisely, $\mathscr{E}_1$ is associated to the error syndrome $(\langle\boldsymbol{\sigma}_Z^1\boldsymbol{\sigma}_Z^2\rangle, \langle\boldsymbol{\sigma}_Z^2\boldsymbol{\sigma}_Z^3\rangle) = (-1,1)$, $\mathscr{E}_2$ to $(-1,-1)$, and $\mathscr{E}_3$ to $(1,-1)$. Together with the two-photon driven dissipation on each mode, this QEC code protects the information against arbitrary single mode errors. In particular, unlike the four-component cat code, the errors induced by the Linblad operator $\sqrt{\kappa_j^{th}}\mathbf{a}_j^\dagger$ are correctable. Indeed, under two-photon driven dissipation, both $\mathbf{a}_j$ and $\mathbf{a}_j^\dagger$ merely act as $\boldsymbol{\sigma}_X^j$ in the cat basis $\{|\mathscr{C}_\alpha^\pm\rangle\}$ (see Chapter 1 for more details). In Subsection 4.3.1, we propose to protect the information by continuously monitoring the error syndromes without correcting for these errors. Alternatively, in direct analogy with the AQEC protocol based on the four-component cat code exposed in Subsection 4.2.2, we show the possibility to realize an autonomous correction scheme using only continuous-wave (CW) drives.

Although the cat amplitude α, set by the two-photon processes through the Lindblad operators $\sqrt{\kappa_{2\mathrm{ph}}}(\mathbf{a}_j^2 - \alpha^2)$, is taken to be the same for all three modes, one could consider distinct cat amplitudes without altering the performances of the QEC schemes presented in this section.

4.3.1 Protection of the information via continuous monitoring of the error syndromes

Following the results of Chapter 3, we present a protection scheme based on the continuous monitoring of the error syndromes $\langle \boldsymbol{\sigma}_Z^1 \boldsymbol{\sigma}_Z^2 \rangle$ and $\langle \boldsymbol{\sigma}_Z^2 \boldsymbol{\sigma}_Z^3 \rangle$.

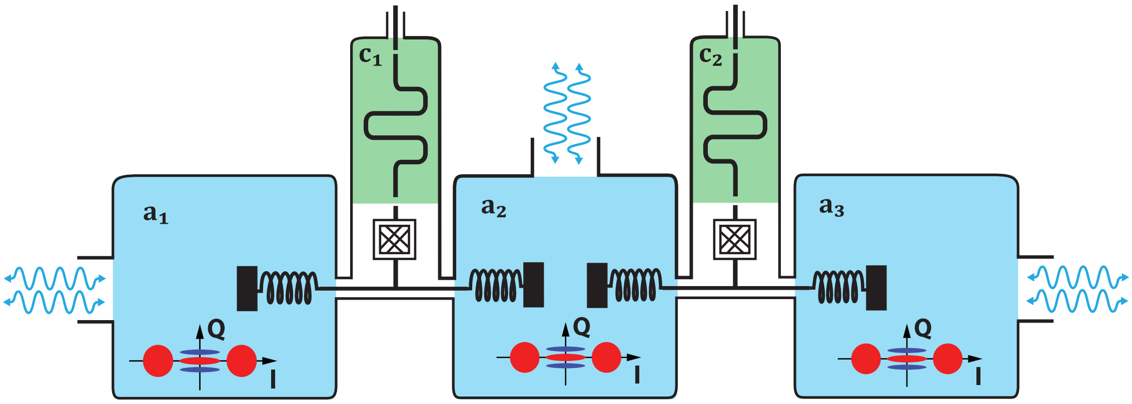

Fig. 4.9 Design for continuous QEC scheme based on three two-component cat qubits in presence of two-photon driven dissipation. The continous monitoring of the error syndromes, i.e the joint parity states of the high-Q modes $\mathbf{a}_j$, is done by coupling two readout modes to the cavities through high-impedance Josephson circuit. On the other side each cavity, one mediates two-photon exchange with the environment.

Let us consider three resonators $\mathbf{a}_1$, $\mathbf{a}_2$ and $\mathbf{a}_3$, whose states are confined to the manifold $\mathscr{M}_{2,\alpha}^{\otimes 3} = \mathrm{span}\{|\mathscr{C}_\alpha^\pm\rangle\}^{\otimes 3}$ via two-photon driven dissipation, and two readout modes $\mathbf{c}_1$ and $\mathbf{c}_2$. As illustrated in Fig. 4.9, the modes $\mathbf{a}_1$ and $\mathbf{a}_2$ are off-resonantly coupled to the mode $\mathbf{c}_1$ through a high-impedance Josephson circuit, resulting in an interaction Hamiltonian of the form $-E_{J_1,\pi}\cos(\frac{\mathbf{\Phi_1}}{\phi_0})$ where

$$\frac{\mathbf{\Phi_1}}{\phi_0} = (\varphi_{a_1,1}\mathbf{a}_1 + \varphi_{a_2,1}\mathbf{a}_2 + \varphi_{a_3,1}\mathbf{a}_3 + \varphi_{c_1,1}\mathbf{c}_1) + h.c.$$

Similarly, the two modes $\mathbf{a}_2$ and $\mathbf{a}_3$ are off-resonantly coupled to the mode $\mathbf{c}_2$, with a Hamiltonian $-E_{J_2,\pi}\cos(\frac{\mathbf{\Phi_2}}{\phi_0})$ and

$$\frac{\mathbf{\Phi_2}}{\phi_0} = (\varphi_{a_1,2}\mathbf{a}_1 + \varphi_{a_2,2}\mathbf{a}_2 + \varphi_{a_3,2}\mathbf{a}_3 + \varphi_{c_2,2}\mathbf{c}_2) + h.c.$$

The Hamiltonian of the system reads

$$\mathbf{H} = \sum_{k=1,2,3} \hbar\omega_{a_k}\mathbf{a}_k^\dagger\mathbf{a}_k + \sum_{k=1,2} \hbar\omega_{c_k}\mathbf{c}_k^\dagger\mathbf{c}_k - E_{J_1,\pi}\big(\cos(\frac{\mathbf{\Phi_1}}{\phi_0}) + \frac{1}{2}\frac{\mathbf{\Phi_1^2}}{\phi_0^2}\big) - E_{J_2,\pi}\big(\cos(\frac{\mathbf{\Phi_2}}{\phi_0}) + \frac{1}{2}\frac{\mathbf{\Phi_2^2}}{\phi_0^2}\big). \tag{4.14}$$

As we explain below, the joint parities $\boldsymbol{\sigma}_Z^1\boldsymbol{\sigma}_Z^2$ and $\boldsymbol{\sigma}_Z^2\boldsymbol{\sigma}_Z^3$ are continuously measured through the readout modes $\mathbf{c}_1$ and $\mathbf{c}_2$. For simplicity sakes, we consider that the single-photon loss rates satisfy $\kappa_{a_j} = \kappa_a$ and $\kappa_{c_l} = \kappa_c$. To avoid any resonances between the modes, the system frequencies are taken to be incommensurable. Here, we consider the regime $\varphi_{a_1,1}, \varphi_{a_2,1}, \varphi_{a_2,2}, \varphi_{a_3,2} \approx 2|\alpha|$ and $\varphi_{c_1,1}, \varphi_{c_2,2} \ll 1$. We assume that the participation of mode $\mathbf{a}_1$ ($\mathbf{a}_3$) in the Josephson circuit $E_{J_2,\pi}$ (resp. $E_{J_1,\pi}$) is small, i.e $\varphi_{a_1,2} \ll 1$ (resp. $\varphi_{a_3,1} \ll 1$). In addition, in the Hamiltonian of Eq. (4.14), we have neglected the participations of the mode $\mathbf{c}_1$ ($\mathbf{c}_2$) in the Josephson circuit $E_{J_2,\pi}$ (resp. $E_{J_1,\pi}$). In the frame rotating at the resonator frequencies, the Zeno dynamics regime, $\hbar\kappa_{2\text{ph}} > E_{J_1,\pi}, E_{J_2,\pi}$, leads to the effective Hamiltonian (see Chapter 3)

$$\mathbf{H}_{\mathscr{M}_{2,\alpha}^{\otimes 3}}/\hbar = -(\frac{\widetilde{\Omega}_a^{1,2}}{2}\boldsymbol{\sigma}_Z^1\boldsymbol{\sigma}_Z^2 + \frac{\widetilde{\Omega}_a^{2,3}}{2}\boldsymbol{\sigma}_Z^2\boldsymbol{\sigma}_Z^3) + \frac{\chi_{a_1,a_2}^{c_1}}{2}\boldsymbol{\sigma}_Z^1\boldsymbol{\sigma}_Z^2\mathbf{c}_1^\dagger\mathbf{c}_1 + \frac{\chi_{a_2,a_3}^{c_2}}{2}\boldsymbol{\sigma}_Z^2\boldsymbol{\sigma}_Z^3\mathbf{c}_2^\dagger\mathbf{c}_2, \tag{4.15}$$

where the expressions of $\Omega_a^{l,l+1}$ and $\chi_{a_l,a_{l+1}}^{c_l}$, $l = 1,2$, depend on $E_{J_l,\pi}$ and can be derived from eq. (3.4). Weak interactions between the modes $\mathbf{a}_1$ and $\mathbf{a}_3$ only induce low-order terms in $\mathbf{a}_1^\dagger\mathbf{a}_1$ and $\mathbf{a}_3^\dagger\mathbf{a}_3$, whose dephasing effects on the modes $\mathbf{a}_1$ and $\mathbf{a}_3$ are effectively suppressed by the two-photon processes. Since at each time, the three-qubit state lies in one of the eigenspaces $\mathscr{E}_{0,1,2,3}$, the first terms in $\Omega_a^{l,l+1}$ simply induce a global phase. The second terms operate a frequency shift $\pm\hbar\chi_{a_1,a_2}^{c_1}/2$ ($\pm\hbar\chi_{a_2,a_3}^{c_2}/2$) on the mode $\mathbf{c}_1$ (resp. $\mathbf{c}_2$) that depends on the error syndrome $\boldsymbol{\sigma}_Z^1\boldsymbol{\sigma}_Z^2$ (resp. $\boldsymbol{\sigma}_Z^2\boldsymbol{\sigma}_Z^3$). In analogy with the standard dispersive measurement of superconducting qubits, we drive the readout modes at their respective resonance frequencies. The error syndromes are imprinted on the phase and/or amplitude of the output fields.

While we give here a brief overview of the performances of this measurement scheme, we refer to Section 3.3 for more details. The error detection rate is given by the smallest of the two measurement rates, i.e

$$\begin{aligned}\Gamma_{\text{detect}} &= \min_{l=1,2} \Gamma_m^{a_l,a_{l+1}} = \min_{l=1,2} \bar{n}_c \chi^{c_l}_{a_l,a_{l+1}} \\ &= \min_{l=1,2} \bar{n}_c \varphi^2_{c_l,l} e^{-\frac{\varphi^2_{c_l,l}}{2}} \frac{E_{J_l,\pi}}{\hbar} \frac{e^{-\frac{1}{2}(\varphi_{a_l,l}-2|\alpha|)^2-\frac{1}{2}(\varphi_{a_{l+1},l}-2|\alpha|)^2}}{2\pi\sqrt{|\alpha|^2\varphi_{a_l,l}\varphi_{a_{l+1},l}}}\end{aligned}$$

Apart from the second order errors (two consecutive single-photon losses on different modes) yielding a logical bit-flip rate $\Gamma^{\text{2nd}}_{\text{eff}} = 3(|\alpha|^2\kappa_a)^2/\Gamma_{\text{detect}}$, two dephasing channels stem from the measurement protocol. The first one arises from the second order Zeno dynamics approximation for small values of $|\alpha|$, and results in a dephasing rate $\Gamma^{\text{Zeno}}_{\text{eff}} = \sum_{l=1,2} f(|\alpha|)E^2_{J_l,\pi}/(\hbar^2\kappa_{2\text{ph}})$, where $f(|\alpha|) = \mathcal{O}(e^{-c|\alpha|})$, $c > 0$ (see Subsection 3.5.2). Note that the coefficient c is larger than in the four-component cat case, so that the dephasing due to second order Zeno correction decreases much faster with $|\alpha|$ in the two-mode case with two-component cat qubits.

The second dephasing channel comes from the second order RWA, and was analyzed in Subsection 3.4.2. It modifies the joint-parity operators $\boldsymbol{\sigma}^1_Z\boldsymbol{\sigma}^2_Z$ and $\boldsymbol{\sigma}^2_Z\boldsymbol{\sigma}^3_Z$ into $\boldsymbol{\sigma}^1_Z\boldsymbol{\sigma}^2_Z + \varepsilon^{12}_1\boldsymbol{\sigma}^1_Z + \varepsilon^{12}_2\boldsymbol{\sigma}^2_Z$ and $\boldsymbol{\sigma}^2_Z\boldsymbol{\sigma}^3_Z + \varepsilon^{23}_2\boldsymbol{\sigma}^2_Z + \varepsilon^{23}_3\boldsymbol{\sigma}^3_Z$ respectively, where the parameters $\varepsilon^{k,k+1}_j \ll 1$ strongly depend on the system frequencies and $E_{J,\pi}$. The measurement collects information about the logical superposition through the single-parities $\varepsilon^{k,k+1}_j\boldsymbol{\sigma}^j_Z$, leading to a dephasing rate of order $\Gamma_{\text{detect}} \max|\varepsilon^{k,k+1}_j|$

By continuously keeping track of the error syndromes of the three-qubit system, one prevents first order single-photon losses from damaging the information. The cat qubits being inherently protected against dephasing via the two-photon dissipation, this three-qubit protocol realizes a complete first order protection of a logical qubit. A summary of the scheme performances is provided in table 4.3.

4.3.2 Autonomous quantum error correction via reservoir engineering

In Subsection 4.2.2, we have shown that a carefully designed coupling between the resonator encoding the qubit and its environment allows one to embed the detection step directly into the correction procedure. Here, by adapting the autonomous four-component cat QEC protocol presented in Subsection 4.2.2 to the three-qubit bit-flip code, we provide an autonomous correction scheme using three two-component cat qubits.

Required timescales	$\kappa_{2\mathrm{ph}} \gg \Omega_a^{l,l+1}$ and $\chi^{c_l}_{a_l,a_{l+1}} \sim \kappa_c \gg \kappa_a$
Corrected errors	
First order single-photon losses (and gains)	detection rate $\Gamma_{\mathrm{detect}} = \min\limits_{l=1,2} \bar{n}_c \chi^{c_l}_{a_l,a_{l+1}}$
Effective decoherence rates	
Second order photon loss	bit-flip rate $\Gamma_{\mathrm{eff}}^{\mathrm{2nd}} = 3(\lvert\alpha\rvert^2\kappa_a)^2/\Gamma_{\mathrm{detect}}.$
Second order RWA	dephasing rate $\sim \Gamma_{\mathrm{detect}} \max \lvert\varepsilon_j^{k,k+1}\rvert$
Second order Zeno dynamics approximation	dephasing rate $\Gamma_{\mathrm{eff}}^{\mathrm{Zeno}} = \sum_{l=1,2} f(\lvert\alpha\rvert) E^2_{J_l,\pi}/(\hbar^2\kappa_{2\mathrm{ph}}),$ where $f(\lvert\alpha\rvert) = \mathscr{O}(e^{-c\lvert\alpha\rvert}),\ c > 0$

Table 4.3 Performances of the QEC scheme using three cat qubits, realized through the continuous measurement of the joint parities.

4.3.2.1 Physical system

The system consists of the three high-Q oscillators $\mathbf{a}_j$, $j = 1,2,3$, encoding the three two-component cat qubits, and three dissipative modes $\mathbf{c}_j$, $j = 1,2,3$. As depicted in Fig. 4.10, each mode $\mathbf{a}_j$ is subject to two-photon driven dissipation, and is coupled to the mode $\mathbf{c}_j$ through a Josephson junction (Josephson energy E_J^j) embedded in a transmission line. Each lossy mode $\mathbf{c}_j$ will be used to evacuate the entropy created by single-photon losses on $\mathbf{a}_j$. Besides, two modes $\mathbf{a}_j$ and $\mathbf{a}_k$, $j,k = 1,2,3$, are strongly coupled through a high-impedance Josephson circuit associated to the Josephson energy $E_{J,\pi}^{jk}$. Through the latter coupling, the energy of the system will depend on the joint parities $\boldsymbol{\sigma}_Z^1\boldsymbol{\sigma}_Z^2$ and $\boldsymbol{\sigma}_Z^2\boldsymbol{\sigma}_Z^3$, upon which the correction procedure will be conditioned. The Hamiltonian of the driven system reads

$$\begin{aligned}
\mathbf{H} = &\sum_{j=1}^{3} \hbar\tilde{\omega}_{a_j}\mathbf{a}_j^\dagger\mathbf{a}_j + \hbar\tilde{\omega}_{c_j}\mathbf{c}_j^\dagger\mathbf{c}_j - \sum_{j=1}^{3} E_J^j\Big(\cos\Big(\frac{\boldsymbol{\Phi}_{\boldsymbol{c}}^{\boldsymbol{j}}}{\phi_0}\Big) + \frac{1}{2}\frac{{\Phi_c^j}^2}{\phi_0^2}\Big)\\
&- \sum_{j<k} E_J^{\pi,jk}\Big(\cos\Big(\frac{\boldsymbol{\Phi}_{a,\pi}^{jk}}{\phi_0}\Big) + \frac{1}{2}\frac{{\boldsymbol{\Phi}_{a,\pi}^{jk}}^2}{\phi_0^2}\Big) + \sum_{j=1}^{3} \hbar\varepsilon_j^a(t)(\mathbf{a}_j + \mathbf{a}_j^\dagger) + \hbar\varepsilon_j^c(t)(\mathbf{c}_j + \mathbf{c}_j^\dagger),\\
\frac{\boldsymbol{\Phi}_{\boldsymbol{c}}^{\boldsymbol{j}}}{\phi_0} = &\varphi_a^{j,1}(\mathbf{a}_1 + \mathbf{a}_1^\dagger) + \varphi_a^{j,2}(\mathbf{a}_2 + \mathbf{a}_2^\dagger) + \varphi_a^{j,3}(\mathbf{a}_3 + \mathbf{a}_3^\dagger) + \varphi_c^{j,j}(\mathbf{c}_j + \mathbf{c}_j^\dagger)\\
\frac{\boldsymbol{\Phi}_{a,\pi}^{jk}}{\phi_0} = &\varphi_{a,\pi}^{jk,1}(\mathbf{a}_1 + \mathbf{a}_1^\dagger) + \varphi_{a,\pi}^{jk,2}(\mathbf{a}_2 + \mathbf{a}_2^\dagger) + \varphi_{a,\pi}^{jk,3}(\mathbf{a}_3 + \mathbf{a}_3^\dagger).
\end{aligned} \tag{4.16}$$

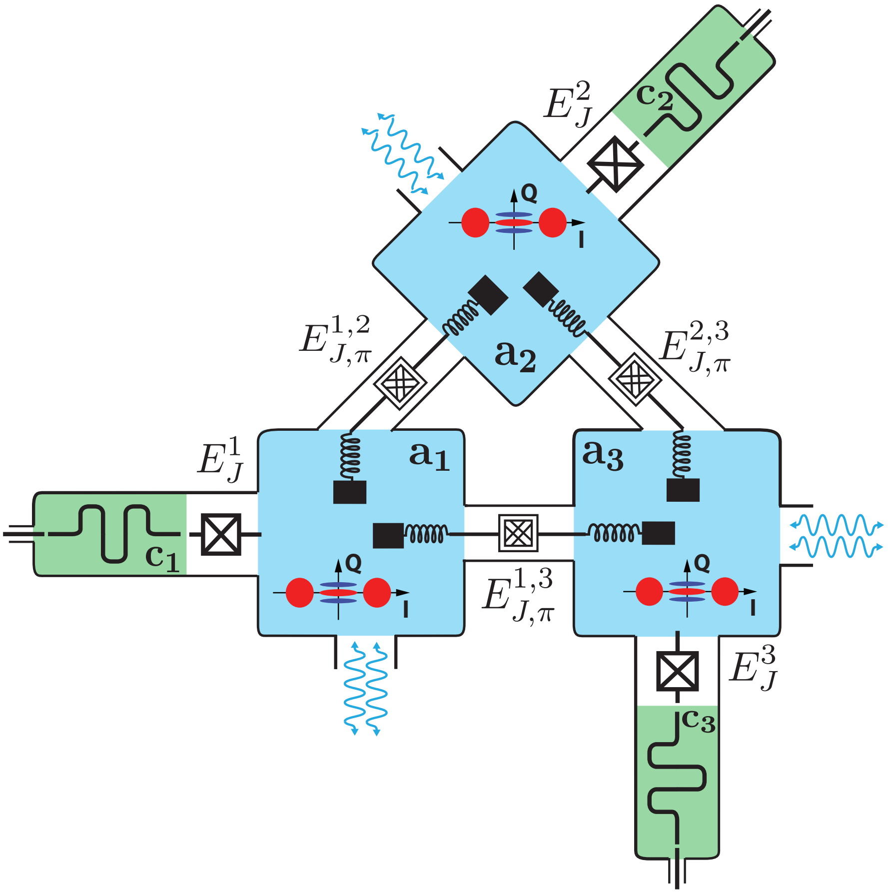

Fig. 4.10 Possible physical realization of the dissipation-induced AQEC scheme using three cat-qubit in presence of two-photon dissipation. Here, on one side of each cavity, a two-photon exchange process is engineered between the high-Q mode $\mathbf{a}_j$ and the environment. Besides, the cavities are two by two coupled through high-impedance Josephson circuits. By capacitively coupling a dissipative mode to each cavity through a Josephson junction, one evacuates the entropy created by bit-flips (or equivalently, errors inducing a parity change).

For simplicity sakes, we have neglected the participation of the lossy modes $\mathbf{c}_l$ in the high-impedance Josephson circuits. Similarly to the four-component cat code AQEC scheme presented in Subsection 4.2.2, a finite participation would not affect the performances of the scheme. The dressed frequencies of the modes $\mathbf{a}_j$ and $\mathbf{c}_k$, $\tilde{\omega}_{a_j}$ and $\tilde{\omega}_{c_k}$, are taken to be sufficiently far from each other to avoid resonances between the modes. Here we note $\varepsilon_j^{a(c)}$ some external drives that might be applied to the modes. We consider the regime where $\varphi_{a,\pi}^{jk,j(k)} \approx 2|\alpha|$. We furthermore consider the Zeno dynamics approximation where the Hamiltonian is a small perturbation relatively to the two-photon driven dissipations acting on the modes $\mathbf{a}_j$. If no external drive is applied, in the frame rotating at the mode frequencies, the effective Hamiltonian takes the form

$$\mathbf{H}_{\mathscr{M}_{2,\alpha}^{\otimes 3}} = -\frac{\hbar\Omega_a^{12}}{2}\boldsymbol{\sigma}_Z^1\boldsymbol{\sigma}_Z^2 - \frac{\hbar\Omega_a^{23}}{2}\boldsymbol{\sigma}_Z^2\boldsymbol{\sigma}_Z^3 - \frac{\hbar\Omega_a^{13}}{2}\boldsymbol{\sigma}_Z^1\boldsymbol{\sigma}_Z^3. \tag{4.17}$$

The derivation of the above Hamiltonian can be justified with the same arguments used for the calculation of the Hamiltonian of eq. (4.2) in the four-component cat case. In particular, the other self-Kerr and cross-Kerr terms act as the identity on the manifold $\mathscr{M}_{2,\alpha}^{\otimes 3}$.

4.3.2.2 Correction scheme : correction on one cat qubit

In this subsection, we focus on correcting the single-photon losses occurring on the resonator $\mathbf{a}_1$. Single-photon losses on modes $\mathbf{a}_2$ and $\mathbf{a}_3$ are not considered here, and one can therefore discard the dissipative modes $\mathbf{c}_2$ and $\mathbf{c}_3$ in this analysis. In the first paragraph, we draw an intuitive picture of the scheme illustrated in Fig.4.11. It is followed by a detailed description of the essential ingredients of this correction protocol.

Global picture of the scheme - Let the system be in the state $[c_+|\mathscr{C}_\alpha^+,\mathscr{C}_\alpha^+,\mathscr{C}_\alpha^+\rangle + c_-|\mathscr{C}_\alpha^-,\mathscr{C}_\alpha^-,\mathscr{C}_\alpha^-\rangle]\otimes|0\rangle_{c_1}$. A single-photon loss (or gain) on the mode $\mathbf{a}_1$ sends the system to the state $[c_+|\mathscr{C}_\alpha^-,\mathscr{C}_\alpha^+,\mathscr{C}_\alpha^+\rangle + c_-|\mathscr{C}_\alpha^+,\mathscr{C}_\alpha^-,\mathscr{C}_\alpha^-\rangle]\otimes|0\rangle_{c_1}$ (black wavy arrows on Fig. 4.11). Through the application of a pump tone at a well chosen frequency, the latter erroneous state is resonantly coupled to the state $[c_+|\mathscr{C}_\alpha^+,\mathscr{C}_\alpha^+,\mathscr{C}_\alpha^+\rangle + c_-|\mathscr{C}_\alpha^-,\mathscr{C}_\alpha^-,\mathscr{C}_\alpha^-\rangle]\otimes|1\rangle_{c_1}$ (purple double-sided arrows). The dissipation on the mode $\mathbf{c}_1$ rapidly projects the system state to the initial state $[c_+|\mathscr{C}_\alpha^+,\mathscr{C}_\alpha^+,\mathscr{C}_\alpha^+\rangle + c_-|\mathscr{C}_\alpha^-,\mathscr{C}_\alpha^-,\mathscr{C}_\alpha^-\rangle]\otimes|0\rangle_{c_1}$ (green wavy arrow).

Detailed construction - We apply a strongly detuned pump tone through the output port of the mode $\mathbf{c}_1$, at frequency $\omega_{p_1} = |\omega_{a_1} - \omega_{c_1} - (\Omega_a^{12} + \Omega_a^{13})|/2$. This results in the effective Hamiltonian

$$\mathbf{H}_{\text{int}}/\hbar = -\frac{\Omega_a^{12}}{2}\boldsymbol{\sigma}_Z^1\boldsymbol{\sigma}_Z^2 - \frac{\Omega_a^{23}}{2}\boldsymbol{\sigma}_Z^2\boldsymbol{\sigma}_Z^3 - \frac{\Omega_a^{13}}{2}\boldsymbol{\sigma}_Z^1\boldsymbol{\sigma}_Z^3 + (\Omega_a^{12} + \Omega_a^{13})\mathbf{c}_1^\dagger\mathbf{c}_1 + \big(\frac{g_1}{2}\mathbf{a}_1\mathbf{c}_1^\dagger + h.c\big), \tag{4.18}$$

where the interaction strength g_1 reads

$$g_1 = -\frac{E_J^1\varphi_a^{1,1}(\varphi_c^{1,1})^3{\varepsilon_{p_1}}^2}{\hbar(\omega_{c_1} - \omega_{p_1})^2},$$

with ε_{p_1} the drive strength. In the regime $\Omega_a^{12},\Omega_a^{13} \gg \kappa_{c_1} \gtrsim |g_1\alpha| \gg \kappa_{a_1}$, through this Hamiltonian one corrects for single-photon loss (or gain) on the oscillator $\mathbf{a}_1$, with an optimal correction rate given by $\Gamma_{c_1} \approx \kappa_{c_1}/2$ (see four-component cat AQEC scheme in Subsection 4.2.2)

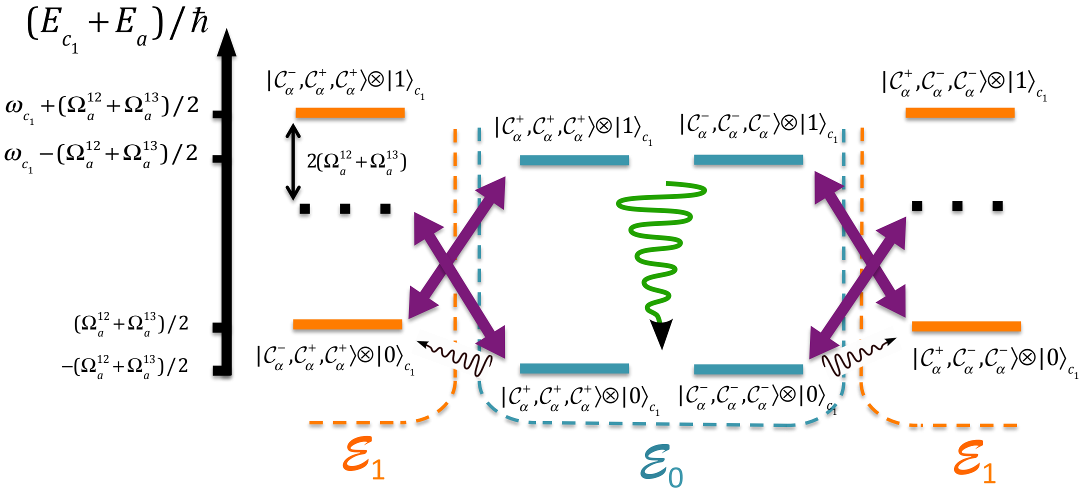

Fig. 4.11 Energy-level diagram of the system as a function of the joint-state of the modes $\mathbf{a}_1$, $\mathbf{a}_2$, $\mathbf{a}_3$ and $\mathbf{c}_1$. As explained through Subsection 4.3.2.2, the lossy mode $\mathbf{c}_1$ never gets populated beyond Fock state $|1\rangle$ and therefore, we restrict the diagram to the space spanned by Fock states $|0\rangle$ and $|1\rangle$. Straight-line purple arrows indicate couplings between two states induced by the pump at frequency ω_{p_1} (resp. ω_{p_2}). Green wavy arrow indicates a common decay channel due to the decay of the single photon in the ancillary resonator $\mathbf{c}_1$, while the black wavy arrows represent single-photon loss occurring on mode $\mathbf{a}_1$.

4.3.2.3 Correction scheme : correction on all three cat qubits

In this Subsection, the three oscillators $\mathbf{a}_1$, $\mathbf{a}_2$ and $\mathbf{a}_3$ suffer from single-photon dissipation at the rates κ_{a_1}, κ_{a_2} and κ_{a_3} respectively. In addition to the pump at frequency ω_{p_1}, we apply two strongly detuned pumps through the output ports of the modes $\mathbf{c}_2$ and $\mathbf{c}_3$, at the respective frequencies $\omega_{p_2} = [\omega_{a_2} - \omega_{c_2} - (\Omega_a^{23} + \Omega_a^{12})]/2$ and $\omega_{p_3} = [\omega_{a_3} - \omega_{c_3} - (\Omega_a^{23} + \Omega_a^{13})]/2$. The effective Hamiltonian reads

$$
\begin{aligned}
\mathbf{H}_{\text{int}}/\hbar = & -\frac{\Omega_a^{12}}{2}\boldsymbol{\sigma}_Z^1\boldsymbol{\sigma}_Z^2 - \frac{\Omega_a^{23}}{2}\boldsymbol{\sigma}_Z^2\boldsymbol{\sigma}_Z^3 - \frac{\Omega_a^{13}}{2}\boldsymbol{\sigma}_Z^1\boldsymbol{\sigma}_Z^3 \\
& + (\Omega_a^{12} + \Omega_a^{13})\mathbf{c}_1^\dagger\mathbf{c}_1 + (\Omega_a^{23} + \Omega_a^{12})\mathbf{c}_2^\dagger\mathbf{c}_2 + (\Omega_a^{13} + \Omega_a^{23})\mathbf{c}_3^\dagger\mathbf{c}_3 \\
& + \big(\frac{g_1}{2}\mathbf{a}_1\mathbf{c}_1^\dagger + h.c\big) + \big(\frac{g_2}{2}\mathbf{a}_2\mathbf{c}_2^\dagger + h.c\big) + \big(\frac{g_3}{2}\mathbf{a}_3\mathbf{c}_3^\dagger + h.c\big).
\end{aligned} \tag{4.19}
$$

Similarly to the correction on mode $\mathbf{a}_1$ discussed in the previous Subsection, in the regime $\Omega_a^{jk} \gg \kappa_{c_j} \gtrsim |\alpha g_j| \gg \kappa_{a_j},\ j = 1,2,3,\ k \neq j$, each dissipative ancilla $\mathbf{c}_j$ evacuates the entropy created by single-photon losses (or gains) of mode $\mathbf{a}_j$ at a rate $\Gamma_{c_j} \approx \kappa_{c_j}/2$. In what follows, we set $\kappa_{c_j} = \kappa_c$ to simplify the analysis of the scheme limitations. Note that a similar form of Hamiltonian was also derived in [36] to realize an AQEC scheme. However, instead of cat qubits, they consider three transmon qubits two by two coupled through magnetic fluxes of well chosen frequencies.

4.3.2.4 Limitations of the scheme

First, if two consecutive photon losses occur on two different cat qubits (say 1 and 2) within a time window smaller than Γ_c^{-1}, the QEC scheme maps the state back to the coding subspace $\mathscr{E}_0$ by flipping the parity state of the third qubit. This event results in a logical bit-flip: such processes lead to an effective bit-flip rate of $\Gamma_{\text{eff}}^{2nd} = 3(|\alpha|^2\kappa_a)^2/\kappa_c$,

Another source of decoherence stems from the second order Zeno correction. This effect, analyzed in detail in Subsection 3.5.2, yields a dephasing rate $\Gamma_{\text{eff}}^{\text{Zeno}} = \sum_{j<k} f(|\alpha|) {E_{J,\pi}^{jk}}^2/(\hbar^2\kappa_{2\text{ph}})$ with $f(|\alpha|) = \mathscr{O}(e^{-c|\alpha|})$, $c > 0$.

Next, the rotating-wave approximation, leading to the joint-parity Hamiltonian to first order, also gives rise to a second order correction (see Subsection 3.5.2 for details) which might constitute a source of dephasing. This second order correction amounts to replacing the joint-parity operator $\boldsymbol{\sigma}_Z^j\boldsymbol{\sigma}_Z^k$ by the operator $\boldsymbol{\sigma}_Z^j\boldsymbol{\sigma}_Z^k + \varepsilon_{jk,j}^{\text{RWA}}\boldsymbol{\sigma}_Z^j + \varepsilon_{jk,k}^{\text{RWA}}\boldsymbol{\sigma}_Z^k$, with $\varepsilon_{jk,j(k)}^{\text{RWA}} \ll 1$. If one applies this replacement in the effective Hamiltonian of eq. (4.19), we obtain

$$
\begin{aligned}
\mathbf{H}_{\text{int}}/\hbar = & -\frac{\Omega_a^{12}}{2}\boldsymbol{\sigma}_Z^1\boldsymbol{\sigma}_Z^2 - \frac{\Omega_a^{23}}{2}\boldsymbol{\sigma}_Z^2\boldsymbol{\sigma}_Z^3 - \frac{\Omega_a^{13}}{2}\boldsymbol{\sigma}_Z^1\boldsymbol{\sigma}_Z^3 \\
& - \left(\frac{\Omega_a^{12}}{2}\varepsilon_{12,1}^{\text{RWA}} + \frac{\Omega_a^{13}}{2}\varepsilon_{13,1}^{\text{RWA}}\right)\boldsymbol{\sigma}_Z^1 - \left(\frac{\Omega_a^{23}}{2}\varepsilon_{23,2}^{\text{RWA}} + \frac{\Omega_a^{12}}{2}\varepsilon_{12,2}^{\text{RWA}}\right)\boldsymbol{\sigma}_Z^2 \\
& - \left(\frac{\Omega_a^{13}}{2}\varepsilon_{13,3}^{\text{RWA}} + \frac{\Omega_a^{23}}{2}\varepsilon_{23,3}^{\text{RWA}}\right)\boldsymbol{\sigma}_Z^3 \\
& + (\Omega_a^{12} + \Omega_a^{13})\mathbf{c}_1^\dagger\mathbf{c}_1 + (\Omega_a^{23} + \Omega_a^{12})\mathbf{c}_2^\dagger\mathbf{c}_2 + (\Omega_a^{13} + \Omega_a^{23})\mathbf{c}_3^\dagger\mathbf{c}_3 \\
& + \left(\frac{g_1}{2}\mathbf{a}_1\mathbf{c}_1^\dagger + h.c\right) + \left(\frac{g_2}{2}\mathbf{a}_2\mathbf{c}_2^\dagger + h.c\right) + \left(\frac{g_3}{2}\mathbf{a}_3\mathbf{c}_3^\dagger + h.c\right).
\end{aligned}
$$

The second order correction lifts the two-fold degeneracy of the Hamiltonian on the subspaces $\mathscr{E}_0, \mathscr{E}_1, \mathscr{E}_2$ and $\mathscr{E}_3$, by introducing non-zero effective qubit frequencies $\omega_j^{\text{eff}} = \sum\limits_{k \neq j} \Omega_a^{jk}\varepsilon_{jk,j}^{\text{RWA}}$. This effect of this symmetry breakdown is very similar to that of the bit-flip correction scheme using transmon qubits presented in Chapter 2 (see Subsection 2.4.2). Each time a single-photon loss occurs, a tiny amount of information is leaked about the superposition

Required timescales	$\kappa_{2\mathrm{ph}} \gg \Omega_a^{ik} \gg \kappa_{c_i} \gtrsim \lvert\alpha g_i\rvert \gg \kappa_{a_i}$
Corrected errors	
First order single-photon losses (and gains)	correction rates $\Gamma_{c_i} = \frac{\lvert\alpha g_i\rvert^2}{\kappa_{c_i}} \lesssim \frac{\kappa_{c_i}}{2}$ on oscillator $\mathbf{a}_i$ optimal for $\lvert\alpha g_i\rvert \approx 0.8\kappa_{c_i}$
Effective decoherence rates	
Second order photon loss	bit-flip rate $\Gamma_{\mathrm{eff}}^{2nd} = 3(\lvert\alpha\rvert^2\kappa_a)^2/\Gamma_c$.
Second order RWA	dephasing rate $\Gamma_{\mathrm{eff}}^{\mathrm{RWA}} \sim \sum_{j=1,2,3} \kappa_{a_j} \lvert \sum_{k\neq j} \Omega_a^{jk} \varepsilon_{jk,j}^{\mathrm{RWA}} \rvert/\Gamma_{c_j}$.
Second order Zeno dynamics approximation	dephasing rate $\Gamma_{\mathrm{eff}}^{\mathrm{Zeno}} = \sum_{j<k} f(\lvert\alpha\rvert) {E_{J,\pi}^{jk}}^2/(\hbar^2\kappa_{2\mathrm{ph}})$ where $f(\lvert\alpha\rvert) = \mathcal{O}(e^{-c\lvert\alpha\rvert})$, $c > 0$

Table 4.4 Performances of the autonomous QEC scheme using three cat qubits in the presence of two-photon dissipation.

state of the logical qubit. This leads to a dephasing rate

$$\Gamma_{\mathrm{eff}}^{\mathrm{RWA}} \sim \sum_{j=1,2,3} \kappa_{a_j} \frac{\left| \sum\limits_{k\neq j} \Omega_a^{jk} \varepsilon_{jk,j}^{\mathrm{RWA}} \right|}{\Gamma_{c_j}}. \tag{4.20}$$

In table 4.4, we provide a summary the performances of the schemes.

4.4 Summary

In this Chapter, we have exploited the ideas of the previous chapters to design four QEC schemes based on the cat code. First, by encoding a logical qubit into the even-parity manifold of the four-component cat manifold and continuously measuring its parity state, one prevents first order single-photon losses from damaging the logical information. The protection against dephasing errors is achieved through four-photon driven dissipation. In a detailed autonomous version of this scheme, we show the possibility to directly implement the detection step into the correction procedure through reservoir engineering. Although the information is encoded in a single mode, it is protected against the dominant error channels. Inspired from these two QEC schemes, we have designed two correction protocols based on the three-qubit bit-flip code concatenated with the two-component cat code. As the two-component cat states are protected against phase-flip errors due to two-photon processes, the three-qubit bit-flip code offers a protection against arbitrary single-qubit errors. While the four-component cat schemes require relatively large cat amplitudes $|\alpha|$ to minimize the induced dephasing errors through second order Zeno dynamics, the two-component cat version is not sensitive to this effect. However, the four-component cat scheme is not affected by the second order rotating-wave approximation, which constitutes a limitation of the two-component cat protocols.

Chapter 5

Conclusions and Perspectives

In this thesis, we investigate two essential subjects related to quantum error correction: autonomous QEC via reservoir engineering and fault-tolerant QEC. This chapter gives a brief summary of the manuscript, along with several comments that intent to put this work into perspective.

In the first part of this thesis, we focus on realizing autonomous QEC with multi-qubit codes. The protection is paradoxically provided by the coupling between the qubits and a dissipative system. More precisely, we have designed an autonomous correction scheme, based on the 3-qubit bit-flip or phase-flip code, where three transmon qubits are carefully coupled to a lossy resonator. The entropy created by possible bit flips is evacuated through the dissipation of the resonator in a continuous and autonomous manner. Such an autonomous scheme presents several benefits over the standard measurement-based QEC protocols. It obviates the need for the quantum/classical interface required for standard measurement-based QEC protocols, thus reducing the possible errors arising from such an interface. Besides, it can lead to major simplifications in the hardware complexity of the system. In particular, our scheme only needs the application of continuous-wave drives and does not require any important experimental calibrations.

Based on this 3-qubit design, we gave preliminary ideas to realize a completely protected qubit using the 9-qubit Bacon-Shor code. However, extending the protection against single bit flips to arbitrary single-qubit errors requires a significant increase of the hardware complexity. Indeed, the 9-qubit protocols that we propose, use 9 transmons qubits coupled to at least 4 lossy resonators, as opposed to 3 transmons coupled to a single dissipative mode for the 3-qubit scheme. This illustrates the experimental challenge that represents the construction of a logical memory based on multi-qubit codes such as the Bacon-Shor code.

The second part of this manuscript uses the so-called cat-qubits encoded in a harmonic oscillator to realize a logical qubit protected in a fault-tolerant manner. Here, we illustrate the vital character of this concept of fault-tolerance in an error syndrome measurement paradigm. Indeed, such a concept ensures that the presence of various imperfections in the measurement scheme does not introduce new error channels that are not correctable by the considered error correction scheme. In the case of multi-qubit codes, such as the 7-qubit Steane code [81], one needs to ensure that the imperfections in the measurement of a parity-type observable, such as the 4-qubit parity observable $Z_1Z_2Z_3Z_4$, do not lead to new error channels, such as correlated two-qubit errors. In this framework, ensuring the fault-tolerance usually comes at the expense of a significant overhead in the hardware (many ancillary qubits to measure a single error syndrome). We need to emphasize that such a fault-tolerance is absolutely crucial when dealing with protected logical gates. Indeed, in the scenario where the QEC is applied to improve the fidelity of a logical gate (different from identity), the absence of fault-tolerance would set a limit on the maximum attainable fidelity. Noting that each step of a non-fault-tolerant QEC introduces, with a certain probability P_{NFT}, a non-correctable error, the fidelity of a corrected gate cannot exceed a value of order $1 - P_{NFT}$. Thus, fault-tolerant QEC is a necessary step towards the realization of a fault-tolerant quantum processor.

The surface codes [21] have emerged as a viable tool to perform fault-tolerant quantum computation. More precisely, they provide a protection against not only data qubit errors but also errors arising from the imperfections of the error syndrome measurements. However, the current fault-tolerant architectures associated to the surface codes [21], require an extensive number of qubits. Indeed, the surface codes encode a single logical qubit protected against errors occurring on at most t distinct qubits (i.e a code of distance $2t+1$), using $n \propto t^2$ *data* qubits. In addition, they require a similar number of ancillary *measurement* qubits to measure the error syndromes [21]. Despite the fault-tolerance provided by the surface code, the number of qubits $n \propto t^2$ needed is rather large in comparison with the minimum number of qubits required. Indeed, the quantum singleton bound [57], stating that the minimum number of qubits n for a code of distance $2t+1$ satisfies $n \geq 4t+1$, indicates a linear scaling $n \propto t$. This is partly due to the fact that the quantum singleton bound does not account for the additional hardware resources often required to measure the error syndrome in a fault-tolerant manner. In Chapters 3 and 4, however, we have presented a fault-tolerant architecture which circumvents the need for these additional qubits.

Instead of increasing the number of qubits, we proposed to design a specific coupling between the data qubits and the readout modes, such that errors due to measurement imperfections cannot propagate to the data qubits. This method is adapted to qubits encoded in a harmonic oscillator, the cat qubits. As shown in the introduction, cat qubits exploit the large Hilbert space of a harmonic oscillator to exhibit a natural protection against phase-flip errors. The correction scheme associated to this phase-flip protection can be realized through the multi-photon driven dissipation presented in [53]. In other words, we deal with qubits subjected to bit flips only, or at least strongly asymmetric noise channels. Note that such a noise channel asymmetry leads to a simplification in the number of qubits required to realize a protected logical quantum memory [32]. For the cat code, the error syndromes associated to bit flips is related to the photon-number parity measurement. In Chapter 3, we have proposed a scheme to continuously monitor the photon-number parity of a resonator in a fault-tolerant manner. The proposal consists in coupling a readout mode to the storage mode through a high-impedance Josephson circuit. In Chapter 4, we have built continuous/autonomous fault-tolerant QEC schemes based upon this measurement scheme. In the following paragraphs, we comment on the fault-tolerant aspect of our proposal, and explain the improvements brought by our new fault-tolerant measurement paradigm through a quantitative analysis. We also provide some insights on the realization of protected logical gates with cat qubits as a future step.

In Chapter 3, we have mentioned that the absence of fault-tolerance in the error syndrome measurements is the limiting factor in the current QEC experiments [59]. Let us give a more quantitative analysis of this statement and explain how our new fault-tolerant measurement paradigm provides a significant improvement of the performance of QEC. This analysis is strongly inspired by those provided in the supplementary materials of [82] and [59]. In the current experiments [82, 59], certain noise channels of the system lead to error mechanisms that are not correctable by the encoding. More precisely, in these experiments, an ancillary transmon qubit is used to measure the photon-number parity in the storage cavity. A T_1 error of this qubit however could propagate to the storage cavity and induce a photon-dephasing type error that is not tracked by our correction mechanism. The purpose of Chapter 3 is precisely to avoid such a possibility. It significantly limits the improvement of the qubit lifetime. In order to see this, let us concentrate on the case of the cat codes with two types of photon-number parity measurements: 1- transmon-based measurement lacking fault-tolerance; 2- continuous measurement using high-impedance Josephson circuit presented in Chapter 3 (a similar type of analysis can be done for any type of error correction scheme). These measurement protocols are characterized by their duration. In the case of the transmon-based measurement this duration is essentially given by $\tilde{T}_m = \pi/\chi$, where χ represents the dispersive coupling strength between the transmon and the storage mode. In the case of the continuous measurement, this measurement time is proportional to $1/\Gamma_m$ where Γ_m represents the measurement rate. Indeed, to achieve the same type of fidelity (around 99%) as in the transmon-based measurement [59], the required measurement time of the continuous protocol is given by $T_m \approx -\ln(.01)/\Gamma_m \approx 5/\Gamma_m$. For the first measurement protocol, one also needs to consider a second parameter, corresponding to the rate at which various imperfections make the system leak out of the correctable code space. We denote this rate by κ_{NFT} (non-fault-tolerance), which in the case of transmon-based measurement is dominantly given by $1/T_1$. This leads to a leakage probability per measurement time given by $P_{NFT} = \kappa_{NFT} T_m \approx T_m/T_1$.

In a fault-tolerant measurement scenario, the best performance of error correction is ensured when the error-syndrome measurement is performed as often as possible. This leads to a first-order error correction: the errors that are not corrected correspond to the events where two photons are lost during a single measurement. The probability for such events is given by $(\bar{n}\kappa T_m)^2/2$, where $\bar{n}$ represents the average number of photons in the cavity and κ corresponds to the cavity decay rate. This leads to an effective decoherence rate, after error correction, given by

$$\kappa_{\text{eff}} = \frac{(\bar{n}\kappa T_m)^2}{2T_m} = \frac{(\bar{n}\kappa T_m)}{2}\bar{n}\kappa.$$

The coherence time is therefore enhanced by a factor of $2/(\bar{n}\kappa T_m)$.

In the case where the error-syndrome measurement induces some leakage out of the code space, repeating the measurement, without any waiting time in between, would lead to an effective coherence time which is at best given $1/\kappa_{NFT}$ (T_1 in the case of transmon-based measurement). Indeed, any such leakage event would yield a complete loss of quantum information. As explained in the supplementary materials of [82] and [59], one should therefore introduce a waiting time T_w between two measurements to balance the probabilities of having more than one error in the total time $\tilde{T}_m + T_w$ and the probability of having a leakage event in $\tilde{T}_m$. This leads to the following optimal choice of the waiting time:

$$\frac{(\bar{n}\kappa)^2(\tilde{T}_m + T_w)^2}{2} = P_{NFT},$$

where the left hand side represents the probability of having two errors during the total time $\tilde{T}_m + T_w$. The effective decoherence rate, after error correction in this scenario, is given by

$$\kappa_{\text{eff}}^{NFT} = \left[\frac{(\bar{n}\kappa)^2(\tilde{T}_m + T_w)^2}{2} + P_{NFT}\right]\frac{1}{\tilde{T}_m + T_w} = \bar{n}\kappa\sqrt{2P_{NFT}}.$$

The enhancement in the coherence time is therefore given by $1/\sqrt{2P_{NFT}} \approx \sqrt{T_1/2\tilde{T}_m}$.

One has therefore to compare the effective decay rates $\kappa_{\text{eff}} = \bar{n}\kappa\frac{(\bar{n}\kappa T_m)}{2}$ and $\kappa_{\text{eff}}^{NFT} = \bar{n}\kappa\sqrt{2\tilde{T}_m/T_1}$. Two important remarks are in order: 1- while in the fault-tolerant scheme the enhancement can be improved linearly through faster measurement $1/T_m$, in the second case this improvement is only in square root $1/\sqrt{\tilde{T}_m}$; 2- while in the fault-tolerant scheme, the measurement time is to be compared to decay time-scale $1/\kappa$ of the storage cavity, in the second case, the measurement time is to be compared to the leakage time T_1. Note that the superconducting cavity modes achieve lifetimes much higher than the best transmon qubits [69] and it is very likely that this advantage will be further enhanced in the near future. In order to finish this analysis, let us provide some prediction of the expected improvements with experimentally achievable parameters. For the case of a transmon-based measurement, taking the transmon's T_1 to be of order of 100μs and the dispersive coupling strength to be of order 1MHz, we can expect a lifetime enhancement of order $\sqrt{T_1/2\tilde{T}_m} \approx 10$. In the fault-tolerant parity measurement case, following the analysis of the main text, we believe that a measurement rate of a few hundred kHz is achievable. This would lead to a measurement time T_m of order 5μs. Therefore, for a cavity mode with a lifetime of 10ms and an average photon number of $\bar{n} = 4$, we could expect an enhancement of order $2/\bar{n}\kappa T_m \approx 1000$.

Through the last set of paragraphs, we have shown that the fault-tolerant measurement scheme developed in Chapter 3 can lead to a significant improvement of the cat qubit lifetime in comparison with a non-fault-tolerant QEC scheme. In Chapter 4, based upon this measurement scheme and the ideas of Chapter 2 on autonomous QEC, we developed a strategy to build logical qubits protected in a fault-tolerant and autonomous manner. In particular, we proposed to realize an autonomous scheme based on the three-qubit bit-flip code with two-component cat-qubits. This strategy seems more interesting than using the four-component cat code, as it provides a protection not only against phase flips and single-photon losses, but more generally against arbitrary single-mode errors. To perform fault-tolerant quantum computation with these logical qubits, one should be able to apply an arbitrary protected logical gate on them. In the following paragraph, we focus on the logical qubit composed of three two-component cat qubits, such that $|0_L\rangle = |\mathscr{C}_\alpha^+, \mathscr{C}_\alpha^+, \mathscr{C}_\alpha^+\rangle$ and $|1_L\rangle = |\mathscr{C}_\alpha^-, \mathscr{C}_\alpha^-, \mathscr{C}_\alpha^-\rangle$, and investigate the possibility of applying fault-tolerant gates. For clarity's sake, an operation on an "elementary" qubit $|\mathscr{C}_\alpha^+\rangle$ is referred to as an "elementary" operation, and a gate on the logical qubit as a "logical" gate.

A universal set of gates is given by arbitrary rotations around the X-axis, a $\pi/2$-rotation around the Z-axis, and a two-qubit entangling gate. First, it was shown in [53] that one can realize arbitrary rotations around the X-axis for a single two-component cat qubit, by applying a simple drive on the resonator corresponding to a Hamiltonian of the form $\hbar\varepsilon\mathbf{a} + \mathbf{h}.\mathbf{c}$. Moreover, a two-qubit entangling gate (on 2 two-component cat qubits) can be obtained through a beam-splitter Hamiltonian of the form $\hbar\varepsilon\mathbf{a}_1\mathbf{a}_2^\dagger + \mathbf{h}.\mathbf{c}$. While protected logical gates can, in principle, be obtained through these elementary operations [57], further studies are required to ensure the preservation of fault-tolerance. More precisely, we need to ensure that the above elementary operations cannot open the system to phase-flip errors that are supposed to be suppressed by the pumping scheme.

References

[1] Ahn, C., Doherty, A. C., and Landahl, A. J. (2002). Continuous quantum error correction via quantum feedback control. *Phys. Rev. A*, 65:042301.

[2] Albert, V., Shu, C., Krastanov, S., Shen, C., Liu, R.-B., Z.-B. Yang, R. S., Mirrahimi, M., Devoret, M., and Jiang, L. (2016). Holonomic quantum control with continuous variable systems. *Phys. Rev. Lett.*, 116:140502.

[3] Aliferis, P. and Preskill, J. (2008). Fault-tolerant quantum computation against biased noise. *Phys. Rev. A*, 78:052331.

[4] Azouit, R., Sarlette, A., and Rouchon, P. (2015). Convergence and adiabatic elimination for a driven dissipative quantum harmonic oscillator. In *IEEE Conference on Decision and Control*. IEEE Conference on Decision and Control.

[5] Azouit, R., Sarlette, A., and Rouchon, P. (2016). Adiabatic elimination for open quantum systems with effective lindblad master equations. arxiv:1603.04630.

[6] Bacon, D. (2006). Operator quantum error-correcting subsystems for self-correcting quantum memories. *Phys. Rev. A*, 73:012340.

[7] Barreiro, J., Muller, M., Schindler, P., Nigg, D., Monz, T., Chwalla, M., Hennrich, M., Roos, C., Zoller, P., and Blatt, R. (2011). An open-system quantum simulator with trapped ions. *Nature*, 470.

[8] Bergeal, N., Schackert, F., Metcalfe, M., Vijay, R., Manucharyan, V., Frunzio, L., Prober, D. E., Schoelkopf, R., Girvin, S., and Devoret, M. (2010). Phase-preserving amplification near the quantum limit with a Josephson ring modulator. *Nature*, 465:64–68.

[9] Brooks, P., Kitaev, A., and Preskill, J. (2013). Protected gates for superconducting qubits. *Phys. Rev. A*, 87.

[10] Brune, M., Haroche, S., Raimond, J.-M., Davidovich, L., and Zagury, N. (1992). Manipulation of photons in a cavity by dispersive atom-field coupling: Quantum-nondemolition measurements and génération of "Schrödinger cat" states. *Physical Review A*, 45(7):5193–5214.

[11] Campagne-Ibarcq, P., Flurin, E., Roch, N., Darson, D., Morfin, P., Mirrahimi, M., Devoret, M., Mallet, F., and Huard, B. (2013). Persistent control of a superconducting qubit by stroboscopic measurement feedback. *Phys. Rev. X*, 3:021008.

[12] Carmichael, H. (2007). *Statistical Methods in Quantum Optics 2: Non-Classical Fields*. Spinger.

[13] Castellanos-Beltran, M., Irwin, K., Hilton, G., Vale, L., and Lehnert, K. (2008). Amplification and squeezing of quantum noise with a tunable josephson metamaterial. *Nature Physics*, 4:928–931.

[14] Chuang, I. L., Leung, D. W., and Yamamoto, Y. (1997). Bosonic quantum codes for amplitude damping. *Phys. Rev. A*, 56:1114–1125.

[15] Cohen, J. and Mirrahimi, M. (2014). Dissipation-induced continuous quantum error correction for superconducting circuits. *Phys. Rev. A*, 90:062344.

[16] Cohen, J., Smith, W. C., Devoret, M. H., and Mirrahimi, M. (2016). Continuous quantum non-demolition measurement of parity-type observables for cat-qubits. *submitted*.

[17] de Lange, G., Ristè, D., Tiggelman, M., Eichler, C., Tornberg, L., Johansson, G., Wallraff, A., Schouten, R., and DiCarlo, L. (2014). Reversing quantum trajectories with analog feedback. *Phys. Rev. Lett.*, 112:080501.

[18] Devoret, M. and Schoelkopf, R. (2013). Superconducting circuits for quantum information: An outlook. *Science*, 339:1169–1174.

[19] DiVincenzo, D. P. and Solgun, F. (2013). Multi-qubit parity measurement in circuit quantum electrodynamics. *New Journal of Physics*, 15(7):075001.

[20] Facchi, P. and Pascazio, S. (2002). Quantum zeno subspaces. *Phys. Rev. Lett.*, 89:080401.

[21] Fowler, A. G., Mariantoni, M., Martinis, J. M., and Cleland, A. N. (2012). Surface codes: Towards practical large-scale quantum computation. *Phys. Rev. A*, 86:032324.

[22] Gambetta, J., Blais, A., Boissonneault, M., Houck, A. A., Schuster, D. I., and Girvin, S. M. (2008). Quantum trajectory approach to circuit qed: Quantum jumps and the zeno effect. *Phys. Rev. A*, 77:012112.

[23] Gambetta, J., Blais, A., Schuster, D. I., Wallraff, A., Frunzio, L., Majer, J., Devoret, M. H., Girvin, S. M., and Schoelkopf, R. J. (2006). Qubit-photon interactions in a cavity: Measurement-induced dephasing and number splitting. *Phys. Rev. A*, 74:042318.

[24] Geerlings, K., Leghtas, Z., Pop, I., Shankar, S., Frunzio, L., Schoelkopf, R., Mirrahimi, M., and Devoret, M. (2013). Demonstrating a driven reset protocol of a superconducting qubit. *Phys. Rev. Lett.*, 110:120501.

[25] Gottesman, D. (1997). *Stabilizer Codes and Quantum Error Correction*. PhD thesis, Caltech.

[26] Gottesman, D., Kitaev, A., and Preskill, J. (2001). Encoding a qubit in an oscillator. *Phys. Rev. A*, 64:012310.

[27] Gramich, V., Kubala, B., Rohrer, S., and Ankerhold, J. (2013). From coulomb-blockade to nonlinear quantum dynamics in a superconducting circuit with a resonator. *Phys. Rev. Lett.*, 111:247002.

[28] Haroche, S. and Raimond, J. (2006). *Exploring the Quantum: Atoms, Cavities and Photons*. Oxford University Press.

[29] Hatridge, M., Vijay, R., Slichter, D. H., Clarke, J., and Siddiqi, I. (2011). Dispersive magnetometry with a quantum limited SQUID parametric amplifier. *Phys. Rev. B*, 83:134501.

[30] Heeres, R., Vlastakis, B., Holland, E., Krastanov, S., Albert, V., Frunzio, L., Jiang, L., and Schoelkopf, R. (2015). Cavity state manipulation using photon-number selective phase gates. *Phys. Rev. Lett.*, 115:137002.

[31] Hofer, P. P., Souquet, J.-R., and Clerk, A. A. (2016). Quantum heat engine based on photon-assisted cooper pair tunneling. *Phys. Rev. B*, 93:041418.

[32] Ioffe, L. and Mézard, M. (2007). Asymmetric quantum error-correcting codes. *Phys. Rev. A*, 75:032345.

[33] Ioffe, L. B., Feigel'man, M. V., Ioselevich, A., Ivanov, D., Troyer, M., and Blatter, G. (2002). Topologically protected quantum bits using josephson junction arrays. *Nature*, 415(503).

[34] Ippoliti, M., Mazza, L., Rizzi, M., and Giovannetti, V. (2015). Perturbative approach to continuous-time quantum error correction. *Phys. Rev. A*, 91:042322.

[35] Kapit, E., Chalker, J. T., and Simon, S. H. (2015). Passive correction of quantum logical errors in a driven, dissipative system: A blueprint for an analog quantum code fabric. *Phys. Rev. A*, 91:062324.

[36] Kapit, E., Hafezi, M., and Simon, S. H. (2014). Induced self-stabilization in fractional quantum hall states of light. *Phys. Rev. X*, 4:031039.

[37] Kelly, J., Barends, R., Fowler, A., Megrant, A., Jeffrey, E., White, T., Sank, D., Mutus, J., Campbell, B., Chen, Y., Chen, Z., Chiaro, B., Dunsworth, A., Hoi, I., Neill, C., O'Malley, P., Quintana, C., Roushan, P., Vainsencher, A., Wenner, J., Cleland, A., and Martinis, J. (2015). State preservation by repetitive error detection in a superconducting quantum circuit. *Nature*, 519:66–69.

[38] Kerckhoff, J., Nurdin, H., Pavlichin, D., and Mabuchi, H. (2010). Designing quantum memories with embedded control: photonic circuits for autonomous quantum error correction. *Phys. Rev. Lett.*, 105:040502.

[39] Kerckhoff, J., Pavlichin, D., Chalabi, H., and Mabuchi, H. (2011). Design of nanophotonic circuits for autonomous subsystem quantum error correction. *New J. Phys.*, 13:055022.

[40] Koch, J., Yu, T., Gambetta, J., Houck, A., Schuster, D., Majer, J., Blais, A., Devoret, M., Girvin, S., and Schoelkopf, R. (2007). Charge-insensitive qubit design derived from the cooper pair box. *Phys. Rev. A*, 76:042319.

[41] Korenev, B. G. (2002). *Bessel functions and their applications*. Analytical methods and special functions v.8. Chapman & Hall/CRC, 1 edition.

[42] Krauter, H., Muschik, C., Jensen, K., Wasilewski, W., Petersen, J., Cirac, J., and Polzik, E. (2011). Entanglement generated by dissipation and steady state entanglement of two macroscopic objects. *Phys. Rev. Lett.*, 107:080503.

[43] Leghtas, Z., Kirchmair, G., Vlastakis, B., Devoret, M., Schoelkopf, R., and Mirrahimi, M. (2013a). Deterministic protocol for mapping a qubit to coherent state superpositions in a cavity. *Phys. Rev. A*, 87:042315.

[44] Leghtas, Z., Kirchmair, G., Vlastakis, B., Schoelkopf, R., Devoret, M., and Mirrahimi, M. (2013b). Hardware-efficient autonomous quantum memory protection. *Phys. Rev. Lett.*, 111:120501.

[45] Leghtas, Z., Touzard, S., Pop, I., Kou, A., Vlastakis, B., Petrenko, A., Sliwa, K., Narla, A., Shankar, S., Hatridge, M., Reagor, M., Frunzio, L., Schoelkopf, R., Mirrahimi, M., and Devoret, M. (2015). Confining the state of light to a quantum manifold by engineered two-photon loss. *Science*, 347:853–857.

[46] Leghtas, Z., Vool, U., Shankar, S., Hatridge, M., Girvin, S., Devoret, M., and Mirrahimi, M. (2013c). Stabilizing a Bell state of two superconducting qubits by dissipation engineering. *Phys. Rev. A*, 88:023849.

[47] Leung, D., Nielsen, M., Chuang, I., and Yamamoto, Y. (1997). Approximate quantum error correction can lead to better codes. *Phys. Rev. A*, 56:2567–2573.

[48] Lin, Y., Gaebler, J., Reiter, F., Tan, T., Bowler, R., Sorensen, A., Leibfried, D., and Wineland, D. (2013). Dissipative production of a maximally entangled steady state of two quantum bits. *Nature*, 504:415–418.

[49] Lloyd, S. (2000). Coherent quantum feedback. *Phys. Rev. A*, 62:022108.

[50] Masluk, N., Pop, I., Kamal, A., Minev, Z., and Devoret, M. (2012a). Microwave characterization of Josephson junction arrays: Implementing a low loss superinductance. *Phys. Rev. Lett.*, 109:137002.

[51] Masluk, N. A., Pop, I. M., Kamal, A., Minev, Z. K., and Devoret, M. H. (2012b). Microwave characterization of josephson junction arrays: Implementing a low loss superinductance. *Phys. Rev. Lett.*, 109(12):137002.

[52] Michael, M. H., Silveri, M., Brierley, R. T., Albert, V. V., Salmilehto, J., Jiang, L., and Girvin, S. M. (2016). New class of quantum error-correcting codes for a bosonic mode. *Phys. Rev. X*, 6:031006.

[53] Mirrahimi, M., Leghtas, Z., Albert, V., Touzard, S., Schoelkopf, R., Jiang, L., and Devoret, M. (2014). Dynamically protected cat-qubits: a new paradigm for universal quantum computation. *New J. Phys.*, 16:045014.

[54] Mirrahimi, M. and Rouchon, P. (2010). Modeling and control of quantum systems. Lecture notes.

[55] Murch, K., Vool, U., Zhou, D., Weber, S., Girvin, S., and Siddiqi, I. (2012). Cavity-assisted quantum bath engineering. *Phys. Rev. Lett.*, 109:183602.

[56] Nakamura, Y., Pashkin, Y., and Tsai, J. (1999). Coherent control of macroscopic quantum states in a single-cooper-pair box. *Nature*, 398:786.

[57] Nielsen, M. and Chuang, I. (2000). *Quantum Computation and Quantum Information*. Cambridge University Press.

[58] Nigg, S., Paik, H., Vlastakis, B., Kirchmair, G., Shankar, S., Frunzio, L., Devoret, M., Schoelkopf, R., and Girvin, S. (2012). Black-box superconducting circuit quantization. *Phys. Rev. Lett*, 108:240502.

[59] Ofek, N., Petrenko, A., Reinhold, R. H. P., Leghtas, Z., Vlastakis, B., Liu, Y., Frunzio, L., Girvin, S., Jiang, L., Mirrahimi, M., Devoret, M., and Schoelkopf, R. (2016). Demonstrating quantum error correction that extends the lifetime of quantum information. *Nature*, 536:441–445.

[60] Paik, H., Schuster, D., Bishop, L., Kirchmair, G., Catelani, G., Sears, A., Johnson, B., Reagor, M., Frunzio, L., Glazman, L., Girvin, S., Devoret, M., and Schoelkopf, R. (2011a). Observation of high coherence in josephson junction qubits measured in a three-dimensional circuit qed architecture. *Phys. Rev. Lett.*, 107:240501.

[61] Paik, H., Schuster, D. I., Bishop, L. S., Kirchmair, G., Catelani, G., Sears, A. P., Johnson, B. R., Reagor, M. J., Frunzio, L., Glazman, L. I., Girvin, S. M., Devoret, M. H., and Schoelkopf, R. J. (2011b). Observation of high coherence in josephson junction qubits measured in a three-dimensional circuit qed architecture. *Phys. Rev. Lett.*, 107:240501.

[62] Paz, J. P. and Zurek, W. H. (1998). Continuous error correction. *Proceedings of the Royal Society of London A: Mathematical, Physical and Engineering Sciences*, 454(1969):355–364.

[63] Penrose, R. (1955). A generalized inverse for matrices. *Mathematical Proceedings of the Cambridge Philosophical Society*, 51(3):406–413.

[64] Pop, I., Geerlings, K., Catelani, G., Schoelkopf, R., Glazman, L., and Devoret, M. (2014). Coherent suppression of electromagnetic dissipation due to superconducting quasiparticles. *Nature*, 508:369–372.

[65] Poyatos, J., Cirac, J., and Zoller, P. (1996). Quantum reservoir engineering with laser cooled trapped ions. *Phys. Rev. Lett.*, 77(23):4728–4731.

[66] Preskill, J. (2015). Chapter 7 : Quantum error correction. Lecture notes.

[67] Prudnikov, A. P., Brychkov, Y. A., and Marichev, O. I. (1992). *Integrals and Series Vol 2 : Special Functions*, volume 2. London: Gordon and Breach, 1st edition.

[68] Puri, S. and Blais, A. (2016). Engineering the quantum states of light in a kerr-nonlinear resonator by two-photon driving. *arXiv:1605.09408*.

[69] Reagor, M., Paik, H., Catelani, G., Sun, L., Axline, C., Holland, E., Pop, I., Masluk, N., Brecht, T., Frunzio, L., Devoret, M., Glazman, L., and Schoelkopf, R. (2013). Reaching 10 ms single photon lifetimes for superconducting aluminum cavities. *Applied Physics Letters*, 102:192604.

[70] Reagor, M., Pfaff, W., Axline, C., Heeres, R. W., Ofek, N., Sliwa, K., Holland, E., Wang, C., Blumoff, J., Chou, K., Hatridge, M. J., Frunzio, L., Devoret, M. H., Jiang, L., and Schoelkopf, R. J. (2016). Quantum memory with millisecond coherence in circuit qed. *Physical Review B*, 94(1):014506–.

[71] Richtmyer, R. D. (1978). *Principles of Advanced Mathematical Physics*, pages 52–67. Springer Berlin Heidelberg.

[72] Rigetti, C., Gambetta, J. M., Poletto, S., Plourde, B. L. T., Chow, J. M., Córcoles, A. D., Smolin, J. A., Merkel, S. T., Rozen, J. R., Keefe, G. A., Rothwell, M. B., Ketchen, M. B., and Steffen, M. (2012). Superconducting qubit in a waveguide cavity with a coherence time approaching 0.1 ms. *Phys. Rev. B*, 86:100506.

[73] Ristè, D., Leeuwen, J., Ku, H.-S., Lehnert, K., and Dicarlo, L. (2012). Initialization by measurement of a superconducting quantum bit circuit. *Phys. Rev. Lett.*, 109:050507.

[74] Roch, N., Flurin, E., Nguyen, F., Morfin, P., Campagne-Ibarcq, P., Devoret, M., and Huard, B. (2012). Widely tunable, non-degenerate three-wave mixing microwave device operating near the quantum limit. *Phys. Rev. Lett.*, 108:147701.

[75] Roch, N., Schwartz, M., Motzoi, F., Macklin, C., Vijay, R., Eddins, A., Korotkov, A., Whaley, K., Sarovar, M., and Siddiqi, I. (2014). Observation of measurement-induced entanglement and quantum trajectories of remote superconducting qubits. *Phys. Rev. Lett.*, 112:170501.

[76] Sanders, J. and Verhulst, F. (1987). *Averaging Methods in Nonlinear Dynamical Systems*. Springer.

[77] Sarma, G. and Mabuchi, H. (2013). Gauge subsystems, separability and robustness in autonomous quantum memories. *New Journal of Physics*, 15.

[78] Schuster, D., Houck, A., Schreier, J., Wallraff, A., Gambetta, J., Blais, A., Frunzio, L., Majer, J., Johnson, B., Devoret, M., Girvin, S., and Schoelkopf, R. J. (2007). Resolving photon number states in a superconducting circuit. *Nature*, 445:515–518.

[79] Shankar, S., Hatridge, M., Leghtas, Z., Sliwa, K., Narla, A., Vool, U., Girvin, S., Frunzio, L., Mirrahimi, M., and Devoret, M. (2013). Autonomously stabilized entanglement between two superconducting quantum bits. *Nature*, 504:419–422.

[80] Shor, P. (1995). Scheme for reducing decoherence in quantum memory. *Phys. Rev. A*, 52:2493–2496.

[81] Steane, A. (1996). Error correcting codes in quantum theory. *Phys. Rev. Lett*, 77(5).

[82] Sun, L., Petrenko, A., Leghtas, Z., Vlastakis, B., Kirchmair, G., Sliwa, K., Narla, A., Hatridge, M., Shankar, S., Blumoff, J., Frunzio, L., Mirrahimi, M., Devoret, M., and Schoelkopf, R. (2014). Tracking photon jumps with repeated quantum non-demolition parity measurements. *Nature*, 511:444–448.

[83] Szegö, G. (1939-1975). *Orthogonal polynomials*. Colloquium publications (American Mathematical Society), v. 23. American Mathematical Society, 4th ed edition.

[84] Tornberg, L., Barzanjeh, S., and DiVincenzo, D. P. (2014). Stochastic-master-equation analysis of optimized three-qubit nondemolition parity measurements. *Phys. Rev. A*, 89:032314.

[85] Touzard, S., Leghtas, Z., Mundhada, S., Axline, C., Chou, K., Blumoff, J., Sliwa, K., Shankar, S., Frunzio, L., Schoelkopf, R., Mirrahimi, M., and Devoret, M. (2016). Encoding quantum information in a stabilized manifold of a superconducting cavity. In *APS March Meeting*. American Physical Society.

[86] Trif, M. and Simon, P. (2015). Photon cross-correlations emitted by a josephson junction in two microwave cavities. *Phys. Rev. B*, 92:014503.

[87] Vijay, R., Macklin, C., Slichter, D., Weber, S., Murch, K., Naik, R., Korotkov, A., and Siddiqi, I. (2012). Stabilizing Rabi oscillations in a superconducting qubit using quantum feedback. *Nature*, 490:77–80.

[88] Vlastakis, B., Kirchmair, G., Leghtas, Z., Nigg, S., Frunzio, L., Girvin, S., Mirrahimi, M., Devoret, M., and Schoelkopf, R. (2013). Deterministically encoding quantum information using 100-photon Schrödinger cat states. *Science*, 342:607–610.

[89] Vool, U., Shankar, S., Mundhada, S. O., Ofek, N., Narla, A., Sliwa, K., Zalys-Geller, E., Liu, Y., Frunzio, L., Schoelkopf, R. J., Girvin, S. M., and Devoret, M. H. (2016). Continuous quantum nondemolition measurement of the transverse component of a qubit. *Phys. Rev. Lett.*, 117:133601.

[90] Wallraff, A., Schuster, D., Blais, A., Frunzio, L., R.-Huang, Majer, J., Kumar, S., Girvin, S., and Schoelkopf, R. (2004). Strong coupling of a single photon to a superconducting qubit using circuit quantum electrodynamics. *Nature*, 431:162–167.

[91] Wang, C., Gao, Y., Reinhold, P., Heeres, R., Ofek, N., Chou, K., C. Axline, M. R., Blumoff, J., Sliwa, K., Frunzio, L., Girvin, S., Jiang, L., Mirrahimi, M., Devoret, M., and Schoelkopf, R. (2016). A schrödinger cat living in two boxes. *Science*, 352:1087–1091.

Résumé

Dans cette thèse, nous développons plusieurs outils pour la Correction d'Erreur Quantique (CEQ) autonome avec les qubits supraconducteurs.

Nous proposons un schéma de CEQ autonome qui repose sur la technique du « reservoir engineering », dans lequel trois qubits de type transmon sont couplés à un ou plusieurs modes dissipatifs. Grâce à la mise au point d'une interaction effective entre les systèmes, l'entropie créée par les éventuelles erreurs est évacuée à travers les modes dissipatifs.

La deuxième partie de ce travail porte sur un type de code récemment développé, le code des chats, à travers lequel l'information logique est encodée dans le vaste espace de Hilbert d'un oscillateur harmonique. Nous proposons un protocole pour réaliser des mesures continues et non-perturbatrices de la parité du nombre de photons dans une cavité micro-onde, ce qui correspond au syndrome d'erreur pour le code des chats.

Enfin, en utilisant les résultats précédents, nous présentons plusieurs protocoles de CEQ continus et/ou autonomes basés sur le code des chats. Ces protocoles offrent une protection robuste contre les canaux d'erreur dominants en présence de dissipation stimulée à plusieurs photons.

Abstract

In this thesis, we develop several tools in the direction of autonomous Quantum Error Correction (QEC) with superconducting qubits.

We design an autonomous QEC scheme based on quantum reservoir engineering, in which transmon qubits are coupled to lossy modes. Through an engineered interaction between these systems, the entropy created by eventual errors is evacuated via the dissipative modes.

The second part of this work focus on the recently developed cat codes, through which the logical information is encoded in the large Hilbert space of a harmonic oscillator. We propose a scheme to perform continuous and quantum non-demolition measurements of photon-number parity in a microwave cavity, which corresponds to the error syndrome in the cat code. In our design, we exploit the strongly nonlinear Hamiltonian of a high-impedance Josephson circuit, coupling a high-Q cavity storage cavity mode to a low-Q readout one. Last, as a follow up of the above results, we present several continuous and/or autonomous QEC schemes using the cat code. These schemes provide a robust protection against dominant error channels in the presence of multi-photon driven dissipation.

Mots-clés

Information quantique, circuits supraconducteurs, correction d'erreur quantique, reservoir engineering, mesure non-destructrice de syndromes d'erreurs, calcul quantique tolérant à l'erreur

Keywords

Quantum information, supraconducting circuits, quantum error correction, reservoir engineering, quantum non-demolition measurement of error syndromes, fault-tolerant quantum computation